Conference Proceedings

Workshop

GRK 2462

"Processes in natural and technical Particle-Fluid-Systems"(PintPFS)

26^{th} & 27^{th} of September 2022
Hamburg, Germany

Editor

J. Grabe

Hamburg University of Technology
Institute of Geotechnical Engineering and Construction Management

Publications by the Institute of
Geotechnical Engineering and Construction Management

54

Editor:

Univ.-Prof. Dr.-Ing. Jürgen Grabe
Hamburg University of Technology
Institute of Geotechnical Engineering and Construction Management
Harburger Schloßstraße 36
D – 21079 Hamburg
E-Mail: *grabe@tuhh.de*

ISBN-13: 978-3-936310-56-6 (first edition)

Printery

Druckzentrum Neumünster GmbH
Rungestraße 4
D – 24537 Neumünster

Published in the same series:

1. J. Grabe (eds.), 2000: Verbrennungsrückstände. Conference Proceedings, ISBN 3-936310-00-9
2. J. Grabe (eds.), 2001: Schaden- und Risikomanagement im Tiefbau. Conference Proceedings, ISBN 3-936310-01-7
3. J. Grabe, 2003. Bodenmechanik und Grundbau. ISBN 3-936310-03-3
4. J. Grabe (eds.), 2003: Euronormen in der Geotechnik – Was ändert sich? Conference Proceedings, ISBN 3-936310-04-1
5. J. Grabe (eds.), 2003: Bodenverdichtung, Experimente - Modellierung - Geräteentwicklung - Baustellenberichte - F+E-Bedarf. Conference Proceedings, ISBN 3-936310-05-X
6. M. Kelm, 2004: Nummerische Simulation der Verdichtung rolliger Böden mittels Vibrationswalzen. Dissertation, ISBN 3-936310-06-8
7. J. Grabe (eds.), 2004: Kaimauern - Messungen und Numerik. Conference Proceedings, ISBN 3-936310-07-6
8. J. Stein, 2005. Experimentelle und numerische Untersuchungen zum Düsenstrahlverfahren. Promotion, ISBN 3-936310-09-2
9. J. Grabe (eds.), 2005: Grenzschicht Wasser und Boden - Phänomene und Ansätze. Conference Proceedings, ISBN 3-936310-10-6
10. J. Grabe (eds.), 2005: FEM in der Geotechnik - Qualität, Prüfung, Fallbeispiele - Conference Proceedings, ISBN 3-936310-11-4
11. B. Mardfeldt, 2006: Zum Tragverhalten von Kaikonstruktionen im Gebrauchszustand. Dissertation, ISBN 3-936310-12-2
12. J. Grabe (eds.), 2006: Optimierung in der Geotechnik - Strategien und Fallbeispiele. Conference Proceedings, ISBN-13: 978-3-936310-13-9
13. T. Bierer, 2007: Bodenschwingungen aus Straßenverkehr auf unebener Fahrbahn im Zeitbereich - experimentelle und theoretische Untersuchungen. Dissertation, ISBN-13: 978-3-936310-14-6
14. J. Grabe (eds.), 2007: Bemessen mit Finite-Elemente-Methoden. Conference Proceedings, ISBN-13: 978-3-936310-15-3
15. K.-P. Mahutka, 2008: Zur Verdichtung von rolligen Böden infolge dynamischer Pfahleinbringung und durch Oberflächenrüttler. Dissertation, ISBN-13: 978-3-936310-16-0
16. J. Grabe (eds.), 2008: Seehäfen für Containerschiffe zukünftiger Generationen. Conference Proceedings, ISBN-13: 978-3-936310-17-7

17. F. König, 2008: Zur zeitlichen Traglastentwicklung von Pfählen und der nachträglichen Erweiterung bestehender Pfahlgründungen. Dissertation, ISBN-13: 978-3-936310-18-4

18. S. Henke, 2008: Herstellungseinflüsse aus Pfahlrammung im Kaimauerbau. Dissertation, ISBN-13: 978-3-936310-19-1

19. J. Grabe (eds.), 2009: Spundwände – Profile, Tragverhalten, Bemessung, Einbringung und Wiedergewinnung. Conference Proceedings, ISBN-13: 978-3-936310-20-7

20. J. Dührkop, 2009: Zum Einfluss von Aufweitungen und zyklischen Lasten auf das Verformungsverhalten lateral beanspruchter Pfähle in Sand. Dissertation, ISBN-13: 978-3-936310-21-4

21. O. Möller, 2009: Zum Langzeit-Kompressionsverhalten weicher organischer Sedimente. Dissertation, ISBN-13: 978-3-936310-22-1

22. J. Grabe (eds.), 2011: Ports of container ships of future generations. Conference Proceedings, ISBN-13: 978-3-936310-23-8

23. S. Kinzler, 2011: Zur Parameteridentifikation, Entwurfs- und Strukturoptimierung in der Geotechnik mittels numerischer Verfahren. Dissertation, ISBN-13: 978-3-936310-24-5

24. G. Qiu, 2012: Coupled Eulerian Lagrangian Simulations of Selected Soil-Structure Problems. Dissertation, ISBN-13: 978-3-936310-25-2

25. X. Ma, 2013: Nutzung der oberflächennahen Geothermie mittels Energiepfählen und Erdwärmesonden. Dissertation, ISBN-13: 978-3-936310-26-9

26. J. Grabe (eds.), 2013: Proceedings of the Conference on Maritime Energy COME 2013. Conference Proceedings, ISBN-13: 978-3-936310-28-3

27. J. Grabe (eds.), 2013: Bemessen mit numerischen Methoden. Conference Proceedings, ISBN-13: 978-3-936310-29-0

28. T. Pucker, 2013: Stoffmodell zur Modellierung von stetigen Materialübergängen im Rahmen der Optimierung geotechnischer Strukturen. Dissertation, ISBN-13: 978-3-936310-30-6

29. S. Henke, 2013: Untersuchungen zur Pfropfenbildung infolge der Installation offener Profile in granularen Böden. Habilitation, ISBN-13: 978-3-936310-31-3

30. J. Grabe (eds.), 2014: Ports for Container Ships of Future Generations. Conference Proceedings, ISBN-13: 978-3-936310-32-0

31. J. Grabe (eds.), 2014: Offshore Basishäfen, Conference Proceedings, ISBN-13: 978-3-936310-33-7

32. C. Rudolph, 2015. Untersuchungen zur Drift von Pfählen unter zyklischer, lateraler Last aus veränderlicher Richtung, Dissertation, ISBN-13: 978-3-936310-34-4

33. J. Grabe (eds.), 2015: Morphodynamics 2015, Conference Proceedings, ISBN-13: 978-3-936310-35-1

34. T. Hamann, 2015: Zur Modellierung wassergesättigter Böden unter dynamischer Belastung und großen Bodenverformungen am Beispiel der Pfahleinbringung, Dissertation, ISBN-13: 978-3-936310-36-8

35. B. Schümann, 2015: Beitrag zum dynamischen Dreiphasenmodell für Boden auf Basis der Finite-Elemente-Methode, Dissertation, ISBN-13: 978-3-936310-37-5

36. M. Milatz, 2015: Untersuchungen zum Einfluss der Kapillarität auf das hydraulisch-mechanische Verhalten von granularer Tragschichten für Verkehrswege, Dissertation, ISBN-13: 978-3-936310-38-2

37. H. Kaya, 2016: Bodenverschleppung und Spaltbildung infolge der Einbringung von Profilen in Dichtungsschichten aus Ton, Dissertation, ISBN-13: 978-3-936310-39-9

38. J. Grabe (eds.), 2017: Proceedings of the Conference on Maritime Energy COME 2017. Conference Proceedings, ISBN-13: 978-3-936310-40-5

39. B. Kocak, 2017: Zur numerischen Modellierung von hydraulisch-mechanisch gekoppelten Prozessen in gesättigten granularen Böden mittels Smoothed Particle Hydrodynamics, Dissertation, ISBN-13: 978-3-936310-41-2

40. K. Siegl, 2017: Zur Pfahldynamik von gerammten Großrohrpfählen und der daraus resultierenden Wellenausbreitung in Wasser und im Meeresboden, Dissertation, ISBN-13: 978-3-936310-42-9

41. J. Grabe (eds.), 2017: Numerical Methods in Geotechnics, Conference Proceedings, ISBN-13: 978-3-936310-43-6

42. J. Grabe (eds.), 2018: Digitale Infrastruktur und Geotechnik (DIG 2018), Conference Proceedings, ISBN-13: 978-3-936310-44-3

43. D. Osthoff, 2018: Zur Ursache von Schlosssprengungen und zu einbringbedingten Lageabweichungen von Spundwänden, Dissertation, ISBN-13: 978-3-936310-45-0

44. E. Heins, 2018: Numerical based identification of the pile-soil interaction in terms of the axial pile bearing capacity, Dissertation, ISBN-13: 978-3-936310-46-7

45. K.-F. Seitz, 2021: Zur Topologieoptimierung von geotechnischen Strukturen und zur Tragfähigkeitssteigerung des Baugrunds durch Scherfugenverfestigung, Dissertation, ISBN-13: 978-3-936310-47-4

46. D. Plenker, 2021: Physical and numerical investigations of the dynamic interaction of saturated granulates and fluid, Dissertation, ISBN-13: 978-3-936310-48-1

47. J. Grabe, J.-O. Backhaus & P. Vogel, 2021: Bauprojektmanagement, ISBN-13: 978-3-936310-49-8

48. M. Kanitz, 2021: Experimental and numerical investigations of particle-fluid systems in geotechnical engineering, Dissertation, ISBN-13: 978-3-936310-50-4

49. J.-O. Backhaus, 2021: A methodology for the numeric time-cost forecast and pareto optimization of large injection projects in tunneling, Dissertation, ISBN-13: 978-3-936310-51-1

50. S. N. Sinduri, 2021: Optimisation of deep compaction as liquefaction mitigation measure, Dissertation, ISBN-13: 978-3-936310-52-8

51. J. Bubel, 2022: Zum Versagen von Unterwasserböschungen im Seegang, Dissertation, ISBN-13: 978-3-936310-53-5

52. J. Grabe (eds.), 2022: Adaptiv Structures At Shore 2022 (ASS2022), Conference Proceedings, ISBN-13: 978-3-936310-54-2

53. J. Grabe (eds.), 2022: Numerische Methoden in der Geotechnik, Conference Proceedings, ISBN 978-3-936310-55-9

Table of Contents

Preface 1

PROCESSES IN NATURAL AND TECHNICAL PARTICLE-FLUID-SYSTEMS (PFS)

Investigation of unsaturated granular soil behavior by means of in situ CT experiments 3
Marius Milatz

Complex multiscale solid-fluid interactions in drying porous media 15
Nima Shokri

DRY AND UNSATURATED PFS

Investigations for the development of a new test method to prevent the alkali-silica reaction . 19
Gyde Hartmut

New findings on alkali-silica-reaction of concrete 33
Andreas Leemann

Numerical investigation of the breakage and crash absorbing behavior of granular materials in ship collisions 37
Sonja Rotter

Virtual elements and their use as deformable particles in DEM 53
Peter Wriggers

Molecular Dynamic studies of liquid / solid interfaces in aqueous and ionic liquid systems . 65
Johannes Gäding

Optimizing liquid solid slip in nanofluidic systems 79
Laurent Joly

xDEM Simulation of Frozen Particle Fluid System subjected to shearing..... 81
Tsz Tung Chan

Application of discrete element method to analyze micromechanics of granular materials .. 95
Sergiy Antonyuk

Experimental investigation of capillary collapse of partially saturated granular media 109
Nicole Hüsener

Micromechanical insights into the capillary collapse of granular materials 123
Jean-Michel Pereira

SATURATED PFS

Imbibition and Wetting Front Broadening in Mesoporous Silica Glass 127
Juan Sánchez Calzado

Condensation-Induced Restructuring of Atmospheric Soot Aggregates 143
Gennady Gor

FUNCTIONALIZED PFS

Influence of coating solution concentration on particle surface structure during fluidized bed spray granulation 155
Maike Orth

About modeling rheology and agglomeration of wet particle systems 169
Stefan Luding

Retention Characteristics of Biopolymer Materials Studied by Inverse Supercritical Fluid Chromatography 177
Isabella Jung

Recent Advances and Uses of Aerogels for Biomedical Applications 189
Carlos Alberto Garcia Gonzalez

Preface

In the framework of Research Training Group GRK 2462 “Processes in Natural and Technical Particle-Fluid-Systems” (PintPFS), funded by the German Research Foundation (DFG), researchers from the fields of civil engineering, mechanical engineering, process engineering, and materials sciences investigate natural and technical Particle-Fluid-Systems (PFS) in an interdisciplinary approach.

As PFS are ubiquitous in everyday life and relevant for many processes in industry, pharmacy, and food production, they represent a highly interesting field of research with potential for promising and useful discoveries in many aspects.

GRK 2462 is formed by eight professors from Hamburg University of Technology leading the PhD research projects of eight junior scientists. In this international conference, the Research Training Group brings together all associated scientists and external guest scientists to present and discuss research results of the first 3 year period. While the junior scientists give insights into their research work at TUHH, the international guest scientists will present on the corresponding state of the art in their related fields of research.

These proceedings have been compiled based on different topics presented in the framework of the conference. They are supposed to preserve the findings for their future scientific and practical use and to share them with the research community.

We are looking forward to the numerous precious contributions, presentations and constructive discussions.

Sincerely yours,

Jürgen Grabe and Marius Milatz

Hamburg, 26$^{\text{th}}$ of August 2022

Investigation of unsaturated granular soil behaviour by means of *in situ* CT experiments

Marius Milatz

Abstract: In this contribution, the non-destructive imaging technique of computed tomography (CT) is applied in geomechanics research on unsaturated granular soils, such as sands, to study the soil behaviour by means of so-called *in situ* CT experiments, *i. e.*, experiments run inside a CT scanning environment. With the help of dedicated miniaturised experimental set-ups applied in CT scanning systems, spatial and temporal data during geomechanical experiments can be acquired and analysed to obtain qualitative and quantitative insights on the grain or pore scale. In this contribution, different experimental set-ups, their application, and selected results of the current research are presented and discussed.

1 Introduction

In unsaturated granular soils under natural conditions, generally three phases are present: the solid or grain phase (soil), the liquid phase (water), and the gas phase (air). Due to the physical phenomenon of capillarity, driven by interfacial tension, the liquid phase tends to minimise its surface when in contact with the solid and gas phase. This leads to the presence of water clusters and liquid bridges inside the pore space of granular soils in the unsaturated state, *i. e.*, when the pore space is partially filled with water as the wetting fluid and air as the non-wetting fluid. In the unsaturated state, capillary pressure builds up inside the pore water and affects the effective stress state of the soil skeleton leading to an increase in shear strength and soil stiffness. Furthermore, the coexistence of air and water in the pore space influences the hydraulic permeability of unsaturated soil with regard to water and air flow. The build-up of capillary pressure p_c, also known as matric suction s, can be related to degree of saturation S_r, defined as the ratio of water volume per pore volume, yielding a so-called water retention curve (WRC) which is typically measured experimentally. The WRC is an important macroscopic relationship as it can be applied to model shear strength and hydraulic conductivity in the unsaturated state (Fredlund & Rahardjo, 1993). The WRC is typically a hysteretic relationship, yielding different suction responses for drainage and imbibition of a soil. This behaviour is believed to originate from several phenomena occurring on the pore scale of a soil.

With the development of imaging techniques in the last decades in the field of materials science, their application in engineering research is also an emerging field. Imaging methods, such as X-ray CT, generally represent non-destructive techniques to obtain 3D information of speci-

mens that are scanned by means of X-ray radiation. According to the principle of CT, 2D radiographies are acquired from different angles from which 2D specimen cross sections and finally the whole specimen can be reconstructed in 3D, based on mathematical reconstruction algorithms. Image contrast is achieved because X-ray photons are attenuated when passing through matter. As the magnitude of X-ray attenuation depends on the density of the scanned materials, a density contrast is achieved in X-ray tomographies, allowing to segment, *i. e.*, differentiate between different material phases present in the scanned specimen.

Besides laboratory X-ray sources, where typically X-ray tubes create polychromatic X-ray beams, also synchrotron radiation, consisting of X-ray photons with a very high brilliance or flux, can be applied for imaging (Wildenschild and Sheppard, 2013). Furthermore, neutrons can be used for CT imaging, yielding a complementary contrast when interacting with matter as compared to X-rays. Due to the high attenuation of neutrons when passing through water, their application in imaging of geomaterials is very useful (Tengattini *et al.*, 2021).

In this constribution, we focus on the application of X-ray CT imaging to study processes with relevance to geomechanics research in unsaturated granular soils. For this purpose, so-called *in situ* CT imaging experiments are applied which generally include the repeated temporal scanning of soil specimens submitted to a physical process to be studied, *e. g.*, mechanical loading or fluid flow. This allows to capture and analyse temporal processes in three dimensions which is known as "4D imaging" (with the time being the 4th dimension). Different custom-built experimental set-ups have been designed and applied in CT imaging experiments with a geomechanics background. The obtained multiphase data are analysed to obtain insights into the physical behaviour of unsaturated granular soils from a pore scale perspective. An overview of selected developed experiments and analysis techniques as well as of experimental findings on the pore scale will be given.

In the presented experiments, two model soils, Hamburg Sand and glass beads (Milatz *et al.*, 2021) are studied. While Hamburg Sand represents a medium coarse to coarse grained model sand used in the soil mechanics lab at TUHH, the polydisperse mixture of soda-lime glass beads mimics the grain size distribution of Hamburg Sand, representing a model soil with nearly perfectly rounded spherical grains.

2 *In situ* CT experiments

In this section, different customised and miniaturised experimental set-ups for *in situ* CT experiments on unsaturated granular soils are presented along with information about the selected hardware and functionality of each individual set-up.

2.1 Uniaxial compression testing

In order to study the shear behaviour of unsaturated granular materials with parallel CT imaging, the miniaturised uniaxial compression apparatus presented in Milatz (2019) has been applied at Laboratoire 3SR at Univ. Grenoble Alpes. With the help of the X-ray tomograph described in Viggiani *et al.* (2015), a sequence of CT images was taken during sequential uniaxial compression steps on cylindrical Hamburg Sand and glass bead specimens.

The miniaturised uniaxial compression device consists of a stepper motor to drive down a loading plate vertically and compress a granular specimen placed on a bottom plate as shown in Figure 1. The compressive force for shearing the specimen is measured by a miniature load cell underneath the bottom loading plate. The hardware is driven by a Raspberry Pi single-board computer and described in detail in Milatz (2019) and Milatz *et al.* (2021).

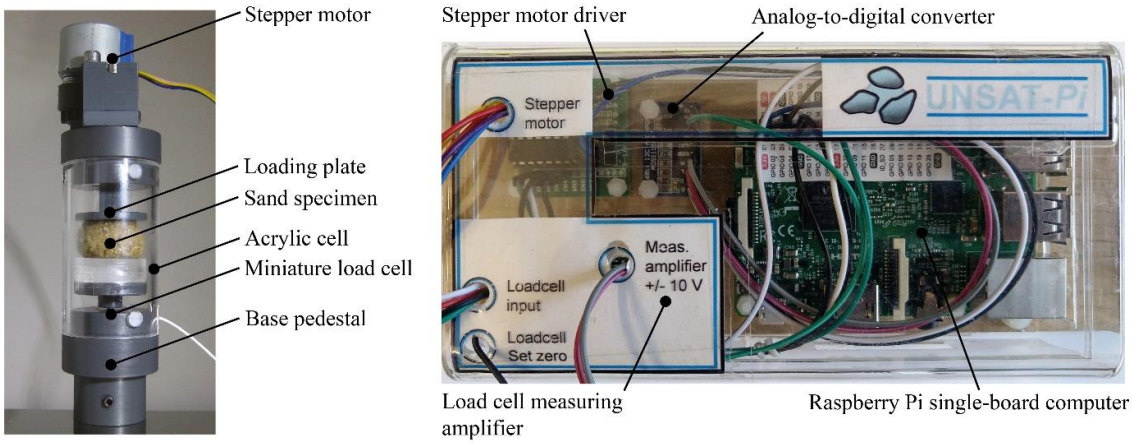

Figure 1: Miniaturised uniaxial compression set-up, named the "UNSAT-*Pi*", consisting of a stepper motor for displacement controlled loading, a loadcell in the base pedestal and a Raspberry Pi single-board computer for experimental control and data acquisition from Milatz *et al.* (2021).

In an experimental campaign reported in detail in Milatz *et al.* (2021), 3D images have been acquired in between different displacement controlled uniaxial compression steps on unsaturated Hamburg Sand and glass bead specimens under variation of their fixed initial degree of saturation S_{r0}. The resulting CT data at a voxel size of 11 µm have been segmented, *i. e.*, separated into the three present phases, solid, water, and air. Afterwards, further image analysis steps have been applied, *e. g.*, to study the evolution of water clusters or interfacial areas during shearing with focus on the evolution of such "*capillary state variables*" characterising the capillary action inside the soil.

2.2 Water retention experiments

A miniaturised flow cell set-up to investigate the transient water retention behaviour of granular soils by means of *in situ* CT imaging on the pore scale has been designed and applied in different imaging environments. The set-up, named the "UNSAT-*Pi* 2", basically consists of a syringe pump and a set of pressure sensors as well as a Raspberry Pi single-board computer to control the pump and to log pore water pressure data in a connected flow cell. Unlike conventional experiments, the WRC of the granular material inside the flow cell is measured based on a prescribed temporal change of degree of saturation at a constant flow rate of pore water. The resulting response of matric suction is measured by means of a sensor system taking readings of negative water pressure inside the specimen. The whole set-up is small enough to operate on the rotation stage of a CT scanning system.

Besides a water retention experiment run at Laboratoire 3SR in Grenoble, using the local laboratory X-ray CT system, on which we focus in this contribution, different experiments have been run at the Institut Laue-Langevin (ILL) in Grenoble using combined X-ray and neutron tomography (Milatz *et al.*, 2019) and at the German Synchrotron Radiation Facility (Deutsches Elektronen-Synchrotron, DESY) in Hamburg, where synchrotron-based X-ray CT with propagation-based phase contrast was applied to study cyclic drainage and imbibition on the pore scale of different granular materials.

The flow cell apparatus with its technical components applied at Laboratoire 3SR is shown in Figure 2. The single-board computer was placed on the floor of the leaden scanning chamber and was connected to the hardware on the rotation stage by means of a flexible cable which could coil during the motion of the rotation stage. The hardware and software layouts are described in further detail in Milatz (2020) and Milatz *et al.* (2022).

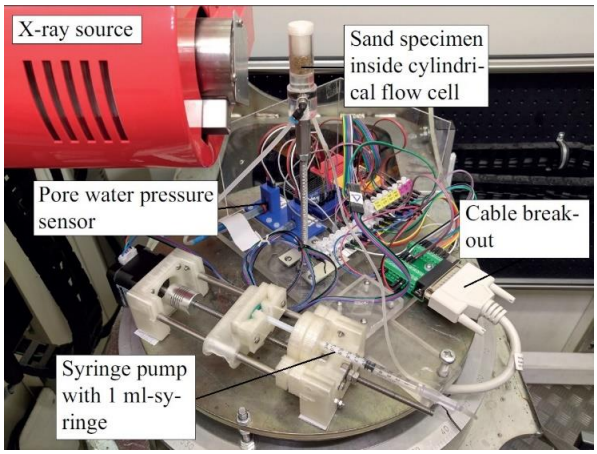

Figure 2: Miniaturised flow cell apparatus "UNSAT-*Pi* 2" for the automated measurement of transient water retention curves of granular media, consisting of the flow cell, a syringe pump, driven by a stepper motor as well as a set of pore water pressure sensors for suction measurement. The actuator of the syringe pump is driven by a Raspberry Pi single-board computer which also logs the response of matric suction upon changing degree of saturation.

In the transient *in situ* water retention experiments with CT imaging, the macroscopic WRC is tracked over time, while 3D tomography data at a voxel size of 10 μm are acquired at different degrees of saturation. During CT imaging, the applied outflow or inflow of pore water is halted while suction is continuously logged. This combined measurement and imaging procedure allows to study the phase distribution as well as the evolution of capillary state variables, such as fluid clusters, interfacial areas, contact angles, and radii of curvature, on different hydraulic paths in an effort to better understand the hysteresis phenomenon of the macroscopic water retention curve and its relationship to pore scale processes (Milatz *et al.*, 2022).

The contact angles θ and radii of curvature R have been measured manually based on different 2D slices captured after all hydraulic steps. Where possible, the measurements have been taken for the same menisci at the same pore throats and are sorted by drainage and imbibition events. While contact angles represent the wettability of solids, the radii of curvature are related to capillary pressure or suction inside the soil.

The amount of measured local contact angles allows to statistically evaluate the wetting properties of the tested sand. Furthermore, the measured radii of curvature can be applied to compute a theoretical capillary pressure or matric suction *s* based on the Young-Laplace equation

$$s = \boldsymbol{\gamma}\left(\frac{\mathbf{1}}{\boldsymbol{R_1}} + \frac{\mathbf{1}}{\boldsymbol{R_2}}\right). \quad (1)$$

For the calculation of *s*, the interfacial tension of water γ = 0.07275 N/m at 20 °C has been assumed. Furthermore, the calculation assumes 2D conditions with *s* depending only on the first principal radius of curvature R_1 measured in 2D. The second principal radius of curvature has been assumed to be $R_2 = \infty$.

3 Selected results

The analysis of multiphase CT data acquired in *in situ* CT experiments allows to investigate the influence of capillarity on the hydro-mechanical behaviour of granular materials. In the following, selected results from miniaturised uniaxial compression tests and water retention tests are presented and discussed.

3.1 Uniaxial compression of unsaturated granular soils

The phase-segmented CT data acquired during uniaxial compression of unsaturated Hamburg Sand and glass bead specimens at given initial degrees of saturation S_{r0} and initial void ratios e_0 is analysed to obtain pore or grain scale insights into the capillary (inter)action during uniaxial compression and shearing. The reconstructed and segmented CT volumes of a Hamburg Sand and glass bead specimen at different axial strains during uniaxial compression are shown in Figure 3.

Figure 4 shows the macroscopic results of axial stress σ_1 and volumetric strain ε_v *vs.* axial strain ε_1 for a series of uniaxial compression tests on Hamburg Sand and glass bead specimens at different initial degrees of saturation. During CT imaging, the loading was halted, leading to a relaxation of stress in some cases. Although the effect of initial degrees of saturation on the measured axial stress of the tested specimens is not clear, it is visible that a higher uniaxial compressive strength is measured for the Hamburg Sand as compared to the glass beads. An interesting finding is the trend of increasing dilatancy (negative ε_v) with decreasing degree of saturation, measured for both materials. Normally, the volumetric strain is not measured in a uniaxial compression test. Here, the volumetric strain is derived from the evolution of the voxelised specimen volume in the CT data sets. The increasing tendency to dilatancy with decreasing degree of saturation evidences the bonding effect of water clusters and liquid bridges and the corresponding increased transfer of capillary forces at elevated degrees of saturation holding the grain skeleton together.

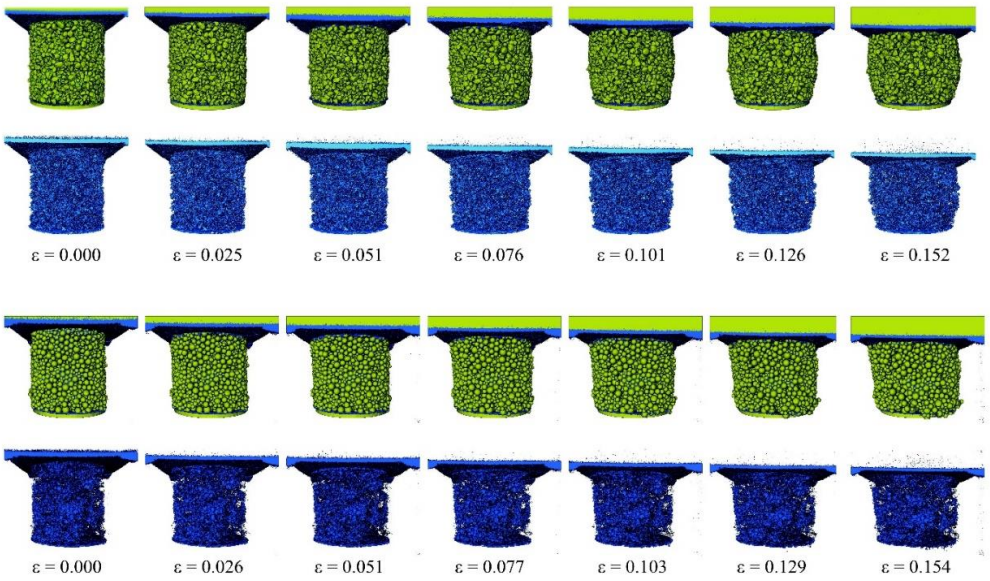

Figure 3: Phase-segmented 3D image sequences of Hamburg Sand (S_{r0} = 0.212, e_0 = 0.631) and glass beads (S_{r0} = 0.325, e_0 = 0.567) at different axial strain levels ε during uniaxial compression (yellow: solid phase, blue: water, air not shown) from Milatz *et al.* (2021).

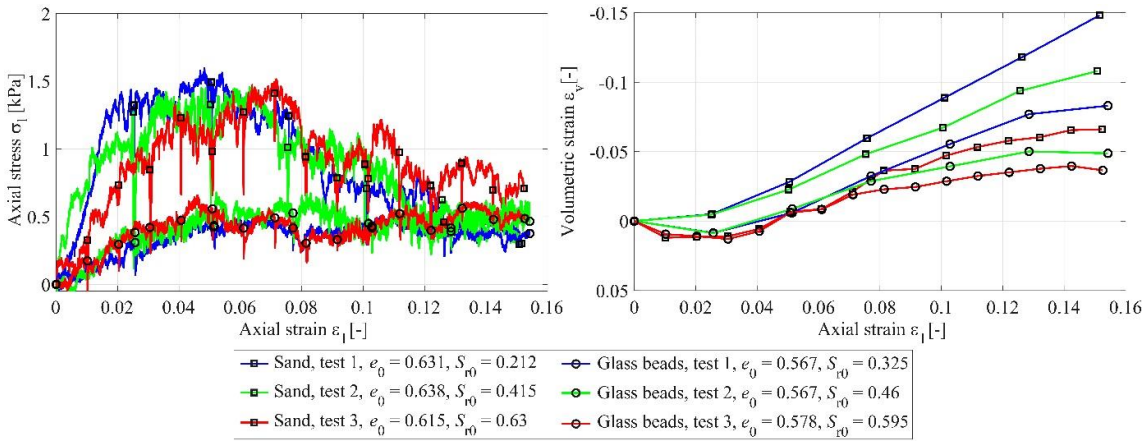

Figure 4: Macroscopic results of uniaxial compression tests with parallel CT imaging on Hamburg Sand and glass beads at different initial degrees of saturation S_{r0}: Axial stress σ_1 (left) and volumetric strain ε_v (right) *vs.* axial strain ε_1.

The analysis of segmented CT data opens the door to study changes of microscopic capillary structures causing capillary cohesion, such as water clusters and capillary bridges, in order to assess the impact of shearing. Based on the evolution of labelled water clusters in different volume size domains, it can be shown that the shearing leads to a degradation of larger into smaller water clusters. Figure 5 shows a visualisation of water clusters in the different domains (a) to (f) at different strain increments in a Hamburg Sand specimen, illustrating the fracturing of initially large water clusters into smaller ones during shearing. This behaviour is also observed for the glass beads. While volume size domain (a) contains all clusters, groups (b) to (f)

include clusters of reducing volume sizes. They contain the largest clusters in group (b), assemblies of liquid bridges of different complexity in groups (c) and (d), rather single capillary bridges in group (e) and the smallest detected water clusters in group (f) which represent fragments of capillary bridges, but which might also be influenced by image noise. The results show that the capillary action, leading to increased shear strength of a soil in its unsaturated state due to a contribution of capillary pressure to effective stress, might be changed as the shearing leads to a change in capillary structures which bond individual soil grains together.

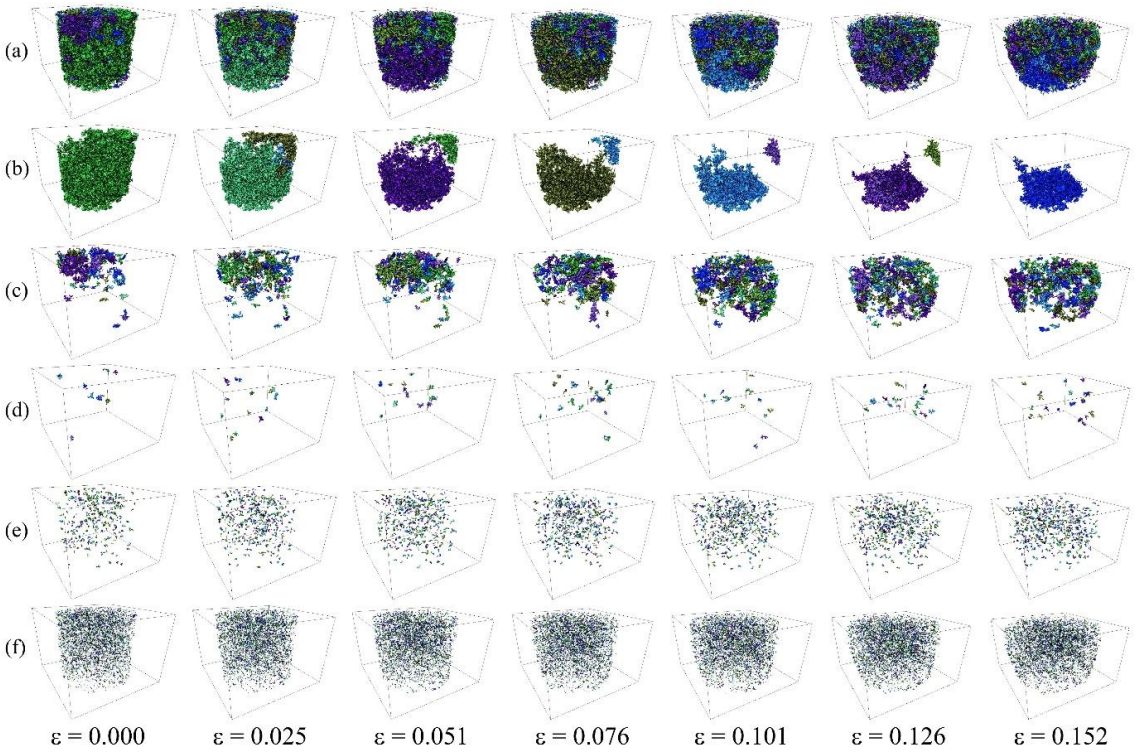

Figure 5: Evolution of individual water clusters in different water volume size domains (V_w) during uniaxial compression of an unsaturated Hamburg Sand specimen (S_{r0} = 0.212, e_0 = 0.631) at different axial strains ε from Milatz *et al.* (2021). Individual water clusters are labelled with a distinct colour. (a) All clusters, (b) $V_w > 1.0664$ mm³, (c) $0.026185 \text{ mm}^3 < V_w \leq 1.0664 \text{ mm}^3$, (d) $0.023567 \text{ mm}^3 < V_w \leq 0.026185 \text{ mm}^3$, (e) $0.0026185 \text{ mm}^3 < V_w \leq 0.005237 \text{ mm}^3$, (f) $V_w \leq 0.0026185$ mm³.

3.2 Water retention behaviour of unsaturated granular soils

The macroscopic water retention curve, measured in an *in situ* CT experiment with 19 hydraulic steps and 20 CT scans on a Hamburg Sand specimen (e_0 = 0.65), is illustrated in Figure 6. Breaks for CT imaging, in which matric suction was logged with flow halted, are plotted in black. Focussing on the hysteresis of the WRC, different hydraulic paths are followed: After primary drainage, the pore water is re-imbibed into the specimen causing a main imbibition path. After main imbibition, further cyclic drainage and imbibition scanning paths with a decreasing range of degree of saturation are applied. The measured WRC shows the typical hysteretic behaviour with different elliptical drainage and imbibition scanning paths in between the

bounding primary drainage and main imbibition paths. Unlike imbibition paths, during drainage, the measured matric suction shows oscillations, especially upon air entry on the primary drainage path. By looking at the multiphase CT data in Figure 7, it is revealed that an air finger is breaking into the pore space upon primary drainage, leading to temporal reduction of matric suction. The reason for other oscillations of matric suction on primary drainage paths is probably related to the phenomenon of the so-called "Haines Jumps" (Haines, 1930), caused by sudden air entry events in larger pores upon their drainage.

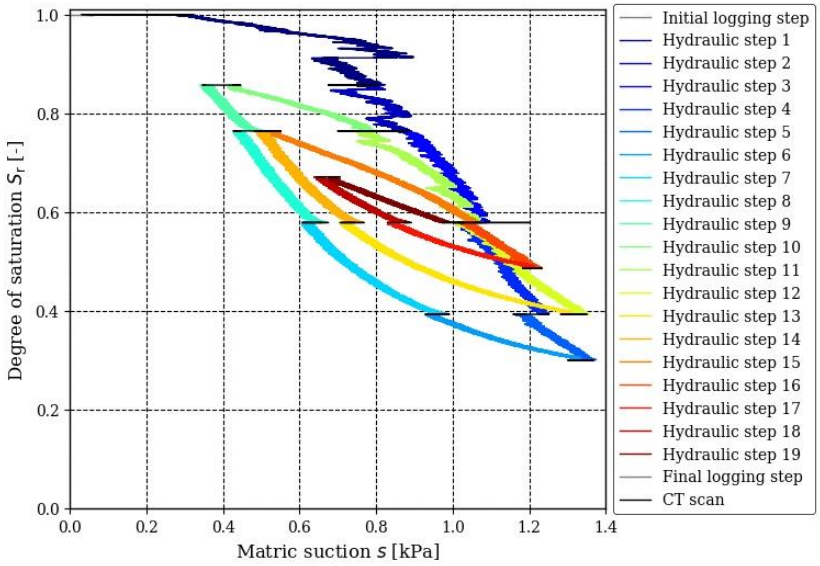

Figure 6: Measured macroscopic WRC for a specimen of Hamburg Sand with different drainage and imbibition paths and stops for CT imaging from Milatz *et al.* (2022). CT imaging steps are plotted in black colour. Hydraulic history is highlighted by a varying line colour from cold (blue) to warm (red).

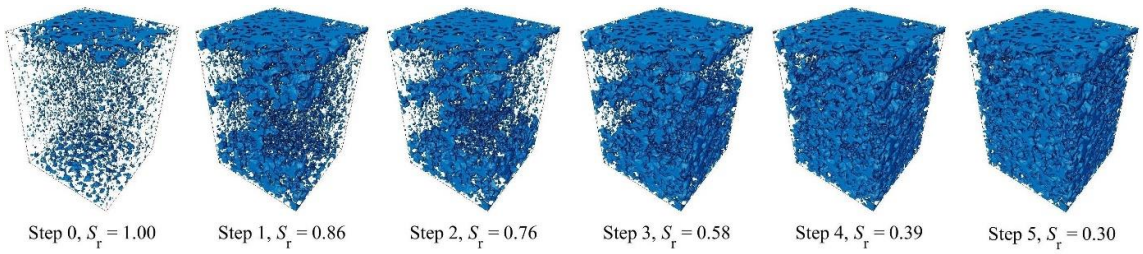

Figure 7: Reconstructed and phase-segmented 3D image sequence of the air phase in a subvolume of (800×800×1145 px) in the initial state and after five hydraulic steps on the primary drainage path from a transient water retention experiment on Hamburg Sand with CT imaging from Milatz *et al.* (2022).

Besides an analysis of the water and air clusters reported in Milatz *et al.* (2022), a closer look at the evolution of capillary state variables, such as the specific, *i. e.*, volume-based, interfacial areas between the non-wetting gas phase and wetting liquid phase (spec. air-water interfacial area) a^{nw} and between the solid phase and wetting liquid phase (spec. solid-water interfacial area) a^{sw} is of high interest, as those quantities might be used for the modelling of effective stress in unsaturated granular soils. Based on the large amount of data at different hydraulic steps, the interfacial areas can be extracted as described in Milatz *et al.* (2022) and plotted *vs.* degree of saturation and macroscopic matric suction as shown in Figure 8 for all applied hydraulic steps based on the corresponding CT data sets.

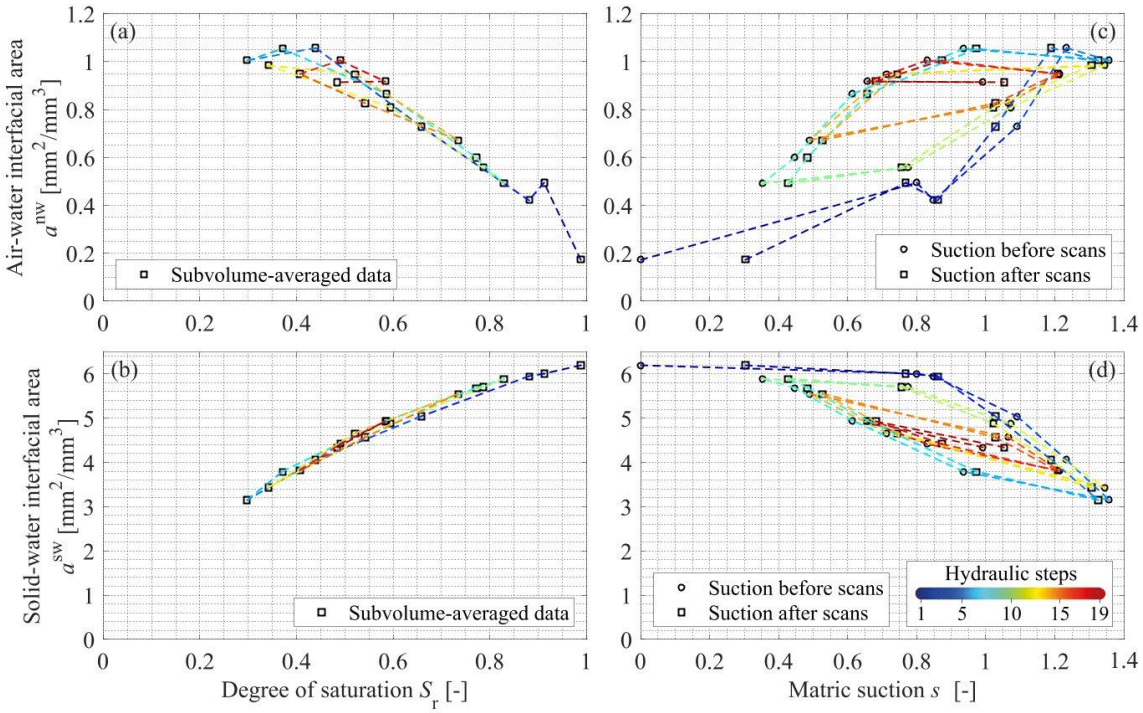

Figure 8: Specific air-water interfacial area a^{nw} (top row) and specific solid-water interfacial area a^{sw} (bottom row) plotted *vs.* subvolume-averaged degree of saturation (left) and macroscopic matric suction measured before and after a CT scan (right) from a transient water retention experiment on Hamburg Sand with CT imaging from Milatz *et al.* (2022).

Interestingly, characteristic relationships for the specific interfacial areas plotted *vs.* degree of saturation and matric suction, similar to the WRC, are obtained. The interfacial areas are measured in a centred cubic subvolume with an edge length of 800 px (8 mm). The interfacial areas show pronounced hysteresis when plotted *vs.* matric suction and follow clear trends: While the solid-water interfacial area follows a monotonic curve logically starting at $a^{sw} = 0$ for $S_r = 0$ and a value which should theoretically correspond to the specific solid surface area of the granular material for $S_r = 1$, the air-water interfacial area a^{nw} follows a non-linear trend, apparently with a peak for some intermediate degree of saturation close to $S_r \approx 0.4$.

Figure 9 shows the results of contact angle and radii of curvature measurements based on 182 measurements on drainage paths and 141 measurements on imbibition paths.

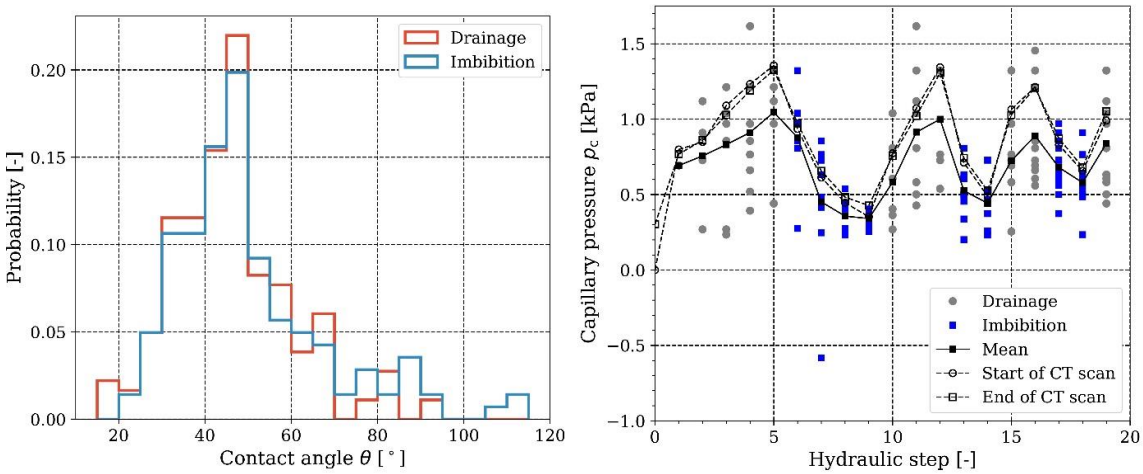

Figure 9: Left: Histogram of measured contact angles θ. Right: Capillary pressure p_c from macroscopic suction measurements before and after a CT scan (dashed lines) *vs.* calculated capillary pressure based on measured 2D radii of curvature (lone markers and their mean, plotted as black line) for all hydraulic steps during a transient water retention experiment on Hamburg Sand with CT imaging from Milatz *et al.* (2022).

Despite a certain spread of data in Figure 9, the measured contact angles show evidence for contact angle hysteresis with the mean drainage contact angle $\theta_{mean,d}$ = 46.478° being lower than the mean imbibition contact angle $\theta_{mean,i}$ = 50.307°. Contact angle hysteresis is one reason for the occurrence of hysteresis in the WRC of soils.

Based on the measured radii of curvature and Equation 1, the theoretical calculated mean capillary pressure is close to the capillary pressure measured by a pressure transducer on the macroscopic level. This highlights, that macroscopic capillary pressure or matric suction is highly linked to the evolution of capillary menisci and their average curvature inside the soil.

4 Summary and outlook

In this contribution, the potential of *in situ* CT imaging experiments for the investigation of capillary effects on the grain or pore scale has been highlighted. The two presented examples of a miniaturised uniaxial compression apparatus and a miniaturised flow cell show that microscopic processes during mechanical loading or fluid flow in unsaturated granular soils can be effectively studied by means of CT imaging and quantitative image analysis. Although customised mini set-ups need to be designed, tested and thoroughly adapted to CT imaging environments, their application yields many benefits as compared to conventional testing methods because volumetric insights into the phase distribution, including information on homogeneity of soil properties as well as boundary effects, can be obtained.

The analysis of capillary state variables based on CT data, such as fluid clusters, interfacial areas, contact angles and radii of curvature, allows to better understand the macroscopic shear behaviour and water retention behaviour. Based on the presented results, a degradation of water clusters during uniaxial compression as well as evidence for the strengthening of the grain skeleton due to capillary cohesion was discovered. Furthermore, different pore scale insights into

microscopic capillary and flow processes, leading to the macroscopic hysteretic water retention curve, could be obtained.

In the future, further *in situ* CT imaging experiments with soil mechanical background are desirable to study different loading scenarios, *e. g.*, direct shearing, or physical phenomena, such as flow-rate dependent effects in the WRC. In order to achieve a better temporal and spatial imaging resolution, better CT scanners or different imaging techniques, such as synchrotron-based CT imaging could be applied. Further experimental findings related to the research presented in this contribution will be published in Milatz (2022).

References

[1] Fredlund D. and Rahardjo H. (1993): *Soil mechanics for unsaturated soils*. John Wiley & Sons.

[2] Haines W. B. (1930): Studies in the physical properties of soil: V. The hysteresis effect in capillary properties and the modes of moisture distribution associated therewith. In: *Journal of Agricultural Science* 20, pp. 97–116.

[3] Milatz M. (2019): Zur Anwendung von Einplatinen-Computern in der bodenmechanischen Forschung und Lehre am Beispiel eines einaxialen Druckversuchs zur Untersuchung teilgesättigter granularer Böden. In: *Geotechnik* 42(1). DOI: 10.1002/gete.201800015.

[4] Milatz M. (2020): An automated testing device for continuous measurement of the hysteretic water retention curve of granular media. In: *Acta Geotechnica* 15. DOI: 10.1007/s11440-020-00922-y.

[5] Milatz M. (2022): Investigation of capillary effects on the grain scale by means of *in situ* experiments, imaging and numerical simulations. Habilitation thesis, Hamburg University of Technology. (Under review).

[6] Milatz M., Andò E., Helfen L., Hüsener N., and Tengattini A. (2019): *Partial saturation in granular media*. Institut Laue-Langevin (ILL). DOI: 10.5291/ILL-DATA.UGA-73.

[7] Milatz M., Andò E., Viggiani G., and Mora S. (2022): In situ X-ray CT imaging of transient water retention experiments with cyclic drainage and imbibition. In: *Open Geomechanics*. (Manuscript under review).

[8] Milatz M., Hüsener N., Andò E., Viggiani G., and Grabe J. (2021): Quantitative 3D imaging of partially saturated granular materials under uniaxial compression. In: *Acta Geotechnica* 16. DOI: 10.1007/s11440-021-01315-5.

[9] Tengattini A., Lenoir N., Andò E., and Viggiani G. (2021): Neutron imaging for geomechanics: A review. In: *Geomechanics for Energy and the Environment* 27. DOI: 10.1016/j.gete.2020.100206.

[10] Viggiani G., Andò E., Takano E., and Santamarina J. C. (2015): Laboratory X-ray Tomography: A Valuable Experimental Tool for Revealing Processes in Soils. In: *Geotechnical Testing Journal* 38(1). DOI: 10.1520/GTJ20140060.

[11] Wildenschild D. and Sheppard A. P. (2013): X-ray imaging and analysis techniques for quantifying pore-scale structure and processes in subsurface porous medium systems. In: *Advances in Water Resources* 51, pp. 217–246. DOI: 10.1016/j.advwatres.2012.07.018.

Acknowledgements

The funding of this research in the framework of research training group GRK 2462 “Processes in natural and technical Particle-Fluid-Systems” (PintPFS) by the German Research Foundation (Deutsche Forschungsgemeinschaft, DFG) is gratefully acknowledged.

Author

Dr.-Ing. Marius Milatz
Hamburg University of Technology (TUHH)
Institute of Geotechnical Engineering and Construction Management
Harburger Schloßstraße 36
21079 Hamburg
Tel.: +49 (0) 40 - 42878 / 3660
Fax: +49 (0) 40 - 42731 / 0807
e-mail: marius.milatz@tuhh.de
Web: www.tuhh.de/gbt

Complex multiscale solid-fluid interactions in drying porous media

Nima Shokri and Salome M.S. Shokri-Kuehni

Abstract: Drying of porous materials is relevant to many industrial and environmental applications ranging from the production of solid particulates, porous building materials, and pharmaceutical products to a wide range of engineering and hydrological processes including drying of paints, wastewater treatment, salt crystallization, soil water evaporation, land-atmosphere interactions, and soil salinization (Scherer 1990; Chauvet et el. 2009; Shokri et el. 2012; Lehmann 2019; Qazi et el. 2019; Hassani et al. 2020; Hassani et al. 2021). Many of the scientific and technical challenges related to accurate characterization of these processes under different boundary conditions hinge on understanding and controlling processes that involve complex solid-fluid interactions in porous media. This work discusses transport mechanisms influencing drying of porous materials and places a particular emphasize on how pore-scale physics and processes control the responses observed at the macro-scale.

The fundamental principles of drying of porous media filled with pure liquid are relatively well-understood. It includes a constant drying rate period supported by capillary-induced liquid flow from wet zones towards the vaporization plane supplying the evaporative demand. When the upward capillary forces are balanced by the downward viscosity and gravity forces, the constant rate period ends which is followed by a falling rate period limited by the diffusive transport inside porous media. However, when the evaporating liquid contains some mobile elements in the suspension (e.g. ions, polymers, colloidal particles, etc.), which is the case in many industrial and environmental applications such as wastewater treatment, production of pharmaceutical products, cements or drying of paints and soil containing soluble salts, the description of the drying process will be more challenging. This is due to the transport and deposition of the mobile elements along the solid surface as a result of advective liquid transport and preferential evaporation at the contact line between the liquid, air and solid interface (see Shokri-Kuehni et al. 2020 for more details). In such cases, advection tends to transport the ions or colloidal particles toward the vaporization plane via capillary induced liquid flow. This results in increasing concentration close to the vaporization plane. At the same time, diffusion tends to spread the ions or colloidal particles homogenously throughout the space (Figure 1a).

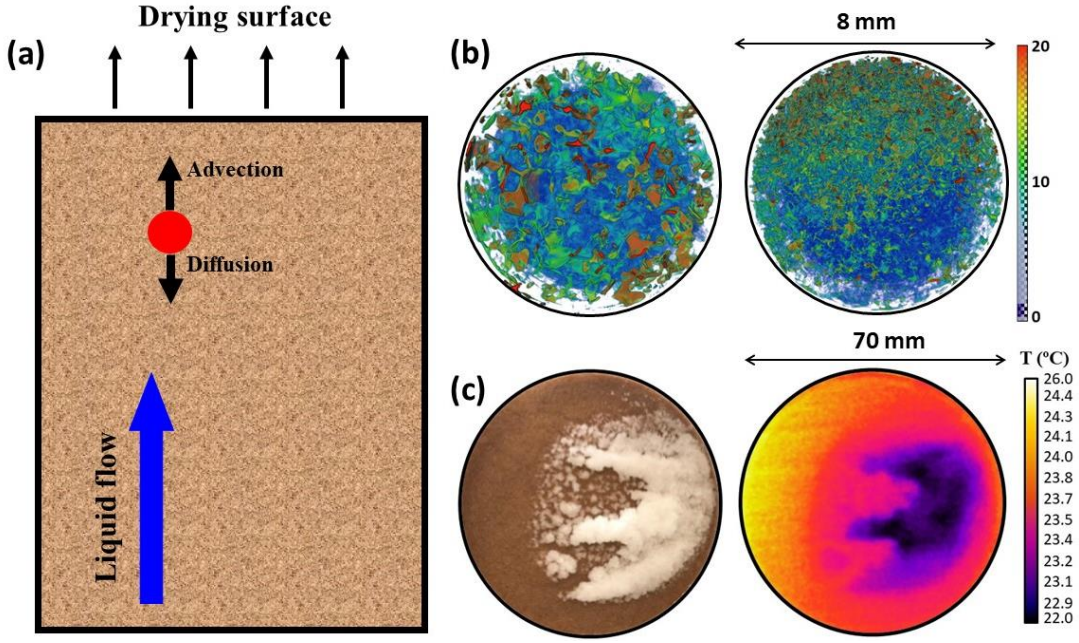

Figure 1. (a) Competition between advective and diffusive transport during evaporation from porous media. (b) Distribution of solute concentration close to the surface of coarse- and fine-textured sands (left and right, respectively) 6 hours after the onset of the evaporation experiments. The sand packs were initially saturated by salt solution containing 5% calcium iodide (by weight). The color map represents the solute concentration percentage, such that the closer to red, the higher the concentration. The images were recorded using synchrotron X-ray microtomography (adapted from Shokri-Kuehni et al. 2018). (c) NaCl precipitation patterns (white color) at the surface of sand during evaporation together with the corresponding temperature distribution at the surface recorded by a thermal camera (FLIR T650sc, FLIR Systems, Inc.). The color map indicates temperature in degrees centigrade. The closer to yellow (brighter color), the higher the temperature (adapted from Shokri-Kuehni et al. 2020).

The resulting competition between advection and diffusion, quantified by the dimensionless Peclet number, determines the dynamics and distribution of the ions or colloidal particles in porous media which is significantly influenced by the solid-fluid interaction (Huinink et al. 2002; Guglielmini et al. 2008). We used state-of-the-art experimental and theoretical tools including synchrotron X-ray microtomography (Figure 1b), thermal imaging (Figure 1c), neutron radiography, pore- and continuum-scale modelling (Jambhekar et al. 2016; Dashtian et al. 2018) to extend the physical understanding required to characterize solid-fluid interactions in drying porous media under different boundary conditions. Our results illustrate the importance of pore-scale processes influenced by the characteristics of particles and evaporating fluids on the macroscopic responses observed during evaporation from porous media. Moreover, we show that preferential nature of the evaporation process results in preferential ion transport and deposition in drying porous media saturated with saline solution (Veran-Zissoires et al 2012). This leads to preferential salt crystallization when the ion concentration exceeds the solubility limit (Desarnaud et al. 2015). How exactly the structure and morphology of the crystalized element influences the subsequent water evaporation dynamics and the effective properties of porous media (e.g. porosity and permeability) is not fully understood (Shokri-Kuehni et al 2022). Our

results highlight the need for additional research to delineate such effects. Without such knowledge, description of the drying process from porous media containing mobile elements would rely on some adjusting parameters which could potentially mask the true physics controlling the process.

References

[1] Scherer, G.W. (1990): Theory of drying. J. Am. Ceram. Soc. 73:3–14

[2] Chauvet, F., Duru, P., Geoffroy, S., Prat, M. (2009): Three periods of drying of a single square capillary tube. Phys. Rev. Lett. 103, 124502

[3] Shokri, N., Sahimi, M. (2012): The structure of drying fronts in three-dimensional porous media. Phys. Rev. E 85, 066312

[4] Or, D., Lehmann, P. (2019): Surface Evaporative Capacitance: How Soil Type and Rainfall Characteristics Affect Global-Scale Surface Evaporation. Water Resour. Res., 55, 519–539

[5] Qazi, M.J., Salim, H., Doorman, C.A.W., Jambon-Piollet, E., Shahidzadeh, N. (2019): Salt creeping as a self-amplifying crystallization process. Sci. Adv., 5, eaax1853

[6] Hassani, A., Azapagic, A., Shokri, N. (2020): Predicting Long-term Dynamics of Soil Salinity and Sodicity on a Global Scale. Proc. Nat. Acad. Sci., 117(52), 33017-33027, doi.org/10.1073/pnas.2013771117

[7] Hassani, A., Azapagic, A., Shokri, N. (2021): Global Predictions of Primary Soil Salinization Under Changing Climate in the 21st Century. Nat. Commun., 12, 6663. doi.org/10.1038/s41467-021-26907-3

[8] Shokri-Kuehni, S.M.S., Bergstad, M., Sahimi, M., Webb, C., Shokri, N. (2018): Iodine k-edge dual energy imaging reveals the influence of particle size distribution on solute transport in drying porous media. Sci. Rep., 10, 10731, London: Nature Publishing Group

[9] Shokri-Kuehni, S.M.S., Raaijmakers, B., Kurz, T., Or, D., Helmig, R., Shokri, N. (2020): Water Table Depth and Soil Salinization: From Pore-Scale Processes to Field-Scale Responses. Water Resour. Res., 56, e2019WR026707. doi.org/ 10.1029/2019WR026707

[10] Huinink, H.P., Pel, L., Michels, M.A. (2002): How Ions Distribute in a Drying Porous Medium: A Simple Model. Phys. Fluids, 14, 1389

[11] Guglielmini, L., Gontcharov, A., Aldykiewicz, A.J. Jr., Stone, H.A. (2008): Drying of salt solutions in porous materials: Intermediate-time dynamics and efflorescence. Phys. Fluids 20, 077101

[12] Jambhekar, V.A., Mejri, E., Schröder, N., Helmig, R., Shokri, N. (2016): Kinetic approach to model reactive transport and mixed salt precipitation in a coupled free-flow-porous-media system. Trans. Porous Med., 114(2), 341-369

[13] Dashtian, H., Shokri, N., Sahimi, M. (2018): Pore-network model of evaporation-induced salt precipitation in porous media: the effect of correlations and heterogeneity. Adv. Water Resour.,112, 59

[14] Veran-Tissoires, S., Marcoux, M., Prat, M. (2012): Discrete Salt Crystallization at the Surface of a Porous Medium. Phys. Rev. Lett. 108, 054502

[15] Desarnaud, J., Derluyn, H., Molari, L., de Miranda, S., Cnudde, V., Shahidzadeh, N. (2015): Drying of salt contaminated porous media: Effect of primary and secondary nucleation. J. Appl. Phys. 118(11), 114901

[16] Shokri-Kuehni, S.M.S., Sahimi, M., Shokri, N. (2022): A personal perspective on prediction of saline water evaporation from porous media. Drying Technol., 40 (4), 691-696, DOI: 10.1080/07373937.2021.1999256

Author

Prof. Dr. Nima Shokri
Head of Institute
Hamburg University of Technology
Institute of Geo-Hydroinformatics B-9
Am Schwarzenberg-Campus 3 (E)
21073 Hamburg, Germany
Email: nima.shokri@tuhh.de
Phone: +49 40 42878 2870

Investigations for the development of a new test method to prevent the alkali-silica reaction

Gyde Hartmut, Frank Schmidt-Döhl

Abstract: A damaging alkali-silica reaction (ASR) takes place within concrete and results in the formation of alkali-silicate gel, which may damage the concrete structure by expansion. The most beneficial approach to avoid an ASR are preventive measures. Besides changing the components of the concrete mixture in quantity and characteristics, a further preventive measure is the use of non-reactive or weakly reactive aggregates. In the Institute of Materials, Physics and Chemistry of Buildings at Hamburg University of Technology (TUHH), a new test method to identify alkali-reactive aggregates is being worked on: an accelerated dissolution experiment that mimics the alkaline character of the concrete pore solution. In this paper we present analytical results and show possibilities to use this new method as an indicator for the reactivity of an aggregate.

1 Introduction

1.1 Mechanism and conditions of the ASR

The alkali-silica reaction (ASR) is a significant damage that occurs in concrete structures. The symptoms of the ASR are surface pop-outs, appearance of reaction-induced gel on the concrete structure, and cracking that can lead to compromised stability of the structure. [1, 2]. ASR takes place in the pore solution of concrete, which is a composite, made of cement, aggregates, water and potential admixtures. These main constituents of the concrete itself are usually the source of the precondition for a damaging ASR: the presence of water, a sufficient concentration of alkaline reagents and reactive aggregates [1, 3].

While an ASR, reactive SiO_2 from the aggregate is dissolved by a nucleophilic attack of hydroxide ions. It reacts with alkali ions to an alkali-silicate gel [4]. This gel expands due to water and calcium absorption into the pore space of the concrete. The continuous swelling pressure of the gel increases until the tensile strength of the concrete is exceeded and the concrete cracks [5].

The water is contained in the concrete as a pore fluid within the pore space. The hydroxide and alkali ions enter the pore space as the hydration of the clinker progresses, during the reaction of cement with water. The alkalis successively go into solution and react with portlandite to form easily soluble alkali hydroxides (NaOH and KOH) [5]. In addition, further sources of alkalis can be the aggregates, chemical admixtures, supplementary cementing materials, like

fly ash, silica fume or natural pozzolans as well as external sources [1, 6]. The reactivity of the aggregate depends on its crystal structure. A reactive aggregate in regard to an ASR holds amorph, disordered or poorly crystallized silica with large surface for reaction [1]. There are fast-reacting aggregates, like opal and chalcedony. They may cause damage in just a few month or years, even when they only occur in amounts less than 1 M.% of the aggregate [2]. Aggregates, like strained quartz, lead to a slow/late ASR. In this case it takes several years for a visible damage to occur and a higher quantity of the reactive material is required [1, 6].

The exclusion of aggregates containing reactive minerals for concrete production has been shown to be the most efficient way to avoid ASR [6].There are several similar national testing methods to identify reactive aggregates. The basic test methods are petrographic investigation, methods based on reaction-dependent expansion of a standardized sample made of concrete or mortar, different chemical methods and long-time testing [7–9].

In petrographic studies, the larger parts of the aggregate known to be alkali-reactive are sorted out by hand [9–11]. This investigation is essential but requires individual testing and much experience. Furthermore, it is not able to give a quantitative rating about the alkali-reactivity.

The most common test procedure - the concrete prism test and the mortar bar test - are based on expansion of the specimen. There are different versions of these test procedures worldwide. What they have in common is the examination of standardized prisms made of concrete or mortar according to a locally given recipe. The specimens are stored under defined conditions, and after a standardized period, the expansion of the prisms is measured. It serves as a classification for the reactivity of the aggregate used. The storage conditions influence the storage time, which ranges between two weeks [12] and 12 months [13, 14]. The specimens are stored in 100% relative humidity (rH) [15] or in 1 M alkaline solution (NaOH or KOH) [16], and the storage temperature differs from 38°C [12] to 80°C [14], which was even withdrawn 2018. The drawbacks of these test methods are a long implementation time, and the requirement of specifically prepared test specimens. Manual preparation of the test specimen can introduce potential systematic errors in the test procedure. Furthermore, the mortar bar test shows some differences to the results of other established test methods.

Chemical methods are used to examine fractured, supposedly fast-reacting aggregates regarding their alkali reactivity. To evaluate, the aggregate is first stored in hot alkaline solution (NaOH) for a specified duration. Concentration and temperature of the alkaline solution and the duration of storage vary according to the test procedure. Reactivity is determined by the loss of mass of the material [9] or by the concentration of dissolved SiO_2 determined from the filtrate of the solution and sodium oxide remaining in the solution [17]. These chemical test methods are just applicable for some aggregates; the material must first be examined petrographically. The preparation of the material and further post-treatment of the aggregate, such as elemental analyses, increase the cost and effort of these tests.

For the classification of an aggregate, using just a single test method is rarely sufficient. An aggregate that has been assessed as reactive is usually tested an additional time using another test procedure before it is finally deemed to be alkali reactive. The national adaptations and sequence of the test procedures are specified in the respective standards. The time required to finally assess the material in terms of reactivity, the need for several test procedures, standardized specimens and petrographic examinations of the material show that there remains a demand for optimization with regard to the identification of alkali-reactive aggregates.

Furthermore, there is a lack of test procedures with which the alkali reactivity of the material can be determined in the short term, as in the case of an incoming goods inspection, and with which the degree of reactivity can be estimated.

The variety of test methods, the complexity of the standardized test procedure, and the lack of an international, consistent testing method are a sign of the need for an optimized testing method. The limits of the present test methods are the long wait for reliable results, the reliability of some results, the non-applicability to unknown or slow/late aggregates, the need for manual produced test specimen, and the missing possibility for precisely measuring the susceptibility of the aggregate to ASR.

1.2 Idea and aims of this study

The objective of this research at Hamburg University of Technology (TUHH) is to develop a fast and reliable test method for categorizing aggregates with respect to their alkali reactivity. This test method is based on dissolution experiments, like in ASTM C289-07 [17] but using a new approach. This approach involves the storage of ground aggregate in hot alkaline solution. During storage, chemical and physical parameters are measured continuously, and changes of these parameters are intended to provide information about the alkali reactivity of the material. By using 1 M potassium hydroxide (KOH) as a solution, the aggregate is also exposed to an alkaline environment comparable to the pore solution and an oversupply of alkali hydroxides. Grinding the aggregate for maximum surface area and the constant experimental temperature of 60°C accelerate the dissolution process of the material. The parameters recorded are pH-value, redox potential, and electrical conductivity.

Initial tests have already been carried out with aggregates of known alkali reactivity. The reactivity of the aggregates was determined by round robin test bases on [9]. It was found that the changes in time of the chemical and physical parameters are reliable and show characteristic points, such as extreme values. These characteristic points further reflect an influence of the type and quantity of the tested material. The aim of these investigations is to identify and isolate the influence of the alkali reactivity of the material in the temporal development of the parameters and thus to derive limit values for the assessment of further aggregates.

The recorded parameters are intended to visualize various processes of aggregate dissolution. The measurement of electrical conductivity provides information about the variation of mobility and distribution of charged particles and the resistivity of the solution. The pH represents the activity of hydroxide and hydroxonium ions in the solution and was therefore selected as a parameter. The redox potential was chosen because it detects changes in species that do not affect the pH-value or electrical conductivity.

This contribution presents investigations of the pH-minimum of two opaline sandstones with different but known alkali reactivity. Investigations of the effect on electrical conductivity and redox potential and further aggregates will be reported in future paper.

In this contribution, we will concentrate on first general results, the analysis of the percentage change of the electrical conductivity, and the reduction of the redox potential after addition of the sample.

1.3 Aggregate dissolution at high ph

The pH reflects the activity of hydroxide and hydroxonoium ions in the solution, which in turn is considerably involved in the dissolution process of the aggregate. A damaging ASR first requires the formation of alkali-silicate gel within the aggregates. This gel expands due to absorption of water and is leading to damage after exceeding the maximum tensile stress of the concrete [5]. For the formation of the gel, reactive SiO_2 from the aggregate, which is dissolved by an attack of hydroxide ions from the pore solution reacts with the alkalis pre the pore solution [4].

Generally, in alkaline solutions, such as the pore fluid, hydroxide ions first deprotonate the silanol groups (Si-OH) on the surface of the solid. This process decreases the concentration of hydroxide ions in the solution - thus the pH and leads to a predominantly negatively charged surface ($Si\text{-}O^-$) of the solid [4, 18]. The alkali cations of the solution counterbalance the negative surface of the silica solid. The charge equilibrium allows the hydroxide ions to approach even the siloxane bonds of the solid. Moreover, the siloxane bonds of the solid silica are attacked by the hydroxide ions, releasing silicic acid into the solution. This reduces the concentration of hydroxide ions and thus, the pH of the solution as well [18]. The released silicates can be dissolved as mono-silicic acid (H_4SiO_4) or as oligomers ($Si_nO_c(OH)_b$ with $2a + b = 4n$) [4]. Mono-silicic acid is a weak acid with the ionization constants $K_1 = 10^{-9.8}$ and $K_2 = 10^{-12.4}$ [19]. Therefore, in highly alkaline solutions, such as the pore solution, the mono-silicic acid deprotonates to its anion $(SiO(OH)_3)^{-1}$ and its dianion $(SiO_2(OH)_2)^{2-}$, consuming hydroxide ions, which increases the ph [19, 20]. Since the equilibrium concentration of the dissolved silicon depends on the amount of mono-silicic acid in the solution, the formation of the anions results in further solution of the solid [4].

Mono-silicic acid and its anions condensate to polysilicic acids, which releases hydroxide ions and the pH of the solution increases [21, 22]. The dissolution rates for crystalline and amorphous silica leads to the assumption that they follow the same reaction pathway, though the dissolution rate of amorphous silica is higher [23]. A lower silica concentration in the solution also leads to slower polymerization of the mono-acid [24]. The new test method uses the different dissolution and condensation behaviors of the individual aggregate species affected by its alkali reactivity shown in the pH.

2 Methods and Material

2.1 Experimental setup

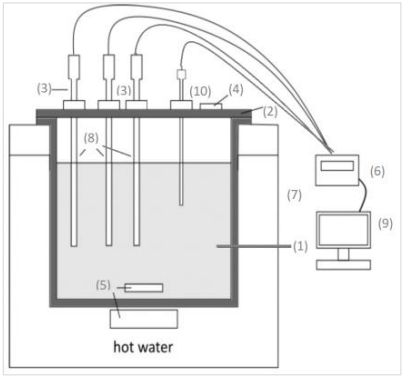

Figure 1. experimental setup

The new test method was first precisely described in Osterhus and Schmidt-Döhl [25]. The experimental setup consists of a test container where reaction kinetics and chemical parameters are directly measured, seen in figure 1. The experimental container (1) and its lid (2) are made of Polytetrafluoroethylene (PTFE). To keep the contact between the KOH solution and air to a minimum, the electrodes (8) and the temperature sensor (10) are attached to the lid of the experimental container (3) and the container itself is also sealed. A further inlet is closable with a PTFE screw (4) for adding the aggregate. Sedimentation of the aggregate is prevented by a magnetic stirrer (5) located at the bottom of the PTFE container. During the experiment, the whole container is heated in a bath with a circulation thermostat (7). In previous research, dissolution experiments with silicate aggregate have been conducted either at much higher temperatures, in lower pH-values, or with a different ratio of dissolving hydroxide ions to soluble silicate aggregate. The approach of dissolving ground aggregate with an excess of alkalis in basic solution at 60°C and deriving the alkali reactivity of the material with the resulting change in chemical and physical parameters has not been attempted to date. Therefore, there are no comparative values in the literature regarding the change of the parameters so far.

2.2 Specimen and test preparation

To increase the surface of the specimen, the aggregates are ground to powder. The 1 M potassium hydroxide solution is made by mixing 56.11 g KOH-platelets with 1 l of distilled water. All electrodes are tested and calibrated before every experiment. The pH electrode is subjected to a four-point-calibration (pH 4, 7, 10 and 13). Upon reaching constant initial conditions of all the measured parameters, the aggregate is added and after 48 hours, the experiment is terminated.

2.3 Evaluation of measured data

The pH, redox potential, temperature, and electrical conductivity are recorded every 30 seconds by the software of the multi-parameter analyzer (C3060 by Consort). The time of adding the aggregate is set as point zero for all measurements. Characteristic points in the data (such as steady states and minima) are identified with Microsoft excel. The calculation of mean, standard deviation, variance, and further statistical analyses of these characteristic points are calculated by R [26].

2.4 Material

The chemical composition of the aggregates was determined by X-ray fluorescence spectroscopy with the RFA Horiba XGT-7200 spectrometer. Results were analyzed using the fundamental parameter method and the "NIST1881s" reference standard. The specific surface was determined according to BET using N_2-sorption with a Micromeritics Accelerated Surface Area and Porosimetry System 2010 (ASAAP 2010). Particle size distribution was measured with a laser diffraction system (Mastersizer 3000 by Malvern). Reference data of an inert aggregate was generated with quartz powder (QP) from "MILLISIL" [27] by Osterhus and Schmidt-Döhl [25, 28].

The investigated aggregate is opaline sandstone, which is classified by [9] as a fast-reacting aggregate and quartz powder was used as a reference of a non-reactive aggregate. Two different opaline sandstones (OSSN, OSSH) were studied, characterized, petrographically analyzed and their alkali reactivity was determined as part of a research report by Franke [29]. OSSH has a true density of 1.69 g/cm^3 without considering the pore space and OSSN a density of 1.48 g/cm^3 [29]. According to the concrete prism test, OSSH was found to be reactive with respect to [9]. The strain of the prism made with OSSH already exceeded the limit value of $\varepsilon > 0.6$ mm/m after 14 days. Using OSSN as an aggregate also lead to strains, but after more than 250 days, it was only 0.257 mm/m, which is well within the acceptable range. Consequently, OSSN was classified as non-reactive according to [9]. However, nearly dissolved opal grains were observed with the microscope in the specimens of both aggregates after the storage period. Accordingly, a reaction also took place in the OSSN classified as non-reactive, which, though, was too small to cause damage. The results of the chemical and physical properties of the aggregates are summarized in table 1. SiO_2 is the main component in both aggregates. Specific surface of both is similar and ranges between 41 and 51 m^2/g. The numbers of the experiments with equal boundary conditions for OSSN, OSSH, and the quartz powder which are the basis for this paper's investigations are listed in table 2. The sample quantities vary between 3 g and 12 g. Thus, an oversupply of potassium hydroxide is guaranteed, and a sufficient amount of aggregate is available to cause significant changes in the measurement parameters.

Table 1. Characterization of the siliceous materials

	BET	**True Density**	**D_{10}**	**D_{50}**	**D_{90}**	**SiO_2**	**Fe_2O**	**K_2O**
	[m^2/g]	[g/cm^3]	[µm]			[%]	[%]	[%]
OSSN	51.56	1.48	2.79	8.63	26.61	83.14	3.8	2.6
OSSH	41.42	1.69	3.71	24.66	111.3	86.93	2.8	2.19
QP	0.9	2.65	10.0	16.00	42.86	99	0.05	-

Table 2. Numbers of experiments with equal boundary conditions

	3 g	**5 g**	**8 g**	**10 g**	**12 g**
OSSN	8	14	4	10	8
OSSH	-	6	8	12	-
QP	-	-	-	4	-

3 Results and discussion

3.1 Results

The change of the pH-value over the course of the dissolution process can be divided into four sections, as shown in figure 2 for 5 g of OSSN.

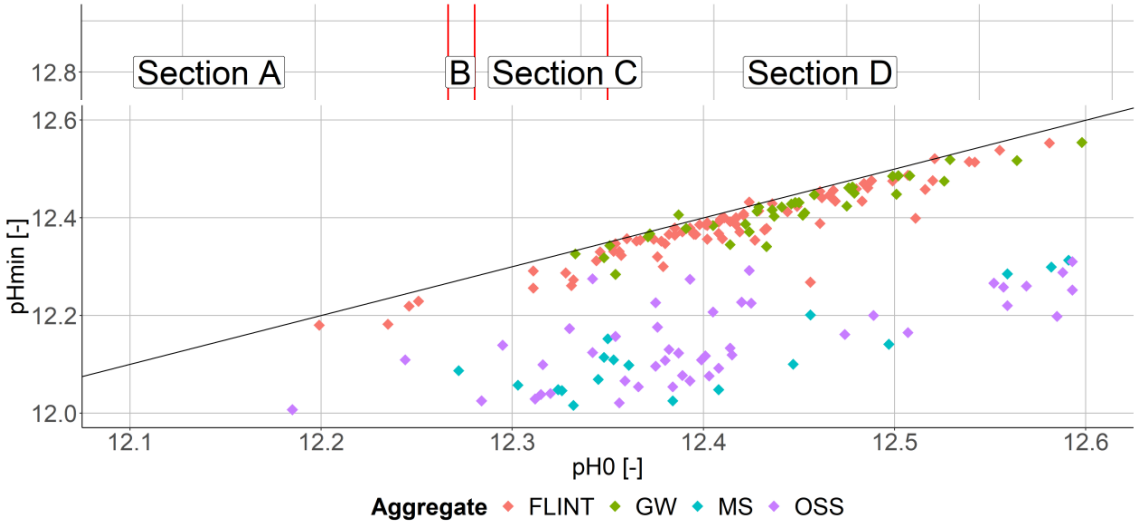

Figure 3: pH_{min} as a function of pH_0; All Experiments

The first section, section A shows the pH, pH_0 before adding the aggregate. pH_0 is constant and depends just on the experimental temperature and the possible measurement inaccuracy while producing the KOH-solution. The mean value over all experiments is pH 12.45. After adding the aggregate at time point zero, the pH-value drops in section B to a significant and global minimum, pH_{min} and increases again in section C until it reaches in section D a constant value again. The pH in section D equals pH_0 from the first steady state and does not change significantly until the end of the experiment. The values of the minimum and steady states and the form of the sections depend on the quantity and nature of the aggregate. Regarding the inert quartz powder, the pH-values remain constant throughout the different sections regardless of the amount of the added aggregate [28]. In this paper, investigations of pH_{min} are presented.When plotting the pH_{min} against the pH_0, a clear linear relationship between the two

variables can be seen. This relationship is even more noticeable when considering the values of all 330 previous tests, as shown in figure 3.

In addition of opaline sandstone (OSS, purple), figure 3 also contains data from experiments with flintstones (FLINT, red), graywackes (GW, green), and microsilica (MS, blue) of varying reactivity. The additional data serve only to illustrate the linear relationship between ph_0 and ph_{min}. Their further detailed analysis will be performed in future papers. Despite differences in reactivity, sample types, and sample amounts, a linear relationship between pH_0 and pH_{min}, as well as two clustering groups, are clearly evident. The pH of the experiments with flintstone and graywacke cluster around one line with a small spread. The pH of microsilica and opaline sandstone are scattered more widely along a different straight line. In comparison, the pH-minima of the experiments with flintstone and graywacke are always larger at the same pH_0 than in the case of microsilica and opaline sandstone.

In order to quantify and evaluate the influence of pH_0 on the pH_{min}, a linear regression model, with $y = \beta_0 + \beta_1 x$ was fitted to the data. For this purpose, pH_0 was first assumed to be the only predictor (x) on the pH-minimum (y). The model was fitted for each aggregate separately. The intercepts (β_0), gradients (β_1) and residuals (R^2) calculated by the regressions are shown in table 3. The adjusted residuals (R^2) of the models range from 0.81 to 0.92. Accordingly, 81% to 92% of the respective data could be represented by these models.

Table 3: Parameters of the linear regression of all sample types as a function of pH_0

	Intercept β_0	Gradient β_1	R^2
Opaline Sandstone	0.713	0.921	0.812
Microsilica	-0.261	0.998	0.920
Flintstone	0.136	0.987	0.884
Graywacke	0.877	0.927	0.863

The assumption that pH_0 is the only predictor of pH_{min} would mean that the expression of the pH_{min} was independent of the type and amount of sample. This assumption can already be disproved only by looking at figure 3, in which a sorting with respect to sample type is clearly visible.

Another influence on the pH_{min} over the course of the dissolution process of the material is the reactive surface area because the dissolution reaction takes place on the surface of the particle. The surface area of the ground aggregate was determined by BET measurement. The measured surface area as a function of mass is shown in table 1. Since the reactive surface area is proportionate to the sample amount and further simplifications regarding the geometry of the individual particles would have to be made when considering the surface as a predictor, only the sample quantity is considered an additional factor influencing the pH-minimum.

In figure 4 the pH-minima are plotted again with respect to pH_0. Within the two accumulation areas, a general classification can be seen with respect to sample amount. This sorting is more evident in the lower accumulation area, which contains the minima of opal sandstone and microsilica. The ph-minima of the dissolution experiments with a larger sample quantity result in a lower minimum. Accordingly, the sample quantity seems to have a proportionate effect on the pH-minimum. In the upper cluster, the individual data is less widely scattered, which makes the sorting with respect to sample quantity less apparent, but the same tendency is noticeable. This reinforces the assumption that, in addition to pH_0 and type of the aggregate, the amount of the aggregate also has a significant influence on the pH_{min}.

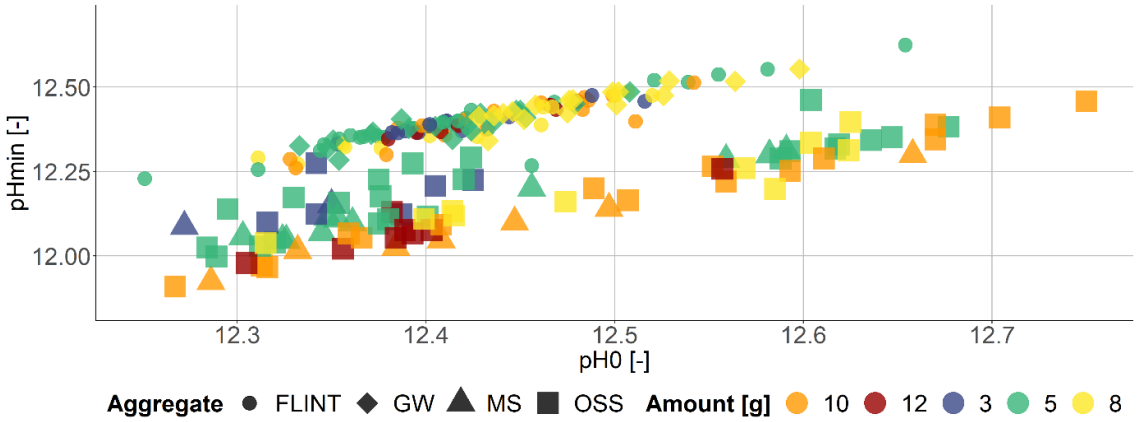

Figure 4: pH_{min} as a function of pH_0 and sample amount; All Experiments

Since the sorting with respect to sample quantity is more pronounced in the lower cluster, an influence of sample quantity on the pH-minima, in addition to ph_0, was first investigated based on opaline sandstone. The linear regression considering both influencing variables as predictors resulted in a larger adjusted residual for the opal sandstones, as can be seen in table 4. With the model considering only pH_0, about 85% of the data points can be explained. After extending the model to include the sample amount as an explanatory variable, R^2 increases to 0.881 and 0.895. Accordingly, the model that takes into account both influencing variables gives a better computational approach to the distribution of the data.

Table 4: Linear regression for opaline sandstone as a function of pH_0 and the sample amount

		Intercept β_0	Gradient β_1	Gradient β_2	R^2
OSSN	pH_0	-0.256	0.997	-	0.856
	pH_0 + sample Amount	0.0378	0.984	-0.011	0.881
OSSH	pH_0	1.383	0.865	-	0.856
	pH_0 + sample Amount	0.454	0.949	-0.014	0.895

The consideration of an influencing variable by linear regression requires a linear relationship between the dependent and independent variables. This relationship is only conditionally given between the sample quantity and the pH-minimum. Although an increased sample amount implies a larger reaction area and thus more reactants that can be dissolved, dissolution rate is largely determined by the concentration of mono-silicic acid contained in the solution. Once this concentration reaches its pH- and temperature-dependent equilibrium with the environment, no further aggregate will be dissolved despite sufficient sample quantity. Accordingly, the pH_{min} does not decrease indefinitely despite a larger sample amount. For simplicity, it is therefore assumed that the sample amount considered here is below this dissolution limit and that a change in the sample amount has a linear effect on the dissolution rate and thus also a linear effect on the conversion of the hydroxide ions and the pH_{min}.

The influence of the sample quantity on the pH_{min} was considered as a function of the different reactive opal sandstones. For this purpose, the linear regression model with pH_0 and sample amount as predictors was reduced by one independent variable. For pH_0, the mean pH-value at the time of sample addition over all previous experiments was used (pH 12.45). The regression model is thus reduced by one dimension, yielding a straight-line equation for each aggregate with sample quantity as the independent variable and ph_{min} as the dependent variable.

Comparing the two straight-lines in figure 5, the pH_{min} of OSSN, the less reactive opal sandstone consistently reaches higher pH-minima and has a lower slope than the regression line of OSSH. Thus, the less reactive material results in a consistently less pronounced pH-minimum and, the change in sample amount has a less significant effect on the pH-minimum than compared to the more reactive opaline sandstone.

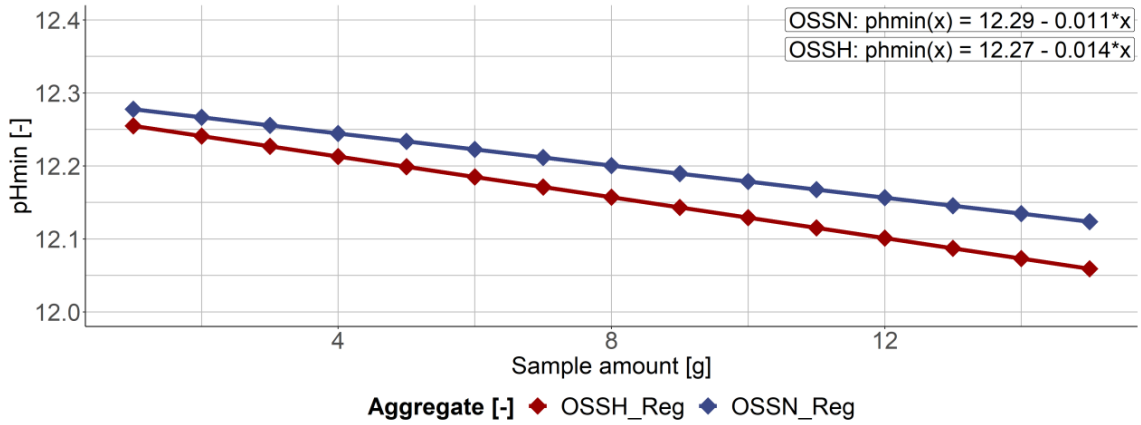

Figure 5: pH_{min} as a function of the sample amount

4 Summary, Conclusion, Outlook

4.1 Summary

A new test method for the detection of ASR aggregates by dissolution experiments was presented. The method is similar to the existing chemical testing but uses a different evaluation system to identify alkali-reactive aggregates. Instead of the use of elemental analyses or mass loss, the chemical changes of the solution medium are recorded and evaluated. This new approach could be used as an incoming-goods control for aggregates. It is based on accelerated dissolution experiments of the aggregates in alkaline solution, with an oversupply of alkali hydroxides.

During the dissolution of the aggregates pH-value, redox potential and electrical conductivity are measured. The first general outcome the predictability of the time courses of the individual physical and chemical parameters. In this paper, a minimum in pH-value was investigated. Investigations of the effects on conductivity and redox potentials will be reported in future papers.

First, the general course of the pH-value was presented. After adding the aggregate, the pH-value decreases to a global minimum, pH_{min} and then increases again to the initial value, pH_0. Further investigations were referred to pH_{min}. A linear relationship was observed between pH_{min} and pH_0. This ratio was found to be linear regardless of sample type and amount. However, the strength of the influence of ph_0 on pH_{min} shows clear dependencies on sample type and sample amount.

The influence of sample quantity was investigated using opaline stones with different reactivities. A linear regression model with the sample amount and pH_0 as predictors yielded residuals of around 0.9. Using this regression model, the pH-minima were calculated as a function of sample amount. To determine the straight lines, the mean value over all experiments was used in the regression model for pH_0.

It was found that the pH minima of the less reactive opaline sandstone, OSSN were always higher than those of the more reactive one, OSSH.

4.2 Conclusion and Outlook

The pH-value at the time of sample addition generally has a strong influence on pH_{min}. Nevertheless, influences of sample amount, sample type and reactivity of the aggregate can also be identified. In the case of opaline sandstone, the change in the pH minimum as a function of the sample amount made it possible to draw conclusions about the reactivity of the aggregate. These results are the first indications that different alkali reactivity could be mapped with this new test method. The important task for the future is to find a valid connection of the results with mortar bar tests and the concrete prism test and to extend the investigated materials.

5 Acknowledgements

The authors greatly acknowledges the funding of this research by the German Research Foundation (Deutsche Forschungsgemeinschaft, DFG) in the framework of Research Training Group GRK 2462: Processes in natural and technical Particle-Fluid-Systems (PintPFS) [30] at Hamburg University of Technology.

6 References

[1] Fernandes I., Broekmans M. A. (2013) Alkali–Silica Reactions: An Overview. Part I. Metallogr Microstruct Anal 2, p. 257–267. https://doi.org/10.1007/s13632-013-0085-5

[2] Thomas M. D., Fournier B., Folliard K. J. (2013) Alkali-aggregate Reactivity (AAR) Facts Book. Federal Highway Administration, Office of Pavement Technology

[3] ACI Committee 221 (2008) Report on Alkali-Aggregate Reactivity (Reapproved 2008): 221.1R-98. Technical Documents

[4] Rajabipour F., Giannini E., Dunant C. et al. (2015) Alkali–silica reaction: Current understanding of the reaction mechanisms and the knowledge gaps. Cement and Concrete Research 76, p. 130–146

[5] Stark J., Wicht B. (2013) Dauerhaftigkeit von Beton. Springer Berlin Heidelberg, Berlin, Heidelberg

[6] Thomas M., Fournier B., Folliard K. J. et al. (2013) Alkali-aggregate Reactivity (AAR) Facts Book. Federal Highway Administration, Office of Pavement Technology

[7] ASTM (2020) Guide for Reducing the Risk of Deleterious Alkali-Aggregate Reaction in Concrete C1778-20. www.astm.org. https://doi.org/10.1520/C1778-20

[8] Nixon P. J., Sims I. (eds) (2016) ILEM Recommendations for the Prevention of Damage by Alkali-Aggregate Reactions in New Concrete Structures: State-of-the-Art Report of the RILEM Technical Committee 219-ACS. Springer Netherlands, Dordrecht

[9] DAfStb (2013) DAfStb-Richtlinie Vorbeugende Maßnahmen gegen schädigende Alkalireaktion im Beton: (Alkali-Richtlinie)

[10] ASTM (2019) Guide for Petrographic Examination of Aggregates for Concrete C295. www.astm.org. https://doi.org/10.1520/C0295_C0295M-19

[11] RILEM TC 191-ARP (2003) AAR-1: Detection of potential alkali-reactivity aggregates: Petrographic method AAR-1. Accessed 22 Feb 2021

[12] RILEM TC 191-ARP (2003) AAR-2: Detection of potential alkali-reactivity aggregates: Accelerated Mortar-Bar Test Method for Aggregates Petrographic method AAR-2. Accessed 22 Feb 2021

[13] RILEM TC 191-ARP (2003) AAR-3: Reactivity 38°C Test Method for Aggregate Combinations Using Concrete Prisms AAR-3. Accessed 22 Feb 2021

[14] ASTM (2010) Test Method for Potential Alkali Reactivity of Cement-Aggregate Combinations (Mortar-Bar Method) C227-10. www.astm.org. https://doi.org/10.1520/C0227-10

[15] ASTM (2020) Test Method for Determination of Length Change of Concrete Due to Alkali-Silica Reaction C1293-20a. www.astm.org. https://doi.org/10.1520/C1293-20A

[16] ASTM (2021) Test Method for Potential Alkali Reactivity of Aggregates (Mortar-Bar Method) C1260-21. www.astm.org. https://doi.org/10.1520/C1260-21

[17] ASTM (2007) Standard test method for potential alkali-silica reactivity of aggregates (chemical method) C289-07. www.astm.org. https://doi.org/10.1520/C0289-07

[18] Bulteel D., Garcia-Diaz E., Vernet C. et al. (2002) Alkali–silica reaction. Cement and Concrete Research 32, p. 1199–1206. https://doi.org/10.1016/S0008-8846(02)00759-7

[19] Eikenberg J. (1990) On the Problem of Silica Solubility at High PH. PSI, p. 57

[20] Visser J. H. (2018) Fundamentals of alkali-silica gel formation and swelling: Condensation under influence of dissolved salts. Cement and Concrete Research 105, p. 18–30. https://doi.org/10.1016/j.cemconres.2017.11.006

[21] Goto K. (1956) Effect of pH on Polymerization of Silicic Acid. J Phys Chem 60, p. 1007–1008. https://doi.org/10.1021/j150541a046

[22] Greenberg S. A. (1957) The Depolymerization of Silica in Sodium Hydroxide Solutions. J Phys Chem 61, p. 960–965. https://doi.org/10.1021/j150553a027

[23] Dove P. M., Han N., Wallace A. F. et al. (2008) Kinetics of amorphous silica dissolution and the paradox of the silica polymorphs. Proc Natl Acad Sci U S A 105, p. 9903–9908. https://doi.org/10.1073/pnas.0803798105

[24] Amjad Z. (ed) (2014) Mineral scales in biological and industrial systems. CRC Press, Boca Raton, Fla.

[25] Osterhus L., Schmidt-Döhl F. (2014) Verbessertes Prüfverfahren zur Beurteilung der Alkalireaktivität von Gesteinskörnungen basierend auf Lösungsversuchen. GDCh Conference Bauchemie 48, p. 41-44

[26] R Core Team (2017) R: A Language and Environment for Statistical Computing. R Foundation for Statistical Computing, Vienna, Austria

[27] Quarzwerke (2021) Datasheet MILLISIL-Mehle. https://www.quarzwerke.com/fileadmin/quarzwerke/Leistungserklaerungen/Leistungserkl-Sortenverz-EN12620-SMF_Revision_1.pdf. Accessed 28 Apr 2021

[28] Osterhus L., Dombrowski C., Schmidt-Döhl F. (2015) Löslichkeitsuntersuchungen zur schnellen Beurteilung der Alkalireaktivität von Gesteinskörnungen. 19. Int. Baustofftagung ibausil 2015, p. 1405–1412

[29] Franke L. (2002) Schnelltest auf Alkalireaktion für deutsche Beton-Zuschläge. Bau- und Wohnforschung. Fraunhofer-IRB-Verl., Stuttgart

[30] DFG Research Training Group GRK 2462: processes in natural and technical Particle-Fluid-Systems (PintPFS). https://gepris.dfg.de/gepris/projekt/390794421. Accessed 22 Feb 2021

Author

M. Sc. Gyde Hartmut
Hamburg University of Technology
Institut of Materials, Physiys and Chemistry of Buildings
Eissendorfer Strasse 42
211073 Hamburg
gyde-hartmut@tu-harburg.de
www.tuhh.de/bp/home.html
www.tuhh.de/grk2462/startseiteh.tlm

Prof. Dr Frank Schmidt-Döhl
Hamburg University of Technology
Institut of Materials, Physiys and Chemistry of Buildings
Eissendorfer Strasse 42
211073 Hamburg
schmidt-doehl@tu-harburg.de

New findings on alkali-silica-reaction of concrete

Andreas Leemann

1 Extended abstract

Alkali-silica-reaction (ASR) is one of concrete's most important deterioration mechanisms, leading to substantial damage to structures worldwide. Any structure like dams, bridges or tunnels can be affected.

The reaction starts with the dissolution of unstable SiO_2 present in aggregates by the highly alkaline pore solution of the concrete (pH 13.0–13.5). The subsequent formation of ASR products in concrete aggregates leads to stress generation. As a result, expansion and cracking of the concrete may occur. Typically, such cracks are formed years or even decades after the affected structures were built. Three prerequisites have to be present for ASR to occur:

(i) sufficient alkalinity of the pore solution (alkalis provided by the cement)

(ii) reactive minerals in the concrete aggregates

(iii) sufficient availability of moisture

Although the phenomenon is in the focus of research for decades, many open questions remain. One major reason for this situation is the difficulty of studying the development reaction and analyzing the products formed. Despite their significant effect on deformation and crack formation of concrete, the volumes of ASR products formed are relatively small. As a result, the reaction sequence is difficult to follow, particularly in the stage before initial cracking occurs. At this stage, the size of ASR products is in the micrometre to sub-micrometre range. Secondly, the typical methods to characterize bulk samples of hydrates are usually not applicable, as the amounts extractable from aggregates are in the range of a few micrograms at best. However, detailed knowledge of the sequence of reaction and an in-depth characterisation of the ASR products are the basis for improving the understanding of ASR and the mechanism leading to expansion and stress generation.

The back-scattering contrast of the ASR products in the scanning electron microscope (SEM) is nearly identical to the one of silicates like quartz. As the initial products formed before aggregate cracking develop as thin layers between adjacent mineral grains in concrete aggregate particles, they are challenging to detect. A coherent view of reaction development is impossible. A novel approach uses Cs as a tracer (Leemann et al. 2019). $CsNO_3$ can be added to the mixing

water of concrete. As an earth alkali, it is bound in the ASR products. Due to its higher atomic number compared to Si, Na, K, Ca and O, it significantly enhances back-scattering contrast and makes ASR products easily recognisable in the SEM (Figure 1). As such, it allows us following the sequence of reactions. With a resolution down to the sub-micrometre scale it provides a complete view of the reaction. However, the challenge of determining these initial products' chemical composition remains. The initial product volume is too small to be analysed with energy-dispersive X-ray spectroscopy (EDS) in a SEM. Within the framework of the collaborative project of several institutes (Leemann et al., 2021), a different way of analysis was developed.

Lamellas were cut with a focused ion beam (FIB) perpendicular to two adjacent quartz grains and subsequently analysed in a transmission electron microscope (TEM) (Boehm-Courjault et al., 2017; Boehm-Courjault et al., 2020). Apart from determining the composition of the initial products, this method additionally allows analyzing whether they are amorphous or crystalline by using selected area electron diffraction.

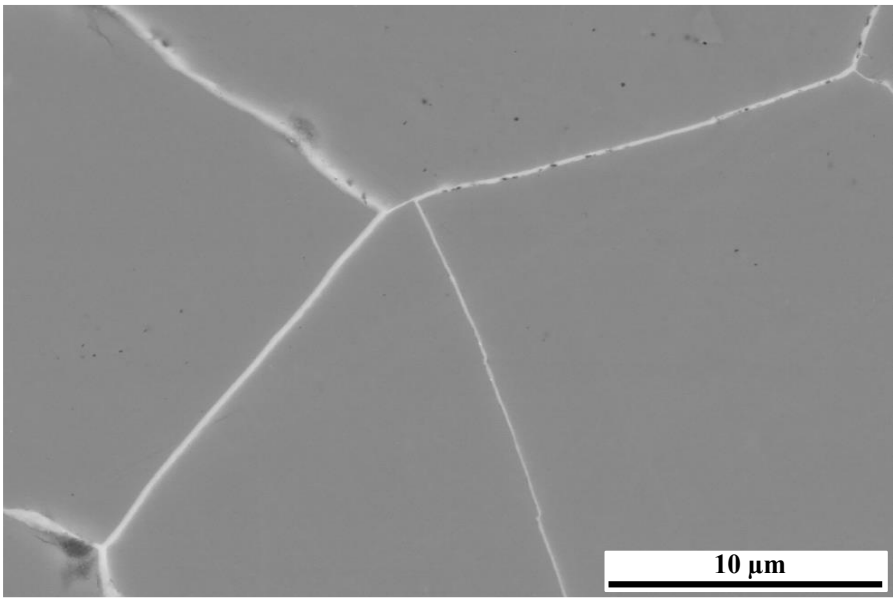

Figure 1: Cs-containing ASR product between adjacent quartz grains in an ASR-affected concrete [1]. SEM-image in the back-scattering mode.

In the second stage of the reaction, concrete aggregates crack, and a part of the ASR products extrudes into the cement paste. A given time point in this process can be observed in samples studied in SEM. However, how such crack systems develop and how the ASR products are extruded has not been possible to observe in a sequence. Here, the approach of using Cs as a tracer has been used again but now in X-ray micro-tomography (XMT) (Shakoorioskooie et al., 2021). Furthermore, $BaSO_4$ was added to the concrete allowing a reliable segmentation between concrete aggregates and cement paste. The resulting tomograms allow following ASR in a 4D-view.

In the reaction's second stage, analysing the elemental composition of the ASR products using SEM and EDS is straightforward. However, analysing their structure remains challenging because the volumes formed are still too small to use conventional bulk analysis. A combination

of Raman microscopy, powder-X-ray diffraction (XRD) in capillaries and synchrotron-based XRD has increased knowledge of these products (Leemann et al., 2020; Geng et al., 2020; Geng et al., 2021). The amorphous product consist of Q^2 (chains of SiO_2 tetrahedra with two linked oxygen) and Q^3-sites (layers of SiO_2 tetrahedra with three linked oxygen). Several different crystalline ASR products formed are distinguishable by their d-spacing of 10.8, 12.3 and 13.4 Å. None of them is swellable, as their analysis of different moisture conditions relevant for concrete has shown. As such, one of the major hypotheses for ASR-induced expansion, swelling of crystalline ASR products due to water uptake, was proven to be wrong.

Despite these advancements in ASR, important questions regarding the mechanism generating expansion are not answered yet. It is clear from microstructural observations that the stress is generated within the aggregates rather than in the cement paste. In principle, possible reasons for stress generation by ASR products can be divided into swelling by water imbibition of the amorphous ASR products, osmotic swelling, crystallisation pressure and mass accumulation in the aggregate or any combination thereof.

References

[1] Boehm-Courjault E, Barbotin S, Leemann A, Scrivener K (2020): Microstructure, crystallinity and composition of alkali-silica reaction products in concrete determined by transmission electron microscopy. *Cement and Concrete Research,* 130:105988

[2] Boehm-Courjault E, Leemann A (2017): Characterisation of ASR products by SEM and TEM, Proceedings of the 16th Euroseminar on Microscopy Applied to Building Materials, Les Diablerets, Switzerland

[3] Geng G, Barbotin S, Shakoorioskooie M, Shi Z, Leemann A, Sanchez DF, Grolimund D, Wieland E, Dähn, R. (2021): An in-situ 3D micro-XRD investigation of water uptake by alkali-silica-reaction (ASR) product. *Cement and Concrete Research,* 141:106331

[4] Geng G, Shi Z, Leemann A, Borca C, Huthwelker T, Glazyrin K, ..., Wieland E (2020): Atomistic structure of alkali-silica reaction products refined from X-ray diffraction and micro X-ray absorption data. *Cement and Concrete Research,* 129:105958

[5] Leemann A, Bagheri M, Lothenbach B, Scrivener K, Barbotin S, Boehm-Courjault E, Geng G, Dähn R, Shi Z, Shakoorioskooie M, Griffa M. (2021) : Alkali-silica-reaction - a multidisciplinary approach. *RILEM Technical Letters,* 15(6):169-87

[6] Leemann A, Münch B (2019): The addition of caesium to concrete with alkali-silica reaction: Implications on product identification and recognition of the reaction sequence. *Cement and Concrete Research,* 120:27-35

[7] Leemann A, Shi Z, Wyrzykowski M, Winnefeld F (2020): Moisture stability of crystalline alkali-silica reaction products formed in concrete exposed to natural environment. *Cement and Concrete Research,* 137: 106190

[8] Shakoorioskooie M, Griffa M, Leemann A, Zboray R, Lura P (2021): Alkali-silica reaction products and cracks: X-ray micro-tomography-based analysis of their spatial-temporal evolution at a mesoscale. *Cement and Concrete Research*, 150:106593

Author

Dr. Andreas Leemann
Empa
Swiss Federal Laboratories for Materials Science and Technology
Concrete and Asphalt Laboratory
Überlandstr. 129
8600 Dübendorf
Switzerland
Tel.: +41 (0) 58 – 765 44 89
e-mail: andreas.leemann@empa.ch
Web: www.empa.ch

Numerical investigation of the breakage and crash absorbing behavior of granular materials in ship collisions

Sonja Rotter, Christian Woitzik, Süreyya Tasdemir, Maksym Dosta, Alexander Düster

Abstract: The collision safety of ships can be improved by filling their double hull with a granular material. To this end, expanded glass granules are investigated numerically using the discrete element method to study their fracture behavior implemening models that can represent this behavior in a satisfying way. The use of a bonded-particle model allows the simulation of non-spherical particles and fracturing. However, special attention must be paid to the model used in terms of its failure behavior. In order to test different models, simulations with single and multiple particles are performed and compared with the corresponding experiments. The single particle experiment, i.e. a uniaxial pressure test, is used to identify parameters of different bond models. Subsequently, a bulk test and a uniaxial compression test are performed to investigate the interaction between multiple particles, and to determine the friction and the influence of their interaction on their fracture behavior.

1 Introduction

In the course of economic globalization and the resulting increase in maritime traffic, the number of ships on our seas is growing. Despite the use of modern navigation assistants like radar and Automatic Identification Systems (AIS) there are still ship collisions due to human error or system failures. Some of these collisions have severe consequences for the crew and ecosystem. For this reason, ship collision safety is a widely studied area. Most research projects try to further improve the construction of the double hull (Ehlers et al., 2012; Ringsberg et al., 2013) which was introduced first to oil tankers in 1996 by the International Maritime Organization (IMO) (IMO, 2022). In (Yamada et al., 2008) the construction and material of the bulbous bow are modified in such a way that it folds or breaks during an impact to minimize the damage on the opponents hull. One of the most recent ideas of increasing the collision safety of double hull ships is to fill the void between the outer and inner hull with a crushable granular material (Schöttelndreyer, 2015; Woitzik et al., 2016). The general idea of this approach is twofold: On the one hand the impact load is transferred from the outer to the inner hull, allowing the whole structure to take up the force. On the other hand the brekage of the granules helps to dissipate energy. Various materials were investigated for this purpose, resulting in the selection of expanded glass particles thanks to their energy dissipation capabilities and chemical properties (Woitzik et al., 2017; Woitzik

et al., 2018; Woitzik et al., 2020). The granular material was investigated in several experiments, including uniaxial pressure tests (Woitzik et al., 2020), friction tests, and uniaxial compression tests (Chaudry et al., 2016). These experiments where numerically studied in (Chaudry et al., 2017) with the discrete element method (DEM) (Cundall et al., 1979). The used DEM approach is based on a parent-child simulation strategy, in which the parent particle breaks into several child particles (Chaudry et al., 2017). Here we focus on a different approach for the numerical investigation of the granular material. The applied DEM algorithm includes a bonded-particle method which allows the simulation of nonspherical, breakable particles. The particle is modeled as an agglomerate of small primary particles connected by solid, massless beams (Potyondy et al., 2004).

The paper is structured as follows: In Section 2 the specific requirements for the granules are summarized and the chosen particles are presented. Section 3 describes the applied DEM as well as the bonded-particle model followed by an investigation of the simulation properties and their influence on the results of a uniaxial pressure test presented in Section 4. Section 5 discusses the simulation of experiments in which multiple particles are involved like a bulk and a uniaxial compression test. The paper is concluded in Section 6 which also gives a short outlook on future work.

2 Expanded glass granules

After thorough investigations of different materials including clay and expanded glass, the latter was found to be better suited for the given purpose as a crah-absorber in a ships double hull. One of the examined glass granules in (Woitzik et al., 2020) is Poraver ® expanded glass. Poraver ® is already being used successfully in many fields e.g. as a building material, filter material, in the automotive industries as well as aviation and marine technologies (Poraver, 2022). Poraver ® meets all requirements to be used in a ships double hull. These requirements include nontoxicity and environmental friendliness since the material is likely to spill in the event of a collision and should not harm the ecosystem. Moreover it has to be incombustible, hydrophobic, light-weighted in order to not decrease the payload of the ship nor harm the stability or safety in the event of a fire. Since the ship has to be maintained regularly the material has to be pumpable to be able to investigate the inside of the double hull. A more detailed list of all requirements and the reasons behind them can be found in (Schöttelndreyer, 2015).

Due to the manufacturing process, the Poraver ® particles have very different shapes and porosities. These differences can be seen in Figure 1, where the inner part of a particle is shown as well as a couple of particles to illustrate the shape and size variety. All of this has a great influence on the breakage behavior of the Poraver ® particles and thus the material parameters like Young's modulus and breakage strength. To reduce the scatter of the material parameters the grains have been divided into three diameter fractions (Woitzik et al., 2017). The grain size range used for the experiments is 2-4 mm, resulting in the diameter fractions listed in Table 1. The table also shows the average material parameters determined from uniaxial compression tests and their standard deviations. The experimental results used to generate the material parameters

Table 1: Diameter and material parameters of Poraver ® particles [18]

Fraction [mm]	Diameter [mm]	Cr. force [N]	Cr. stress [MPa]	Cr. strain [%]	E-Modulus [MPa]	Tests [-]
2.0-2.5	2.16±0.15	14.81±5.19	4.05±1.45	16.49±4.12	564.26±260.60	94
2.5-3.125	2.68±0.18	17.88±5.45	3.19±0.99	16.01±4.98	453.79±158.65	102
3.125-4.0	3.28±0.22	21.62±6.82	2.59±0.87	14.66±4.91	364.84±127.85	106

are shown in Figure 2 as stress-strain curves for a diameter of 2.5-3.125 mm. These curves clearly indicate the huge scatter of the test results. Taking these differences into account for the numerical investigation is quite challenging and will be discussed in detail in Section 4.

(a) Inner structure (b) Form and diameter variation

Figure 1: Porosity and form of Poraver ® particles

3 Numerical method

The ability of simulating the breakage of particles is of great importance in the described application as crash absorber in a ships double hull, since the energy dissipated in the crushing process plays a key role. For this reason, the discrete element method is used, as it offers the possibility to simulate single particles. In combination with a bonded-particle model, the porous material of the expanded glass particles can be optimally taken into account. The utilized simulation tool and the underlying models will be introduced in the following sections.

3.1 Simulation tool

For all computations shown in Section 4 and 5 the open source framework MUSEN (MUltiscale Simulation ENvironment) (Dosta et al., 2020) is used. MUSEN is based on a soft-sphere DEM

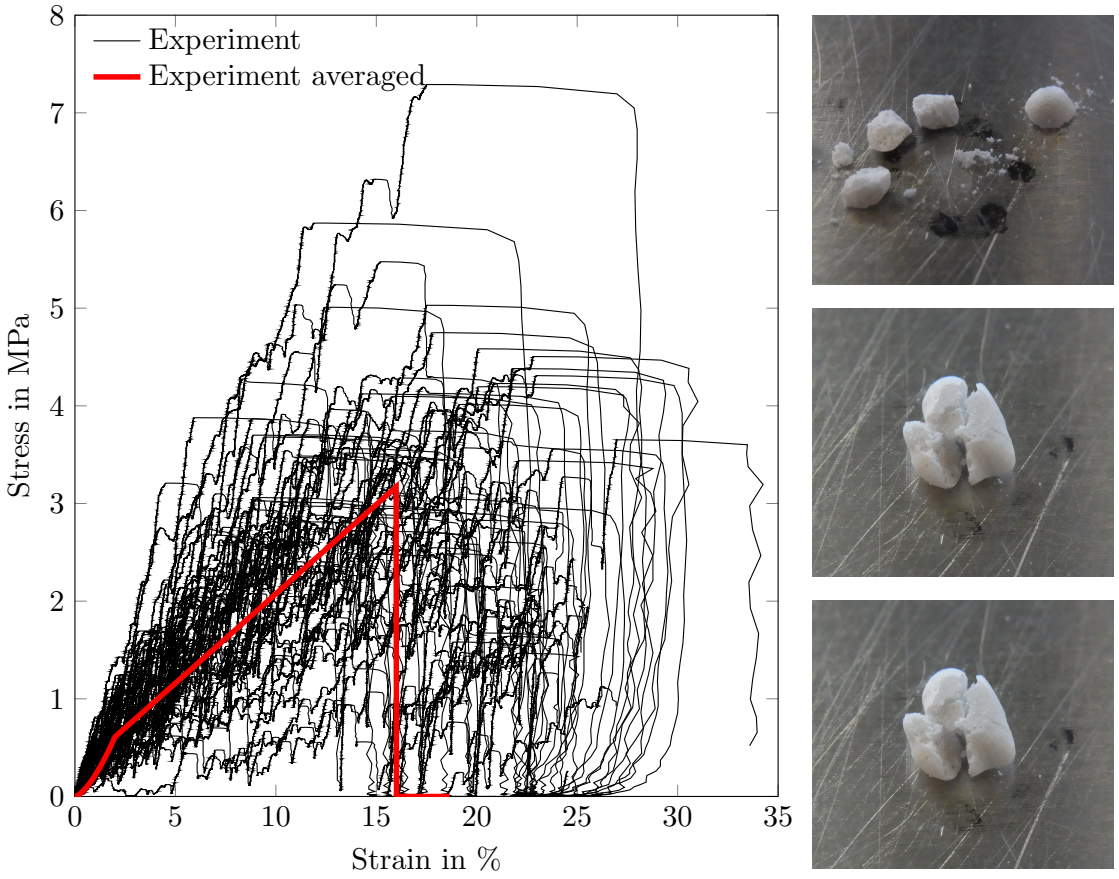

(a) Results of the uniaxial pressure test for a diameter fraction of 2.5-3.12 mm with 102 particles in black and the average stress-strain curve in red

(b) Exemplary broken particles

Figure 2: Scattering of uniaxial pressure test results

approach (Zhu et al., 2007) simulating the dynamic behavior of discrete quasi rigid bodies (Wriggers et al., 2020). To compute the interaction between these bodies, their neighborly relations have to be detected. This is done with Verlet lists (Verlet, 1967) in combination with a linked-cell algorithm (Quentrec et al., 1973) in order to reduce computational time, since this is one of the most expensive parts of DEM simulations. Thus detected contacts lead to forces between the particles and particles and walls which are calculated with a contact model. MUSEN provides a number of different contact formulations (Dosta et al., 2020) including the Hertz-Mindlin model (Deresiewicz et al., 1952) which is the most suitable one for describing the occurring contact forces in the performed simulations. The resulting contact forces combined with the forces coming from the bonds and all acting volume forces lead to particle movements, which are calculated using Newton's laws of motion. These equations are integrated with an explicit scheme based on the leapfrog algorithm (Young, 2013). In this way, momentum is propagated through the field of particles.

3.2 Bonded-particle model

The simulation of non-spherical objects with DEM becomes possible by combining it with a bonded-particle method. With this method particles are simulated as agglomerates consisting of primary particles connected by solid bonds. These bonds are either introduced as a couple of springs or beams connecting two particles (Xizhong et al., 2022). In this work the bonds are modeled as beams and the bond forces are computed with a linear elastic model proposed by (Potyondy et al., 2004). In each time step, an increment of these forces in normal $\Delta \boldsymbol{F}_{b,n}$ and tangential $\Delta \boldsymbol{F}_{b,t}$ direction as well as increments of torsional $\Delta \boldsymbol{M}_{b,n}$ and bending $\Delta \boldsymbol{M}_{b,t}$ moments are calculated. To obtain the increments of forces and moments the relative translational and rotational velocities $\boldsymbol{v}_{rel}$ and $\boldsymbol{\omega}_{rel}$ together with the simulation time step Δt are used. To enable the breakage of the bond a fracture criterion is introduced. If the normal or tangential strength of the bond is exceeded by the current stress in the bond it is removed from the simulation leaving the two adjacent particles unconnected and thus leading to a crack in the agglomerate. For an in depth explanation of this bond model, hereafter called Model 1, see (Potyondy et al., 2004). In addition a second bond model, which will be referred to as Model 2, is used for the simulations which takes the micro cracking of the particles into account. This model is based on a plastic approach limited by a yield condition together with a stress reduction algorithm modeling the energy dissipation which occurs due to the micro cracks (Kraus et al., 2021). How the bond model influences the breakage of the agglomerate and thus the results of the simulation, is shown in the following section.

4 Single particle simulations

Uniaxial compression tests were carried out to investigate the fracture behavior of Poraver ®. For this test, individual grains are compressed between two metal plates using a uniaxial compression tester Texture Analyser TA.XTPlus see Figure 3a. The simulation setup depicted in Figure 3b contains an agglomerate consisting of 361 primary particles connected by 2159 bonds between two metal plates. The initial simulations are performed with the material parameters derived from the experiments, see Table 1, a particle diameter of 2.16 mm for the agglomerate and 0.25 mm for the primary particles, and a porosity of $44\,\%$.

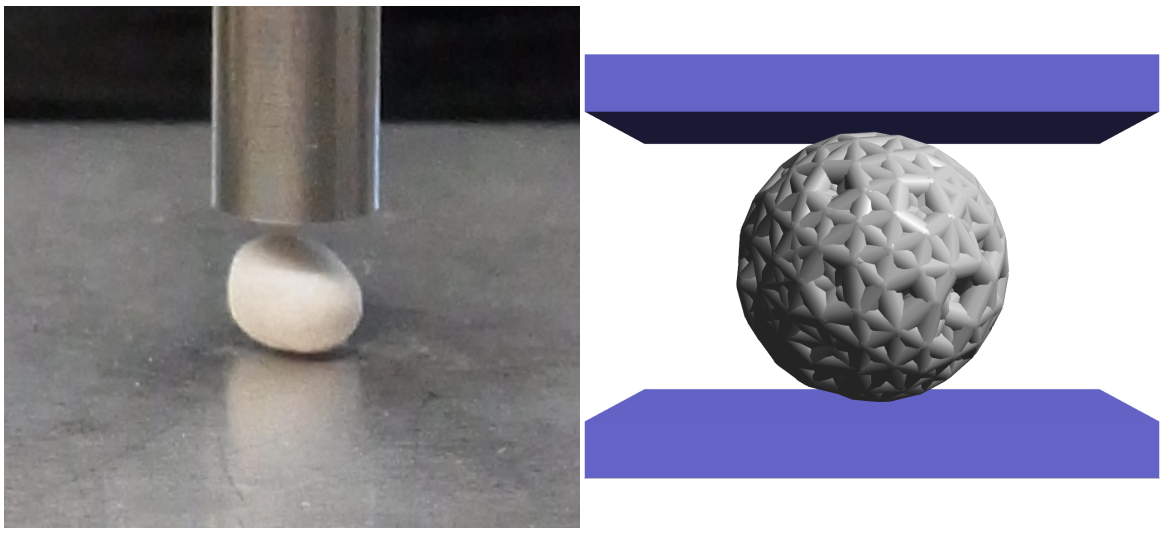

(a) Experimental setup (b) Simulation setup

Figure 3: Uniaxial pressure test setups

To obtain the best possible comparison of the influence of the bond model on the simulation, the same agglomerate is calculated with both models. The stress-strain curves derived from these simulations are shown in Figure 4a compared to the average experimental results from (Woitzik et al., 2017). In addition to stress, fracture ratio of the number of remaining bonds is also plotted against strain. Where 0 means that no bond is broken, while 1 means that all bonds are broken. Both stress-strain curves are well off the average experimental results, especially for the first few percent of strain. However, looking at the gradient of the simulation results, the green curve illustrating the results determined with Model 2 is quite similar to the experimental average. In addition, the breaking bonds are better distributed over the strain for Model 2, resulting in less abrupt drops in the number of remaining bonds. The breaking patterns depicted in Figure 4b for Model 1 at the top and Model 2 at the bottom both show reasonable results compared to Figure 2. Since the results of Model 2 are overall more promising, this model will be applied for further investigations.

4.1 Influence of geometric simulation parameters

Based on the simulation setup described in Section 4, three geometrical simulation parameters and their influence on the stress-strain behavior of the agglomerate are investigated. The parameters considered are the porosity of the agglomerate, the diameter of the primary particles, and the shape of the agglomerate.

The porosity describes the volume fraction of the analytical geometry that is not filled with primary particles. In the cases discussed here, the analytical volume is a sphere with the diameter of the grain to be represented. Since the primary particles are also spheres, the porosity has a limit at which the overlap of these particles is too large, leading to tensions between the primary

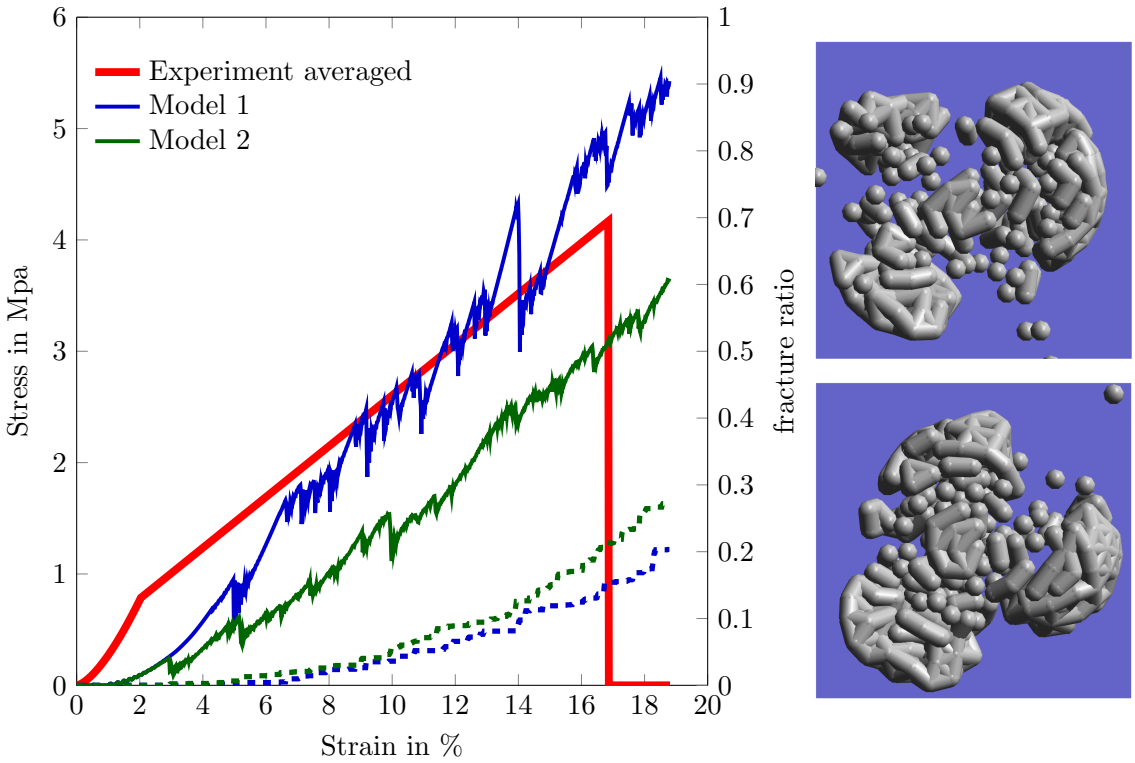

(a) Stress-strain curves for Model 1 and Model 2

(b) fracture pattern

Figure 4: Simulation results

particles and thus destruction of the agglomerate at the very beginning of the simulation. This early breakage can be seen in Figure 5a illustrated in light green. The remaining curves show he influence of an increasing porosity and thus more space between the primary particles. The higher the porosity, the lower the slope of the curve and thus the stiffness and crushing stress. However, the breakage strain increases with porosity. The main influence can be seen only after two percent of strain, so that the Young's modulus stays equal. It can also be seen that porosity at about $40\,\%$ to $45\,\%$ leads to a similar gradient to the average experimental results.

The influence of the primary particle diameter on the result of the simulation is not significant, see Figure 5b. It is noticeable here, especially at the beginning of the simulation, that the upper plate moves downward without any increase in stress for particle diameters above 0.4 mm. This indicates that the particles in the analytical volume are placed in such a way that the primary particles do not touch the upper plate at the start of the simulation. If the stress-strain curve were adjusted for this effect, it would be visible that larger primary particles result in a somewhat stiffer agglomerate. Primary particle diameters of 0.3 mm and less lead to the best results and the stress-strain curves for these particle sizes also overlap.

Since the Poraver ® granules are not exactly spherical but rather elliptical, the agglomerates are slightly flattened at the top and bottom. Since the particles automatically position themselves on their flattened side when placed under the texture analyzer, this approach results in a realistic

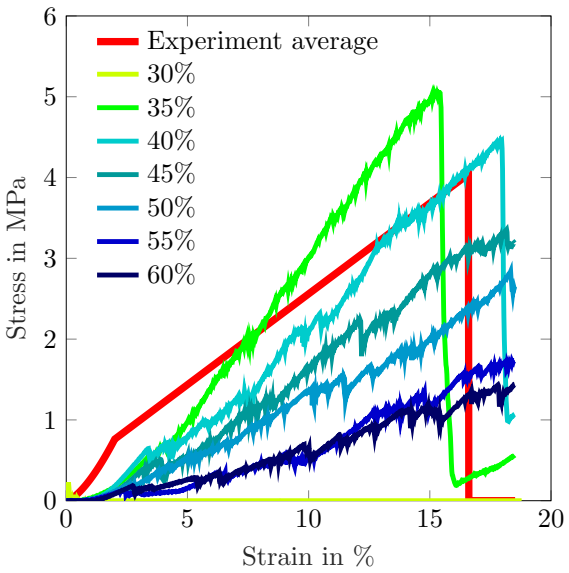

(a) Variation of porosity between 30 % and 60 %

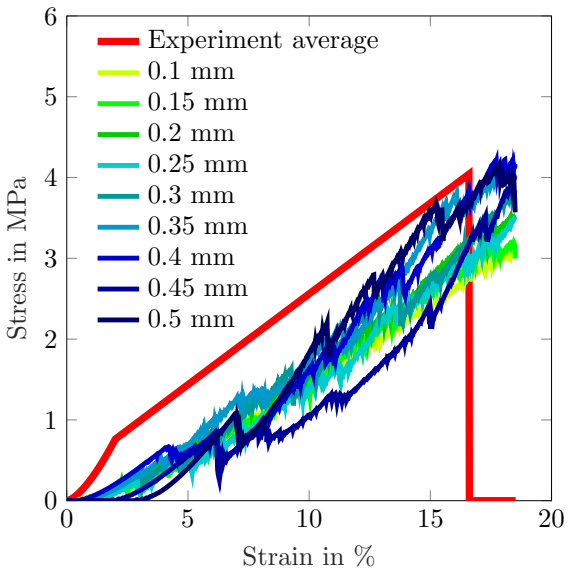

(b) Variation of primary particle diameter from 0.1 mm to 0.5 mm

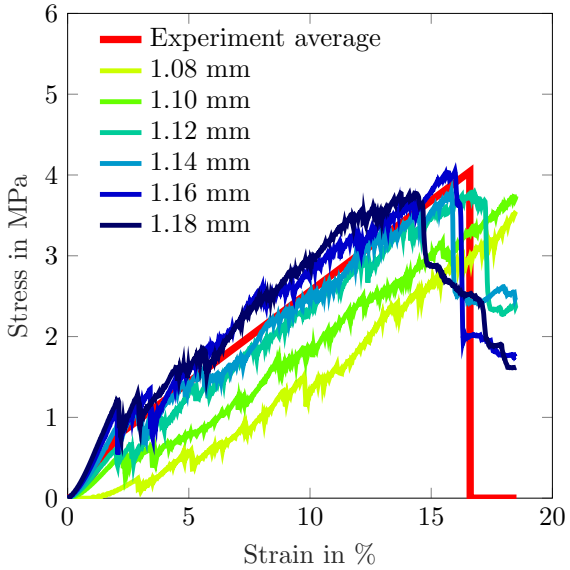

(c) Flattening the agglomerate at the top and bottom by varying the radius from 1.08 mm to 1.18 mm

Figure 5: Influence of microstructure and shape of agglomerate on its mechanical behavior

particle shape. To flatten the particles, the top and bottom plate remain 2.16 mm apart, while the radius of the analytical volume is increased in small increments from 1.08 mm yielding a sphere, to 1.18 mm leading to a more oval shape. The analytical volume is filled with primary particles, with the restriction that they cannot be generated inside the plates. The resulting stress-strain curves are depicted in Figure 5c, showing a great influence on the initial slope and thus on the Young's modulus of the agglomerate. Due to the flattening, more primary particles

connect to the top plate right at the beginning of the simulation, leading to a stiffer response. The gradient of the remaining part of the simulation seams to be independent of this. The crushing stress of all simulations is also similar but the crushing strain decreases slightly for flatter agglomerates. In summary, a flattened agglomerate leads to a stress-strain curve similar to the averaged experimental results.

4.2 Influence of material parameters

Keeping these findings in mind the influence of the material parameters are investigated for a slightly flattened agglomerate with a porosity of $43.6\,\%$ and a primary particle diameter of 0.25 mm. In order to achieve a thorough understanding of the material parameters influence on the breakage of the agglomerates five parameters, namely the Young's modulus and breakage strength of primary particle and bond and the bonds yield strength are varied ten times. This gives the opportunity to also investigate how the material parameters correlate with each other. A detailed study can be found in (Tasdemier, 2022). The main findings of this work are that the influence of the crushing strength of bonds and primary particles on the breakage of the agglomerate is negligible. However, the Young's modulus of the bond has an effect on the crushing strength and strain as can be seen in Figure 6a showing a selection of the most significant stress-strain curves from the parameter variation. Up to a Young's modulus of 800 MPa the crushing strength increases to again decrease if the Young's modulus is raised further. Nevertheless, the bonds Young's modulus has no significant influence on the agglomerates Young's modulus which is evident from the initial slope of the stress-strain curves. In contrast to this the primary particles Young's modulus has a visible influence on the agglomerates initial stiffness. This is also reflected in the coefficient of variation of Young's modulus of 8.287 MPa and 72.258 MPa respectively. The bonds yield strength, which is one of the leading parameters in the applied bond model, also has no significant influence on the agglomerate breakage unless it is smaller than 1 MPa, see Figure 6c, which leads to a visible reduction in the crushing stress. From these findings a selection of parameters was conducted leading to a nearly perfect stress-strain curve as shown in Figure 7 with a bonds Young's modulus of 500 MPa and yield strength of 2 MPa and a primary particles Young's modulus of 600 MPa. This result shows the ability of simulating a single particle test to a satisfactory extend giving the opportunity to use these agglomerates in more complex multi particle simulations.

5 Multi particle simulations

The objective of this work is to investigate particles for use in ship double hulls in large quantities. Besides the analysis of single particles, it is also important to study the interaction of the particles with different tests.

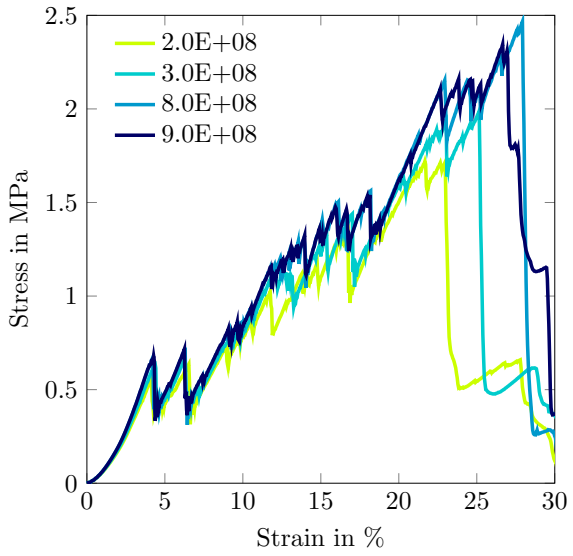

(a) Variation of the bonds Young's modulus

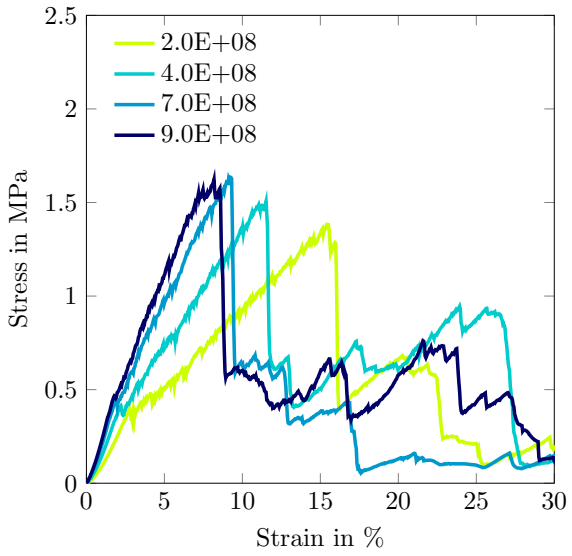

(b) Variation of the primary particles Young's modulus

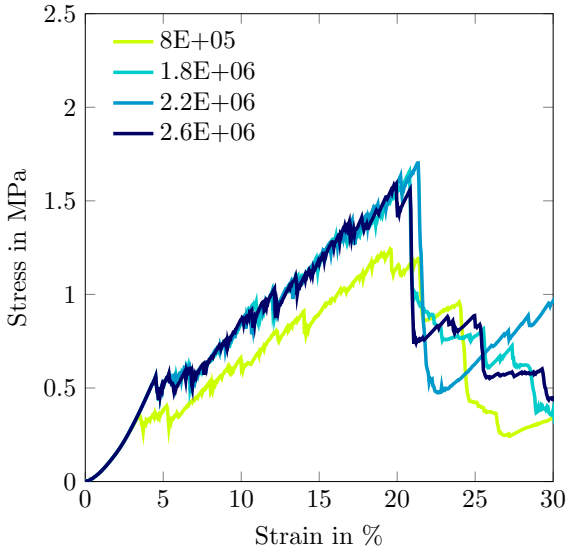

(c) Variation of the bonds yield strength

Figure 6: Influence of material parameters on the breakage of the agglomerate

5.1 Bulk test

In order to gain a better understanding of the friction values used in the simulations a bulk test as depicted in Figure 8a has been carried out with a pouring velocity of 20 mm/s. The sliding friction coefficient has been set to 0.87 with regard to experiments from (Woitzik et al., 2020) and the rolling friction coefficient is varied from 0.06 to 0.8 leading to the resulting cone heights presented in Table 2 and illustrated in Figure 8b. The average cone height derived from the bulk

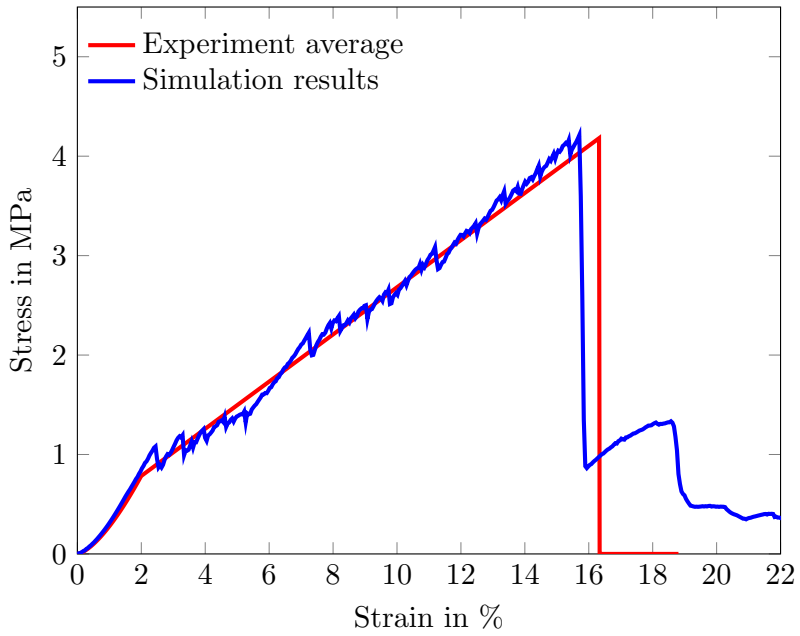

Figure 7: Stress-strain curve of a simulation with selected parameters, a bonds Young's modulus of 500 MPa, yield strength of 2 MPa and a primary particles Young's modulus of 600 MPa

tests is 18.3 mm indicating a rolling friction of 0.16 for further simulations.

Table 2: Bulk test simulation results (20 mm/s)

Sliding friction	Rolling friction	Cone height [mm]	Cone diameter [mm]
0.87	0.8	21.3	43
0.87	0.6	21	44
0.87	0.4	18.8	46
0.87	0.2	18.7	47
0.87	0.1	17.3	48
0.87	0.08	16.9	48
0.87	0.06	16.1	48

5.2 Uniaxial compression test

Since the interaction of particles under pressure is of interest due to the given purpose, a uniaxial compression test was performed as shown in Figure 9a. For this a steel cylinder with a diameter of 50 mm was filled with Poraver ® particles and compressed with a steady velocity of 1 mm/s. To allow for an optimal simulation setup, the number of particles used in the experiment and their weight were determined. The simulation was then set up with the same number of 1394 agglomerates distributed over all three diameter fractions, resulting in a weight of 7.1 g. The

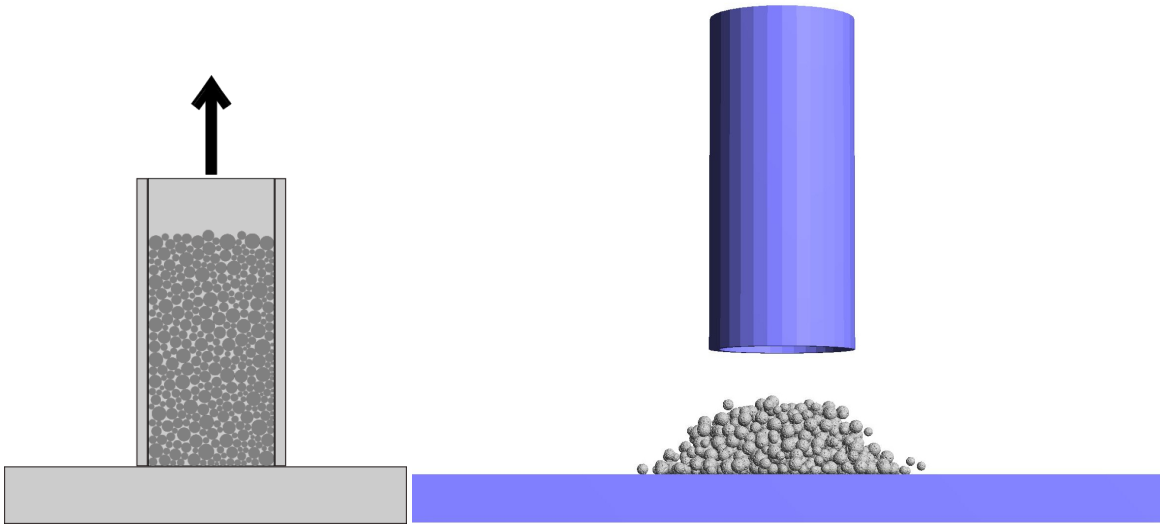

(a) Test setup (b) Bulk test simulation result for a rolling friction coefficient of 0.16

Figure 8: Bulk test

agglomerates were introduced in the cylinder and slowly settled, taking gravity into account, resulting in a loose package that represents the experimental conditions. After the experimental initial conditions have been reproduced, the actual crushing of the particles follows. This last step was performed twice with the two bond models introduced, resulting in the stress-strain curves illustrated in Figure 9b. A major influence of the bond model on the simulation results can be seen right at the beginning of the simulation. Model 2 leads to a stiffer behavior of the agglomerates for the first $10\,\%$ of strain and is overtaken by the results of Model 1, which shows an increasing stiffness as the strain progresses. Thus, Model 2 leads to a better, but not yet fully satisfactory, description of the crushing behavior of a number of interacting particles. This stress development computed with Model 1 is consistent with the results from the uniaxial pressure test, where the stress-strain curve is much steeper than the one obtained with Model 2. However, since the results from the uniaxial compression test are the foundation of the subsequent work, some effort will be put into finding more suitable simulation settings to ensure an even better result.

6 Conclusion and outlook

In this paper the influence of a newly developed bonded-particle model on the outcome of single- and multi-particle simulations with the brittle glass granule Poraver ® is presented. The use of a bonded-particle model in a DEM approach allows the simulation of crushing particles in a simple and stable way. The results of Section 4 show the significant influence of two bond models on the simulation of breaking agglomerates, leading to the conclusion that a model accounting for the microcracking of the particles is more suitable for simulating their fracture behavior. In addition, the influence of porosity, primary particle diameter and agglomerate shape

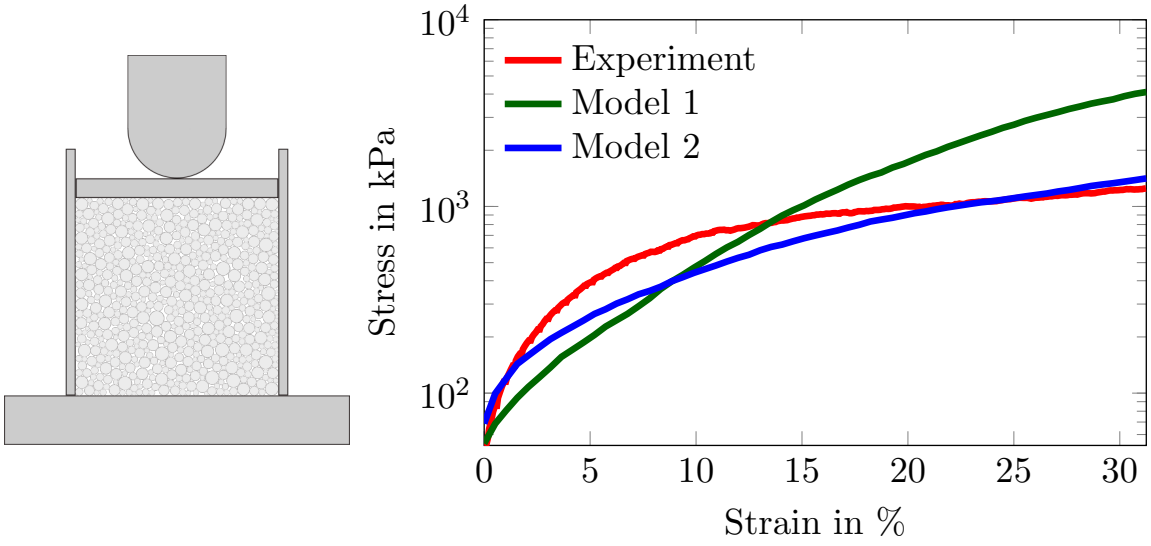

(a) Test setup

(b) Comparison between experimental and numerical results for both types of models

Figure 9: Simulation results for uniaxial compression of bulk material

is presented with the results, that a porosity of about $40\,\%$ to $50\,\%$ in combination with a slightly flattened agglomerate consisting of primary particles with a diameter of 0.3 mm or less gives the best geometric setup. For an agglomerate generated considering these findings, the influence of various material parameters is investigated. The result of this investigation shows that the Young's modulus of the bond and the primary particles have the most significant influence on the agglomerates breakage. An increase of the bonds Young's modulus leads to an increase of the agglomerates crushing strength and strain, while the initial stiffness is not affected. An increase of the primary particles Young's modulus, on the other hand, leads to an increase in the Young's modulus of the agglomerates and thus the initial stiffness and the crushing strength, while the crushing strain decreases. Taking these findings into account, an agglomerate is derived whose properties are very similar to the average experimental results. Following these single particle tests, multi particle simulations were performed, i.e., a bulk test and a uniaxial compression test. The bulk test, performed to better understand the frictional behavior of Poraver ® particles, results in a rolling friction of 0.16. As with the single particle test, simulation of a uniaxial compression test with 1394 particles using both bond models leads to the conclusion that Model 2 is much better at representing the fracture behavior of Poraver ®. The results of the uniaxial compression test are promising, but there is still room for improvement. For example, future work should investigate the interaction of the agglomerates in more detail to provide the best possible basis for DEM-FEM coupling approaches.

References

[1] International Maritime Organization. IMO. (2022) URL:https://www.imo.org/ (visited on 05/30/2022)

[2] S. Ehlers, K. Tabri, J. Romanoff and P. Varsta (2012): Numerical and experimental investigation on the collision resistance of the X-core structure *Ships and Offshore Structures* Volume 7, pp. 21-29

[3] J. Ringsberg and P. Hogström (2013): A methodology for comparison and assessment of three crashworthy side-shell structures: The X-core,Y-core and corrugation panel structures *Proceedings of The 6th International Conference on Collision and Grounding of Ships (ICCGS6)* Volume 6, pp. 323-330

[4] B. Werner, C. Daske, H. Heyer, M. Sander, M. Schöttelndreyer and W. Fricke (2014): The Influence of Weld Joints on the Failure Mechanism of Scaled Double Hull Structures under Collision Load in Finite Element Simulations *Procedia Materials Science* Volume 3, pp. 307-312

[5] Y. Yamada, H. Endo, and P. Pedersen (2008): Effect of Buffer Bow Structure In Ship-Ship Collision *International Journal of Offshore and Polar Engineering* Volume 18, pp. 133-141

[6] M. Schöttelndreyer (2015): Füllstoffe in der Konstruktion: Ein Konzept zur Verstärkung von Schiffsseitenhüllen *PhD thesis. Technische Universität Hamburg*

[7] C. Woitzik, M. Chaudry, P. Wriggers and A. Düster (2016): Experimental and numerical investigation of granular materials for an increase of the collision safety of double-hull vessels *PAMM* Volume 17, pp. 409-410

[8] C. Woitzik and A. Düster. (2017): Modelling the material parameter distribution of expanded granules *Granular Matter* Volume 19, pp. 52

[9] C. Woitzik, M. Chaudry, P. Wriggers and A. Düster (2018): Modelling and experimental testing of expanded granules as crash-absorber for double hull ships *PAMM* Volume 18, pp. 1-2

[10] C. Woitzik and A. Düster. (2020): Experimental investigation of granules as crash-absorber in ship building *Ships and offshore structures* Volume 16, pp. 314-325

[11] M. Chaudry, C. Woitzik, C. Weißenfels, A. Düster and P. Wriggers (2016): DEM-FEM coupled numerical investigation of granular materials to increase crashworthiness of double-hull vessels *PAMM* Volume 16, pp. 311-312

[12] M. Chaudry, C. Woitzik, A. Düster and P. Wriggers (2017): Experimental and numerical characterization of expanded glass granules *Computational Particle Mechanics* Volume 5, pp. 297-312

[13] M. Chaudry and P. Wriggers (2017): On the computational aspects of comminution in discrete element method *Computational Particle Mechanics* Volume 5, pp. 1-15

[14] D.O. Potyondy, and P.A. Cundall (2004): A bonded-particle model for rock *International Journal of Rock Mechanics and Mining Sciences* Volume 41, pp. 1329-1364

[15] Poraver® website. (2022) URL:https://poraver.com/en/poraver/ (visited on 05/30/2022)

[16] M. Dosta and V. Skorych (2020): MUSEN: An open-source framework for GPU-accelerated DEM simulations *SoftwareX* Volume 12:100618

[17] H.P. Zhu and Z.Y. Zhou and R.Y. Yang and A.B. Yu (2007): Discrete particle simulation of particulate systems: Theoretical developments *Chemical Engineering Science* Volume 62, pp. 3378-3396

[18] L. Verlet (1967): Computer "Experiments" on Classical Fluids. I. Thermodynamical Properties of Lennard-Jones Molecules *Phys. Rev.* Volume 159, pp. 98-103

[19] B. Quentrec and C. Brot (1973): New method for searching for neighbors in molecular dynamics computations *Journal of Computational Physics* Volume 13, pp. 430-432

[20] H. Deresiewicz and R.D. Mindlin (1952): Elastic Spheres in Contact Under Varying Oblique Forces *Columbia University. Department of Civil Engineering*

[21] P. Young (2013): The leapfrog method and other "symplectic" algorithms for integrating Newton's laws of motion *Physics* 115/242

[22] X. Chen, D. Peng, J. P. Morrissey and J. Ooi (2022): A comparative assessment and unification of bond models in DEM simulations *Granular Matter* Volume 24, Article number 29

[23] S.Kraus, C. Woitzik, M. Dosta and A. Düster (2021): Simulation of granular materials with the discrete element method to investigate their suitability as crash-absorber in ship collisions *PAMM* Volume 21, pp. 36-38

[24] S. Tasdemier (2021): Influence of various parameters on the breakage behavior of particles in DEM simulations

[25] P. Wriggers and B. Avci (2020): Discrete Element Methods: Basics and Applications in Engineering *Modeling in Engineering Using Innovative Numerical Methods for Solids and Fluids, Springer International Publishing* pp 1-30

[26] P. A. Cundall and O. D. L. Strack (1979): A discrete numerical model for granular assemblies *Géotechnique* Volume 29, pp 47-65

Authors

Sonja Rotter M.Sc.
Technische Universität Hamburg
Numerische Strukturanalyse mit Anwendungen in der Schiffstechnik
Institut für Konstruktion und Festigkeit von Schiffen
Am Schwarzenberg Campus 4 C
21073 Hamburg
Tel.: +49(0)40/42878-4764
Fax: +49(0)40/42878-6090
e-mail: sonja.rotter@tuhh.de
Web: www2.tuhh.de/skf

Dr.-Ing. Christian Woitzik
Technische Universität Hamburg
Institut für Konstruktion und Festigkeit von Schiffen
Am Schwarzenberg Campus 4 C
21073 Hamburg
Tel.: +49(0)40/42878-6103
Fax: +49(0)40/42878-6090
e-mail: christian.woitzik@tuhh.de
Web: www2.tuhh.de/skf

Süreyya Tasdemir
e-mail: suereyya.tasdemir@tuhh.de

Dr.-Ing. Maksym Dosta
*Institut für Feststoffverfahrenstechnik und Partikeltechnologie
e-mail: maksym.dosta@gmail.com

Prof. Dr.-Ing. habil. Alexander Düster
Technische Universität Hambur
Numerische Strukturanalyse mit Anwendungen in der Schiffstechnik
Institut für Konstruktion und Festigkeit von Schiffen
Am Schwarzenberg Campus 4 C
21073 Hamburg
Tel.: +49(0)40/42878-6083
Fax: +49(0)40/42878-6090
e-mail: alexander.duester@tuhh.de
Web: www2.tuhh.de/skf

Virtual elements and their use as deformable particles in DEM

Peter Wriggers, Alfredo Gay Neto, Blaz Hudobivnik, Tiago Fernandes Moherdaui

1 Introduction

The Discrete Element Method (DEM) is a computational strategy to address the mechanics of granular media, first published in (Cundall et al., 1979). The method has similarities with molecular dynamics. The modelling of a system of particles includes several challenges. Usually, the main one consists of handling the contact interactions between particles: (i) they tend to be numerous and require computational tools to be solved, and (ii) they usually involve complex interface rules (laws), such as the Hertzian contact, see (Johnson, 1987), when concerning spherical or super ellipsoid particles, see e.g.: (Luding, 2008), (Wellmann et al., 2012).

DEM numerical implementations include distinct shapes of particles, such as spheres, super ellipsoids, polyhedra, see e.g. (Nassauer et al., 2013), or NURBS-based shapes, see e.g. (Andrade et al., 2012). The shape of the particles is very important to capture phenomena such as particle interlocking, playing a crucial role in some applications of granular media. The present work proposes a novel methodology to consider particle flexibility in the DEM context. Each particle is represented as a general flexible polyhedron, using a continuum description. The Virtual Element Method (VEM) is applied to construct a particle with only a single-element which can assume a complex shape and is able to represent the overall particle flexibility. Each vertex has three displacement degrees of freedom. We discuss the effects of the so-called stabilization parameters of the VEM formulation, both in overall stiffness and natural frequencies of the particle, and their expected influences in practical DEM model solution. By the herein proposed approach, the flexibility of an assembly of polyhedra-based particles is well approximated. Contact between particles is modeled by the technique presented in (Gay Neto et al., 2022).

2 Continuum description of particles

In this section we define quantities and fields for a given particle. All concepts herein discussed are part of nonlinear continuum mechanics, for details see e.g. (Wriggers, 2006).

A particle is a continuum region in the 3D Euclidean space. We define a point in the initial (reference) configuration of the particle using the position vector $\boldsymbol{X}$ within the region $\mathcal{B}$. The

deformed configuration of the particle is represented the mapping between the position vectors in reference and deformed configuration $\boldsymbol{x} = \boldsymbol{\varphi}(\boldsymbol{X},t)$, where $\boldsymbol{\varphi}$ maps the position vectors.

The displacement field is defined by $\boldsymbol{u}(\boldsymbol{X},t)$, such that $\boldsymbol{x} = \boldsymbol{X} + \boldsymbol{u}$. The deformation process is described locally by the deformation gradient $\boldsymbol{F} = \frac{\partial \boldsymbol{x}}{\partial \boldsymbol{X}} = \nabla \boldsymbol{x}$ together with the Jacobian $J_F = \det \boldsymbol{F}$. The material time-derivatives of displacements are denoted by the velocity $\dot{\boldsymbol{u}}(\boldsymbol{X},t)$ and the acceleration $\ddot{\boldsymbol{u}}(\boldsymbol{X},t)$.

Loading of a particle only occurs through the body force $\bar{\boldsymbol{b}}$ defined on $\mathcal{B}$. Traction loads are not considered on $\partial\mathcal{B}_\mathrm{t}$. Contact between particles is addressed as a pointwise action, as will be described later. Since particles move freely in space, Dirichlet boundary conditions do not have to be specified.

The differential equations of motion for a given flexible particle $\mathcal{B}$ can be written in the weak form given by

$$\int_{\mathcal{B}} \boldsymbol{P} : \delta\boldsymbol{F} \,\mathrm{d}V - \int_{\mathcal{B}} \bar{\boldsymbol{b}} \cdot \delta\boldsymbol{u} \,\mathrm{d}V + \int_{\mathcal{B}} \rho_0 \ddot{\boldsymbol{u}} \cdot \delta\boldsymbol{u} \,\mathrm{d}V = 0 \,, \tag{1}$$

where $\boldsymbol{P}$ is the First Piola-Kirchhoff stress tensor, and $\delta\boldsymbol{F} = \nabla\delta\boldsymbol{u}$ is the gradient of the virtual displacement field $\delta\boldsymbol{u}$.

We assume that the constitutive behaviour of a particle is hyperelastic. Among many possible hyperelastic material models, we propose a Neo-Hookean form, see (Wriggers, 2006),

$$\psi_\mathrm{i}(\boldsymbol{F}) = \frac{\mu}{2}\left(J_F^{-\frac{2}{3}} \operatorname{tr}(\boldsymbol{F}^\mathrm{T}\boldsymbol{F}) - 3\right) + \frac{\kappa}{4}\left({J_F}^2 - 1 - 2\log(J_F)\right) \tag{2}$$

with the first Piola-Kirchhoff stress

$$\boldsymbol{P} = \frac{\partial \psi_\mathrm{i}}{\partial \boldsymbol{F}} \,. \tag{3}$$

3 Discretization

The numerical solution of the DEM-VEM system needs two ingredients: a temporal and a spatial discretization.

We adopt an implicit method as time-integration scheme. This has usually higher computational cost per time-step than an explicit method, but is unconditionally stable. Our choice is the Newmark Method, see e.g. (Wriggers, 2008), in which approximations for time-dependent quantities are dependent on the adopted time-step Δt and on the history data.

For the spatial discretization we employ the VEM, due to its generality when dealing with polyhedral elements of arbitrary-shape. This permits to use only one virtual element per particle. The virtual element method was first published in 2013 and its basic principles were presented in (Beirão da Veiga et al., 2013). A first formulation for nonlinear elastic and inelastic problems can be found in (Beirão da Veiga et al., 2015). For elastic problems, formulations regarding

compressible and incompressible cases for finite deformations were discussed in (Hudobivnik et al., 2019). Elastodynamics were explored in (Park et al., 2019) using explicit time integration, and with implicit time integration in (Cihan et al., 2021). One example of the state-of-the-art regarding mechanics applications is the use of mixed formulations to treat incompressible dynamic elastoplastic analysis in three dimensions in (Cihan et al., 2021).

Let $\mathbf{p}_E$ be the chosen degrees of freedom (DOF) for a single element E. The weak form for E is given by $\delta W_E(\mathbf{p}_E)$. The ansatz of the VEM for the displacement field is $\boldsymbol{u}_h$ which is unknown within the element, but known only at the edges. However, a projected displacement field $\boldsymbol{u}_\Pi$ can be constructed based on the ansatz function $\mathbf{N}_\Pi(\boldsymbol{X})$. Generally the E^{th} element contribution to the wek from $\delta W_E(\mathbf{p}_E)$ can be split into two parts

$$\delta W_E(\mathbf{p}_E) = \delta W_E^{\text{con}}(\boldsymbol{u}_\Pi) + \delta W_E^{\text{sta}}(\boldsymbol{u}_h - \boldsymbol{u}_\Pi). \tag{4}$$

The first is the so-called consistency part δW_E^{con}, a function only of $\boldsymbol{u}_\Pi$, which alone yields rank deficient stiffness and mass matrices. The second term is the stability part δW_E^{sta}, needed to restore the rank of the formulation

In the present work a linear ansatz is used for the discretization. This is a simple and convenient choice to approximate fields within polyhedra:

$$\boldsymbol{u}_\Pi = \mathbf{A}\,\mathbf{N}_\Pi \quad \text{with } \mathbf{N}_\Pi = (1,X,Y,Z)\,. \tag{5}$$

The matrix $\mathbf{A}$ contains a set with twelve unknown parameters and defines together with the monomials in matrix $\mathbf{N}_\Pi$ a complete polynomial. The goal now is to compute a map that links $\mathbf{A}$ to the nodal degrees of freedom $\mathbf{p}_E$ of the virtual element.

The computation of $\mathbf{A}$ is based on the requirement that the gradient of $(\boldsymbol{u}_h - \boldsymbol{u}_\Pi)$ is orthogonal to the gradient of $\boldsymbol{u}_p$, see e.g. (Beirão da Veiga et al., 2013). This yields

$$\int_\Omega \left[\, \nabla \boldsymbol{u}_p \cdot (\nabla \boldsymbol{u}_h - \nabla \boldsymbol{u}_\Pi)\right] \mathrm{d}\Omega = 0\,. \tag{6}$$

Since both $\nabla \boldsymbol{u}_p$ and $\nabla \boldsymbol{u}_\Pi$ are constant at the element level, (6b) can be simplified and yields with the divergence theorem

$$\nabla \boldsymbol{u}_\Pi |\Omega| = \int_{\partial\Omega} \boldsymbol{u}_h \otimes \boldsymbol{N}\, \mathrm{d}A\,, \tag{7}$$

where $\boldsymbol{N} = (N_X\ N_Y\ N_Z)$ is the outward unit normal to the element reference boundary surface. From this form all components of $\mathbf{A}$ can be computed in terms of the nodal unknown $\mathbf{p}_E$ that are linked to X,Y and Z. For the constant terms the condition

$$\sum_{i=1}^{n_v} \boldsymbol{u}_\Pi(\boldsymbol{X}_i) = \sum_{i=1}^{n_v} \boldsymbol{u}_h(\boldsymbol{X}_i) \tag{8}$$

is explored, where n_v is the number of vertices of the element and $\boldsymbol{u}_h(\boldsymbol{X}_i)$ is a vector of nodal displacements at node i: $\boldsymbol{u}_h(\boldsymbol{X}_i) = (\mathbf{p}_E)_{i\in(3\,i-2,\,3\,i-1,\,3\,i)}$. With this, the matrix $\mathbf{A}$ in (5) is

determined as a function of the vertex displacements $\mathbf{p}_E$, . Hence the displacement $\boldsymbol{u}_\Pi$ is now a function of the vertex displacements: $\boldsymbol{u}_\Pi = \mathbf{A}(\mathbf{p}_E)\mathbf{N}_\Pi$. By inserting this result into the stress divergence term of the weak form, the consistency part (3) of the virtual element can be computed.

3.1 Stabilization

Since the consistency part $W_E^{\mathrm{con}}(\boldsymbol{u}_\Pi)$ alone yields rank deficient stiffness and mass matrices, a stabilization needs to be introduced. This can be done in the form of an additional energy, as proposed in (Wriggers et al., 2017), based on the work in finite element methods by (Krysl, 2015) as follows

$$\delta W_E^{\mathrm{sta}} = \delta\widehat{W}_E(\boldsymbol{u}_h) - \delta\widehat{W}_E(\boldsymbol{u}_\Pi)\,. \tag{9}$$

In this work, the sub-mesh stabilisation introduced in (Hudobivnik et al., 2019) for three-dimensional virtual elements is employed.

The tangent matrix and mass matrix is then given by

$$\mathbf{K}_{E\mathrm{i}} = \frac{\partial \delta W_{E\mathrm{i}}(\mathbf{p}_E)}{\partial \mathbf{p}_E} \quad \text{and} \quad \mathbf{M}_E = \frac{\partial \delta W_{E\mathrm{d}}(\mathbf{p}_E)}{\partial \mathbf{p}_E}. \tag{10}$$

In summary, the full element residual $\mathbf{R}_E$ and its consistent linearization $\mathbf{K}_E$ are given by

$$\begin{aligned} \mathbf{R}_E &= \mathbf{R}_{E\mathrm{i}} - \mathbf{R}_{E\mathrm{e}} + \mathbf{R}_{E\mathrm{d}} \\ \mathbf{K}_E &= \mathbf{K}_{E\mathrm{i}} + \alpha_1 \mathbf{M}_E. \end{aligned} \tag{11}$$

The beauty of VEM is that arbitrary shaped polyhedral particles can be approximated by only one element. A single-element-per-particle approach can represent the particle flexibility well for a complex particle-geometry, while retaining low computational cost required for a simulation with a large number of particles.

4 Contact model

Contact contributions between the particles have to be introduced. Here we follow the ideas and the formulation proposed in (Gay Neto et al., 2022) for rigid particles. Adaptations have been introduced to handle flexible virtual elements by using the barrier method. The reader can refer to (Gay Neto et al., 2022) for further details and implementation strategies.

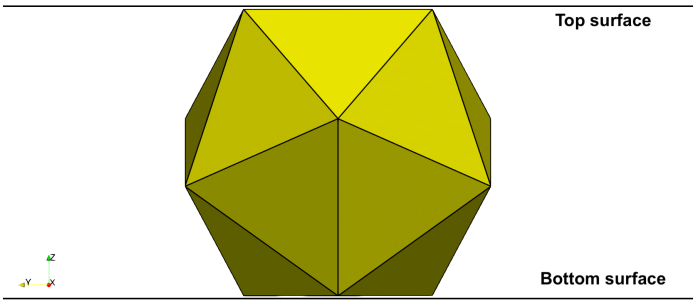

Figure 1: Proposed scenario for studying the sqeezing of a single particle

5 Global time stepping scheme

For the solution of a system of particles in the time-domain we have to start with initial conditions for all particles, which comprises positions of all vertices and their initial velocities. This is referred to as the reference configuration of the system, associated with a zero strain within all particles. Note that in a barrier contact strategy penetration between particles is not permitted in the initial configuration. The simulation in the time domain relies on a step-wise solution for given time-step Δt.

The choice of the nodal unknowns $\mathbf{p}_E$ that relate to the solution can be the total displacement $\mathbf{p}_E^{t+1}$ following a total Lagrangian description. Alternatively, incremental displacements $\Delta\mathbf{p}_E^{t+1}$ can be used as nodal unknowns, composing the total displacement in $\mathbf{p}_E^{t+1} = \mathbf{p}_E^t + \Delta\mathbf{p}_E^{t+1}$. Due to the use of the software structure of the platform Giraffe (Gay Neto, 2020) the updated Lagrangian description is employed.

6 Numerical examples

Two examples are considered in order to demonstrate the performance of the proposed method. The numerical simulations are performed with Giraffe (Gay Neto, 2020).The residual and tangent contributions stemming from VEM as well as the contact models were generated using the AceGen tool (Korelc et al., 2016).

6.1 Compression of a single particle

The behaviour of the new flexible particles is investigated in by means of this example, particularly with respect to: (i) influence of the stiffness stabilization and (ii) comparison with a refined-mesh solution to judge the flexibility of a single virtual element used as a particle. A flexible particle is positioned between two rigid flat surfaces, named "top" and "bottom", as depicted in Fig. 1.

The bottom surface is fixed, while the top surface is moved downwards with a prescribed displacement. Contact between the particle and both surfaces is considered during the deformation. To verify the results of the single virtual element particle, they were compared with a reference model employing the commercial FEM software Abaqus. The same physical scenario was considered, but a well-refined mesh with 4000 quadratic elements was employed for each particle using the hyperelastic material model described in (2).

Figures 2 shows a force versus strain plot. Here all values β_{i} of the stabilization have the same tendency, but smaller β_{i} lead to smaller stiffness. The reference solution results in an even less stiff behaviour. The particle is not so flexible due to the few degrees of freedome.Nevertheless the single particle models provides the expected mechanical behavior, even with the limitations and characteristics of coarse surface meshes.

6.2 Particle pack under compression

This example investigates the behaviour of a pack of particles in a box under compression. To establish the particle shapes, a uniform Voronoi-type mesh was generated, in which every element has a unique shape with varying number of nodes and faces. Each element was then, transformed into a particle shape. The mesh was generated with Neper. An initial packing of 515 particles was established by a simulation of the free-fall of the particle set into a box. The box has a square bottom with side length of 8 mm, located at height $z = 0$. For the process of filling the particles were assumed to be rigid bodies, using the formulation from (Gay Neto et al., 2022). In a next step particle flexibility was introduced by releasing the particles to initiate re-positioning and re-orientation, due to flexibility effects and the actual interface law described next.

Next, the pack is compressed by a "lid" surface above the pack. The lid is prescribed as a series of vertical displacements, such that a desirable strain level sequence can be produced as in a displacement-controlled experiment.

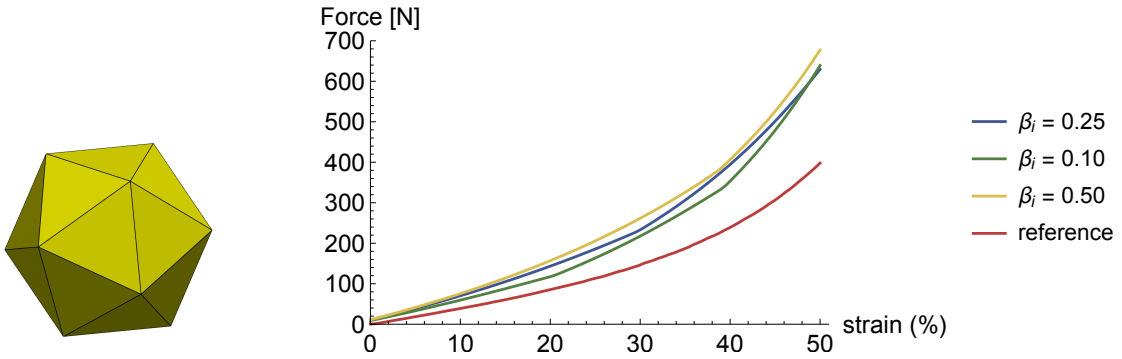

Figure 2: Icosahedron with edge length 0.02 m. Contact activation threshold $\bar{g}_n = 3.023\text{E-}4$ m. Results considering distinct values for β_{i} and a reference refined FEM result

The vertical motion of the lid, in z direction positionis ranges from $z = 7$ mm to $z = 4.9$ mm within the loading and unloading in the time span of 0.8 s . As the initial pack peak is located at approximately $z = 6$ mm, one expects a maximum compressive strain of ϵ_c =18.33%, when the lid achieves the maximum compression. During the prescribed displacement time-series of the lid motion the vertical reaction force is evaluated. Fig. 5 depicts a plot of this reaction force versus thecompressive strain in the pack. The Newmark coefficients adopted in this simulation are $\beta = 0.3$ and $\gamma = 0.6$, which induce numerical damping while the particles touch each other and the boundary surfaces. The time-step is adaptively changed during the model evolution and needs very small values during reordering phases of the particles.

The simulation is split into four time-periods. The resulting force versus strain plot is depicted in Fig. 5:

- Loading 1: from time 0.0 s - 0.2 s. The first compression of the pack of particles is characterized by many geometrical re-arrangements of particles, as the lid pushes the pack downwards.

- Unloading 1: from time 0.2 s - 0.4 s. After achieving a maximum compressive strain of ϵ_c =18.33%, the pack is released and recovers only a small part (elastic) of the initial prescribed strain. The permanent (inelastic) strain stems from the rearrangements in grains geometry and friction forces, during the first compression. The unloading 1 is characterized by a smooth force versus strain behavior.

- Loading 2: from time 0.4 s - 0.6 s. The second compression of the pack of particles is not characterized by many re-arrangements of particles, instead, follows a smoother force versus strain behavior, close to the previous unloading stage. However, it does not achieve

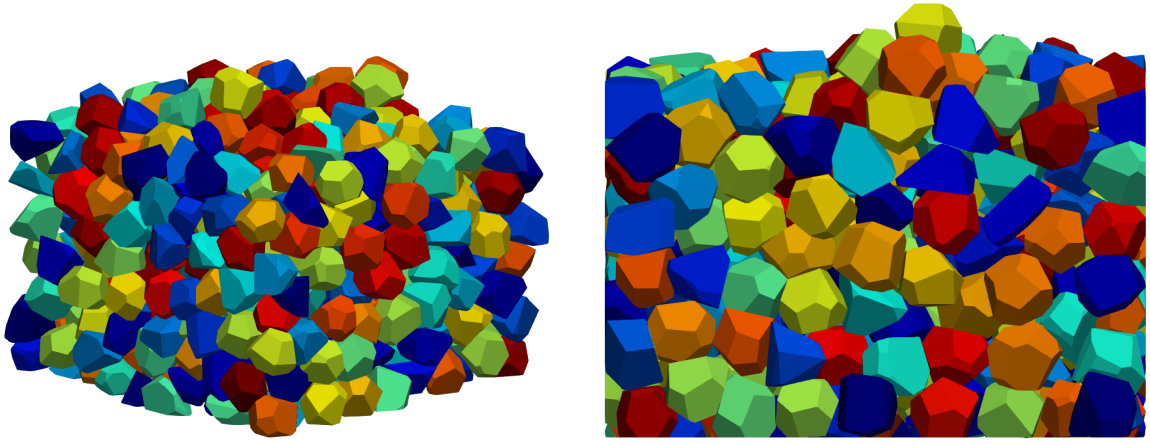

(a) (b)

Figure 3: Pack configuration after the box filling and initial accommodation of particles (a) isometric view (b) lateral view

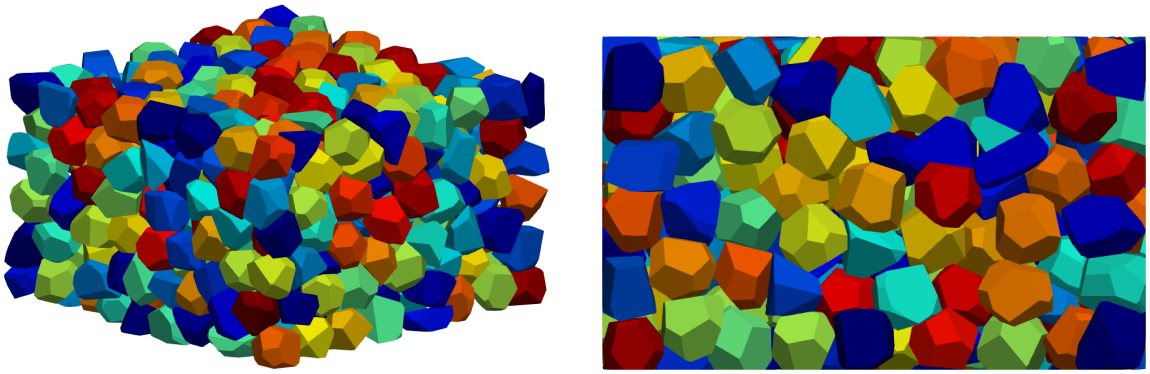

(a) (b)

Figure 4: Pack configuration when deformed at the level of 18.33% of compressive strain (a) isometric view (b) lateral view

the same force level as in the previous compression stage, due to the inelastic, frictional state related to the loading 1 and unloading 1 phases.

- Unloading 2: from time 0.6 s - 0.8 s. After achieving again a maximum compressive strain of ϵ_c =18.33%, the pack is released and follows a path very close to the loading 2 path in the Fig. 5 which means that no further internal frictional sliding between the particles occurs.

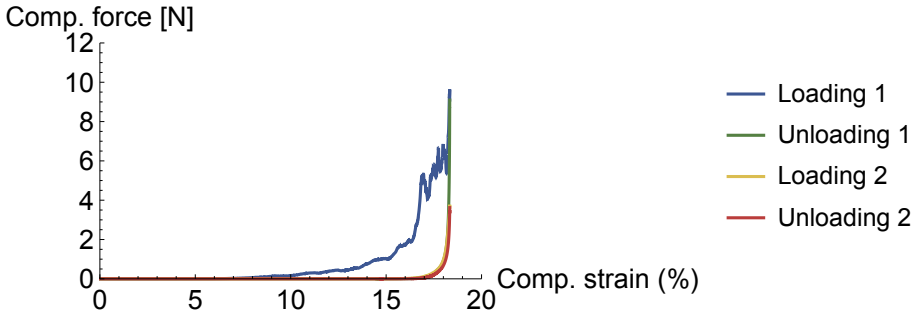

Figure 5: Force vs. strain plot for the various stages of the simulation of example 6.2

This example demonstrates that the proposed model is capable of recovering the expected physical behavior for a compressive test of a pack of particles, including important and complex effects such as the geometrical accommodation of particles, the elasticity effects of the particles and the contact interaction forces in normal and tangential direction.

References

[1] Jose E. Andrade et al." Granular element method for computational particle mechanics." In: Computer Methods in Applied Mechanics and Engineering 241 - 244 (2012), pp. 262?274. issn: 00457825. doi: 10.1016/j.cma.2012.06.012.

[2] L. Beirao da Veiga, F. Brezzi, and L. D. Marini. "Virtual Elements for Linear Elasticity Problems". In: SIAM Journal on Numerical Analysis 51.2 (2013), pp. 794 - 812. issn: 0036-1429. doi: 10.1137/ 120874746. url: http://epubs.siam.org/doi/10.1137/120874746.

[3] L. Beirao da Veiga, C. Lovadina, and D. Mora. "A Virtual Element Method for elastic and inelastic problems on polytope meshes". In: Computer Methods in Applied Mechanics and Engineering 295 (2015), pp. 327 - 346. issn: 00457825. doi: 10.1016/j.cma.2015.07.013. arXiv: arXiv:1503.02042v1.

[4] L. Beirao da Veiga et al. "Basic Principles of Virtual Element Methods". In: Mathematical Models and Methods in Applied Sciences 23.01 (2013), pp. 199 - 214. issn: 0218-2025. doi: 10 . 1142 / S0218202512500492. url: http://www.worldscientific.com/doi/abs/10.1142/S0218202512500492.

[5] Mertcan Cihan et al. "3D Mixed Virtual Element Formulation for Dynamic Elasto-Plastic Analysis". In: Computational Mechanics (2021), pp. 1-32. issn: 1432-0924. doi: 10.1007/s00466-021-02010-8. url: https://doi.org/10.1007/s00466-021-02010-8.

[6] P.A. Cundall and O.D.L. Strack. "A discrete numerical model for granular assemblies". In: Geotechnique 29.1 (1979), pp. 47 - 65.

[7] A. Gay Neto. Generic Interface Readily Accessible for Finite Elements (GIRAFFE). User?s Manual. Available at: sites.poli.usp.br/p/alfredo.gay/giraffe.html, 2020.

[8] A. Gay Neto and P. Wriggers. "Discrete Element Model for General Polyhedra". In: Computational Particle Mechanics 9 (2022), pp. 355 - 380. doi: 10.1007/s40571-021-00415.

[9] Blaz Hudobivnik, Fadi Aldakheel, and Peter Wriggers. "A low order 3D virtual element formulation for finite elasto?plastic deformations". In: Computational Mechanics 63.2 (2019), pp. 253-269. issn: 01787675. doi: 10.1007/s00466-018-1593-6. url: https://doi.org/10.1007/s00466-018-1593- 6.

[10] K.L. Johnson. Johnson. Cambridge University Press, 1987.

[11] J. Korelc and P. Wriggers. Automation of Finite Element Methods. Springer International Publishing Switzerland, 2016. isbn: 9783319390031.

[12] P. Krysl. "Mean-strain eight-node hexahedron with optimized energy-sampling stabilization for largestrain deformation". In: International Journal for Numerical Methods in Engineering 103 (2015), pp. 650-670. doi: 10.1002/nme.4907Mean-strain.

[13] Stefan Luding. "Introduction to discrete element methods: Basic of contact force models and how to perform the micro-macro transition to continuum theory". In: European Journal of Environmental and Civil Engineering 12.7-8 (2008), pp. 785?826. issn: 19648189. doi: 10.1080/19648189.2008.9693050.

[14] Benjamin Nassauer, Thomas Liedke, and Meinhard Kuna. "Polyhedral particles for the discrete element method: Geometry representation, contact detection and particle generation". In: Granular Matter 15.1 (2013), pp. 85-93. issn: 14345021. doi: 10.1007/s10035-012-0381-9.

[15] Kyoungsoo Park, Heng Chi, and Glaucio H. Paulino. "On nonconvex meshes for elastodynamics using virtual element methods with explicit time integration". In: Computer Methods in Applied Mechanics and Engineering 356 (2019), pp. 669-684. issn: 00457825. doi: 10.1016/j.cma.2019.06.031. url: https://doi.org/10.1016/j.cma.2019.06.031.

[16] Christian Wellmann and Peter Wriggers. "A two-scale model of granular materials". In: Computer Methods in Applied Mechanics and Engineering 205-208.1 (2012), pp. 46?58. issn: 00457825. doi: 10.1016/j.cma.2010.12.023. url: http://dx.doi.org/10.1016/j.cma.2010.12.023.

[17] P.Wriggers. Computational contact mechanics. Springer-Verlag Berlin Heidelberg, 2006. isbn: 9783540326083.

[18] P. Wriggers. Nonlinear finite element methods. Springer-Verlag Berlin Heidelberg, 2008. isbn: 978-3- 540-71000-4.

[19] P. Wriggers et al. "Efficient virtual element formulations for compressible and incompressible finite deformations". In: Computational Mechanics 60.2 (2017), pp. 253-268. issn: 01787675. doi: 10.1007/ s00466-017-1405-4.

Authors

Prof. em. Dr.-Ing. habil. Dr. h.c. mult. Dr.-Ing. E.h. Peter Wriggers
Leibniz Universität Hannover
Institute for Continuum Mechanics
An der Universität 1
30823 Garbsen
Tel.: +49 511 762 2220
e-mail: wriggers@ikm.uni-hannover.de
Web: https://www.ikm.uni-hannover.de

Prof. Dr. Eng. habil. Alfredo Gay Neto
University of São Paulo
Department of Structural Engineering and Geotechnical (PEF)
Jardim Universidade Pinheiros
São Paulo - SP, 05508-070, Brasilien
e-mail: alfredo.gay@usp.br
Tel.: +55 3091-5572 Web: http://sites.poli.usp.br/p/alfredo.gay/#me-section

Dr. Blaz Hudobivnik
Leibniz Universität Hannover
Institute for Continuum Mechanics
An der Universität 1
30823 Garbsen
Tel.: +49 511 762 17570
e-mail: hudobivnikikm.uni-hannover.de
Web: https://www.ikm.uni-hannover.de

Tiago Fernandes Moherdaui M.Sc.
University of São Paulo
Department of Structural Engineering and Geotechnical (PEF)
Jardim Universidade Pinheiros
São Paulo - SP, 05508-070, Brasilien
e-mail: tiago.moherdaui@usp.br
Web: https://sites.usp.br/pef/

Molecular Dynamic studies of liquid / solid interfaces in aqueous and ionic liquid systems

Johannes Gäding, Gabriele Tocci, Juan Sánchez, Patrick Huber, Robert Meißner

Abstract: In this project, the structural and dynamic properties of various liquid/solid interfaces are investigated using computer-aided molecular dynamics simulations. These methods will be used to investigate on the atomic / molecular scale how different substrates affect the resulting interactions with liquids. The substrates vary in their basic chemical composition as well as in their surface structure. Both aqueous systems and systems consisting of ionic liquids are being investigated. With regard to the aqueous systems, serious differences are observed in the structure of the water molecules in the first water contact layer, with partly significant effects on the dynamical water behaviour depending on the substrate. For ionic liquids, the so-called "quasi superionic state", which describes a cancellation of the coulombic order in nanometer pores, has been discovered. In addition, the effect of polarisable surfaces on the dynamic behaviour was investigated.

1 Introduction

In today's world there is an almost indefinite number of systems described as so-called particle-fluid systems. They occur in almost all areas, be it in water-saturated soils, in porous rock formations as well as in the oceans and e.g. in the capillaries of plants. Besides these natural systems, and to a large extent inspired by them, many technical processes also fall within the scope of particle-fluid interactions. Almost all industrial syntheses and transformation processes that take place in any step at the solid/liquid phase boundary or are influenced there, can belong to this category. The main technical applications are, for example, the solid/liquid catalysts of the chemical industry, as well as all energy storage systems that work with a (partly) liquid electrolyte. In addition, many energy conversion processes take place at a solid/liquid interface. Be it the conventional membrane technology for energy generation or decarbonization using the osmotic effect or the energy generation by means of diffusio-osomotic processes, which have gained in importance in recent years.

To a large extent, these processes are significantly influenced by the prevailing solid-liquid interactions and the interactions within the respective phase. For example, maximizing the accessible surface area of a catalyst or electrode can improve the efficiency of synthesis or the stored energy density by several orders of magnitude. This will lead to higher process yields in an economic sense and to lower energy consumption, which is favourable in a ecological sense.

In order to push technical progress in existing fields, as well as to establish new processes, whether by either driving efficiency improvements or by completely new developments based on discovered relationships, a precise understanding of these particle-fluid systems is essential. Due to their broad nature, a number of different length scales are crucial for these processes, starting from the macro scale of a few centimetres down to the atomic scale for adsorption of an atom on a catalyst particle. To cover these scales, a wide variety of methods are utilized to study these systems.

In the scope of project A6 of the PintPFS computer-aided molecular dynamic studies are used to investigate different systems of solid/liquid interfaces in order to archive fundamental insights into the structure as well as the dynamics of these particle-fluid interactions. The use of molecular dynamic studies allows the simulation and observation of solid/liquid interfaces in the nano- and subnanometer range. On this scale, the effects of small chemical changes – e.g. by altering functional groups, structural material properties on an atomic scale as well as molecular charge shifts and altered interactions at the surface – on the resulting interactions with the liquid can be investigated. To characterize the results, statistical methods are used to classify the structures on the molecular/atomic level and to study relationships between structural features and resulting dynamic behaviour.

1.1 Structure and dynamics of the water contact layer on metallic and two-dimensional materials

Systems involving a water-solid interface emerge as very general systems, which nevertheless have a wide relevance for natural as well as technical particle-fluid systems. Since the medium water occurs both in nature and in a multitude of technical processes – whether as a carrier medium, reaction medium or as a contaminant – there are always efforts to gain a deeper insight, despite many years of successful research (Björneholm et al., 2016; Farnesi Camellone, Negreiros Ribeiro, Szabová, Tateyama, & Fabris, 2016; Huang, Cheng, Binks, & Yang, 2015; Peng, Guo, Ma, & Jiang, 2022; Tocci, Bilichenko, Joly, & Iannuzzi, 2020; Zhang et al., 2019). On the one hand, this is due to the improvement of the simulation methods used and the computer infrastructure, and on the other hand, it is due to new discoveries in this field in general.

To study some of the most interesting and actual systems containing water/solid interfaces, four different materials are considered on the solid side. With Graphene and Molybdenium-disulphides (MoS_2), two representatives of the so-called two-dimensional materials, are examined; additionally, various gold and platinum surfaces, already widely used metallic components in various chemical and electrochemical processes, are considered.

Graphene in particular has been the subject of increased interest within the materials science community in recent years. In the beginning, it stood out due to its promising mechanical properties, including high tensile strength and elasticity, as a reinforcing material for composite materials. However, its electrical properties in particular, which make it an exceptionally good conductor material -- with high chemical stability at the same time -- have repeatedly pushed the material into the field of electrochemistry (Stoller, Park, Zhu, An, & Ruoff, 2008; Worsley et al., 2010). Due to its metallic behaviour, it can be used there as a conductor, electrode material or sensor (Soldano, Mahmood, & Dujardin, 2010). In addition, the generation of energy from

the mixing of salt and fresh water by means of a diffusion-osmotic process inside carbon nanomaterials is a promising new field of application (Liu, Chen, Xu, & Wang, 2018).

The increased interest in thin-layered Molybdenium-disulphide (MoS_2) also results from this field of energy generation. In initial theoretical investigations, MoS_2 single layer nanopores used as osmotic generators exhibit a power density of 10^6 watts per square meter produced from a salt gradient (Feng et al., 2016). Other promising applications together with Graphene are the desalination or purification of water flows using nanoporous structures. In addition, its chemical stability and high melting point make it a promising material for catalysts (Mao, Wang, Zheng, & Deng, 2018).

As already mentioned, both materials belong to the so-called two-dimensional materials. Two-dimensional materials consist of very thin layers. The layers have a thickness between one atom (Graphene) or one molecule (MoS_2). The structure thus only spans along the surface in two dimensions. In this case, both Graphene and Molybdeniuim-disulphide have a hexagonal arrangement, as shown in Figure 1. However, while Graphene has a completely planar structure consists of sp^2-hybridised carbon atoms, a MoS_2 single-layer structure has a stepped topology.

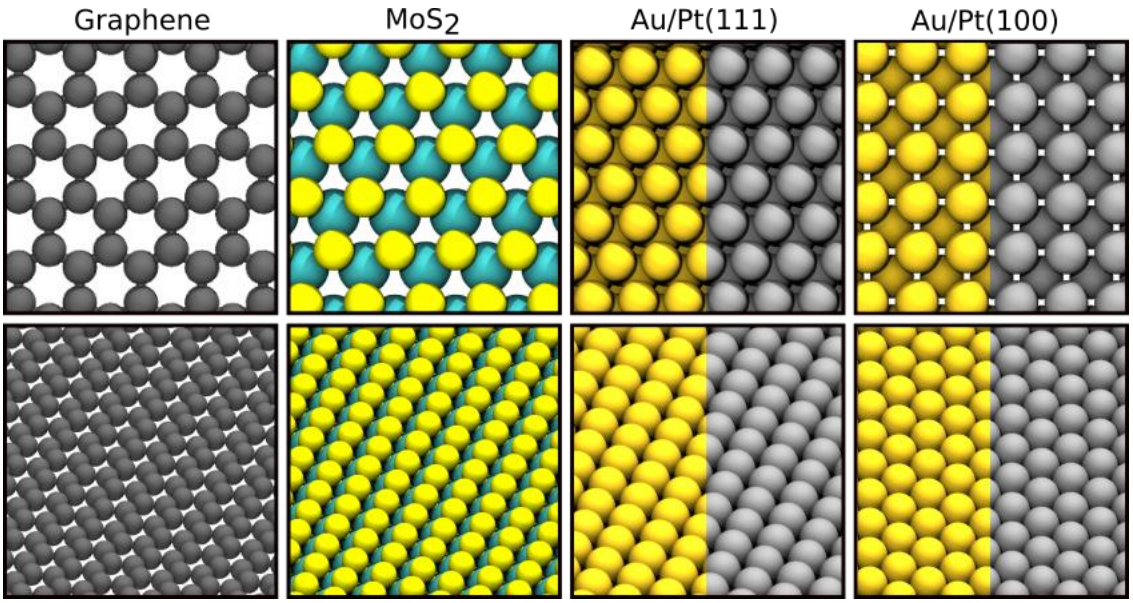

Figure 1: Snapshots of the investigated surface materials of Graphene, MoS_2, Gold/Platin (111) and Gold/Platin (100). First row: Top view on the surface structures. Second row: 45° angle view on the surface structures. Colors of the elements: C - grey; S - yellow, Mo - teal, Au - gold; Pt - silver.

In addition to the two-dimensional materials, four metallic surfaces consisting of Gold (Au) and Platinum (Pt) are also investigated. Both surface orientations under consideration [(111) and (100)] differ in their topology. These metals have been widely used in the chemical industry for some time, e.g. as catalyst surfaces, electrically conductive coating material or as complete electrode material (Boudart, Aldag, Benson, Dougharty, & Girvin Harkins, 1966; Farnesi Camellone et al., 2016; Marangon, Di Lecce, Brett, Shearing, & Hassoun, 2022; Villa et al., 2016). Since the surfaces result from different cuts along the crystal lattice, they have different

surface structures, as can be seen in Figure 1. While the Au/Pt(111) surfaces show a hexagonal arrangement, similar to that of Graphene and MoS_2, the Au/Pt(100) surfaces result in a rectangular arrangement of the surface atoms, as seen in Figure 1.
In order to provide the largest possible specific surface area for the processes, mainly porous structures of the materials are used in catalysis and as electrodes. Due to the high computational requirements for large systems, slit pore like geometries are often utilized in molecular dynamics simulations to model small pore systems in the porous solids.
Within these slit-like structures water forms a layered arrangement. Due to the increased interactions between the liquid (in this case water) and the solid material near the surface, the so-called water contact layer is formed. This water contact layer, or liquid contact layer, forms at almost every liquid / solid interface. The contact layer consists of a layer with increased density at a distance of approx. 0.3 nm from the solid surface.

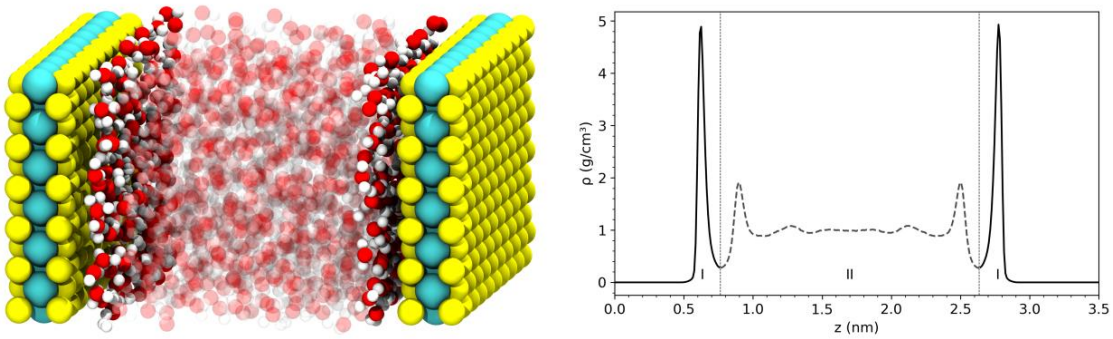

Figure 2: (left) Snapshot of a MoS_2 slit-pore confinement. (right) Water density profile in the respective MoS_2 slit-pore. Layer – I: Contact layer, Layer – II: Bulk-like layer

Colours: Sulphur - yellow; Molybdenum - teal; Oxygen - red; Hydrogen - white.

As can be seen from the density profile in Figure 2, the first compact water contact layer [cf. Layer – I Fig. 2 (left)] on a MoS_2 substrate has a density corresponding to four up to five times the usual water bulk density. In the direction of the bulk phase, the first contact layer is separated by a pronounced density minimum. The exact structure of the water contact layer depends strongly on the material of the underlying substrate. On the one hand, the absolute strength of the interactions is decisive for the extent to which the water attaches to the surface; on the other hand, the topology, i.e. the geometric surface composition, also influences the structure of the formed water contact layer.

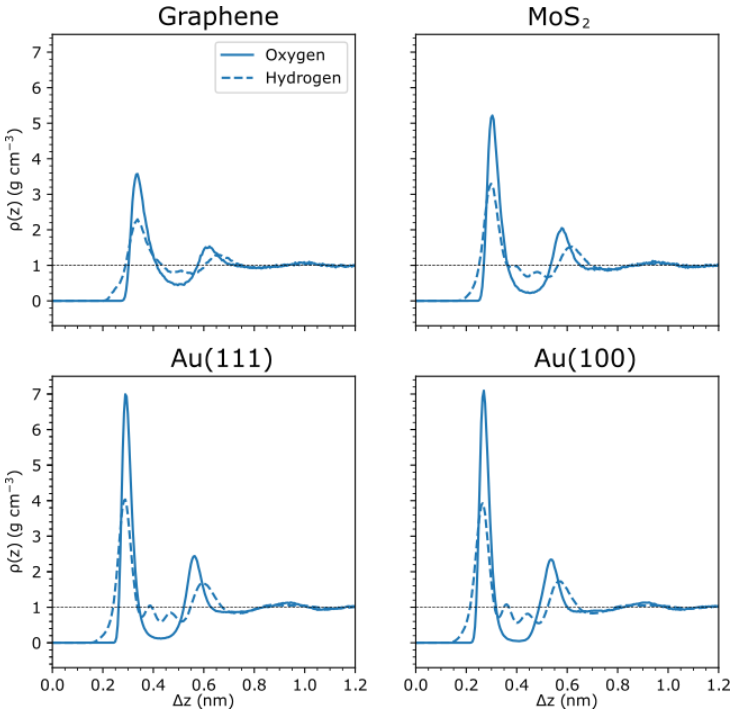

Figure 3: Water density profiles for the symmetric slit pore confinements from surface up to the middle of the pore.

Figure 3 shows the water density profiles on the individual substrate materials. It can be seen that the materials alone have a very different effect on the density within the first contact layer. In the case of Graphene, for example, the first contact layer only shows an increase in density to three to four times the bulk value, whereas on the gold surfaces, for example, it increases by more than seven times. The distinction between the contact layer and the subsequent diffuse or bulk layer also changes with the substrate material. In the case of a substrate made of Graphene the density decreases by only 20 % in the transition region. On a Gold substrate however, the Oxygen atoms are almost completely displaced in this region with just some occurring Oxygen bonded Hydrogen atoms.

In addition to the general formation of the dense contact layer near the surface, there are also different influences on the structure and arrangement of the water molecules within these contact layers by the substrate material.

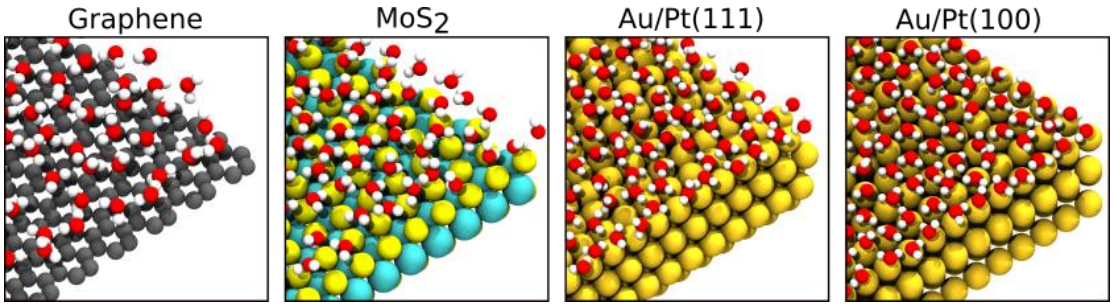

Figure 4: Snapshots of the water ordering in the first contact layer on a Graphene, MoS_2 Au(111) and Au(100) substrate.

Colours: Oxygen – red; Hydrogen – white, Carbon – grey, Sulphur – bright yellow, Molybdenum – teal, Gold – yellow.

Figure 4 shows a snapshot of the water molecules within the water contact layer on the respective surfaces. While the increase in density within the water contact layer from Graphene via MoS_2 to Gold can be seen by eye, influences on the exact structure or arrangement of the

water molecules are rather difficult to recognize. Only for the Au(100) surface a relatively pronounced pattern in the water arrangement can be recognized, in which the molecules are predominantly adsorbed to the surface in a rectangular arrangement. Within the rectangular arrangement the water molecules strive to align the hydrogen atoms mainly along the surface dimensions in an alternating pattern to allow for a hydrogen bridge network that is as inherently closed as possible.

Apart from the Au(100) surface, the other substrates also show influences on the structure within the water contact layer, but they differ greatly in their manifestations.
In order to further investigate the influences and the resulting structure on all surfaces, they are measured and analysed in the current project using correlation functions. Subsequently, links between these static properties and the dynamic behaviour will be investigated. The results are used to determine the extent, to which the particular structures of the water contact layer and various material behaviour such as wettability, adsorption strength and dynamic transport properties e.g. the friction coefficient and the general water diffusion within the contact layer are influenced by each other. As this project is currently the subject of ongoing research and is about to be published as a preprint, these insights are to be regarded as a preview.

1.2 Ionic Liquids in confined Graphene structures, influence of geometric confinement and polarization

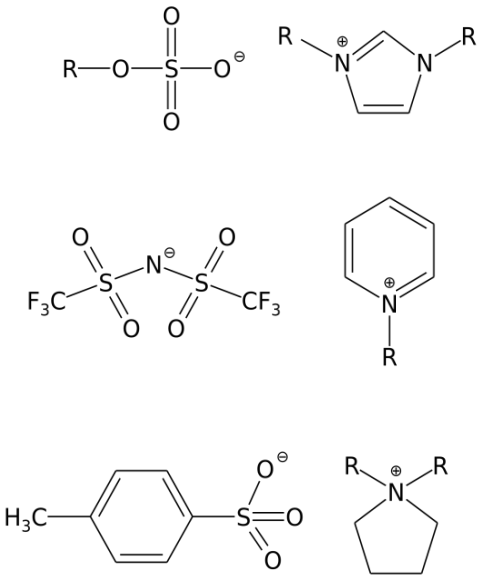

Figure 5: Selection of some of the most common cation and anion pairs of Ionic Liquids.

In addition to the water-containing systems, the so-called Ionic Liquids currently represent a new class of promising materials. Ionic Liquids, also called “Room Temperature Ionic Liquids” (RTILs), describe salts whose melting temperature is less than 100 °C, often even below the general room temperature. Like ordinary salts, they are formed from pairs of anions and cations. The cations and anions in Ionic Liquids have sterically very demanding molecular structures, in combination with pronounced charge delocalization within the whole or large parts of the molecule (Rodríguez-Fernández, Varela, Schröder, & Lago, 2022; Shimizu, Bernardes, & Lopes, 2014). These two properties are the main reasons for the relatively low melting temperatures of Ionic Liquids, as even a small amount of thermal energy is sufficient to overcome the lattice energy. The physicochemical properties of Ionic Liquids can be influenced and adjusted over a wide range by various combinations and variations of the anion-cation pairs. Some of the most common used cation and anion pairs are shown in Figure 5.

Due to these possibilities to adjustment specific properties, Ionic Liquids are also called "designer solvents". Because of their low vapor pressure, Ionic Liquids are particularly suitable as non-volatile solvents in a variety of chemical processes, e.g. in catalysis, aerogel production or in the pharmaceutical industry (Aaltonen & Jauhiainen, 2009; Dai, Zhang, Huang, & Lei, 2017; Ding, Radosz, & Shen, 2005; H.-P. Zhu, Yang, Tang, & He, 2003; S. Zhu et al., 2006). They are also a promising electrolyte in battery systems and so-called supercapacitors (Balducci, Bardi, Caporali, Mastragostino, & Soavi, 2004; Brandt, Pohlmann, Varzi, Balducci, & Passerini, 2013; Frackowiak, Lota, & Pernak, 2005; Lewandowski, Olejniczak, Galinski, & Stepniak, 2010).

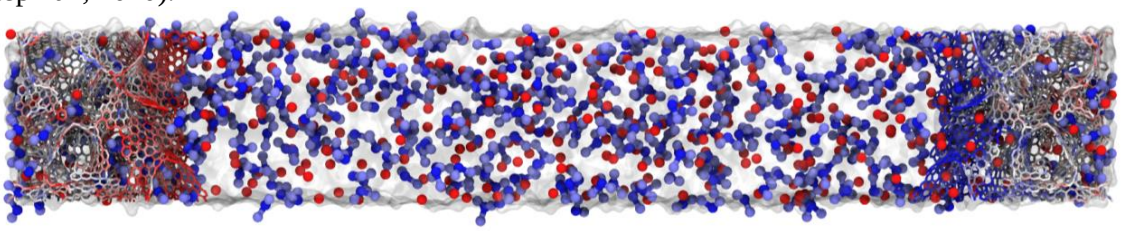

Figure 6: Schematic representation of a supercapacitor with an Ionic Liquid infused carbonous electrodes. Colours materials: Carbon - grey; Cations - blue; Anions – red. Colours charges: positive charge – red, negative charge – blue.

Due to their thermal and chemical stability, they can cover larger potential ranges than ordinary electrolytes and prevent flammability of energy storage systems. Both in catalysis and in battery systems, but especially in supercapacitors, the Ionic Liquids come into contact with highly porous carbon structures, which are a widely used electrode material. The ionic liquid diffuses into the small pore spaces of the porous electrode structure (*cf.* Figure 6) to accumulate on the surface depending on the charged state.

The pore sizes are often in the nano- to subnanometer range and thus correspond to the same order of magnitude as the size of the ionic liquid molecules.

In order to optimize the porous structure on the solid side, e.g. by adapting the pore diameter to the respective ionic liquid, or to make general statements about the use of different Ionic Liquids depending on the application, precise modelling of the materials used in these systems is essential.

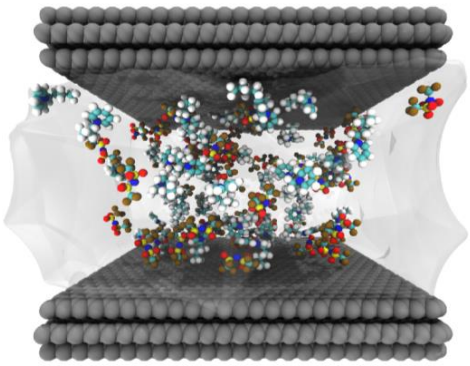

Figure 7: Snapshot of a carbon slit pore confinement infused by an Ionic Liquid.

Due to the complex structure and the relatively variable charge distribution within the molecules of Ionic Liquids, the explicit integration of atomic polarization is considered to play a significant role in the accurate description by developed force fields (Bedrov et al., 2019).

Within the scope of this project, a fully polarisable force field for the explicit ionic liquid 1-butylpyridinium [BuPy] + [Tf_2N] was reparametrized according to experimental values to accurately describe the system in terms of dynamic properties such as self-diffusion as well as structural properties such as density (Busch et al., 2020). With the

reparametrized force field, different slit pore systems are studied in order to investigate the general influence of the confinement on the dynamic behaviour of the Ionic Liquid and to show to what extent a polarisable description of the surfaces is necessary for an accurate modelling. Figure 7 shows a snapshot of one of the used slit pore models.

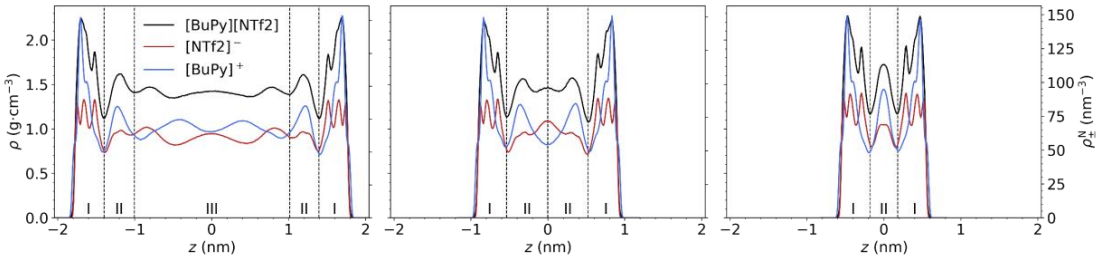

Figure 8: Density profiles of the Ionic liquid in three different slit pore confinements with a diameter of 4.09 nm, 2.36 nm and 1.65 nm. The overall liquid density is shown in black, cation and anion number densities are shown in blue and red, respectively.

The density profiles in Figure 8 show very clearly the layered arrangement of the liquid within the pore already described in subproject I. The contact layer (Layer – I) has a slightly increased density, followed by a diffuse layer (Layer – II) until the bulk density is reached in the bulk-like layer (Layer – III).

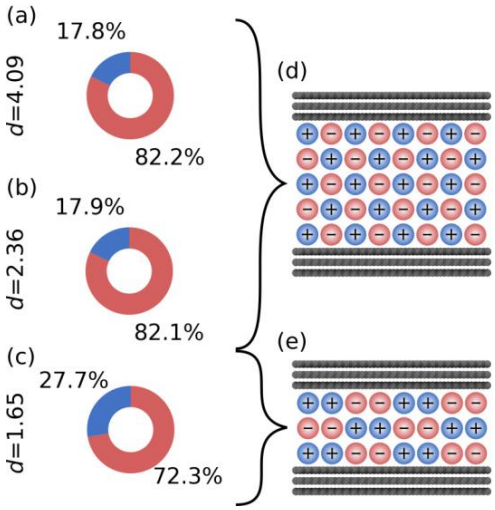

Figure 9: (a-c) Ratio of the cation (blue) and anion (red) coordination number in the diffuse layer (Layer – II) in all three confinements. (d) Schematic representation of the coulombic ordering and of the (e) "quasi superionic state".

Since Ionic Liquids are molten salts, the individual molecules are present with certain partial charges. Due to these charges and the distinct molecular sizes, an alternating arrangement of anions and cations takes place within the pore. As in this case, this already happens for neutrally charged cells, i.e. surfaces that are neutral charged in themselves. With increasing restriction due to a decreasing pore diameter, this arrangement now changes to the effect that initially the bulk-like area disappears and the first contact layers are only separated from each other by two diffuse layers that merge into each other. With a further decreasing confinement diameter, the diffuse layers start to overlap resulting in the formation of a merged layer. From the density profile of the smallest confinement in Figure 8 it can be seen that there is no stoichiometric number of cations and anions in this newly formed layer [*cf.* Layer – 2 in Fig. 8 (left)]. To further illuminate the effect of this rearrangement for an ion, the closest neighbourhood was analysed. Thus, Figure 9 shows the ratio of neighbouring cations and anions the first hydrate shell of a cation in the diffuse layers (Layer – II) for each confinement. In the general case, i.e. in pores as well as in the bulk phase, the arrangement of the ions follows the so-called Coulombic order. The coulombic order is based on the charge. Thus, the first hydrate shell consists mainly of counterions to balance the charge of the respective ion [*cf.* Figure 9 (d)]. A

dissolution of the Coulombic order was already observed by S. Kondrat with the "superionic state" (Groda, Dudka, Kornyshev, Oshanin, & Kondrat, 2021; Kondrat, Georgi, Fedorov, & Kornyshev, 2011). However, the "superionic state" described by S. Kondrat was only observed for pore diameters in the sub-nanometer range and mainly takes place by screening mirror charges in the surface. In the current study a "quasi superionic state" was observed for pore diameters around 1.65 nm, in which the Coulombic order is influenced in such a way, that the number of neighbouring ions of the same type increases [17.8 % - 27.7 %, see Figure 9 (a - c)]. Since this condition could be observed using both polarisable surfaces and non-polarisable surfaces, it is, in contrast to the previously observed "superionic state", a pure effect of geometric confinement and is not caused by induced mirror charges (Futamura et al., 2017; Gäding, Tocci, Busch, Huber, & Meißner, 2022).

In contrast to the structural properties, which are not greatly influenced by a possible surface polarization at these pore diameters, there are partly significant influences with regard to the dynamic behaviour of the confined ionic liquid.

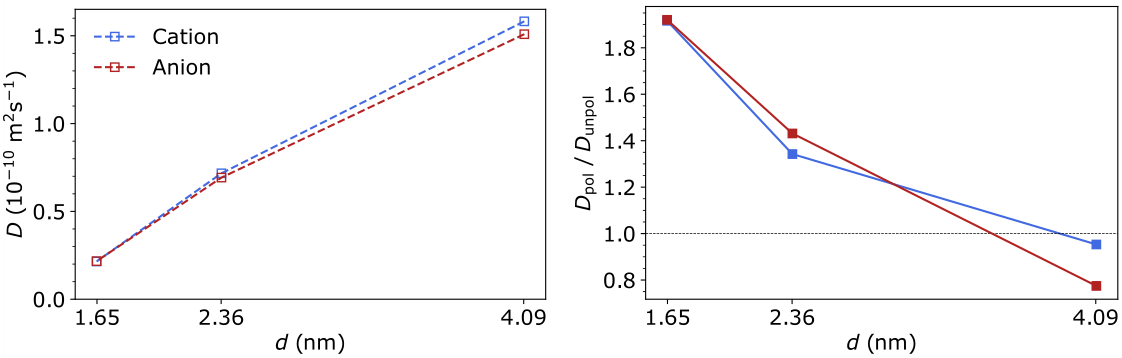

Figure 10: Diffusion coefficient of the cation (blue) and anion (red) confined in different slit pore structures with diameter d. (Right) Increase of the diffusion coefficient between polarisable and non-polarisable surfaces.

In general, the diffusion rate decreases significantly with decreasing pore diameter due to the increasing restriction of the ionic mobility by the pore walls. The diffusion of cations and anions decreases by more than 90 % when the pore diameter decreases from 4.09 nm to 1.65 nm [cf. Figure 10 (left)]. This can be mainly attributed to the increasing steric hindrance of the ions by the surfaces and by the condensed ions. Additionally, the proportion of ions interacting with the surface increases steadily with decreasing pore diameter. As a result, more ions experience the increased interaction with the surface and, consequently, they are also more frequently encountered in the compacted contact layer, which has a lower diffusion due to the increased density. In the subsequent consideration of a surface polarization, the effect on the dynamic behaviour of the Ionic Liquids therefore increases with decreasing pore diameter. Figure 10 (right) shows the ratio of the diffusion coefficients within the pores with polarisable surfaces to those with non-polarisable surfaces. Here, the mobility of the ionic liquid almost doubles when the surface polarization is considered. Since, based on autocorrelation measurements, the friction coefficients between the Ionic Liquid and the surface do not decrease significantly when polarisable surfaces are considered, the increase in diffusion is due to a decrease in ion-ion interaction. Due to the induced dipoles in the surface, shown in Figure 11, the charges of the individual ions are more strongly screened, especially in the first contact layer, so that the

strength of the fixation by Coulombic interactions with the surrounding counter ions decreases – this results in a decrease in viscosity and increased mobility of the ions in the contact layer.

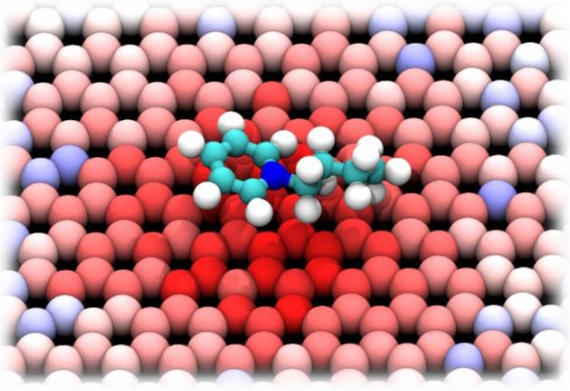

Figure 11: Schematic representation of the induced dipoles in the substrate by an [BuPy] cation. The colors in the substrate represent the charges felt by the molecule: red – positive, blue – negative.

In summary, in this project a fully polarisable all-atom force field for the Ionic Liquid [BuPy] + [Tf2N] has been reparameterised to agree very precisely with experimental results. Using the reparametrized force field, it was shown that especially for pore diameters from 1.65 nm an explicit integration of the polarisable description of the surfaces shows significant effects on the dynamic behaviour of the confined Ionic Liquid. In addition to the general effects of the geometric restriction, a previously unknown phenomenon was observed with the "quasi superionic state". Furthermore, the strength of the surface-induced dipoles was investigated in the published study, as well as their behaviour with changes in the pore diameter and their propagation within the surface structure.

References

[1] Aaltonen, O., & Jauhiainen, O. (2009). The preparation of lignocellulosic aerogels from ionic liquid solutions. *Carbohydrate Polymers*, *75*(1), 125–129.

[2] Balducci, A., Bardi, U., Caporali, S., Mastragostino, M., & Soavi, F. (2004). Ionic liquids for hybrid supercapacitors. *Electrochemistry Communications*, *6*(6), 566–570.

[3] Bedrov, D., Piquemal, J.-P., Borodin, O., MacKerell, A. D., Roux, B., & Schröder, C. (2019). Molecular Dynamics Simulations of Ionic Liquids and Electrolytes Using Polarizable Force Fields. *Chemical Reviews*, *119*(13), 7940–7995.

[4] Björneholm, O., Hansen, M. H., Hodgson, A., Liu, L.-M., Limmer, D. T., Michaelides, A., Pedevilla, P., et al. (2016). Water at Interfaces. *Chemical Reviews*, *116*(13), 7698–7726.

[5] Boudart, M., Aldag, A., Benson, J. E., Dougharty, N. A., & Girvin Harkins, C. (1966). On the specific activity of platinum catalysts. *Journal of Catalysis*, *6*(1), 92–99.

[6] Brandt, A., Pohlmann, S., Varzi, A., Balducci, A., & Passerini, S. (2013). Ionic liquids in supercapacitors. *MRS Bulletin*, *38*(7), 554–559.

[7] Busch, M., Hofmann, T., Frick, B., Embs, J. P., Dyatkin, B., & Huber, P. (2020). Ionic liquid dynamics in nanoporous carbon: A pore-size- and temperature-dependent neutron

spectroscopy study on supercapacitor materials. *Physical Review Materials*, *4*(5), 055401.

[8] Dai, C., Zhang, J., Huang, C., & Lei, Z. (2017). Ionic Liquids in Selective Oxidation: Catalysts and Solvents. *Chemical Reviews*, *117*(10), 6929–6983.

[9] Ding, S., Radosz, M., & Shen, Y. (2005). Ionic Liquid Catalyst for Biphasic Atom Transfer Radical Polymerization of Methyl Methacrylate. *Macromolecules*, *38*(14), 5921–5928.

[10] Farnesi Camellone, M., Negreiros Ribeiro, F., Szabová, L., Tateyama, Y., & Fabris, S. (2016). Catalytic Proton Dynamics at the Water/Solid Interface of Ceria-Supported Pt Clusters. *Journal of the American Chemical Society*, *138*(36), 11560–11567.

[11] Feng, J., Graf, M., Liu, K., Ovchinnikov, D., Dumcenco, D., Heiranian, M., Nandigana, V., et al. (2016). Single-layer MoS2 nanopores as nanopower generators. *Nature*, *536*(7615), 197–200.

[12] Frackowiak, E., Lota, G., & Pernak, J. (2005). Room-temperature phosphonium ionic liquids for supercapacitor application. *Applied Physics Letters*, *86*(16), 164104.

[13] Futamura, R., Iiyama, T., Takasaki, Y., Gogotsi, Y., Biggs, M. J., Salanne, M., Ségalini, J., et al. (2017). Partial breaking of the Coulombic ordering of ionic liquids confined in carbon nanopores. *Nature Materials*, *16*(12), 1225–1232.

[41] Gäding, J., Tocci, G., Busch, M., Huber, P., & Meißner, R. H. (2022). Impact of confinement and polarizability on dynamics of ionic liquids. *The Journal of Chemical Physics*, *156*(6), 064703.

[15] Groda, Y., Dudka, M., Kornyshev, A. A., Oshanin, G., & Kondrat, S. (2021). Superionic Liquids in Conducting Nanoslits: Insights from Theory and Simulations. *The Journal of Physical Chemistry C*, *125*(9), 4968–4976.

[16] Huang, J., Cheng, F., Binks, B. P., & Yang, H. (2015). PH-Responsive Gas–Water–Solid Interface for Multiphase Catalysis. *Journal of the American Chemical Society*, *137*(47), 15015–15025.

[17] Kondrat, S., Georgi, N., Fedorov, M. V., & Kornyshev, A. A. (2011). A superionic state in nano-porous double-layer capacitors: Insights from Monte Carlo simulations. *Physical Chemistry Chemical Physics*, *13*(23), 11359.

[18] Lewandowski, A., Olejniczak, A., Galinski, M., & Stepniak, I. (2010). Performance of carbon–carbon supercapacitors based on organic, aqueous and ionic liquid electrolytes. *Journal of Power Sources*, *195*(17), 5814–5819.

[19] Liu, G., Chen, T., Xu, J., & Wang, K. (2018). Blue energy harvesting on nanostructured carbon materials. *Journal of Materials Chemistry A*, *6*(38), 18357–18377.

[20] Mao, J., Wang, Y., Zheng, Z., & Deng, D. (2018). The rise of two-dimensional MoS2 for catalysis. *Frontiers of Physics*, *13*(4), 138118.

[21] Marangon, V., Di Lecce, D., Brett, D. J. L., Shearing, P. R., & Hassoun, J. (2022). Characteristics of a gold-doped electrode for application in high-performance lithium-sulfur battery. *Journal of Energy Chemistry*, *64*, 116–128.

[22] Peng, J., Guo, J., Ma, R., & Jiang, Y. (2022). Water-solid interfaces probed by high-resolution atomic force microscopy. *Surface Science Reports*, *77*(1), 100549.

[23] Rodríguez-Fernández, C. D., Varela, L. M., Schröder, C., & Lago, E. L. (2022). Charge delocalization and hyperpolarizability in ionic liquids. *Journal of Molecular Liquids*, *349*, 118153.

[24] Shimizu, K., Bernardes, C. E. S., & Lopes, J. N. C. (2014). The complex structure of ionic liquids at an atomistic level: From "red-and-greens" to charge templates. *Pure and Applied Chemistry*, *86*(2), 119–133.

[25] Soldano, C., Mahmood, A., & Dujardin, E. (2010). Production, properties and potential of graphene. *Carbon*, *48*(8), 2127–2150.

[26] Stoller, M. D., Park, S., Zhu, Y., An, J., & Ruoff, R. S. (2008). Graphene-Based Ultracapacitors. *Nano Letters*, *8*(10), 3498–3502.

[27] Tocci, G., Bilichenko, M., Joly, L., & Iannuzzi, M. (2020). *Ab initio* nanofluidics: Disentangling the role of the energy landscape and of density correlations on liquid/solid friction. *Nanoscale*, *12*(20), 10994–11000.

[28] Villa, A., Dimitratos, N., Chan-Thaw, C. E., Hammond, C., Veith, G. M., Wang, D., Manzoli, M., et al. (2016). Characterisation of gold catalysts. *Chemical Society Reviews*, *45*(18), 4953–4994.

[29] Worsley, M. A., Pauzauskie, P. J., Olson, T. Y., Biener, J., Satcher, J. H., & Baumann, T. F. (2010). Synthesis of Graphene Aerogel with High Electrical Conductivity. *Journal of the American Chemical Society*, *132*(40), 14067–14069.

[30] Zhang, R., Pearce, P. E., Duan, Y., Dubouis, N., Marchandier, T., & Grimaud, A. (2019). Importance of Water Structure and Catalyst–Electrolyte Interface on the Design of Water Splitting Catalysts. *Chemistry of Materials*, *31*(20), 8248–8259.

[31] Zhu, H.-P., Yang, F., Tang, J., & He, M.-Y. (2003). Brønsted acidic ionic liquid 1-methylimidazolium tetrafluoroborate: A green catalyst and recyclable medium for esterification. *Green Chemistry*, *5*(1), 38.

[32] Zhu, S., Wu, Y., Chen, Q., Yu, Z., Wang, C., Jin, S., Ding, Y., et al. (2006). Dissolution of cellulose with ionic liquids and its application: A mini-review. *Green Chemistry*, *8*(4), 325.

Author

Johannes Gäding, M.Sc.
Technische Universität Hamburg
Institut für Kunststoffe und Verbundwerkstoffe (M-11)
Denickestr. 15
D-21073 Hamburg
Raum 1018, Gebäude Q
Tel: +49 40 42878 2572
E-mail: johannes.gaeding@tuhh.de
Home: http://www.tuhh.de/kvweb

Optimizing liquid-solid slip in nanofluidic systems

Laurent Joly

Abstract: Nanofluidic systems, e.g. natural nanoporous materials or engineered nanochannels made from new 2D materials, could provide alternative solutions to critical societal challenges such as water desalination or energy harvesting. At the nanoscale, surface effects become crucial; in particular, liquid-solid slip arising from low liquid-solid friction can boost the performance of nanofluidic systems. In that context, I will illustrate with some recent work how molecular dynamics simulations can help understand the molecular mechanisms of liquid-solid friction, and optimize liquid-solid slip. First, I will briefly discuss some recent progress regarding the molecular modeling of interfacial slip and friction (Oga et al, 2021), and show how ab initio molecular dynamics can provide a new insight into the structural and dynamical origin of liquid-solid friction (Tocci et al, 2020). Then, I will discuss a challenge related to nanofluidic systems for electricity production: optimal performance indeed requires charged and slipping surfaces, while these two properties are contradictory. Here we have shown that the charge-friction relationship strongly depends on how the surface charge is generated, and identified promising candidates for optimal charge-friction coupling (Xie et al, 2020). Finally, I will show that water slip can be boosted when the liquid is "supercooled", and investigate the origin of this unexpected effect (Herrero et al, 2020).

References

[1] C. Herrero, G. Tocci, S. Merabia, L. Joly: “Fast Increase of Nanofluidic Slip in Supercooled Water: the Key Role of Dynamics”, *Nanoscale* 12, 20396 (2020)

[2] H. Oga, T. Omori, C. Herrero, S. Merabia, L. Joly, Y. Yamaguchi: “Theoretical framework for the atomistic modeling of frequency-dependent liquid-solid friction”, *Phys. Rev. Research* 3, L032019 (2021)

[3] G. Tocci, M. Bilichenko, L. Joly, M. Iannuzzi: “Ab initio Nanofluidics: Disentangling the role of the energy landscape and of density correlations on liquid/solid friction”, *Nanoscale* 12, 10994 (2020)

[4] Y. Xie, L. Fu, T. Niehaus, L. Joly: “Liquid-solid slip on charged walls: the dramatic impact of charge distribution”, *Phys. Rev. Lett.* 125, 014501 (2020)

Author

Laurent Joly
Institut Lumière Matière - Université Lyon 1
Campus de la Doua, bâtiment Brillouin
43 bd du 11 novembre 1918
69622 Villeurbanne Cedex, France
Tel.: +33 (0) 4 724 326 11
e-mail: laurent.joly@univ-lyon1.fr
Web: http://ilm-perso.univ-lyon1.fr/~ljoly/

xDEM Simulation of Frozen Particle Fluid System subjected to shearing

Tsz Tung Chan, Stefan Heinrich, Jürgen Grabe

Abstract: This paper aims to resolve the difficulties in the numerical analysis of the mechanical behaviour of frozen particle fluid system (PFS) under shearing conditions. Tools used for the numerical analysis are the extension of the mesh-free discrete element method (DEM) and bonded particle method (BPM). A new solid bond model considering creep is developed and integrated into the simulation framework (MUSEN). In this paper, shear tests have been committed to validating the developed solid bond model's capability and further calibrating the solid bond's material model. During the experiment, particle types and loading speed are alternated to cover the broadest possible range of interest. Material parameters will remain the same as the calibrated value used in the previous paper, in which only the tangential strength is alternated. Simulation performed using the newly developed solid bond model provides a good agreement compared to the experiment result.

1 Introduction

Frozen particle fluid system (PFS) is vastly investigated in academic and industrial fields, such as frozen agglomerate or frozen soil. The properties are crucial in different areas, including building projects in the arctic region, agglomeration of food particles under freezing temperature, cryogenic grinding, permafrost and avalanches. Regarding natural science, frozen soils have been investigated since the 19th century. The building project was developed closer to the arctic region, and artificial ground freezing (AGF) was introduced for construction and mining projects (Arenson, Springman, and Sego 2007). Apart from fields related to terrestrial projects, understanding frozen PFS is also crucial in understanding the mechanical behaviour of icy asteroids in the solar system, which is critical to the future deep space mission (Weertman 1983).

For technical particles, freezing was widely used in the food and powder industries, such as freeze drying or cryogenic grinding for temperature-sensitive material. Understanding the frozen PFS mechanical properties and developing simulation models for such usage is crucial for exploring such techniques in industry and natural fields.

A considerable portion of frozen PFS is constructed by ice, which has existed on earth for centuries, with numerous research regarding ice. Mechanical properties of ice were well developed

throughout different scopes, such as viscoelastic properties (Jellinek and Brill 1956), creep behaviour (Glen 1955), mechanical properties of polycrystalline ice and columnar-grained ice (Goodman et al., 1981; Gold, 1972), temperature effects on creep behaviour (Mellor and Testa 1969), surface properties effect on adhesion performance (Hassan, Lee, and Lim 2010). The artificial neural network has been trialled to predict ice mechanical behaviour regarding different strain rates, types and temperatures presented in the most recent work (Kellner et al., 2019).

In addition, simulation tools were applied for investigating ice mechanical behaviour, such as the interaction between ship structure with broken ice by the elastic ice model (Wang et al. 2020), the finite element model (FEM) used for the high dynamic behaviour of ice(Pernas-Sánchez et al. 2012) or discrete element method (DEM) used for interaction between a conical system with sea ice in the Arctic region (Long, Liu, and Ji 2021).

Apart from the bond material alone, the composite of frozen PFS has been investigated for centuries due to different applications related to frozen soils. Many available works of literature have explored rheology on frozen soil. The field of frozen soil has been investigated for decades—literature regarding permafrost dates back to the 17th century (Yershov 2004). Additionally, artificial ground freezing (AGF) was introduced in the 18th century. Numerous examples of AGF are used in the construction industry to resolve different geotechnical engineering problems (Harris 1995). With another experiment regarding frozen soil in the other boundary conditions, understanding of frozen soil has vastly enriched (Arenson, Springman, and Sego 2007).

Particle-based Discrete element method (DEM) is a numerical model for understanding the particle dynamic by the interaction of each discrete element, which was introduced by Cundall and Strack (1979)(Cundall and Strack 1979). Bonded particle method (BPM) is an extension of the discrete element method (xDEM) (Dosta et al. 2016), in which either a solid or liquid bond connects the primary particle. Both BPM and DEM have been applied for tackling different mechanical problems, including damage progress of concrete or high-performance concrete (Rybczyński et al., 2020; Beckmann et al., 2012), cemented sand (Obermayr et al., 2013), rock mechanics (Ouyang, Yang, and Chen 2017) or mechanical behaviour of biopolymer aerogel (Dosta, Jarolin, and Gurikov 2019).

In the previous paper (T.T.Chan, S. Heinrich, J. Grabe, M. Dosta, submitted), the solid bond material parameter was calibrated according to numerous uniaxial compression tests, including Young's modulus, Poisson's ratio, and Normal strength regarding different particle surface properties and strain rates. In this paper, the shear test is aimed to be performed. The material parameter can be further calibrated with the shear test, and the bond model can also be validated.

This paper is separated into two main sections. In the first section, the experiment performed in-house details were presented, including the appliance, specimen preparation method, procedure, and result. Furthermore, the numerical approach is demonstrated. The model couples the strain-dependent and time-dependent creep behaviour to formulate the viscoelastic behaviour of ice coupled in the DEM framework. Simulation and experiment result comparisons were presented in this part for model validation. Finally, the conclusion is given in the last section.

2 Experimental setup

To prevent specimen failure due to thermal failure rather than mechanical failure, a climate chamber built with 3D printed parts, a computer radiator and radial fans were developed. The radiator is connected with the cryogenic unit (IKA Temperature Control, RC2 basic, lowest temperature: -20°C). In this experiment, the climate chamber is aimed to maintain the ambient temperature at around -10ºC. The climate chamber is coupled with TA.XT plus texture analyzer (Stable Micro System Ltd., Surrey, United Kingdom, force resolution: 0.1g, displacement resolution: 0.001mm, lowest compression speed: 0.01mm/s).

Nonetheless, a special clamp has to be developed for the shear test. The metal punch consists of two main parts: the shear clamp and the shear punch. Two straight sliver steel columns guided the shear punch during the force applying process. Metal punch applied force onto the shear punch with constant speed, marked by the blue arrow. Force response is then measured accordingly. To ensure the barrier-free specimen loading process, the specimen holder part had a slightly bigger diameter than the specimen. The inner diameter of the specimen holding part was 10.5mm. Such can ensure no obstacle during the specimen loading process. The CAD design of the climate chamber coupled with the special clamp and the setup of the shearing clamp is presented in Figure 1.

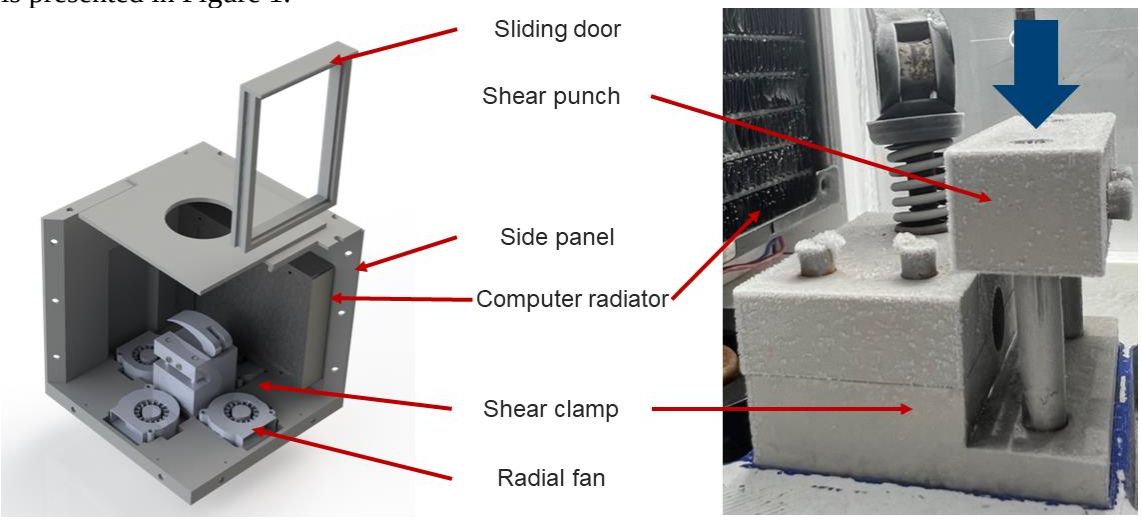

Figure 1: Left: CAD design of climate chamber coupled with a shear clamp; Right: Shear clamp setup

2.1 Specimen preparation

Specimen preparation is crucial for the experiment data's accuracy since undesired defects influence the spread of data. Nevertheless, specimen prepared by incorrect method leads to entirely different mechanical responses.

Different particles were considered to cover the broadest range of interests for the frozen PFS specimen. Silicon mould with 10mm diameter and a height to diameter ratio of around 1.8 is created for the specimen preparation. Table 1 shows the particle choice, ranging from different

surface properties and sizes. The diameter of the technical particle ranged from 1.6 to 2.1 mm, with the quartz sand particle around 0.5 mm.

Table 1: choice of particles

Choice of Particle	**Soft**	**Hard**	**Natural**
Smooth surface	Polyethene	Glass bead	-
Rough surface	-	Alpha alumina	Quartz sand

First, particles were poured into the mould to prepare the Frozen PFS specimen. Deionized water was then injected from the bottom of the mould and passed to the degassing chamber to ensure no gas bubbles in the agglomerates. PFS specimens were frozen overnight in a normal refrigerator (-18ºC). A sample of Frozen PFS with glass beads is presented in Figure 2
.

Figure 2: Frozen PFS with constructed by Glass bead

2.2 Experiment parameter

Only the shear speed was alternated in the experiment, as ice is a typical material review of massive creep behaviour. The shear punch is driven in 0.02mm/s and 0.2mm/s. The sheer speed is chosen according to the experiment performed previously.

2.3 Experiment result

2.3.1 Mechanical behaviour of Frozen PFS under shearing

According to the literature, four types of mechanical behaviour can be observed in the Frozen PFS under uniaxial compression: brittle behaviour, brittle behaviour with failure after yield, ductile behaviour with strain hardening, and ductile behaviour with strain softening. However, such cannot be applied to the frozen PFS under shearing. Most PFS experienced brittle failure, in which the failure of the specimen happens abruptly. There may be a slight difference in the failure point, which the specimen experience yielding just before failure. Figure 3 shows the

stress-strain curve of some representative experiments for PFS with sand and alpha-alumina primary particles under high shearing speed (HS) and low shearing speed (LS).

One distinct difference occurs in the Frozen PFS constructed by alpha alumina under low-speed shearing, in which there is no brittle failure happened during the shearing process. The failure process was vastly lengthened, which showed strain hardening and strain softening after specific points. It might be related to the distinct surface properties of Alpha-alumina. The alpha alumina has porous surface properties, allowing a diffused structure to form between the bond material (ice) and particle surface. Under the slow shearing, the bond material is elongated till failure. However, the shearing block provided a massive contact patch with the specimen—the broken bonds attached to the particle reform bond with the adjacent bond. In terms, the internal structure is regenerated under the shearing process. Such can be explained that after the highest force, the force-displacement curve provided a slight wavy pattern, and no apparent failure was reviewed.

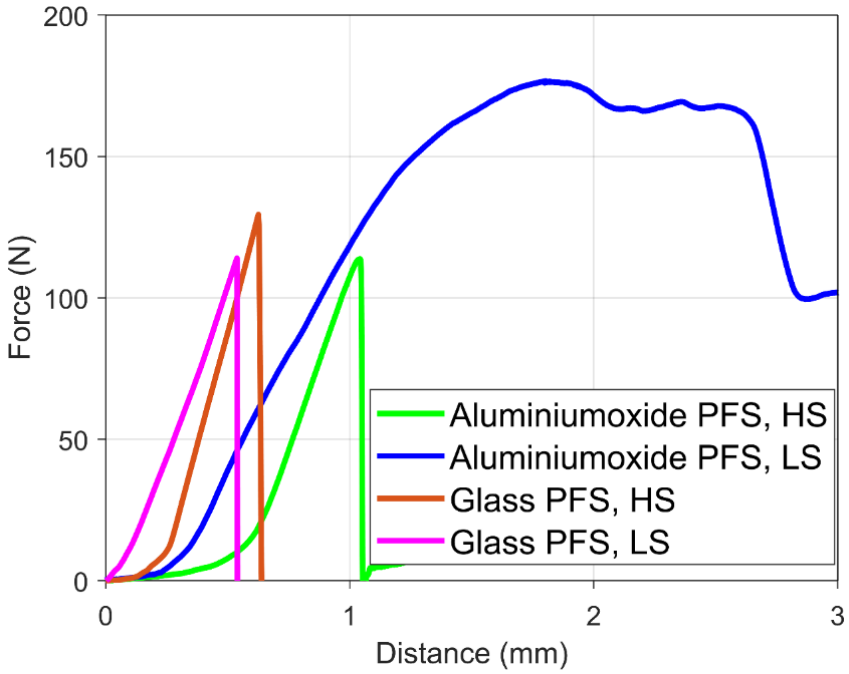

Figure 3: Representative force-distance curve of frozen PFS under shearing (LS: low speed, $0.02 mms^{-1}$; HS: high speed, $0.2 mms^{-1}$)

The overview of the shearing failure force and distance is listed in Figure 4. Shear speed influenced the breakage force slightly. A lower force was required to achieve breakage with the higher shear speed. However, such a phenomenon cannot be reviewed in frozen PFS constructed by sand particles. In contrast, the breakage distance provided a slightly deviated outcome. Frozen PFS constructed by polymer particles provided a slight higher breakage distance under higher shear speed. However, other frozen PFS provided slightly higher breakage distance under lower shear speed. In particular, alpha-alumina PFS gave a much higher breakage distance at low shear speed than at high shearing speed. It can be correlated to the previous assumption that the alpha-alumina PFS bonds were regenerating under the slow shearing progress.

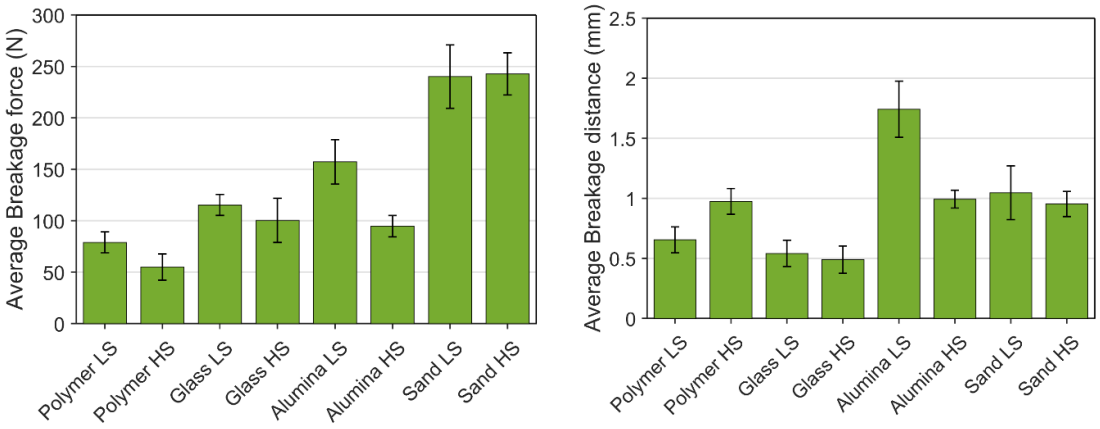

Figure 4: Average breakage force and breakage distance of different PFS (Left: Breakage force; right: Breakage distance)

Apart from the mechanical parameter, an overview of mechanical behaviour is presented for a clearer picture.

Table 2: Mechanical response overview concerning shearing speed and types of particle

	Smooth particle	**Rough particle**	**Natural particle**
Low shearing speed	Brittle failure	Ductile behaviour with strain hardening followed by strain softening	Brittle failure just after yield point
High shear speed	Brittle failure	Brittle failure just after yield point	Brittle failure

Under shearing, particle surface properties imposed the most distinctive influence on the frozen PFS's mechanical behaviour.

3 xDEM approach

GPU-accelerated DEM Framework MUSEN is used to describe the behaviour of Frozen PFS, in which bonded particle model (BPM) is also available (Dosta and Skorych 2020). In BPM, the particles interact with other non-contacting particles according to different bond characteristics. In addition, the bond can be generated with overlap, extra dimension and material. Bonds can be created (sintering, wet bond) or destroyed (breakage) during simulation.

Agglomerate is generated with two consecutive steps. Pack particles are developed in a logical volume (pseudo space) according to the force-bias algorithm (Mosciñski et al. 1989). All particles are randomly generated in the pseudo space, with the algorithm's centre position and radius known. The sphere position changes according to the 'Force' acted on each interacted

particle in every iteration. The force on each pair of particles is proportional to the overlap area. Generation is completed when the maximum overlap is lower than the target value. To complete the agglomerate, particles are connected with solid bonds. The generation is governed by the maximum and minimum distance between the surface of spheres. If the requirement is fulfilled, bonds are generated between particles. In addition, bonds can be generated with overlapping.

3.1 The solid bond model approach

The most important effect being considered is the strain-rate dependent behaviour. A new solid bond model considering the creep behaviour has been developed. Both the particle-particle and particle-wall relationships are calculated according to the Hertz-Mindlin model. The normal force is calculated according to Hertzian theory (Tsuji, Tanaka, and Ishida 1992), and the tangential force is calculated according to Mindlin's theory. (Mindlin and Deresiewicz 1953). The detailed equation can refer to the literature, which particle young's modulus, Poisson ratio, friction coefficient and rolling friction are the necessary data for calculation (Spettl et al., 2015; Maksym Dosta, Matthias Weber, Volker Schmidt, 2019).

This paper is mainly focusing on the bond behaviour in the tangential direction. The bond force calculation is described briefly here. As mentioned, ice is a typical creep material, and power law is used to describe the creep behaviour of ice. The power law defines the creep strain rate $\dot{\varepsilon}_{cr}$ according to two parameters and the current stress. The two parameters A and m, can be adjusted according to temperature and material.

$$\dot{\varepsilon}_{cr} = A\,\sigma^{m} \tag{1}$$

Strain in the normal direction $\varepsilon_{n,to}$ is calculated with the bond initial length L_I and current length L_c:

$$\varepsilon_{n,to} = \frac{L_c - L_I}{L_I} \tag{2}$$

The normal strain consists of two distinct parts, the elastic part $\varepsilon_{n,el}$ and the permanent deformed part. The creep strain represents the permanently deformed strain $\varepsilon_{n,cr}$:

$$\varepsilon_{n,to} = \varepsilon_{n,el} + \varepsilon_{n,cr} \tag{3}$$

Bond normal stress is calculated by :

$$\sigma_n = E\,\varepsilon_{n,el} \tag{4}$$

E denotes the bond's Young's modulus.

Temperature change during simulation is not considered to maintain the model's simplicity. Permanent strain change due to creep after every consecutive time step is calculated by:

$$\varepsilon_{n,cr}(t + \Delta t) = \varepsilon_{n,cr}(t) + \Delta t\,A\,(\sigma_n(t))^{m} \tag{5}$$

By coupling the previous equations together, the normal bond force can be calculated according to:

$$F_{n,b}\ (t+\ \Delta t) =\ E\ A_b \left(\varepsilon_{n,to} - \varepsilon_{n,cr}(t+\Delta t)\right) \tag{6}$$

which A_b is the cross-section area of the bond.

For the simplicity of the mode, the same creep behaviour and creep parameter as the normal direction is used for the creep behaviour in the tangential direction. To calculate the tangential bond force, tangential bond deformation $\vec{\delta}_t$ must be calculated. Bond tangential deformation is calculated according to the relative motion in the previous timestep:

$$\vec{\delta}_t(t+\Delta t) = T\ \vec{\delta}_t(t) +\ \vec{v}_{t,rel}\ \Delta t \tag{7}$$

T is the rotation matrix to consider the motion of connected particles, and $\vec{v}_{t,rel}$ is the relative velocity at the contact point in the tangential direction.

The tangential stress σ_t can be calculated with the tangential deformation:

$$\sigma_t = \frac{\left|\vec{\delta}_t\right|}{L_I}\ \frac{E}{2\ \cdot(1+v)} \tag{8}$$

v denotes the Poisson's ratio. During the calculation of tangential strain, relative rotation of the bond compared to the previous timestep has to be considered. The deformation, according to creep, has to align with the new direction of the bond. In terms, the creep deformation must multiply with the bond's unit vector $\vec{r}_t$:

$$\vec{\varepsilon}_t(t+\Delta t) = \vec{\varepsilon}_t(t) +\ \varepsilon_{t,cr}\ (\Delta t)\ \vec{r}_t \tag{9}$$

The bond's vector can calculate the unit vector of the bond $\vec{\delta}_t(t)$ and bond's length $\left|\vec{\delta}_t(t)\right|$:

$$\vec{r}_t\ = \frac{\vec{\delta}_t(t)}{\left|\vec{\delta}_t(t)\right|} \tag{10}$$

By combining all the equations mentioned previously, the tangential bond force can be calculated by:

$$\vec{F}_{t,b} =\ \frac{\vec{\delta}_t(t+\Delta t)}{L_I}\ \frac{E}{2\ \cdot(1+v)}\ A_b \tag{11}$$

One of the crucial features of BPM is mimicking the agglomerates' breakage behaviour. To achieve such a purpose, bonds can be broken during simulation. By comparing the bond's normal and tangential stress with the bond's normal σ_{max} and tangential strength τ_{max}. The existence of the bond during simulation can be considered. Apart from comparing the bond normal and tangential strength, bond breakage due to strain is also considered due to the creep behaviour of the bond material.

$$\frac{\vec{F}_{n,b}}{A_b} + \frac{\vec{M}_{n,b}\, R_b}{I} \geq \sigma_{max} \tag{12}$$

$$\frac{\vec{F}_{t,b}}{A_b} + \frac{\vec{M}_{t,b}\, R_b}{J} \geq \tau_{max} \tag{13}$$

$$\varepsilon_{n,to} \geq \varepsilon_{n,max} \tag{14}$$

R_b is the bond radius, $\vec{M}_{n,b}$ and $\vec{M}_{t,b}$ are the bending and torsional moments of the bond, respectively, I is the moment of inertia, and J is the polar (torsional) moment of inertia of the bond's cross-section.

The previous literature proposes an algorithm for determining the bond's normal strength according to strain rate (Petrovic 2003). However, coupling the relationship into the solid bond model proved unreasonable, as the bond strength fluctuated massively during the simulation. The bond normal and tangential strength alternation due to strain rate and particle surface properties is compensated by changing the bond material modelling parameter.

3.2 Simulation setup

As mentioned, the agglomerate has been generated, with the particle diameter tailored to the particle used in the experiment. Upper pressing geometry moves 200 times as the experiment compression speed to reduce the total time required for simulation. The creep parameter and restitution coefficient have been tuned accordingly. For the technical particle, the spherical particle is used for representing the particles. However, the spherical particle is used for the natural particle to maintain the simulation, as contact detection occupies a significant amount of calculation power in DEM simulation. Determining the collision of the spherical particle is easy by calculating whether the centre distance is larger or smaller than the combined radius (Descantes, Tricoire, and Richard, 2019).

The particle-particle and particle-wall relationships were alternated (Gu, Zhang, and Huang, 2020). Agglomerate setup is presented in Table 3.

Table 3: agglomerate setup of different PFS

Technical particle PFS		Natural particle PFS	
Particle diameter (mm):	1.65-1.8	Particle diameter (mm):	0.5
Bond diameter (mm):	1.0	Bond diameter (mm):	0.3
No. of particles:	≈230	No. of particles:	≈11200
No. of bonds:	≈1100	No. of bonds:	≈66000
Porosity:	0.44	Porosity:	0.42
Particle-wall friction:	0.1	Particle-wall friction:	0.5
Particle-particle friction:	0.05	Particle-particle friction:	0.45
Restitution coefficient:	0.1	Restitution coefficient:	0.7

The bond material parameters were calibrated according to the uniaxial compression test performed in the previous paper. Young's modulus and Poisson's ratio have been kept unchanged throughout all the simulations. Young's modulus is set as 350 MPa, tailored according to the in-house uniaxial compression experiment. The Poisson's ratio is set as 0.31 (Petrovic 2003). Simulation performed here have a different tangential and normal strength value, further tailoring the bond material parameter under different strain rates and concerning different particle surface properties.

Table 4: Material modelling for bonds under different circumstances

Primary particles	Polyethene	Glass	Alpha-alumina	Natural sand
Normal strengths				
High shear speed [MPa]	3.5	4.2	20	20
low shear speed [MPa]	6	2.7	20	20
Tangential strengths				
high shear speed [MPa]	1.3	0.8	22	2.6
low shear speed [MPa]	2.2	1.5	1	6.9
Creep parameter A [-]	0.1	0.1	0.3	0.1
Creep factor m [-]	0.1	0.1	0.16	0.1

At least five individual simulations have been performed for every single combination. The reason is to compensate for the internal structure difference of the agglomerates. The agglomerates were placed into the clamp randomly. The difference in the internal structure differed, which led to a slight difference in the failure profile, further changing the breakage distance and force. Numerous simulation with internal structure generated randomly is performed to compensate for the effect of the randomness of the internal structure during the experiment.

3.3 Simulation and experiment result comparison

The simulation data showed a promising result without the alternation of Young's modulus and Poisson's ratio. In most cases, the simulation has achieved a very close value to the experiment result. However, in Glass PFS under low shear speed, the simulation has an even higher deviation than the experiment result. This may be related to the number of simulations performed is not enough. In this case, more simulations must be committed to gathering more data to rule out improper cases.

In the breakage distance, a higher deviation can be reviewed. This can be related to the clamp used in the experiment. The inner diameter of the shear clamp is slightly bigger than the specimen's diameter. Under the shear motion, the specimen is tilted somewhat and then subjected to pure shearing force. However, due to the specimen preparation process, the length of the specimen cannot be ensured to be identical across every specimen. Due to the uncertainty, the tilted angle cannot be assured, which leads to differences in the breakage distance.

In the alpha-alumina PFS, the simulation result significantly deviated from the experiment result. It was related to the assumption made in the previous part, as the bond was regenerated during the shear progress. However, due to the nature of the bond model, such a phenomenon is not considered. Leading the internal structure in the simulation is not a close representation of the agglomerate under experiment conditions.

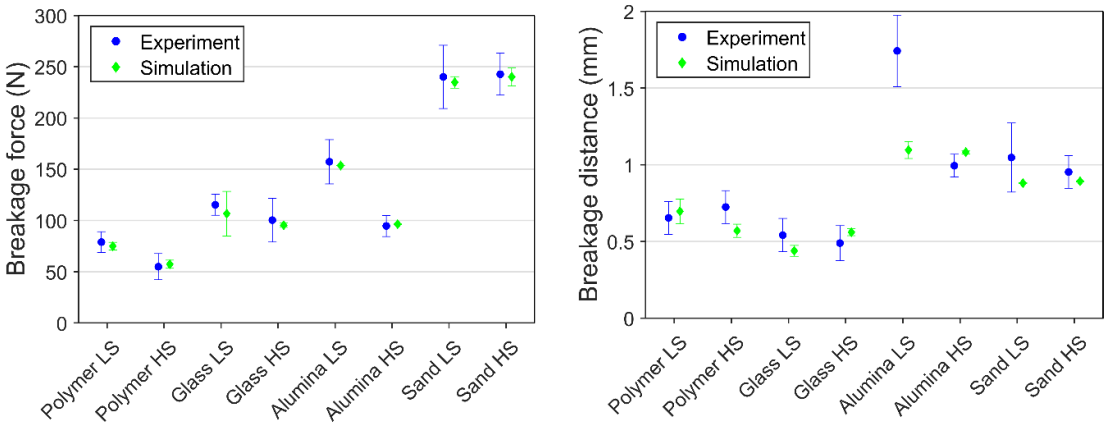

Figure 5: Comparison of experimental and simulation results

4 Conclusion

Experiments and simulations were performed for frozen PFS and ice in this contribution. Under the shearing condition, particle surface properties significantly influence the frozen PFS mechanical behaviour and parameters.

The extended Discrete Element Method (xDEM), Bonded Particle Model (BPM) is used to tackle the problem. BPM is available in the in-house developed DEM framework MUSEN. A new solid bond model considering creep behaviour in normal and tangential directions is developed and coupled into the framework. Combining the material parameter obtained previously and the material parameter modelled in this work. The model shows a promising result in both uniaxial and shearing conditions. The solid bond model can tackle the bond material's strain rate-dependent behaviour.

References

[1] Arenson, Springman, and Sego. (2007)"The rheology of frozen soils," Appl. Rheol., vol. 17, no. 1, 2007, doi: 10.1515/arh-2007-0003.

[2] Weertman. (1983) "Creep deformation of ice," Annu. Rev. Earth Planet. Sci., vol. 11, no. 1, pp. 215–240, 1983, doi: 10.1146/annurev.ea.11.050183.001243.

[3] Jellinek and Brill. (1956) "Viscoelastic properties of ice," J. Appl. Phys., vol. 27, no. 10, pp. 1198–1209, 1956, doi: 10.1063/1.1722231.

[4] Glen. (1955) "The creep of polycrystalline ice," Proc. R. Soc. London. Ser. A. Math. Phys. Sci., vol. 228, no. 1175, pp. 519–538, 1955, doi: 10.1098/rspa.1955.0066.

[5] Goodman, Frost, and Ashby. (1981) The plasticity of polycrystalline ice, vol. 43, no. 3. 1981.

[6] Gold. (1972) "The process of failure of columnar-grained ice," Philos. Mag., vol. 26, no. 2, pp. 311–328, 1972, doi: 10.1080/14786437208227430.

[7] Mellor and Testa. (1969) "Effect of Temperature on the Creep of Ice," J. Glaciol., vol. 8, no. 52, pp. 131–145, 1969, doi: 10.3189/s0022143000020803.

[8] Hassan, Lee, and Lim. (2010) "The variation of ice adhesion strength with substrate surface roughness," Meas. Sci. Technol., vol. 21, no. 7, 2010, doi: 10.1088/0957-0233/21/7/075701.

[9] Kellner et al. (2019) "Establishing a common database of ice experiments and using machine learning to understand and predict ice behavior," Cold Reg. Sci. Technol., vol. 162, no. January, pp. 56–73, 2019, doi: 10.1016/j.coldregions.2019.02.007.

[10] Pernas-Sánchez, Pedroche, Varas, López-Puente and Zaera. (2012) "Numerical modeling of ice behavior under high velocity impacts," Int. J. Solids Struct., vol. 49, no. 14, pp. 1919–1927, 2012, doi: 10.1016/j.ijsolstr.2012.03.038.

[11] Wang, Hu, Tian, Guo, and Wang. (2020) "Numerical simulation of ice loads on a ship in broken ice fields using an elastic ice model," Int. J. Nav. Archit. Ocean Eng., vol. 12, pp. 414–427, 2020, doi: 10.1016/j.ijnaoe.2020.03.001.

[12] Long, Liu, and Ji. (2021) "Breaking characteristics of ice cover and dynamic ice load on upward–downward conical structure based on DEM simulations," Comput. Part. Mech., vol. 8, no. 2, pp. 297–313, 2021, doi: 10.1007/s40571-020-00331-8.

[13] Yershov. (2004) "General Geocryology," Cambridge Univ. Press, 2004, doi: https://doi.org/10.1017/CBO9780511564505.

[14] Harris. (1995) "Ground freezing in practice," Thomas Telford, 1995.

[15] Cundall and Strack. (1979) "A discrete numerical model for granular assemblies," Géotechnique, vol. 29, no. 1, pp. 47–65, 1979, doi: https://doi.org/10.1680/geot.1979.29.1.47.

[16] Dosta, Dale, Antonyuk, Wassgren, Heinrich, and Litster. (2016)"Numerical and experimental analysis of influence of granule microstructure on its compression breakage," Powder Technol., vol. 299, pp. 87–97, 2016, doi: 10.1016/j.powtec.2016.05.005.

[17] Rybczyński, Dosta, Schaan, Ritter, and Schmidt-Döhl. (2020) "Numerical study on the mechanical behavior of ultrahigh performance concrete using a three-phase discrete element model," Struct. Concr., vol. 23, no. 1, pp. 548–563, 2022, doi: 10.1002/suco.202000435.

[18] Beckmann, Schicktanz, Reischl, and Curbach. (2012) “DEM simulation of concrete fracture and crack evolution,” Struct. Concr., vol. 13, no. 4, pp. 213–220, 2012, doi: 10.1002/suco.201100036.

[19] Obermayr, Dressler, Vrettos, and Eberhard. (2013) "A bonded-particle model for cemented sand," Comput. Geotech., vol. 49, pp. 299–313, 2013, doi: 10.1016/j.compgeo.2012.09.001.

[20] Ouyang, Yang, and Chen. (2017) "Bonded-particle model with nonlinear elastic tensile stiffness for rock-like materials," Appl. Sci., vol. 7, no. 7, 2017, doi: 10.3390/app7070686.

[21] Dosta, Jarolin, and Gurikov. (2019) "Modelling of mechanical behavior of biopolymer alginate aerogels using the bonded-particle model," Molecules, vol. 24, no. 14, p. 2543, 2019, doi: 10.3390/molecules24142543.

[22] Chan, Heinrich, Grabe, Dosta. (submitted) "Microscale modelling of frozen particle fluid systems with a bonded particle method," Granul. matter.

[23] Dosta and Skorych. (2020) "MUSEN: An open-source framework for GPU-accelerated DEM simulations," SoftwareX, vol. 12, p. 100618, 2020, doi: 10.1016/j.softx.2020.100618.

[24] Mosciński, Bargie, Rycerz, and Jacobs. (1989) "The Force-Biased Algorithm for the Irregular Close Packing of Equal Hard Spheres," Mol. Simul., vol. 3, no. 4, pp. 201–212, 1989, doi: 10.1080/08927028908031373.

[25] Tsuji, Tanaka, and Ishida. (1992) "Lagrangian numerical simulation of plug flow of cohesionless particles in a horizontal pipe," Powder Technol., vol. 71, no. 3, pp. 239–250, 1992, doi: 10.1016/0032-5910(92)88030-L.

[26] Mindlin and Deresiewicz. (1953) "Elastic Spheres in Contact Under Varying Oblique Forces," pp. 327–344, 1953, doi: 10.1115/1.4010702.

[27] Spettl, Dosta, Antonyuk, Heinrich, and Schmidt. (2015) "Statistical investigation of agglomerate breakage based on combined stochastic microstructure modeling and DEM simulations," Adv. Powder Technol., vol. 26, no. 3, pp. 1021–1030, 2015, doi: 10.1016/j.apt.2015.04.011.

[28] Dosta, Weber, Schmidt. (2019) "DEM analysis of breakage behavior of bicomponent agglomerates," Part. contact, pp. 165–183, 2019.

[29] Petrovic. (2003) "Review mechanical properties of ice and snow," J. Mater. Sci., vol. 38, no. 1, pp. 1–6, 2003, doi: 10.1023/A:1021134128038.

[30] Descantes, Tricoire, and Richard. (2019) "Classical contact detection algorithms for 3D DEM simulations: Drawbacks and solutions," Comput. Geotech., vol. 114, 2019, doi: 10.1016/j.compgeo.2019.103134.

[31] Gu, Zhang, and Huang. (2020) "DEM analysis of monotonic and cyclic behaviors of sand based on critical state soil mechanics framework," Comput. Geotech., vol. 128, no. June, p. 103787, 2020, doi: 10.1016/j.compgeo.2020.103787.

Author

Research Assistance M.Sc. Tsz Tung Chan
Technische Universität Hamburg-Harburg
Institute of Solids Process Engineering and Particle Technology
Denickestr. 15
21073 Hamburg
Tel.: +49 (0) 40 - 42878 / 3414
Fax: +49 (0) 40 - 42878 / 3621
e-mail: chan.tsz.tung@tuhh.de
Web: https://www.tuhh.de/spe

Univ.-Prof. Dr.-Ing. Jürgen Grabe
Technische Universität Hamburg-Harburg
Institut für Geotechnik und Baubetrieb
Harburger Schloßstraße 20
21079 Hamburg
Tel.: +49 (0) 40 - 42878 / 3762
Fax: +49 (0) 40 - 42878 / 4020
e-mail: grabe@tu-harburg.de
Web: www.tu-harburg.de/gbt

Univ.-Prof. Dr.-Ing. habil. Dr. h.c. Stefan Heinrich
Technische Universität Hamburg-Harburg
Institute of Solids Process Engineering and Particle Technology
Denickestr. 15
21073 Hamburg
Tel.: +49 (0) 40 - 42878 / 3750
Fax: +49 (0) 40 - 42878 / 2678
e-mail: stefan.heinrich@tuhh.de
Web: https://www.tuhh.de/spe

Application of discrete element method to analyze micromechanics of granular materials

Sergiy Antonyuk

Abstract: The filter cake is a saturated particle packing that formed in the filtration process due to particle separation from the suspension on a filter medium. The micromechanics of the filter cake formation (interactions between particles, particles and fluid, and filter medium) must be considered to predict pore clogging, filter cake growth and consolidation correctly. A precise 3D modeling approach to describe these effects is the resolved 4-way coupling of the Computational Fluid Dynamics with the Discrete Element Method (CFD-DEM). This work focuses on the development and validation of a CFD-DEM model, which can accurately predict filter cake formation during solid-liquid separation.

1 Introducion

Many industrial applications use cake filtration for the separation of solid particles from liquids by a porous filter medium on which a filter cake is formed [1]. The packing structure and porosity of the filter cake is a crucial factor affecting the pressure drop or energy effort of filtration process, influences the product quality and one of the keys to the success of downstream processes, such as washing and removing the residual moisture [2]. The filter cake structure is affected by the particle-particle/filter medium, particle-fluid interactions, the size distribution of particles and their mechanical and adhesive properties [3-5]. Further, for a filter cake formed from non-spherical particles, the shape and the orientation of the particles also affect the structure of the filter cake. In addition to this, the filter cake may undergo consolidation (change in void fraction) due to the fluid forces [6, 7]. Therefore, a detailed investigation of the filter cake structure and interactions between filter medium and particles is necessary to determine and describe specific parameters like the resistances of the filter cake and the filter medium. For the description of these micro processes, the numerical multiphase flow simulation can be applied.

2 Numerical approaches for modeling of filter cake formation

Different numerical approaches can be used for the simulation of filter cake formation. The interactions between particles and the fluid can be considered entirely or just in parts. The 1-way coupling methods focus on the fluid flow influencing the particles, while particle movement does not affect the fluid flow field. The 2-way coupling methods also include the impact

of the moving particle on the fluid flow. At low particle concentrations in suspensions with very stiff, non-adhesive and ideal spherical particles, the filtration process can be simulated by the Computational Fluid Dynamics (CFD) using models of the porous structure (Euler), two-phase CFD models (Euler-Euler) and CFD with Lagrangian particle tracking. In our previous work, the filter cake formation at static filtration [8], fractionation in cross-flow filtration [9] and particle deposition in the electret nonwovens [10] were studied with Lagrangian particle tracking. The same method was used by Hosseini and Tafreshi [11] for simulation of the aerosol flow through nanofiber filter media. The deformation, adhesion, relative movement and reorganization of the particles in the filter cake are important mechanisms of the cake formation, which cannot be predicted by either 1-way coupling or 2-way coupling.

In this context, the Discrete Element Method (DEM) is a powerful method to simulate the motion and interactions of individual particles in particulate systems under the influence of different forces and moments [12, 13]. The forces can include contact, adhesion, drag, buoyancy, gravity, etc. Thus, the kinematics and dynamics of each individual particle and the entire particle collective can be obtained, taking into account effects such as particle size distribution, irregular particle shape, deformation, sticking and breakage of particles.

The coupling of the DEM with the CFD considers the interactions between particles, particles and filter medium as well as fluid-particle interactions in 4-ways (Figure 1). CFD-DEM coupled methods can then also be divided into two groups of volume-averaged and resolved simulations. In the volume-averaged simulations, the CFD-DEM coupling does not fully resolve the fluid flow around each individual particle. The flow is calculated on the basis of the volume-averaged Navier-Stokes equations. Since the majority of the numerical studies of fluid-particle flows in literature were performed with the unresolved coupling, the CFD-DEM is a commonly used term for the volume-averaged method [14]. Vångö et al. [15] gave an overview of unresolved coupling methods for the solid-liquid packed bed simulations.

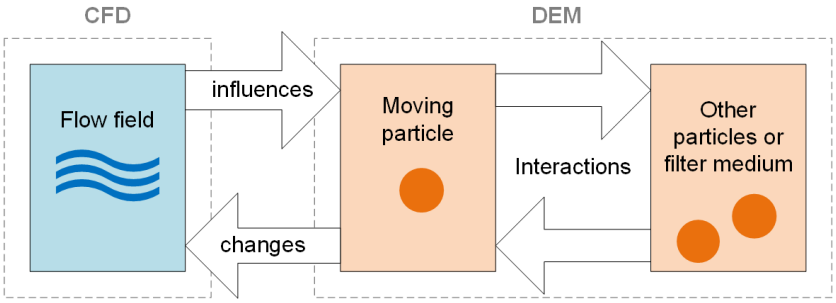

Figure 1: 4-way CFD-DEM coupling. Each interaction is illustrated by an arrow

The unresolved coupling works well if the volume of the grid cells is much larger than the particle volume. If the volume of a grid cell approaches the particle volume, the cell might be fully occupied by a particle, which results in numerical problems. The collision behaviour of the particles can also be affected by viscous forces [16]. The viscous forces can influence the cake formation [17] and separation process [19]. The numerical studies based on the unresolved CFD-DEM coupling cannot calculate these forces directly and need therefore an additional model, which considers the energy dissipation due to surrounding fluid.

The unresolved CFD-DEM models are not suitable for the direct prediction of the influence of particle concentration (swarm effect) and need specific correlations for the drag force [17, 18]. However, these complex particle-fluid interactions which also have a strong influence on the particle contact interactions can be simulated by the resolved coupling of DEM with CFD. In this approach, the DEM calculates the kinetics and dynamics for each single particle depending on all relevant forces including the contact interactions between particles and with the filter medium surface, such as the deformation, adhesion and friction forces. The above-mentioned drag, buoyancy and viscous forces due to flow are obtained by CFD simulation of the flow and explicitly considered via coupling in the momentum balance of the DEM.

One of the most accurate 3D modeling approaches to describe the flow is Direct Numerical Simulation (DNS). For this, the Lattice-Boltzmann Method (LBM) is used as an especially well-suited numerical scheme to approximate the transient Navier-Stokes equations with moving boundaries [20, 21]. Rettinger and Rüde [23] proposed a new algorithm for the 4-way coupling LBM of suspensions.

In this work, the numerical study of the micro processes between the particles during filter cake formation is achieved by the resolved coupling between CFD and DEM methods. The experimental investigations complement the simulation results and the numerically calculated filter resistances represent the experimentally obtained results of the filter cake formation processes.

3 Experimental measurement of the filter curve

3.1 Filtration equation

The cake filtration process (Figure 2) is characterized by the resistances, which can be divided into the two pressure drops of the filter cake $R_C(t)$ and the filter medium resistance R_M. The filtration Equation (1) [1] describes the flow velocity $v_F(t)$ of the filtrate depending on the total pressure difference Δp and both resistances:

$$v_F(t) = \frac{\Delta p}{\mu \cdot (R_C(t) + R_M)} \tag{1}$$

where μ is the dynamic viscosity of liquid.

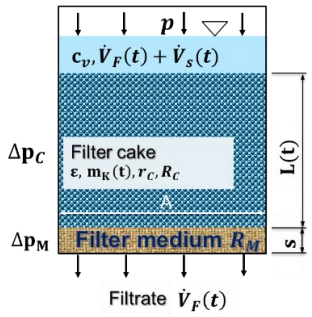

Figure 2: Representation of resistances in the cake filtration

The resistance of the filter medium can be divided into the pure filter medium resistance R_{M0} and the interference resistance R_{MI}, which describes the resistance of the filter medium under consideration of the first particle layer on the medium, that can block the medium pores [30].

The results of filtration experiments and simulations are evaluated by the filter equation (2) [1]:

$$\frac{t}{V_F} = \frac{\mu \cdot r_c \cdot K_S}{2 \cdot A^2 \cdot \Delta p} \cdot V_F + \frac{\mu}{A \cdot \Delta p} \cdot R_M \qquad (2)$$

where t is the filtration time, V_F is the filtrate volume, r_c is the specific filter cake resistance, K_S is the filtration constant and A is the filter area.

3.2 Parameters of the filtration experiments

For the validation of the simulation, the filtration experiments were performed. The resistances of filter cake and medium are measured in accordance with the VDI guideline 2762 [29]. The experiments are carried out with a laboratory scale pressurized housing at constant pressure Δp= 1 kPa, which is maintained by a constant liquid level above the filter medium. The used aqueous suspension contains spherical silica glass particles (Potters-Ballotini) with sizes in the range of 63-100 µm. The filter medium mounted in the pressurized housing is a twill weave woven wire cloth produced by Haver & Boecker. The parameters of filtration and properties of the filter medium are listed in Table 1.

Table 1: Parameters of the experiment

Property	Unit	Value
mesh size d_{Pore}	µm	32
wire diameter d_F	µm	28
filter area A	cm^2	20
pressure difference Δp	Pa	1000
particle density ρ_P	$kg \cdot m^{-3}$	2200
particle size median/modal values $x_{50,3}/x_{mod,3}$	µm	82.2/82.7

4 Simulation model and parameters

The calculated numerical model is based on resolved CFD-DEM coupling. DNS calculates the fluid flow directly by solving the Navier-Stokes equations (NSE). The used Lattice-Boltzmann method (LBM) allows computation of the laminar fluid flow for low Reynolds numbers or even higher Reynolds numbers if the lattice dimensions are small enough to resolve the turbulent movement of the fluid. The first subsection outlines the principles of the CFD method. DEM is used to calculate the movement of the particles and will be explained in the second section. The third section describes the method for the coupling of the fluid flow with the particle movement and the calculation of interactions. The model was implemented in the in-house developed software DNSlab [31] that is used for the simulation of filtration processes [32], [8], [10], [33].

4.1 Fluid flow calculation with CFD

The CFD calculations are carried out by the LBM, meaning that the equations for conservation of mass (3) and momentum (4) in the fluid phase corresponding to the transient Navier-Stokes equations are approximated using the D3Q15 discretization scheme and velocity boundary conditions applied at the particle boundaries [24, 25]:

$$\frac{\partial \rho}{\partial t} + \nabla \cdot (\rho \cdot v) = 0 \tag{3}$$

$$\rho\left(\frac{\partial v}{\partial t} + (v \cdot \nabla)v\right) = f - \nabla p + \mu \Delta v \tag{4}$$

where v is the velocity vector, f describes the volume forces like gravitation force, and ∇p is the pressure gradient, $(v \cdot \nabla)v$ represents the Navier term (inertial effects) and $\mu \Delta v$ is the Stokes term (viscous effects). ρ, v and p depend on the position in the flow domain $x \in \Omega$ and the time t.

4.2. Particle dynamics calculation with DEM

The movement of each single particle and its interactions with other particles and filter media are calculated with the DEM by solving Newton's second law given as:

$$m_i \cdot \frac{dv_i}{dt} = \sum_j F_{ij}^c + F_i^f + F_i^g \tag{5}$$

with particle mass m_i, contact force F_{ij}^c between particle i and particle or filter medium j, fluid-particle interaction force F_i^f and gravitational force F_i^g. In the present study, contact forces acting between particles as well as particles and filter medium surface are calculated using the well-known Hertz-Mindlin model [26-28].

4.3 The resolved CFD-DEM coupling

The resolved coupling between the LBM for CFD and the DEM method is based on the transfer of momentum from the particles to the fluid and the fluid volume displacement due to particle motion. Figure 3 (left) illustrates the particle moving in the direction of the arrow in a time step. Then, in this rigid lattice structure, former fluid nodes (white) become particle nodes and former particle nodes become fluid nodes (blue). Pressure and velocity values are interpolated from surrounding fluid nodes when new fluid nodes arise from particle movement.

The resistance force on the particles is described by an integration of shear and pressure forces over the particle surface. The fluid-particle interaction force F_i^f considered in DEM in Equation (5) includes the buoyancy force F_i^b (Equation (6)), the shear force F_i^s (Equation (7) and the pressure force F_i^P (Equation (8)).

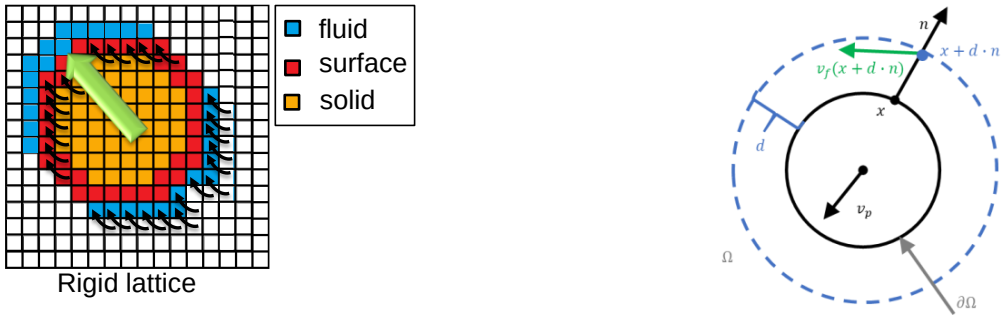

Figure 3: LBM coupling scheme: (left) Particle movement in one simulation time step with particle (orange), particle boundary (red) and fluid (white) nodes. New fluid nodes (blue) after particle movement, surrounding layer of fluid nodes used to compute viscous and pressure forces which act on the particle; (right) Variables used for shear force calculation

$$F_i^b = \rho \cdot V_P \cdot g \tag{6}$$

$$F_i^S = \frac{\mu}{d} \int_{\partial\Omega} (v_{rel})^{tangential} dx \tag{7}$$

$$F_i^P = -\int_{\partial\Omega} p \cdot n \, dx \tag{8}$$

with the particle volume V_P.

Figure 3 (right) explains the calculation of F_i^S. The particle moves with velocity v_p through the flow region Ω. $\partial\Omega$ denotes the solid-liquid interface, i.e., the particle surface. A fluid layer around the particle with thickness d is needed for the evaluation of the local flow velocities and pressures. x is a point on the particle surface and n the unit vector in the normal direction in this point. The shear force acting from the fluid on the particle depends on the tangential part of the relative flow velocity $v_{rel} = v_f(x + d \cdot n) - v_p$.

4.4 Simulation setup and parameters

For the CFD-DEM simulation of the filter cake formation, a 3D model (Figure 4a) is generated as a voxel grid, which uses a cubic lattice for the computation. The model has periodic boundary conditions on the sides and the porous filter medium on the bottom. The microstructure of the experimentally used filter medium is analyzed with an X-Ray Computed Microtomography (TomoScope L, Werth Messtechnik GmbH, minimum voxel size of 500 nm). The cross-section view in Figure 4 (b) shows at the bottom a µCT image and at the top the voxel structure of the generated woven model for the simulation. It outlines a section of the filter area including 16 woven wires with periodic boundary conditions, representing the real weave structure completely. The chosen voxel length of 2.5 µm leads to a coarsening of both pores and wares.

Analogous to the experiment, the filtration simulation is performed at a constant pressure difference. The solid particles are randomly distributed in the inflow plane of the container at the top of the model. The generation rate of particles corresponds to the concentration of 10^{11} m^{-3}. Table 2 summarizes the relevant parameters of the filtration simulation.

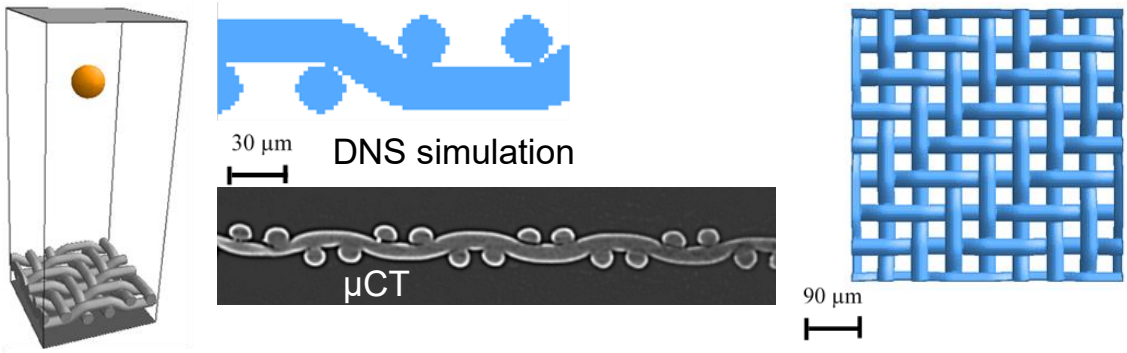

(a) (b) (c)

Figure 4: Basic model geometry (a) with filter medium: (b) side view in a sectional plane through a wire: (top) DNS simulation, (bottom) µCT image, (c) top view of the complete model wire cloth structure

Table 2: Model parameters of the woven wire cloth filter medium, particles and fluid

Property	Unit	Value
Model size (L × W × H)	µm	320 × 320 × 802
Wire diameter d_W	µm	28
Pore size d_{Pore}	µm	32
Particle density ρ_P	kg·m^{-3}	2200
Particle diameter d_P of the generated fractions	µm	55
		63
		72
		83
		95
		109
Particle concentration c_n	m^{-3}	10^{11}
Pressure difference Δp	Pa	1000
Fluid density ρ	kg·m^{-3}	1000
Fluid viscosity μ	Pa·s	0.001

5 Results

5.1 Filtration resistances from experiments

The measure filtration data are described by the filtration curve according to the filtration Equation (2). The filter resistances (filter medium and specific filter cake resistance) are evaluated by the slope and y-intercept of the filtration curve. The slope of the graph reveals the experimental specific filter cake resistance of $r_{c,Exp}$ = 7.7·10^{10} m^{-2}, and the y-intercept of the graph yields the filter medium resistance to $R_{M,Exp}$ = 6.3·10^{7} m^{-1}. Because of the slightly varying pressure difference in the experiments, the pure filter medium resistance $R_{M0,Exp}$ values are obtained in the range between 2.1·10^{6} m^{-1} and 3.9·10^{6} m^{-1}.

5.2 Simulation of the filter cake formation

Figure 5 illustrates the instantaneous fluid velocities and particle positions obtained by the numerical computations. In Figure 5 (a) the filter medium model is shown before the particle generation. In Figure 5 (b) the calculated flow velocities and the initial particle positions are shown at the beginning of the filtration when the first particles are reaching the filter medium and the fluid passes through the filter medium. The local flow velocity maxima in the area of the pores can be seen. Accordingly, the time-dependent filtrate velocity in Figure 6 (a) shows a maximum before this point of time because of the minimum pressure loss that is determined only by the filter medium. In Figure 5 (c) it can be seen that some particles are already clogging the pores of the filter medium, which leads to the increase of the pressure drop and the resulting decrease of the filtrate volume flow at 3.9 ms in Figure 6 (a). In Figure 5 (d) the further filter cake formation process at the real time of 98 ms and filter cake height of 0.5 mm is shown.

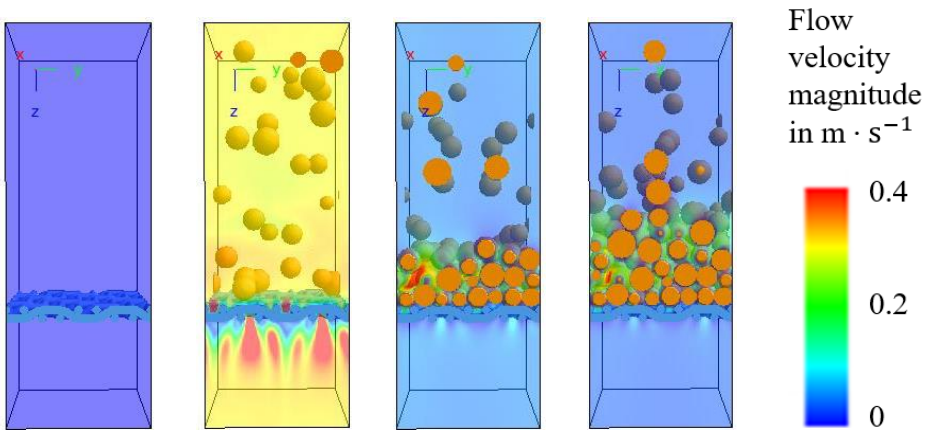

Figure 5: CFD-DEM simulation of the filtration process: (a) filter medium model, before the process starts at t = 0 ms, (b) first closing of pores by particles of suspension at t = 3.9 ms, (c) particles are retained by the filter medium t = 40 ms, (d) filter cake formation at t = 98 ms

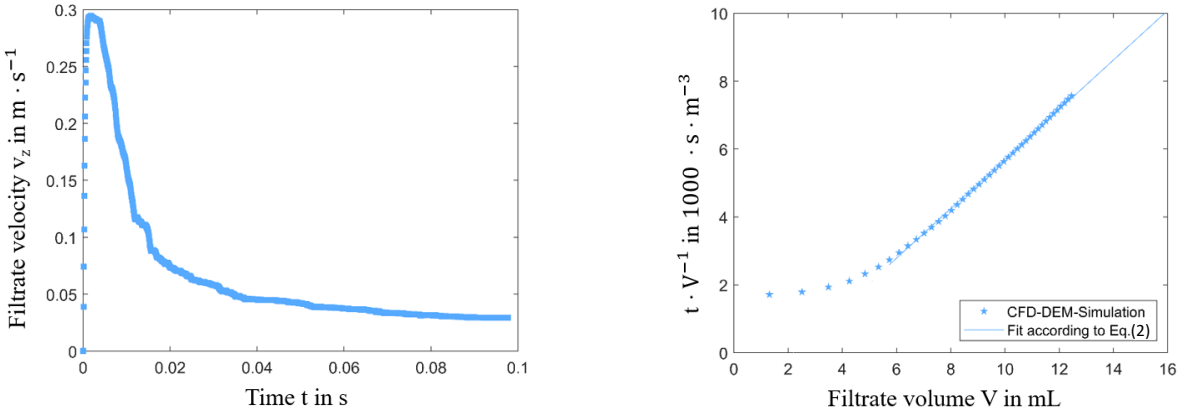

Figure 6: (a) Time-dependent filtrate velocity and (b) filter curve obtained with CFD-DEM simulation and described by filter equation in Equation (2)

After 98 ms of filtration, the filtrate velocity is nearly constant. Figure 6 (b) represents the simulation results concerning the time-dependent filtrate volume V in the form of the linear filter Equation (2). The graph within the first 2 mL of filtrate volume represents the pure fluid running through the medium. The resulting pure filter media resistance is $R_{M0,Sim}$ = 3.4·10^{6} m^{-1}. After the particle-free fluid flow through the filter, the slope of the curve increases and after 6 mL of filtrate volume becomes linear. When the linear section of the graph begins, the linear fit represents the specific filter cake resistance. The slope of it according to Equation (2) leads to the specific filter cake resistance of $r_{K,Sim}$ = 7.8·10^{10} m^{-2} (Figure 6 b).

5.3 Comparison of simulation and experiment

The results of the simulation describe the beginning of the filtration and filter cake formation. To compare with the experimental results (significant higher number of particles and higher filter cakes), the linear fit of the calculated filter curve was extended to the experimentally obtained filtrate volume. The experimentally obtained and calculated filter curves are compared in Figure 7.

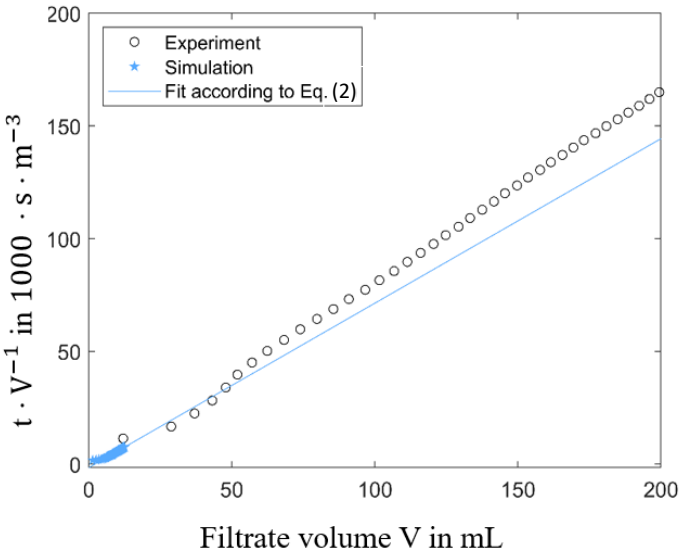

Figure 7: Comparison of experimentally obtained and calculated filtration curves

The fitted linear slope of the simulated filtration curve shows a good agreement with the experimental data. The specific filter cake resistance obtained with the simulation $r_{c,Sim}$ = 7.8·10^{10} m^{-2} matches the experimental value of $r_{c,Exp}$ = 7.7·10^{10} m^{-2}. The experimentally obtained values of $R_{M0,Exp}$ were in the range between 2.1·10^{6} m^{-1} and 3.9·10^{6} m^{-1}, which is in good agreement with the simulation results of $R_{M0,Sim}$ = 3.4·10^{6} m^{-1}.

6 Conclusions

In this work, a numerical model of the cake filtration process was developed based on the resolved coupling of CFD and DEM methods. This model describes the interactions between particles, particles with the filter medium, and particles with the flow due to the use of the Lattice-Boltzmann Method for solving the Navier-Stokes equations in a fine voxel grid.

The resulting filter medium and filter cake resistances from the cake filtration simulations are in good agreement with the results obtained by pressurized housing experiments. The simulation was performed only for the beginning of the filtration. This small period of time can hardly be obtained in experimental investigations, and the numerical investigations allow to resolve the micro processes between particles, medium and fluid during filter cake formation.

The performed comparison between 3D simulation and experimental investigation demonstrates a great potential of resolved CFD-DEM coupling for analyzing and optimizing cake filtration processes.

References

[1] S. Ripperger, W. Gösele, C. Alt, and T. Loewe (2013). Filtration, 1. Fundamentals. In Ullmann's Encyclopedia of Industrial Chemistry, (Ed.). 2013; pp. 1–38, ISBN 1435-6007, Wiley-VCH Verlag GmbH & Co. KGaA, Weinheim, Germany.

[2] S. Ripperger, W. Gösele, C. Alt, T. Loewe, Filtration, 1. fundamentals, Ullmanns Encycl. Ind. Chem. (2000) 1–38.

[3] A.P. Shapiro, R.F. Probstein, Random packings of spheres and fluidity limits of monodisperse and bidisperse suspensions, Phys. Rev. Lett. 68 (1992) 1422.

[4] R.Y. Yang, R.P. Zou, A.B. Yu, S.K. Choi, Pore structure of the packing of fine particles, J. Colloid Interface Sci. 299 (2006) 719–725.

[5] G.D. Scott, D.M. Kilgour, The density of random close packing of spheres, J. Phys. Appl. Phys. 2 (1969) 863.

[6] C. Tien, Granular Filtration of Aerosols and Hydrosols: Butterworths Series in Chemical Engineering, Butterworth-Heinemann, 2013.

[7] R.J. Wakeman, E.S. Tarleton, Filtration: equipment selection, modelling and process simulation, Elsevier, 1999.

[8] D. Hund, K. Schmidt, S. Ripperger, S. Antonyuk: Direct numerical simulation of cake formation during filtration with woven fabrics. Chemical Engineering Research and Design 2018, 139, 26–33, doi:10.1016/j.cherd.2018.09.023.

[9] P. Lösch, K. Nikolaus, S. Antonyuk: Fractionating of finest particles using cross-flow separation with superimposed electric field. Separation and Purification Technology 2021, 257, 117820, doi:10.1016/j.seppur.2020.117820.

[10] M. Kerner, K. Schmidt, A. Hellmann, S. Schumacher, M. Pitz, C. Asbach, S. Ripperger, S. Antonyuk: Numerical and experimental study of submicron aerosol deposition in electret microfiber nonwovens. Journal of Aerosol Science 2018, 122, 32–44, doi:10.1016/j.jaerosci.2018.05.004.

[11] Hosseini, S.A.; Tafreshi, H.V. 3-D simulation of particle filtration in electrospun nanofibrous filters. Powder Technology 2010, 201, 153–160, doi:10.1016/j.powtec.2010.03.020.

[12] Cundall, P.A.; Strack, O.D.L. A discrete numerical model for granular assemblies. Géotechnique 1979, 29, 47–65, doi:10.1680/geot.1979.29.1.47.

[13] Pöschel, T.; Schwager, T. Computational granular dynamics: Models and algorithms; Springer: Berlin, Germany, 2005, ISBN 9783540277200.

[14] Qian, F.; Huang, N.; Lu, J.; Han, Y. CFD–DEM simulation of the filtration performance for fibrous media based on the mimic structure. Computers & Chemical Engineering 2014, 71, 478–488, doi:10.1016/j.compchemeng.2014.09.018.

[15] Vångö, M.; Pirker, S.; Lichtenegger, T. Unresolved CFD–DEM modeling of multiphase flow in densely packed particle beds. Applied Mathematical Modelling 2018, 56, 501–516, doi:10.1016/j.apm.2017.12.008.

[16] Joseph, G.G.; Zenit, R.; Hunt, M.L.; Rosenwinkel, A.M. Particle–wall collisions in a viscous fluid. Journal of Fluid Mechanics 2001, 433, 329–346, doi:10.1017/S0022112001003470.

[17] Deshpande, R. Investigation of the Filter Cake Formation Process using DEM-CFD Simulation with Experimentally Calibrated Parameters; Fraunhofer Verlag: Stuttgart, 2019, ISBN 3839615194.

[18] Deshpande, R., Antonyuk, S., Iliev, O.: Study of the filter cake formed due to the sedimentation of mono and bi-dispersed particles using DEM-CFD simulations, AIChE Journal 65, (2019) 4, 1294-1303 https://doi.org/10.1002/aic.16529

[19] Heuzeroth, F.; Fritzsche, J.; Werzner, E.; Mendes, M.A.A.; Ray, S.; Trimis, D.; Peuker, U.A. Viscous force — An important parameter for the modeling of deep bed filtration in liquid media. Powder Technology 2015, 283, 190–198, doi:10.1016/j.powtec.2015.05.018.

[20] Krause, M.J.; Klemens, F.; Henn, T.; Trunk, R.; Nirschl, H. Particle flow simulations with homogenised lattice Boltzmann methods. Particuology 2017, 34, 1–13, doi:10.1016/j.partic.2016.11.001.

[21] Cook, B.K.; Noble, D.R.; Williams, J.R. A direct simulation method for particle-fluid systems. Engineering Computations (Swansea, Wales) 2004, 21, 151–168, doi:10.1108/02644400410519721.

[22] Kuruneru, S.T.W.; Marechal, E.; Deligant, M.; Khelladi, S.; Ravelet, F.; Saha, S.C.; Sauret, E.; Gu, Y. A Comparative Study of Mixed Resolved–Unresolved CFD-DEM and Unresolved CFD-DEM Methods for the Solution of Particle-Laden Liquid Flows. Archives of Computational Methods in Engineering 2019, 26, 1239–1254, doi:10.1007/s11831-018-9282-3.

[23] Rettinger, C.; Rüde, U. A coupled lattice Boltzmann method and discrete element method for discrete particle simulations of particulate flows. Computers & Fluids 2018, 172, 706–719, doi:10.1016/j.compfluid.2018.01.023.

[24] Gervais, P.-C.; Bémer, D.; Bourrous, S.; Ricciardi, L. Airflow and particle transport simulations for predicting permeability and aerosol filtration efficiency in fibrous media. Chemical Engineering Science 2017, 165, 154–164, doi:10.1016/j.ces.2017.03.002.

[25] Golshan, S.; Sotudeh-Gharebagh, R.; Zarghami, R.; Mostoufi, N.; Blais, B.; Kuipers, J.A.M. Review and implementation of CFD-DEM applied to chemical process systems. Chemical Engineering Science 2020, 221, 115646, doi:10.1016/j.ces.2020.115646.

[26] H. Hertz, Über die Berührung fester elastischer Körper, Journal für die reine und angewandte Mathematik (1881) 156–171.

[27] R.D. Mindlin, H. Deresiewicz, Elastic Spheres in Contact under Varying Oblique Force, Journal of Applied Mechanics (1953) 327–344.

[28] Y. Tsuji, T. Tanaka, T. Ishida, Lagrangian numerical simulation of plug flow of cohesionless particles in a horizontal pipe, Powder Technology 71 (1992) 239–250.

[29] Verein Deutscher Ingenieure e.V. VDI 2762: Filtrierbarkeit von Suspensionen Bestimmung des Filterkuchenwiderstands. VDI Richtline. VDI-Handbuch Verfahrenstechnik und Chemieingenieurwesen, Band 5: Spezielle Verfahrenstechniken, Verein Deutscher Ingenieure e.V., Düsseldorf, Germany, 2010.

[30] Hund, D.; Lösch, P.; Kerner, M.; Ripperger, S.; Antonyuk, A. CFD-DEM study of bridging mechanisms at the static solid-liquid surface filtration. Powder Technology 2020, 600–609, doi:10.1016/j.powtec.2019.11.072.

[31] Puderbach, V., Schmidt, K., Antonyuk, S.: A coupled CFD-DEM model for resolved simulation of filter cake formation during solid-liquid separation, Processes 9 (2021) 5, 826; https://doi.org/10.3390/pr9050826.

[32] DNSLab®, URL: https://www.it4e-gmbh.com/dnslab-uebersicht/

[33] Kerner, M., Schmidt, K., Schumacher, S., Asbach, C., Antonyuk, S.: Ageing of electret filter media due to deposition of submicron particles - experimental and numerical investigations, Separation and Purification Technology 251 (2020) 117299 doi: 10.1016/j.seppur.2020.117299

Author

Prof. Dr.-Ing. Sergiy Antonyuk
Technische Universität Kaiserslautern
Institute of Particle Process Engineering
Postfach 3049
67653 Kaiserslautern
Tel.: +49 (0)631 205 3524
Fax: +49 (0)631 205 3055
e-mail: sergiy.antonyuk@mv.uni-kl.de
Web: www.uni-kl.de/mvt

Experimental investigation of capillary collapse of partially saturated granular materials

Nicole Hüsener, Jürgen Grabe

Abstract: The capillary collapse is an irreversible reduction in volume of partially saturated soils caused by the provision of water at essentially unchanging total vertical stress. Despite extensive research, however, the processes involved are still not fully understood and will therefore be investigated in more detail as part of the project. As a special characteristic of opencast mining soils, which are particularly at risk of capillary collapse in Germany, the influence of porous lignite particles will be investigated. For this purpose, the structure of the lignite particles is also examined at the micro level with the help of scanning electron microscopy. In addition, by varying the initial water content, the relationship between the water content near the optimum condition and the collapse potential will be analysed.

1 Introduction

1.1 Partially saturated soil behaviour: capillary cohesion and capillary collapse

Since the hydraulic and mechanical behaviour of partially saturated soils is significantly influenced by capillary effects, they behave differently than in a dry or water-saturated state. Through friction, the capillary pressure in unsaturated soils can lead to an increase in shear strength independent of external loads, which contributes significantly to the cohesion of the grain structure. Since this so-called capillary cohesion results from matric suction, it disappears in both dry and saturated conditions and is therefore also referred to as *„apparent cohesion“*. In the case of an increasing degree of saturation, there is a risk of loss of stability due to the increasing dissolution of the capillary bridges, especially in the case of loosely bedded soils. This is often associated with a sudden rearrangement of the grain structure, which is also referred to as capillary collapse and, under the appropriate conditions, can lead to sometimes very large settlements of a soil, which are also known as sagging.

In addition to the reduction or loss of capillary cohesion, other factors such as the dissolution of solid bridges and cementation, e.g. in the form of crystallised salts, can also be involved in the collapse process. These can additionally stabilise the grain structure via the formation

of cohesive aggregates. Upon contact with water, however, these bonds gradually dissolve, a multitude of freely moving particles instead of aggregates is formed and the contact surfaces change. The velocity of the collapse process depends largely on the nature of the bonds. In the case where the cohesion of the grain structure is based only on capillary forces, the collapse occurs immediately, whereas, in the case of chemical cementation, the addition of water leads to delayed collapse settlements. However, in sandy soils, solid bonds usually play only a minor role (Al-Rawas, 2000; Grimmer, 2006).

1.2 Soils at risk and influencing factors

Collapsible soils can occur both naturally and as a result of human activities and are found worldwide, especially in arid and semi-arid regions. As collapsible soils are a major geotechnical and civil engineering problem, geotechnical engineers are confronted with multiple challenges when dealing with this type of soil (Al-Obaidi, 2014). Capillary collapse is a complex process that is influenced by a variety of soil physical and external boundary conditions. In general, however, some basic conditions must be met for a soil to be at risk of capillary collapse.

External influencing factors include the initial water content and history of water content changes, the degree of compaction or bulk density, as well as external loading and stress history. The main factor responsible for capillary collapse is the presence of a metastable, inadequately compacted soil structure that could be subjected to further compaction in the case of water ingress. Any initial compaction reduces the volume of air-filled macropores and thus reduces the collapse potential. The potential settlements are therefore lower the higher the initial bulk density is. External loads lead to a compaction of the soil and thus also reduce the collapse potential. The degree of compaction of the soil at a given load is also influenced by the water content. A higher initial water content leads to a significant reduction of the collapse potential, as does repeated saturation. The largest settlements therefore occur at the first ingress of water and, in the case of sands, usually develop within a few minutes (Woźniak, 2015; Al-Rawas, 2000; Grimmer, 2006). Particularly worth mentioning in this context are partially saturated, loosely bedded, sandy soils, in which the stabilising capillary bridges allow larger void ratios than the maximum void ratio $e_{\max}$ determined experimentally on dry soils in its loosest state (Milatz et al., 2021).

In addition to the external factors, there are is a number of soil physical parameters that control the type of soil and its susceptibility to capillary collapse. Besides the type of bonding already described, these include factors such as the spatial arrangement and size of the grains and pores, the uniformity coefficient as well as the grain shape and water permeability. In general, the risk of capillary collapse increases with decreasing uniformity coefficient and grain diameter as well as increasing sphericity/circularity coefficient (Woźniak, 2015; Grimmer, 2006). While there is partly contradictory information in the literature on some other factors such as wetting rate, other factors such as the influence of irrigation direction (from above/below) have been insufficiently studied so far. In summary, however, it can be said that partially saturated soils with a low water content or degree of saturation and a metastable, loose bedding are particularly at risk of capillary collapse. These include in particular aeolian, colluvial and alluvial deposits, loess soils and residual soils, but also loose fills (Al-Rawas, 2000).

1.3 Special risk of capillary collapse of opencast mine dump soils

Opencast mine dump soils are a special case among engineered fills, which are essentially uncontrolled overburden fills from opencast mining. The lignite mining process destroys the original, natural structure of the soil and different soils are randomly mixed together. In consequence, dump soils are lithologically diversified and have a highly porous, unstable structure and unstable physical-mechanical properties. In addition, the soil can be subjected to various alterations and transformations as a result of external influences. For example, dump soils almost always contain residual particles of the extracted raw materials, such as lignite, which come into contact with air for the first time in the course of the extraction process. This can trigger chemical and/or biological transformation processes that can significantly change the structure and properties of the soil and the pore water as well as the hydraulic-mechanical behaviour of the soil. Compared to the already relatively well-understood collapse settlements of natural soils and construction fills, opencast mine dump soils have been insufficiently studied so far (Woźniak, 2015). For example, it is still unclear how the lignite particles contained in opencast mine dump soils affect collapse behaviour.

In general, opencast mine dump soils are only exposed to low external loads due to the sparse building development, which means that the technically conditioned loose bedding remains preserved in most cases. Although the bulk density increases with depth due to the soil's weight, the upper layers remain at high risk of capillary collapse. During ongoing opencast mining operations, large-scale lowering of the groundwater level down to great depths is required. This results in another risk factor after closure, as a particularly large re-rise of the groundwater level is to be expected then, which is very problematic with regard to capillary collapse. Capillary collapse is also conceivable as a result of water infiltration from above, e.g. due to rainfall events or agricultural use, as the case study presented by Hou et al. (2019) impressively shows using the example of a loess soil.

2 Materials and methods

2.1 Tested materials

The investigated soil is a dump soil from the Lusatia region, which is derived from the overburden of opencast lignite mining. In order to ensure the representativeness of the investigated soil specimens in small-scale computed tomography experiments, all particles with a diameter larger than or equal to 2 mm were removed by sieving. The grain size distributions of the natural opencast mine dump soil as well as the model soil obtained by sieving are shown in Figure 1. The proportion of lignite particles and their particle size distribution were determined by loss on ignition. The result was a very low content of only 0.26 wt%. The composition of the total lignite content from particles of the different grain size fractions can be found in Table 1. It should be noted that the proportion of fine lignite particles smaller than 0.063 mm could only be determined by back calculation, which is why their particle size distribution is not known.

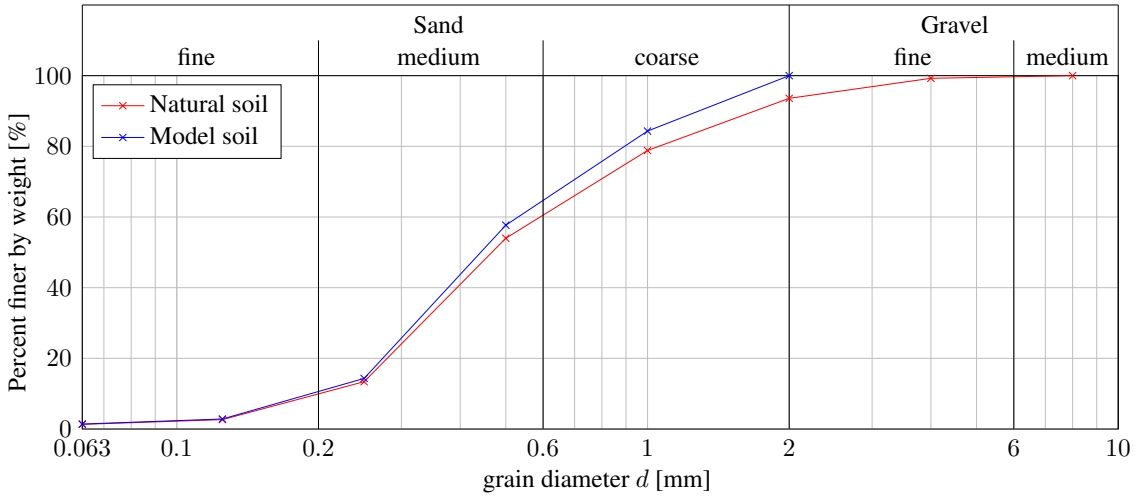

Figure 1: Grain size distribution of the natural, untreated soil (red) and the model soil (blue)

Table 1: Composition of the total lignite content from particles of the different grain size fractions

grain size fraction [mm]	respective lignite proportion [wt%]
< 0.063	52.41
$0.063 \leq x < 0.125$	4.88
$0.125 \leq x < 0.25$	12.27
$0.25 \leq x < 0.5$	15.17
$0.5 \leq x < 1.0$	10.05
$1.0 \leq x < 2.0$	5.22

It was found that the fine lignite particles with a diameter below 0.063 mm account for more than half of the total lignite content, while the proportion of medium-sized grain diameters of the lignite particles between 0.125 mm and 1 mm is relatively similar and lies approximately between 10 and 15 %. Since the influence of lignite particles on the collapse behaviour is still unknown, a variant without organic components was investigated in addition to the model soil. The most important properties of the investigated sample variations are summarised in Table 2.

Table 2: Properties of tested materials

Parameter	ρ_s	$e_{\min}$	$e_{\max}$	$d_{\min}$	$d_{\max}$	d_{50}	d_{10}
Unit	[g/cm^3]	[-]	[-]	[mm]	[mm]	[mm]	[mm]
Opencast mine dump soil	2.607	0.517	0.782	0	< 8.0	0.4650	0.2175
Model soil	2.609	0.472	0.754	0	< 2.0	0.4404	0.2100
Model soil without organics	2.604	0.445	0.716	0	< 2.0		

In order to investigate whether there are differences between coarse and fine lignite particles in their influence on the behaviour of the soil, a further soil variation without fine particles and another variant without fines and lignite, which thus consists solely of sand grains, are also investigated. Furthermore, a glass bead packing (soda-lime glass SiLibeads type S / type Solid,

manufactured by Sigmund Lindner GmbH, Germany) with a grain size distribution similar to the model soil is also examined. With the help of the comparative experiments on almost ideally round glass beads, it is not only possible to draw conclusions about the influence of the grain shape, but the results obtained will also allow easier validation and (further) development of numerical models in the future, whose range of application has so far been limited to spherical particles. However, these additional model soils are not addressed in this paper.

2.2 Laboratory single oedometer tests

A wide range of methods and classification criteria are available for identifying and classifying soils that may be at risk of capillary collapse (Al-Rawas, 2000; Grimmer, 2006), with many methods based on oedometer tests. A basic distinction is made between so-called *single* and *double oedometer tests*. The procedure for the more common single oedometer tests is described in the international standard ASTM D5333-03:2003 and enables a comparison of the collapse index I_e or the collapse potential I_c of different soils under standardised boundary conditions. The soil sample is installed with its natural water content as well as a defined bulk density, loaded stepwise (load increments: 5 kPa seating stress for 5 minutes, 12, 25, 50, 100 and 200 kPa for one hour respectively) and then the settlement after saturation in one step is measured after 24 hours. The collapse index or collapse potential is defined as the relative magnitude of soil collapse determined at 200 kPa (collapse index) or at any stress level (collapse potential) according to equation 1. The classification is then carried out based on the limits listed in Table 3 (ASTM D5333-03:2003).

$$I_c = \left[\frac{\Delta e_c}{1 + e_0}\right] \cdot 100 \quad [\%] \qquad (1)$$

where:

Δe_c = change in void ratio due to wetting [-],
e_0 = initial void ratio at seating stress [-]

Table 3: Classification of Collapse Index

Degree of specimen collapse	Collapse Index I_e [%]
None	0
Slight	0.1 - 2.0
Moderate	2.1 - 6.0
Moderately severe	6.1 - 10.0
Severe	> 10

A common hypothesis regarding collapsible soils is that soils with a water content below the optimum (*dry of optimum condition*), i.e. below the so-called critical degree of saturation, are collapsible, while soils with a higher water content are assumed to show almost no collapse settlement when saturated. To examine this hypothesis, the optimum water content of the soil is first determined using the Proctor test. Then, in an experimental series, three different initial water contents (one below the determined optimum in the water content range typical for collapsible soils of less than 10 %, the optimum water content and another above the optimum) will be investigated.

2.3 Scanning electron microscopy (SEM)

The scanning electron microscope (SEM) is a versatile measuring instrument for analysing the surface structure and surface material of solid samples. However, in contrast to conventional light microscopy, the image formation is not achieved by optical imaging but by point-by-point object scanning with a finely focused electron beam and the resulting locally triggered interaction processes (formation of secondary and back-scattered electrons). The emitted secondary and back-scattered electrons are captured by detectors and converted into an image via the intensity of the signals. The examination of the samples takes place in a high vacuum (airless space) because the presence of other materials such as air in the specimen column would also lead to undesired interactions with the electrons and thus reduce the image quality. To avoid local electrostatic charges in the specimens, conductive metal layers (e.g. gold) are sometimes vapour-deposited after prior structure-preserving drying to increase electrical conductivity (Bauch, 2017). Scanning electron microscopy was used to investigate the microstructure or surface structure of the lignite particles naturally occurring in opencast mine dump soils.

2.4 X-ray computed tomography (CT)

Numerous studies showed that the microstructure is a key factor in the collapse process (Li et al., 2016). But for a long time, adequate methods were lacking to investigate the structure and influence of the microstructure in more detail. However, with the application of newer technologies such as computed tomography (CT) in geotechnical engineering, it is now possible to gain increasing insight into the microscopic processes. Computed tomography is a non-destructive method for the three-dimensional visualization of the internal and external structure of objects, which was originally developed for medical applications. The principle is based on the material- and path-length-dependent attenuation of X-rays as they penetrate objects. By superimposing 2D X-ray images of the sample from different angles, usually by stepwise rotation of the sample, a 3D image of the object is reconstructed using mathematical algorithms. Absorption-specific gray-scale images are obtained, which allow different materials to be distinguished based on their density through different intensities (Bauch, 2017).

With the help of in-situ CT examinations, it is possible not only to capture momentary images, but also to examine changes in the specimen under changing boundary conditions over the course of several successive scans. In geotechnical engineering, the use of CT in this way enables the investigation of soil mechanical and hydraulic processes at grain scale. First CT studies on the collapse process in sandy soils were carried out by Bruchon et al. (2013), Moscariello, Salager et al. (2016) and Moscariello, Cuomo et al. (2018). More comprehensive insights into the processes occurring during capillary collapse at the micro level are given by Bruchon (2014). Metallic objects within the examined specimen, as they can be contained in soils, for example via metal oxides in individual sand grains, lead to the formation of star-shaped artefacts in the area of the metallic object in computed tomography, which significantly impair the image quality. In order to reduce the risk of such artefacts, all magnetic particles are therefore removed from the examined soil specimens with the help of a strong magnet before the start of the experiment.

3 Experimental results

3.1 Laboratory single oedometer tests

Performing the single oedometer tests, it became apparent relatively early on that there was a large scatter in the results. This can be attributed to several effects that may overlap each other. Even with the same void ratio and bulk density obtained through the use of defined sample quantities and volumes, the microstructure created during specimen preparation can only be controlled to a limited extent, but has a major influence on the collapse behaviour. Also, different settlements due to the initial seating stress of 5 kPa strongly influence the results, as the corresponding specimen height serves as a reference for determining the collapse potential. Despite initially uniform void ratios and bulk densities prior to application of the seating stress, the bases for determining the collapse potential are therefore often different. Accordingly, it is recommended to always carry out several tests per investigated scenario in order to estimate the scatter range and to better assess the associated collapse potential.

Within the scope of this paper, three individual tests were carried out, of which the average results were analysed. Overall, despite the low lignite content, the lignite-containing soil showed significantly more pronounced settlement under load than the variation without organic content for all three water contents investigated (cf. Figure 2). A clear influence of the irrigation direction, on the other hand, does not seem to be recognisable, since with the exception of the curve of the model soil when irrigated from below with an initial water content of 16 %, the results for both irrigation directions are close to each other. Therefore, further investigations seem to be necessary here.

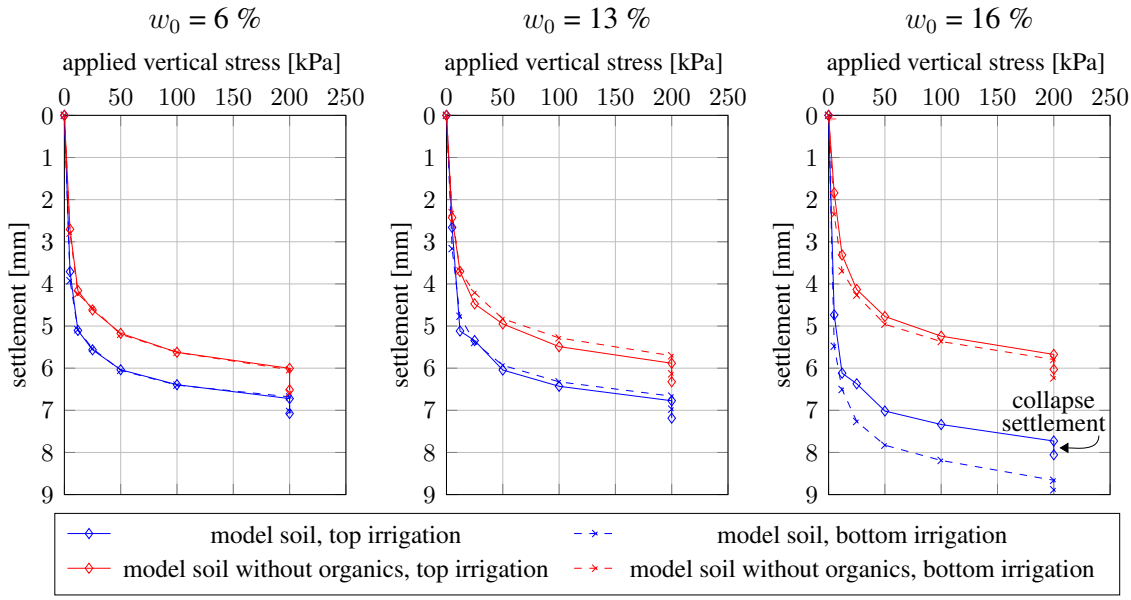

Figure 2: Compression curves of the Collapse Potential Test for three different initial water contents, left: 6 %, centre: 13 %, right: 16 %

At first glance, the collapse settlements for both variations of the model soil (with and without lignite) appear to be relatively similar. Since these are crucial for the calculation of the associated collapse potential, one could assume that higher collapse potentials should result for the model soil containing lignite due to the higher total settlements. Therefore, first, the collapse settlements are determined for all investigated variations (cf. Figure 3, left). In contrast to the settlements under load, however, the larger collapse settlements occurred for the soil without organic components. While the lignite particles lead to greater soil settlement under vertical loading, they appear to attenuate collapse settlements and thus lead to a discernible change in the hydraulic-mechanical behaviour of a soil, even with a small proportion. The lower collapse settlements due to irrigation result in lower collapse potentials for the lignite-containing model soil despite the higher total settlement (see Figure 3, right).

Overall, however, the collapse potential for both model soils and for both irrigation directions is low (< 3,2 %). This could also be due to the high vertical load of 200 kPa, which already leads to a significant compaction of the soil specimens before the actual irrigation. With an increase of the initial water content, a decreasing tendency of the collapse potential can be observed, whereby the collapse settlements and collapse potentials below the determined optimum water content are higher than with an initial water content above the optimum. The results, therefore, indicate a confirmation of the hypothesis on the influence of the optimal water content. Nevertheless, it would be interesting to investigate the collapse behaviour also for further initial water contents and for lower loads. Furthermore, the sample size should be increased to reduce the effect of the natural, relatively large scatter on the results.

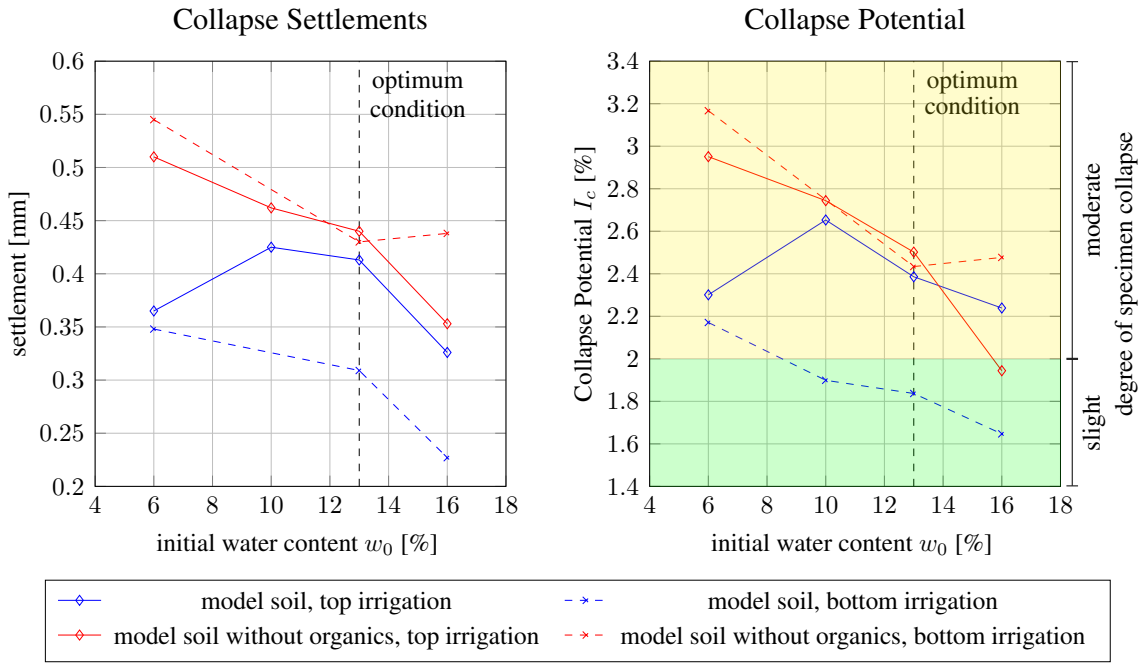

Figure 3: Development of the collapse settlements and the Collapse Potential of the model soil with organics (blue) and without organics (red) with increasing initial water content near the optimum condition

A major criticism of the conventional investigation of the collapse potential using single oedometer tests is based on the fact that the collapse potential is classically determined when the soil sample is saturated in only one step. However, under real conditions, as they are found in nature, saturation does not take place in only one step. Rather, in most cases it is a gradually progressing irrigation process, which cannot be correctly reproduced with the conventional investigation methods. In addition to the preceding classical oedometer tests, incremental wetting tests should therefore be carried out, which can provide results that are closer to reality.

The irrigation rate could also be a possible influencing factor that is not taken into account in the classical investigations, especially since the often very simple structures also do not allow for targeted regulation of the irrigation rate, so that no standardised boundary conditions are available with regard to the irrigation rate. Therefore a more detailed investigation of the possible influence of the irrigation rate on the collapse behaviour is planned for the future.

3.2 Scanning electron microscopy

Lignite is an organic sedimentary rock that is formed from dead plant material during the coalification process. Due to the low loading during the formation process, only a low consolidation takes place and a high water content remains, which gives lignite a highly microporous and micro-cracked structure. The lignite surface was examined using a scanning electron microscope at various magnifications (cf. Figure 4). It can be seen clearly that the lignite particles are highly inhomogeneous and that, in addition, the capillary structure often resembles the original plant substance. Both effects are a result of the incomplete and non-uniform conversion. Lignite, as a special case among coals, contains all pore sizes (ultra-micro-, micro-, meso- and macropores), whereby the largest specific surface area results from the micropores. Due to the microporosity and the colloidal character of the humic acids it contains, lignite is strongly hygroscopic and is usually present in an almost water-saturated condition (Lechner, 2012; Zimmermann, 2010).

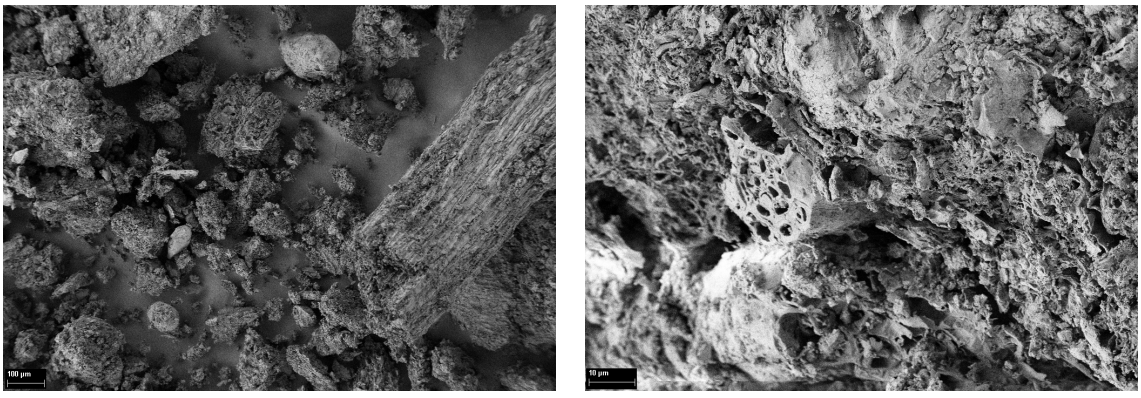

(a) (b)

Figure 4: SEM images of the lignite particles of the model soil 2 from investigations at the Electron Microscopy Unit (in German: *Betriebseinheit Elekronenmikroskopie, BeEM*) of the Hamburg University of Technology (TUHH). (a) magnification 200x, (b) magnification 2500x

3.3 X-ray tomography

In a first step, the structure of a lignite-containing soil at different degrees of saturation was examined in the micro-CT of the Institute of Biomechanics at the Hamburg University of Technology (TUHH). The bulk density was also varied in the process. However, it was shown that the jerky incremental rotation of the scanner leads to undesired particle movements when the sample is bedded loosely. This is not only problematic with regard to the quality of the images (blurred, out of focus), but also for the investigation of the collapse process itself, as the grain movements due to the sample rotation overlap with the sagging triggered by the capillary collapse and the cause of the individual particle movements can thus not be concluded. The scan duration is also extremely long compared to the small field of view (FoV) and the low resolution that can be achieved. The CT scanner used is therefore not suitable for in-situ CT investigations, which is why other CT devices with a slow, continuous rotation must be used for this purpose.

When processing the reconstructed CT data for further analyses, segmenting the lignite particles contained in the opencast mine dump soil as a single phase proved to be difficult. The reason for this problem is that their density is similar to that of water and the image data in computed tomography, as described above, are obtained based on density. However, as can be seen in Figure 5, with the help of various filters and other processing tools, it has already been possible to make the lignite particles visually recognisable even in the lower-quality micro-CT images.

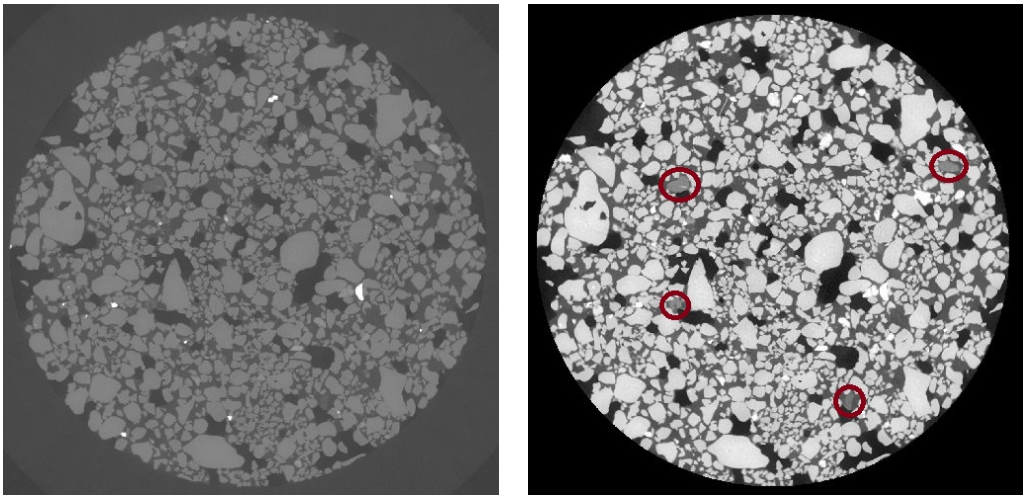

(a) (b)

Figure 5: Horizontal slices of X-ray CT image of lignite-containing soil 1 (a) raw image, (b) preprocessed image, with particles in the red circles = lignite particles

In order to be able to investigate the processes leading to capillary collapse at the micro scale, a miniaturised experimental set-up for in situ CT experiments was developed based on Milatz (2020). The sample irrigation is carried out through a porous filter stone and a filter paper via the specimen bottom and can be controlled with the help of a single-board computer (Raspberry Pi), which drives a syringe pump. Both the added water volumes and the irrigation rate can be regulated very precisely. The experimental set-up is shown schematically in Figure 6 and has already been successfully tested under laboratory conditions.

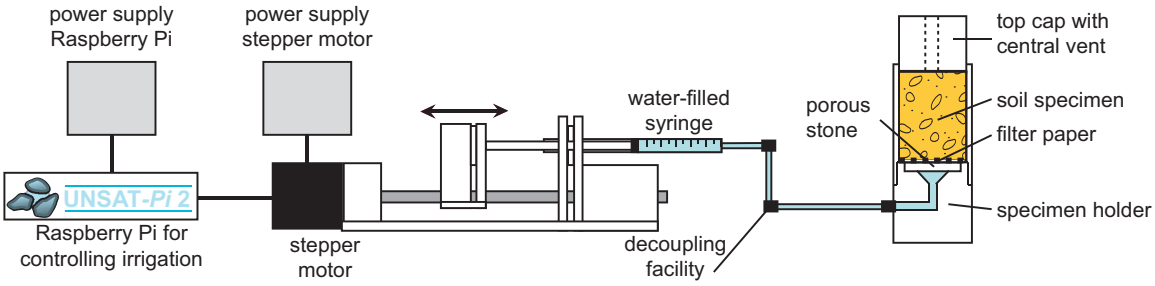

Figure 6: Schematic illustration of the experimental set-up for miniaturised wetting collapse experiments

During a three-day measurement period (26.03.–29.03.2021) at the Institut Laue-Langevin (ILL) in Grenbole, France, first insights into the processes taking place at the micro scale could be gained (Hüsener et al., 2021). A special feature here is the parallel/combined X-Ray CT and neutron tomography, as the neutrons are water-sensitive and thus can increase the phase contrast at initially low water content. However, an alternative sandy soil (Hostun Sand) and a different experimental set-up were used in the experiments. Therefore, further experiments with the presented miniaturised set-up on the model soils investigated in the project, which were obtained from an opencast mine dump soil, are planned for the future.

4 Summary and Outlook

In this study, a model soil obtained from a natural dump soil of opencast lignite mining was first characterised in terms of soil mechanics, the grain structure was investigated in CT and the surface structure of the coal particles contained was examined at the micro scale with the aid of scanning electron microscopy. Subsequently, so-called single oedometer tests were carried out on two soil variations (one with and one without lignite particles) according to the ASTM D5333-03 standard, which allow the collapse potential of a soil to be determined and compared under standardised boundary conditions. The widely accepted hypothesis that especially soils at dry of optimum condition are collapsible seemed to be confirmed for both model soils. Interestingly, lower collapse potentials were found for the lignite-containing soil despite larger total settlements. This is due to the fact that the presence of coal particles led to reduced collapse settlements upon wetting, while larger settlements occurred under load. Although tendencies could be clearly identified, the large scatter range is to be criticised, so that further tests should be carried out in the future. Since the lignite particles already seem to strongly influence the hydraulic-mechanical behaviour of a soil, even at a low proportion, this should be investigated in more detail. Variations in the load applied before irrigation are conceivable here, for example. Since the triggering microscopic processes are still not fully understood, a miniaturised experimental setup was developed and presented, which in future will allow in situ CT experiments and thus insights into grain kinematics during the collapse process at the micro level.

References

[1] Al-Obaidi A. (2014): Hydro-Mechanical Behaviour of Collapsible Soils. Schriftenreihe des Lehrstuhls für Grundbau, Boden- und Felsmechanik der Ruhr-Universität Bochum, Heft 54

[2] Al-Rawas A. (2000): State-of-the-Art-Review of Collapsible Soils. *Sultan Qaboos University Journal for Science [SQUJS]*, 5:115–135

[3] ASTM D5333-03 (2003): Standard Test Method for Measurement of Collapse Potential of Soils. American Society for Testing and Materials

[4] Bauch J. (2017): Physikalische Werkstoffdiagnostik: Ein Kompendium wichtiger Analytikmethoden für Ingenieure und Physiker, Berlin: Springer Vieweg

[5] Grimmer S. (2006): Sackungsprozesse in natürlichen Lockergesteinsfolgen infolge Grundwasserwiederanstiegs. Mathematisch-Naturwissenschaftlich-Technische Fakultät der Martin-Luther-Universität Halle-Wittenberg

[6] Hou X., Vanapalli S. K. and Li T. (2019): Wetting-induced collapse behavior associated with infiltration: A case study. *Engineering Geology*, 258

[7] Hüsener N., Helfen L., Milatz M. and Tengattini, A. (2021): Combined X-ray- and neutron-tomography imaging of capillary collapse in unsaturated granular soils. Institut Laue-Langevin (ILL)

[8] Milatz, M. (2020): An automated testing device for continuous measurement of the hysteretic water retention curve of granular media. *Acta Geotechnica*, 56:2239–2257

[9] Milatz M., Hüsener N., Andò E., Viggiani G. and Grabe J. (2021): Quantitative 3D imaging of partially saturated granular materials under uniaxial compression. *Acta Geotechnica*, 16:3573–3600

[10] Wożniak H. (2015): Collapse settlement of dump soils revealed by studies on soil samples of modelled lithology and lump-size distribution. *Geological Quarterly*, 59.

Author

Nicole Hüsener
Hamburg University of Technology (TUHH)
Institute of Geotechnical Engineering and Construction Management
Harburger Schloßstraße 36
21079 Hamburg
Tel.: +49(0)40/42878-4668
Fax: +49(0)40/42878-3721
e-mail: nicole.huesener@tuhh.de
Web: www.tuhh.de/gbt

Univ.-Prof. Dr.-Ing. Jürgen Grabe
Hamburg University of Technology (TUHH)
Institute of Geotechnical Engineering and Construction Management
Harburger Schloßstraße 36
21079 Hamburg
Tel.: +49(0)40/42878-3762
Fax: +49(0)40/42878-3721
e-mail: grabe@tuhh.de
Web: www.tuhh.de/gbt

Micromechanical insights into the capillary collapse of granular materials

Jean-Michel Pereira

Abstract: This communication focusses on the role played by the microstructure on the behaviour of unsaturated granular materials. First, we present an experiment where the collapse of a sand specimen under oedometric conditions and subjected to wetting while being 3D scanned using X-ray computed tomography. X-ray CT combined with Digital Image Correlation allowed us to track the deformation and changes in water content that occurred within the specimen during wetting. Despite a strong heterogeneity observed at the local scale, the behaviour at the scale of the REV is found to be fully consistent with the average behaviour observed at the scale of the specimen itself. Then, different modelling strategies that account for microscale features of the material are discussed, including effective stress approaches at the continuum scale and numerical techniques considering the particle level.

1 Wetting-induced collapse of a loose sand

Wetting experiments have been performed on an unsaturated sand specimen in an oedometer cell (70 mm diameter). Specifically, Hostun sand has been used (reference HN31, median grain size d_{50} of 300 μm, coefficient of uniformity C_u of 2). In order to ease the post-treatment process, the reference sand has been sieved to remove the smallest grains (cut-off at 250 μm). The sand has been mixed with water at a water content of $w = 7.2\ \%$ and then placed in an oedometric cell using a pluviation device. The capillary pressure in the specimen has been controlled using the negative water column technique and reduced in steps to perform the imbibition.

X-ray CT scans have been acquired on two different length scales (full specimen and smaller region of interest in the centre of the specimen) at each imbibition step. For each scan, 1,440 projections have been recorded during the 360-degree rotation of the specimen. The local scans have been segmented considering two phases only: voids on one hand and the mixture of sand and water on the other hand. These local scans have been used to compute the local water content and deformation of the specimen.

The strain and water content fields have been evaluated using DIC and also the evolution of grey levels (for changes in water content). The results are shown in Figure 1. It can be observed that strains and water content are heterogeneously distributed within the specimen, this heterogeneity increasing with the imbibition steps. However, it has been shown that the macroscopic behaviour

has been consistent with the local one, with relationships between the main quantities of interest (deformation, water content, and capillary pressure) following similar trends at both scales.

The microstructure of the specimen has been further investigated using segmented images. It has been concluded that the preparation procedure induced the presence of sand-water clusters with two families of pores: one within these clusters and one between them. This initial microstructure is responsible for the subsequent behaviour when the specimen has been subjected to wetting. In fact, the collapse became perceptible at the macroscopic scale when water filled the small pores within the clusters and when the latter started to merge.

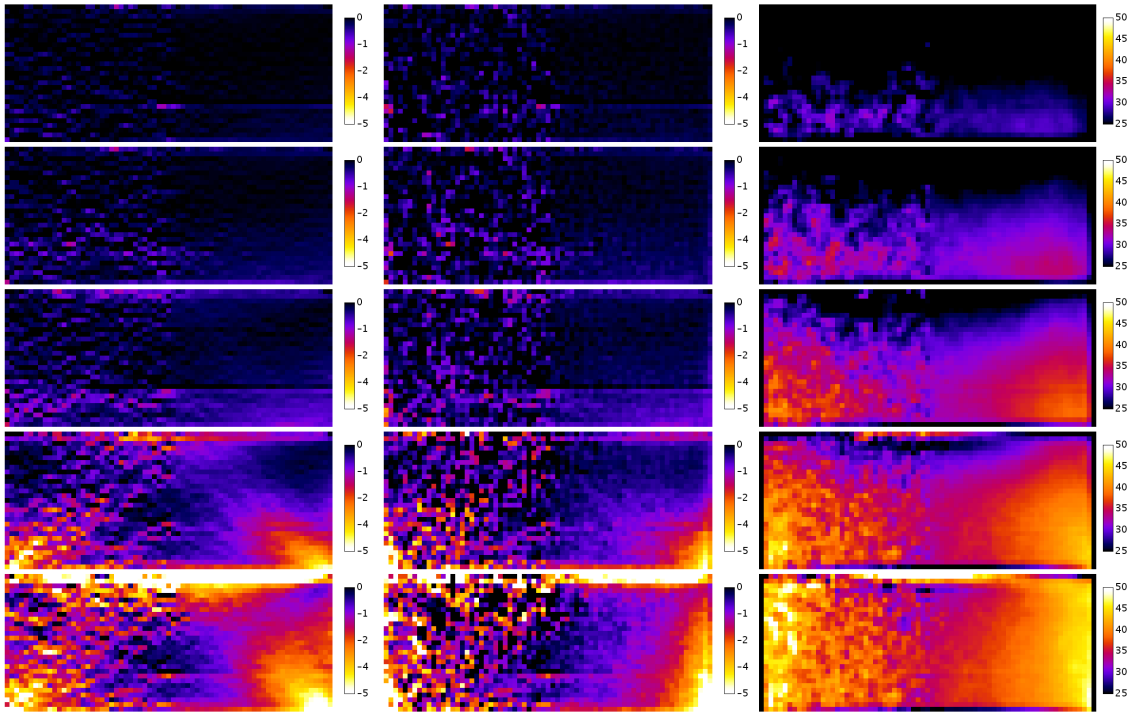

Figure 1: Maps of vertical strains (left), volumetric strains (centre) and water content (right) at various imbibition steps (from top to bottom rows). Each map is made of a half vertical slice in the xz plane (left half of the map) and a radial-average (right half of the map). Scale of color bars is percentage values. The central vertical axis of the maps and the central axis of the specimen coincide. Picture from (Bruchon et al., 2013)

2 Microstructure and modelling

The influence of the microstructure of geomaterials, from granular to fine ones, has finally been discussed in a modelling framework. On the continuum scale, the definition of a microstructurally based effective stress for unsaturated soils, following (Alonso et al., 2010) and (Niu et al., 2021), is presented, and its links to microstructural features (mainly Pore Size Distribution) are

discussed. Other modelling strategies are finally presented, considering the scale of particles and the presence of water menisci that affect the intergranular forces (Than et al., 2017).

Acknowledgments

The author would like to express his deepest gratitude to M. Bornert, J.-F. Bruchon, S. Brisard, Y. J. Cui, P. Delage, M. H. Khalili, N. Lenoir., J. Muñoz-Castelblanco, G. Niu, J.-N. Roux, I. Stefanou, A. M. Tang, V. D. Than, and M. Vandamme who immensely contributed to the work presented here.

References

[1] Alonso E. E., Pereira J. M., Vaunat J. and Olivella S. (2010): A microstructurally based effective stress for unsaturated soils. *Géotechnique*, 60(12):913–925

[2] Bruchon J.-F., Pereira J. M., Vandamme M., Lenoir N., Delage P. and M. Bornert. (2013): Full 3D investigation and characterisation of capillary collapse of a loose unsaturated sand using X-ray CT. *Granular Matter*, 15(6):783–800.

[3] Niu G., Cui Y.-J., Pereira J. M., Shao L. and Sun D. (2021): Determining Bishop's parameter χ based on pore size distribution. *Géotechnique Letters*, 11(1):1–28

[4] Than V. D., Khamseh S., Tang A. M., Pereira J. M., Chevoir F. and Roux J.-N. (2017): Basic mechanical properties of wet granular materials: a DEM study. *Journal of Engineering Mechanics*, 143(1):C4016001

Author

Prof. Dr.-Ing. Jean-Michel Pereira
Laboratoire Navier
Ecole des Ponts, Univ Gustave Eiffel, CNRS
6-8 avenue Blaise Pascal
77420 Champs-sur-Marne
France
Tel.: +33 (0)1 64 15 35 48
e-mail: jean-michel.pereira@enpc.fr
Web: https://navier-lab.fr/

Imbibition and Wetting Front Broadening in Mesoporous Silica Glass

Juan Sanchez, Laura Gallardo, Yannick Tetzner, Pouyan Sadeghian, Johannes Gäding, Robert Meißner and Patrick Huber

Abstract: We explore the capillary rise of water in hydrophilic mesoporous silica glass (Vycor glass) and demonstrate that classical hydrodynamics still provide accurate flow rate predictions at pore scales of about 10 nm diameter, if we assume a reduction of the effective pore size due to the presence of monolayers of water molecules strongly bounded to the pore walls. A detailed parametrization of the pore geometry and wetting conditions is required in order to properly describe the time dependent capillary rise by means of the classical Lucas-Washburn model. Our choice of boundary conditions leads to a dynamic law for the capillary rise that explicitly depends on the saturation degree of the porous matrix prior to imbibition. We combine our theoretical study with optical experiments that allow for direct observation of the filling process, revealing complex rising dynamics and broadening of the imbibition front.

1 Introduction

Fluid transport in porous media comprises a wide variety of phenomena that play crucial roles in numerous natural and technological processes. Understanding the properties of porous solids and their response when interacting with fluid phases is crucial in research fields ranging from oil or natural gas extraction, transport through bio membranes and protein folding to CO_2 capture. Processes such as capillary flow, adsorption or condensation have been extensively studied due to their importance in multiple biological processes like liquid transport in plants or blood circulation, leading to the development of multiple bio-inspired technologies (Feng et al. 2017).

Wood, concrete, bricks or sandbeds are just a few examples of porous materials. While different in composition and structural properties, their internal structure can be commonly described as a solid matrix containing pores. The pores can widely vary in size, geometry and distribution. Nevertheless, most research deals with well-defined porous structures and pore sizes in the micrometer range. At this scale, spontaneous capillary rise happens since the relatively high capillary pressures involved can act against gravity, providing a prolific framework for

technological applications. Although in more recent years, the study of fluids confined in scales down to the nanometric is attracting more interest (Huber 2015).

Classical hydrodynamics theory provides an accurate description for fluid flow in porous media from macroscopic down to microscopic scales (Kavokine et al. 2021). However, this approach cannot be assumed valid when dealing with pore sizes in the nanometer range, and the typical molecular size is in the order of the confinement spaces (Sparreboom et al. 2010) (Vincent et al. 2016). In the mesoscopic range (pore radii from 2 to 50 nm) deviations from continuum theory are to be expected (Faucher et al. 2019). Such deviations, commonly attributed to the limit of validity of the continuum approach, can be explained in terms of the liquid-wall interaction and subsequent modifications of the slip boundary conditions in the pore walls (Gruener et al. 2009). In our work, we explore the capillary rise of water in highly hydrophilic materials with pore sizes below 10 nm and test the validity domain of continuum hydrodynamics to provide accurate flow rate predictions under high confinement conditions.

2 Theoretical fundaments

In order to properly describe the capillary-driven flow of water in hydrophilic nanoporous media, we need to model both the porous structure and the fluid dynamics. Here we try to enhance the connection between transport laws in the macroscopic scale and the fluid-solid interaction at the single nanopore scale.

2.1 The geometry of the pore space

In most cases, the geometry of the porous structure, for both naturally and artificially produced porous materials, is hard to describe due to its complexity. Often one can find that the material porous properties are highly heterogeneous or that the pores characterization requires to work with different length scales (Gries 2020). When studying porous media, the aim is to quantify the pore structure by using simple defined parameters that can be measured. Therefore, a mathematical description of the matrix structure requires working with idealized pore geometries. A commonly used approach is to consider first a single cylindrical capillary of length L_1 and radius r_p, that works as a representative element of the whole matrix. The choice of a cylindrical pore is not arbitrary, since many porous materials can be described as an array of elongated pores, more or less interconnected. Furthermore, some technological materials like artificial porous silicon or Anodic Oxidized Alumina (AAO) can be synthetized in the shape of thin membranes (thickness in the order of 10-100 µm), and present parallel cylindrical-like pores oriented perpendicularly to the plate plane (see figure 1).

It is reasonable to expect that the geometrical properties, even in the case of very homogeneous structures, will differ among the different constitutive elements. Therefore, the magnitudes characterizing the matrix must be the result of averaging along the porous host.

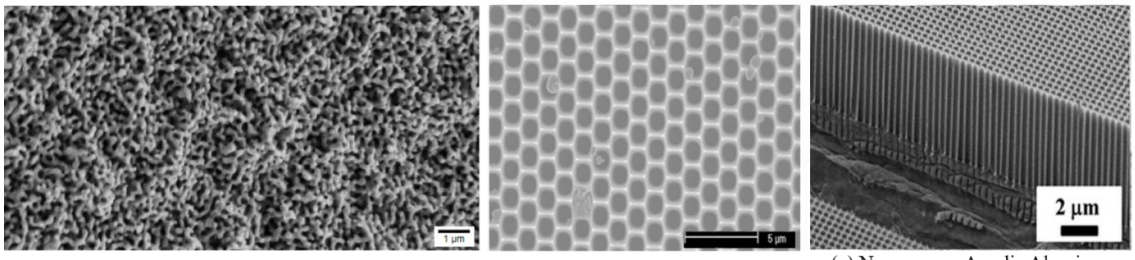

(a) Nanoporous Vycor glass (b) Microporous Silicon (c) Nanoporous Anodic Aluminum Oxide

Figure 1: Scanning Electron Microscopy (SEM) pictures of different pore structures. Pictures (b) and (c) adapted from (Zakar et al. 2016) and (Zhao et al. 2014) respectively.

2.1.1 Pore size distribution and porosity

The pore size distribution and the porosity are the two main properties of the porous matrix. They are both accessible via measuring a sorption isotherm for the material. The porosity Φ_o represents the fraction of the total volume occupied by the pores, and therefore is the space susceptible to be filled by a fluid phase. It is calculated as the ratio between the total pore volume V_{pore} over the total volume of the host V_T:

$$\Phi_o = \frac{V_{pore}}{V_T} \tag{1}$$

The pore size distribution is the probability distribution of every pore size value in a representative element of the material. We will not detail here how to calculate such probability function, but rather focus on its use. Figure 3 b shows the pore size distribution for two different samples of porous Vycor glass. A narrow distribution is indicative of an homogeneous material pore wise. Assuming we work in such a scenario, the peak value of the distribution is taken as mean pore radius and is the value we assign to our representative pore size r_p.

2.1.2 Hydraulic permeability

The hydraulic permeability is the ratio of the volume rate to the hydraulic gradient driving the flow, in our scenario, a pressure gradient. It describes the resistance of a porous or granular solid matrix to the fluid flux throw its cross section. It can be written in terms of the fluid density and viscosity and the intrinsic permeability of the material K. This magnitude denotes the material geometry and its degree of saturation, and it is independent of the fluid. Parametrizing K it is not trivial for most porous structures.

2.1.3 Tortuosity

Tortuosity is a parameter that describes the geometry of the pore network with respect to the interconnectivity and the meandering of pore segments. It can be understood as a correcting factor for the permeability, to consider the rather non-ideal geometry of the pores. In its most simple version, it accounts for the orientation of the pores with respect to the direction of the flow. This is, if we have a network of interconnected cylindrical pores, oriented in all 3 directions, only 1/3 of the pores contributes to the flow and therefore $\tau = 3$. If we have an array

of parallel cylindrical pores all oriented in the direction of the flow, then the totality of the pores contributes to the flow and $\tau = 1$.

But the tortuosity can also reflect the deviations of our pore structure with respect to the above-mentioned arrays of interconnected pores, linking our idealized pore geometry with the real one. Some materials present meandering pores rather than straight. This means that the flow needs to cover a distance l_p (path length) through the pores to advance between two points separated by a distance D (direct interconnection between the points). Obviously for not straight pores we find $l_p > D$. The previously defined tortuosity can be corrected then by a factor L_p / D resulting in tortuosity values that may not be integers. For instance, the tortuosity of nanoporous silicon can be slightly higher than 2 when the pores present some conicity (Acquaroli et al. 2011). And other materials like nanoporous Vycor glass, with a porous structure more similar to a 3D network of interconnected pores (figure 1), can have a tortuosity higher than 3 (Lin et al. 1992).

This definition is the most complete and it is the one that is in agreement with the calculated values of tortuosity for porous materials. Such calculations are based on 3D geometrical reconstructions of the pore network via imaging techniques such as neutron-based tomography and pore morphology simulations (Crossley et al. 1991).

2.2 Theoretical hydrodynamics

When we bring a porous material into contact with a wetting liquid, spontaneous imbibition occurs, i.e. capillary driven infiltration of the fluid phase into the inner pore space. Once the porous matrix and its influence over the flow has been characterized, we can describe the volume rate of a liquid with dynamic viscosity η, that flows through a porous matrix with a constant cross-sectional area A, and driven by a pressure drop Δp, via:

$$\dot{V} = \frac{dV}{dt} = \frac{AK\Delta p}{\eta\, h}, \tag{2}$$

which is the well-known Darcy's law. Here, the magnitude h represents the distance along which the pressure drop is acting. Note that such distance will increase as the liquid front moves, and consequently $h = h(t)$. Therefore, h also denotes the capillary rise or position of the liquid front (see figure 2). For macroscopic capillaries the pressure drop Δp is determined by the balance between capillarity and gravity, being the latter one also time dependent for the case of vertical imbibition. The capillary pressure or Laplace pressure p_L is given by Laplace's law and can be written as: $p_L = 2\,\gamma / r_L$, with γ being the surface tension of the liquid and r_L representing the radius of curvature of the interfacial meniscus. When working with nanocapillaries, the Laplace's equation leads to capillary pressures in the order of 10^2 bar. This allows to neglect the gravity term when working with samples with lengths under the expected gravity-capillarity equilibration height (in the order of kilometers). Such approximation leads to a rather simple version of (2) that can be integrated provided we know the proportionality constant K. We will be working with nanoporous Vycor glass. Such material presents a so-called *sponge-like porous structure*, consisting on an array of cylindrical-like interconnected pores, with homogeneous

distribution and orientations (see figure 3c). This geometry is not unique to Vycor glass, but also representative of other nanoporous systems such as nanoporous amorphous carbon or nanoporous gold (Weissmueller et al. 2010). And for porous structures that can be reasonable described as a set of homogeneous cylindrical pores, the permeability can be written as:

$$K = \frac{1}{8}\frac{r_h^4\ \Phi_o}{r_p^2\ \tau}. \tag{3}$$

Here r_h is the hydrodynamic radius or radius for the parabolic velocity profile (see figure 2). Generally, r_h does not match the pore radius r_p. This will depend on the boundary conditions of the system. With K being known, we can now rewrite the volume infiltrated as a function the capillary rise as

$$V = h(t)A\ \Phi_{\mathrm{i}} \rightarrow \frac{dV}{dt} = \frac{dh(t)}{dt}A\ \Phi_i. \tag{4}$$

Notice here that we introduced a new porosity $\Phi_i \leq \Phi_o$ (reduced porosity). This magnitude represents the effective porosity in the case of having a matrix that is already partially filled when the infiltration experiment starts, due to the presence of pre-adsorted substances in the pore walls. For nanopores, even a single monolayer of adsorted molecules can already have a non-neglectable effect in the reduction of the porosity. Then finally, by combining (2), (3) and (4) we get a simple differential equation

$$\frac{dh(t)}{dt}h(t) = \frac{\gamma\ \Phi_o}{4\ \eta\ \tau\ \Phi_i}\ \frac{r_h^4}{r_L\ r_p^2}\ , \tag{5}$$

whose solution leads to a time dependent expression for the capillary rise

$$h(t) = \sqrt{\frac{\gamma\ \Phi_o}{4\ \eta\ \tau\ \Phi_i}\ \frac{r_h^4}{r_L\ r_p^2}\ t}\ , \tag{6}$$

also known as Lucas-Washburn law **(LW).** This relation reveals the diffusive nature of imbibition processes and describes the time dependent capillary rise as proportional to the Squared root of time with the proportionality factor depending on both material morphological properties and confined liquid properties.

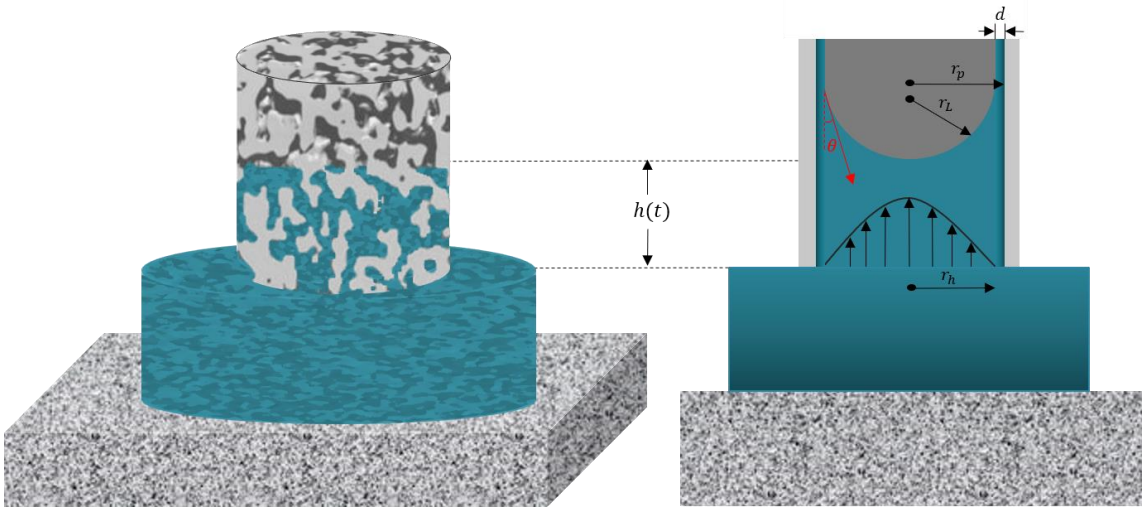

Figure 2: Schematic representation of the capillary rise. The left figure represents the liquid imbibing the complex pore structure. The right picture shows the flow dynamics on a representative cylindrical capillary with pore radius r_p equal to the mean pore radius of the porous system. In the figure it is also represented the difference between pore radius and curvature radius of the interfacial meniscus r_L. The parabolic velocity profile of the moving flow is shown as well, with the hydrodynamical radius $r_h \neq r_p$.

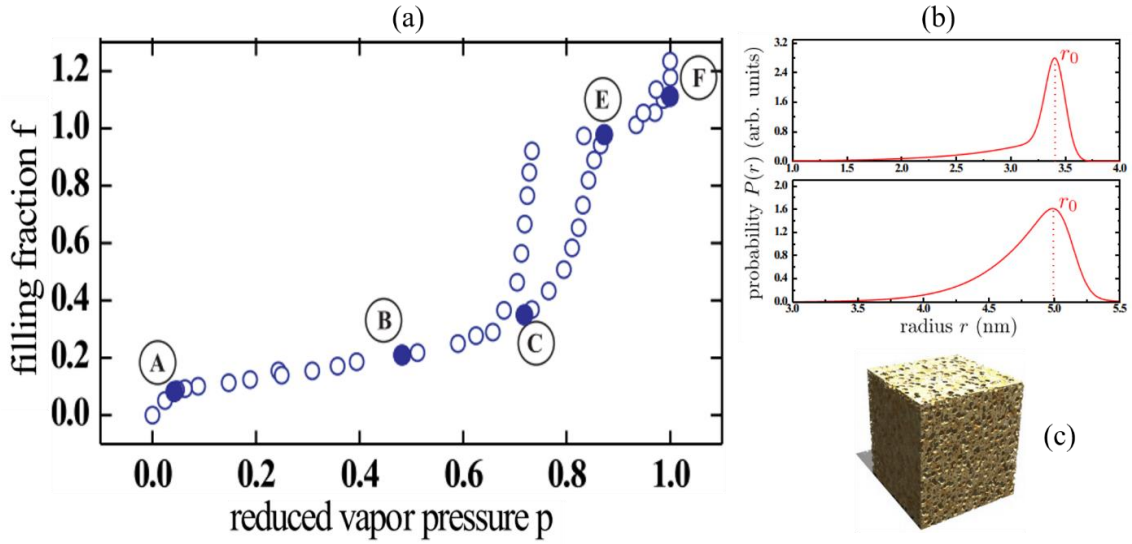

Figure 3: (a) Water sorption isotherm of a nanoporous Vycor glass host with 3.4 nm mean pore radius recorded at T = 4 ºC. In (b) it is shown the pore size distribution for the same porous host (top) compared with a wider distribution associated to a larger pore size (bottom). The subfigure (3) is a 3D model of the sponge-like porous structure representative of the real Vycor glass porous matrix adapted from (Grüner 2010).

2.2.1 Boundary conditions

Equation (6) governs the imbibition dynamics and shows how the capillary rise explicitly dependence on the pore radius, initial porosity and tortuosity; which are measurable properties of the porous body. Ideally, we want to work with an expression that only depends on already known quantities. In order to do so, it is necessary to properly define the boundary conditions of our case of study.

In our study, we work with porous Vycor glass (Corning glass 7930). The samples have a mean pore radius of 3.4 nm and porosity of 31%, measured via Nitrogen sorption isotherms (see figure 3). The particular samples we use are monoliths with cylindrical shape (~11 mm height), and were previously used by Simon Gruener et al. in their study of imbibition dynamics via gravimetry measurements, were they thoroughly characterized the porous Vycor host (Gruener et al. 2009). The high density of silicane (Si-OH) groups in the pore walls translate into high hydrophilicity. Therefore, when the samples are in equilibrium with a humid atmosphere, the presence of adsorted monolayer of water molecules on the pore walls is expected. The sorption isotherm data (figure 3) reveals the formation of a first monolayer at a very low value of p_v (reduced vapor pressure) as shown by (A) in the plot. Such monolayer will be strongly attached to the pore walls via hydrogen bonding. A second monolayer will grow with increasing p_v and will b complete formed at $p_v \sim 0.5$ (B) and a third one at $p_v \sim 0.75$ (C).

Based on the presence of such pre-adsorbed layers of water molecules prior to imbibition, we take into account their effect on the effective pore radius and porosity of our sample. Such consideration should be also extended to other materials with similar hydrophilicity and pore size. If we assume such monolayers to be strongly bounded to the walls and therefore immobile, we can impose a non-slip boundary condition, with a slip length -*d*, were d represents the thickness of the monolayers. One can estimate $d = n \cdot 0.25$ nm (n = 1, 2, 3, ...) with n being the number of monolayers, and 0.25 nm representing the mean diameter of a water molecule. This way the hydrodynamic radius gets reduced by:

$$r_h = r_p - d\,. \tag{8}$$

Also, considering the interfacial meniscus to be a spherical cap, the radius of curvature can be related to the pore radius (figure 1) by:

$$r_L = (r_p - d)/\cos(\theta), \tag{9}$$

were θ represents the contact angle. In the case of a free pore wall (no pre-adsorted layers) θ is the liquid-wall contact angle and in an already wet wall, θ represents the imbibing-liquid-wall-liquid contact angle. The problem can be simplified even more by choosing water as infiltrating liquid. This way:

$$\theta = 0 \rightarrow r_L = r_h. \tag{10}$$

Finally, the inclusion of pre-adsorted layers justifies the distinction between Φ_i and Φ_o. The reduced porosity Φ_i is easily accessible via measuring the mass difference of the sample before and after the imbibition experiment. This allows to calculate the infiltrated volume, and its rate to the sample volume gives the reduced porosity. We introduce here a new porosity reduction factor that can be defined as $\xi = \Phi_i / \Phi_o$. By simplifying the pores morphology to perfect cylinders, it is easy to calculate a first approximation to the porosity reduction factor:

$$\xi = \frac{\Phi \mathrm{i}}{\Phi \mathrm{o}} \approx \left(\frac{r_p - d}{r_p}\right)^2. \tag{11}$$

All the conditions and factors described just above can be easily modified to fit diverse scenarios such as experiments carried out in different atmospheres or the use of various imbibing liquids. In this work we focus on the particular case of water imbibition in a hydrophilic nanoporous material with a sponge-like porous structure. By including the conditions (8), (9) and (10); and introducing the factor (11) in the **LW** equation we can describe the capillary rise as

$$h(t) = \sqrt{\frac{\gamma}{4\,\eta\,\tau\,\xi}\ \frac{(r_p - d)^3}{r_p^2}\ t}\,. \tag{12}$$

This modified version of the **LW** (**MLW**) matches the classical macroscopic law when one neglects the effect of pre-adsorted layers, since in that case $d \rightarrow 0$ and $\xi \rightarrow 1$. Simple calculations lead to deviations bellow 1% (relative error) when working with pore sizes with values $r_p \geq 100$ nm. Value over which the classical **LW** expression captures the imbibition dynamics with reasonable precision. But when working with pores with $r_p \leq 10$ nm the MLW equation reveals considerably slower dynamics compared to the macroscopic classical approach. Equation (12) can be simplified by introducing the approximation for the porosity reduction factor showed in (11):

$$h(t) = \sqrt{\frac{\gamma\,(r_p - d)}{4\,\eta\,\tau}\ \ t}\,. \tag{13}$$

Nevertheless, in this work we decided to use equation (12) for our calculations, and to measure ξ experimentally.

3 Experiments and results

We monitor the imbibition dynamics via optical measurements. The optical properties of Vycor glass in a way justify its choice as object of study. The difference in the refractive index between empty and filled pore can be used to track the filling process. To do so we illuminate the sample with white light while this is being imbibed. The filling-induced light scattering allows to infer the overall filling state of the porous matrix as well as the position of the advancing liquid front. It is important to note that the use of light in the visible spectrum restricts the observable phenomenon to scattering occurring along length scales characteristic of the used light wavelength. As a result, we cannot expect to resolve the filling state at the local scale of the pores, but rather a rougher visualization of the macroscopic imbibition front.

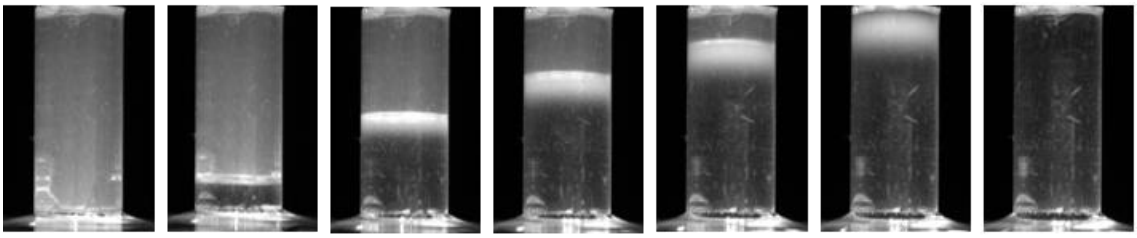

Figure 4: Snapshots of an imbibition experiment of water infiltrating into a porous Vycor glass sample (pore radius 3.4 nm, height 1.12 mm and diameter 6.82 mm). The water imbibition front is visible as a white area between the empty part of the monolith (translucid) and the filled one (transparent). The interval between pictures is 15 minutes.

In combination with the light source, a CCD monochrome camera (Imagine Source DMK 41BF02) is employed to acquire the optical data. This way we obtain pictures of the imbibition process with a time frequency of 0.18 pics/sec (or 1 picture every 5.5 sec). The cylindrical Vycor monolith (1.12 mm height and 6.82 mm diameter) is brought into contact with a reservoir of deionized water through its bottom face. The top face and the lateral surface are sealed via a highly hydrophobic adhesive tape (TESA®) to prevent evaporation during imbibition. The experiment is carried out at 24.7 ºC and 50.3% humidity (both constant during the experiment). Prior to the experiment, the sample is exposed to such conditions for over 24 hours, to assure that it is in equilibrium with that atmosphere. For this purpose, the weight of the Vycor piece is measured with a microbalance along the exposure time.

Upon imbibition, the transparency of the sample changes. The empty matrix is translucid, turning into totally transparent when filled with water. Figure 4 shows snapshots of the process, and it can be observed how the filled volume increases with time. Particularly interesting here is the appearance of a white front that moves from bottom to top of the sample, vanishing at the end of the process. This phenomenon can be explained in terms of the liquid distribution in that region. At the local pore size scales, the meandering pores vary in diameter shape and orientation resulting in different local imbibition speeds. It is reasonable to think then, that taken any cross section of the porous host, not all of the pores contained in it will be filled simultaneously. The coexistence of empty and filled pores along a path length in the scale of the visible light wavelength will induce intense light scattering, leading to the appearance of the whitened area. Therefore, we find that there is not sharp transition between empty and filled parts of the matrix, but rather a diffuse advancing front. Additionally, it can be observed that

the front broadens, increasing its characteristic thickness with time. Therefore, we find the concept of capillary rise hard to define at the macroscopic level.

At this point we analyze the two dynamical aspects of the imbibition front, its position and its width. To do so we take two different approaches. The front mean position is determined via taking a grey scale pixel profile along a vertical axis of the sample. The boundaries of the broadening front can be easily determined by comparison with the reference pictures of both the fully empty and fully filled sample. The python code used in the image analysis has been written and optimized by members of this research team. We redefine the capillary size height then as the middle point between the upper and lower limit of the imbibition front. We can repeat the process along different vertical lines and average to reduce the measurement error.

Figure 5 (top) shows the calculated mean capillary rise height of water in our nanoporous Vycor glass host. The experimental data (blue points) can be acceptably fitted by a scaling function $y(t) = C \cdot t^{1/2}$, with fitting coefficient C_{fit} = (0.133 ± 0.009) mm / $s^{1/2}$, unveiling the imbibition dynamics diffusive behavior. We can compare such result with the theoretical prediction given by the **MLW** modeling. In the calculation we use the tabled data for water at 24 ºC and 1 atm, giving $\gamma = 0.072$ n/m and $\eta = 1.0016$ mPa·s. For the porous matrix we assume $\tau = 3.6 \pm 0.4$ and the data sorption isotherm data provides $r_p = (3.6 \pm 0.1)$ nm and $\Phi_o = (0.31 \pm 0.2)$. The isotherm data suggest that at the laboratory humidity at least two monolayers of water should be consider and therefore we take d = 0.5 nm. The mass uptake upon imbibition (0.110 ± 0.001) g leads to

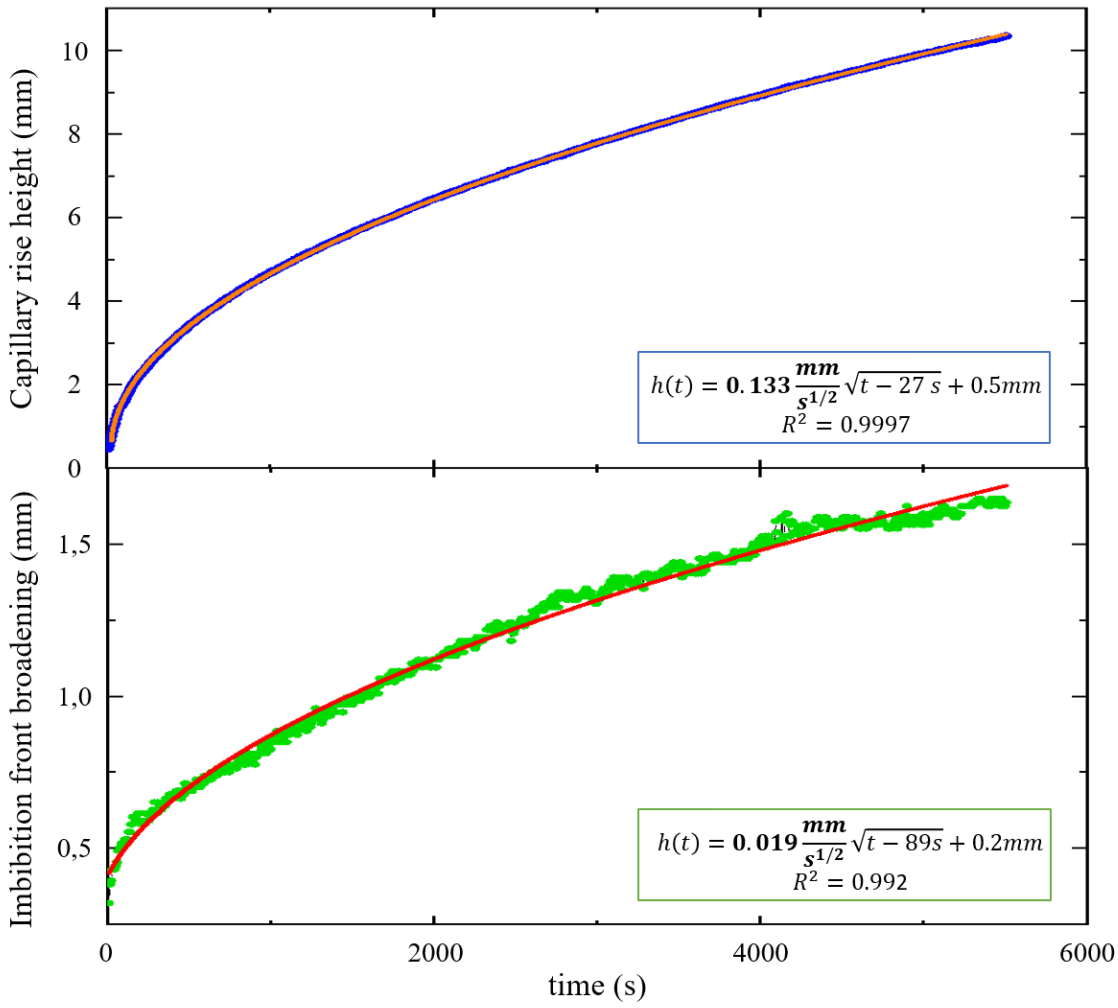

Figure 5: Dynamics of water imbibition in nanoporous Vycor glass (3.4 nm pore size). The top figure represents the experimental time dependent capillary rise in mm (blue circles) and the fitting curve (orange line). The bottom figure shows the broadening of the imbibition front (in mm) as a function of time (green circles) and its fitting curve (red line). In both plots, the experimental uncertainty is included within the circles size in the figures.

Φi = (0.25 ± 0.2) which means that the porosity reduction factor is ξ = 0.82 ± 0.01. The same value can be reached via equation (11). Including all the model parameters in equation (12) we get the proportionality C_{teor} = (1.32 ± 0.02) · 10^{-4} m / $s^{1/2}$y factor to $\sqrt{t}$ or imbibition coefficient C_{teor} = (1.32 ± 0.02) · 10^{-4} m / $s^{1/2}$, or alternatively C_{teor} = (0.132 ± 0.002) mm / $s^{1/2}$ with shows a remarkable degree of agreement with the experimental value. Just as an illustration, when neglecting the pre-adsorted monolayers contribution, the classical LW law leads to a value of C_{class} = (1.84 ± 0.02) mm / $s^{1/2}$, which is one order of magnitude (140 %) faster than the measured dynamics.

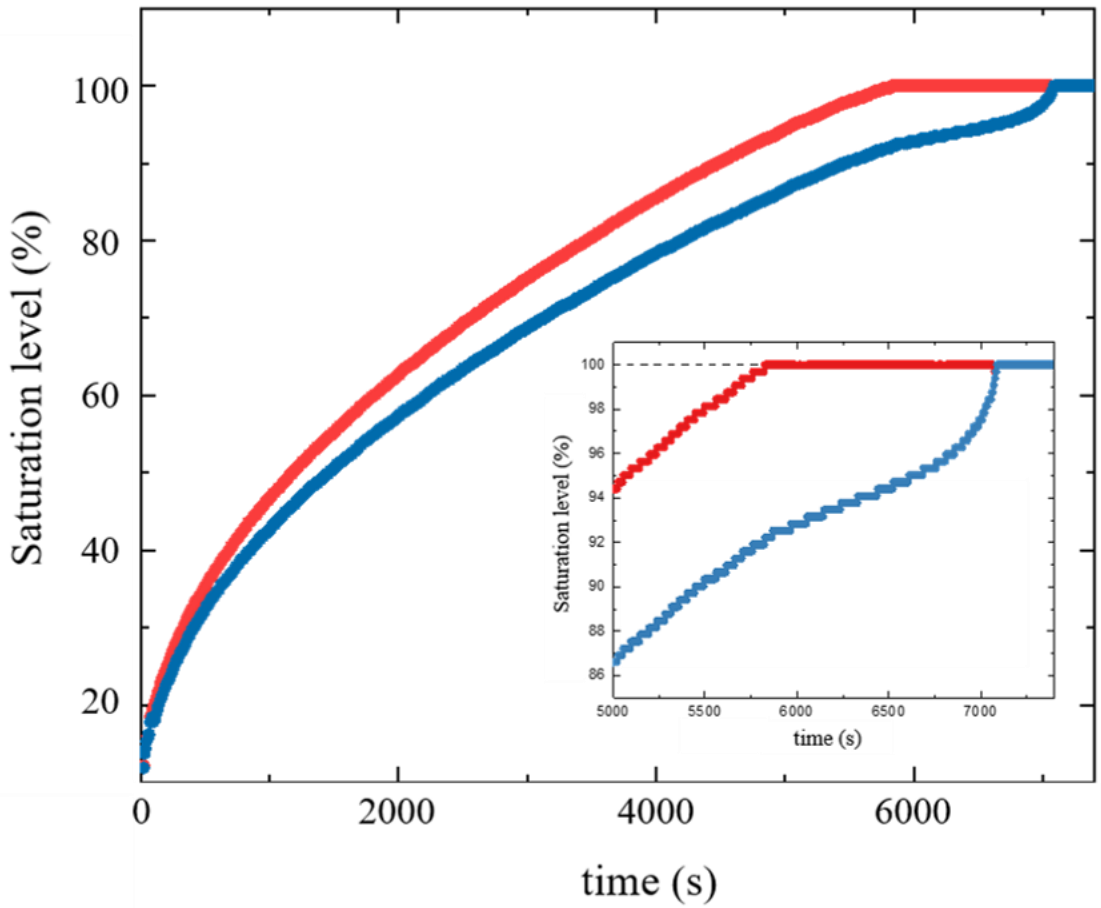

Figure 6: Dynamics of the broadening imbibition front of water in Nanoporous Vycor glass (3.4 nm poresize). The position of each boundary is represented by the red (top) and blue (bottom) lines, as a function of the saturation (normalized height). The dynamic evolution of both fronts at latter times is highlighted in the amplified plot.

In figure 5 (bottom) we represent the broadening imbibition front dynamics, i.e. the thickness of the diffuse front as a function of time. The signal in this case is comparably noisier than the capillary rise one due to the scanning method itself. The pixel color at the same height can slightly vary between scanning lines leading to different values of the broadening front boundaries. Among other reasons, this can be related to the non-flat lateral surface of the sample. Nevertheless, the overall behavior is still latent and it is clear that the imbibition front increases in thickness also following the same scaling law as the capillary rise ($\sqrt{t}$). Such result is in agreement with prior observations by Simon Grüner using neutron radiography (Grüner 2010).

The analysis method just described, while practical, has limitations when it comes to explore the early and late stages of the process. The reflections produced by the water in the proximity of the water-sample contact regions, do not allow for proper scanning of the front. Only after the first 30 seconds the code is able to resolve the formation and movement of the front.

Additionally, our definition of capillary rise level is limited to times prior to the upper limit of the front reaching the top of the sample. Afterwards, calculating the middle value between the front boundaries is not possible anymore and therefore we lose information regarding the final stage of the experiment.

A second approach towards the data analysis can be taken if we want to focus on the broadening effect. By defining horizontal scanning pixel lines, we can calculate the overall brightness in the grey scale at every height level. This way the imbibition front boundaries appear more uniform and therefore their advancement is easier to track (figure 6). Also, we can visualize properly the final stages of the experiment. On the other hand, with this method we lose temporal resolution. Besides the limitations, the data accounts for qualitative description of both the upper and lower front dynamics. Furthermore, a closer look to the final stages of imbibition reveal an acceleration of the lower front after the upper one reaches the top of the sample.

The interesting dynamics of the capillary, and particularly the broadening of the front, highlight the complexity of the pore matrix. The non-existence of an abrupt empty-filled boundary evidences the limits of our single-pore geometry approximation. The meandering character of the highly tortuous pores and their connectivity explains the existence of different advancing profiles. As an example, one can think of a capillary that subdivides to two other ones, differing in diameter (channel junction). If well one should expect faster dynamics through the wider one as determined by the **LW** law, the water would be subjected to a higher driving pressure through the thinner one due to the increase of Laplace's pressure with decreasing radius. This way, the liquid finds preferred or optimal paths during its ascension. Such phenomenon is known as meniscus arrest effect (Sadjadi et al. 2015).

This explains not only the broadening of the front but also its acceleration towards the end. Some of the larger pores are still pending to be filled when the upper fast front reaches the top of the sample, and when the pressure conditions necessary for the filling of such pores are satisfied, the dynamics will be comparably faster due to their larger cross-section.

4 Conclusions

We studied water imbibition dynamics in a nanoporous hydrophilic matrix via simple optical methods. We proved that classical macroscopic hydrodynamics can successfully describe the capillary rise dynamics, provided a good description of the solid fluid boundary at the single pore scale. By correcting the effective pore size and porosity in the LW model, a remarkable agreement between the experimental observation and the theoretical predictions is achieved.
Furthermore, we highlighted how the non-consideration of pre-adsorted water layers attached to the pore walls leads to unrealistic dynamics one order of magnitude faster than our observations.

Additionally, the formation of a diffused front that broadens in time is addressed in this work, although further analysis is required. The connection of the broadening dynamics to the pore size distribution needs to be considered for a more quantitative approach, involving analysis of different geometries and pore sizes. The difficulties to analyze the early and late stages of imbibition reveals the need of optimizing both the data-acquiring process and scanning codes.

At the time of writing this conclusion, new experiments are being carried out, focused on the late stages of imbibition and the reversibility of the process. Additionally, we are working on a better reconstruction of the pore geometry in attempt to properly describe the late accelerated dynamics in relation to the pore sizes and connectivity, a question that so far remains open.

References

[1] Acquaroli LN, Urteaga R, Berli CLA, Koropecki RR. (2011). Capillary Filling in Nanostructured Porous Silicon. *Langmuir*. 27(5):2067–72

[2] Crossley PA, Schwartz LM, Banavar JR. (1991). Image-based models of porous media: Application to Vycor glass and carbonate rocks. *Applied Physics Letters*. 59(27):3553–55

[3] Faucher S, Aluru N, Bazant MZ, Blankschtein D, Brozena AH, et al. (2019). Critical Knowledge Gaps in Mass Transport through Single-Digit Nanopores: A Review and Perspective. *The Journal of Physical Chemistry C*. 123(35):21309–26

[4] Feng Y, Zhu W, Guo W, Jiang L. (2017). Bioinspired Energy Conversion in Nanofluidics: A Paradigm of Material Evolution. *Advanced Materials*. 29(45):1702773.

[5] Gries, S. (2020). Silbernanopartikel induzierte nasschemische Synthese von hierarchisch porösem Silizium und dessen strukturelle Charakterisierung. *Master Thesis: Hamburg Universiy of Technology*.

[6] Gruener S, Hofmann T, Wallacher D, Kityk A v, Huber P. (2009). Capillary rise of water in hydrophilic nanopores. *Phys. Rev. E*. 79:67301

[7] Grüner SA. (2010). Rheology and Dynamics of Simple and Complex Liquids in Mesoporous Matrices. *Dissertation Universitaet des Saarlandes.*

[8] Huber P. (2015). Soft matter in hard confinement: Phase transition thermodynamics, structure, texture, diffusion and flow in nanoporous media. *Journal of Physics Condensed Matter*. 27(10)

[9] Kavokine N, Netz RR, Bocquet L. (2021). Fluids at the Nanoscale: From Continuum to Subcontinuum Transport. *Annual Review of Fluid Mechanics*. 53(1):377–410

[10] Lin MY, Abeles B, Huang JS, Stasiewski HE, Zhang Q. (1992). Viscous fiow and difFusion of liquids in microporous glasses *Phys. Rev*. B 46:10701

[11] Sadjadi Z, Jung M, Seemann R, Rieger H. (2015). Meniscus Arrest during Capillary Rise in Asymmetric Microfluidic Pore Junctions. *Langmuir*. 31(8):2600–2608

[12] Sparreboom W, van den Berg A, Eijkel JCT. (2010). Transport in nanofluidic systems: A review of theory and applications. *New J. Phys.* 12: 015004

[13] Vincent O, Szenicer A, Stroock AD. (2016). Capillarity-driven flows at the continuum limit. *Soft Matter*. 12(31):6656–61

[14] Weissmueller J, Duan H-. L, Farkas D. (2010). Deformation of solids with nanoscale pores by the action of capillary forces. *Acta Materialia*. 58(1):1–13

[15] Zakar A, Park SJ, Zerova V, Kaplan A, Canham L, et al. (2016). *MWIR Optical Modulation Using Structured Silicon Membranes*

[16] Zhao H, Wang C, Vellacheri R, Zhou M, Xu Y, et al. (2014). Self-Supported Metallic Nanopore Arrays with Highly Oriented Nanoporous Structures as Ideally Nanostructured Electrodes for Supercapacitor Applications. *Advanced Materials*. 26(45):7654–59

Author

Juan Sanchez, M.Sc.
Hamburg University of Technology
Institute for Material and X-Ray Physics (M-2)
Center for Hybrid Nanostructures (CHyN)
22761 Hamburg
E-mail: juan.sanchez@tuhh.de
Home: https://www.mxp.tuhh.de/index.php/en/group

Condensation-Induced Restructuring of Atmospheric Soot Aggregates

Gennady Y. Gor, Ella V. Ivanova, Alexei F. Khalizov

Abstract: Soot is a major pollutant and climate forcer. The optical properties of soot that determine its impact on the climate strongly depend on its morphology. When initially generated, soot nanoparticles are branched fractal aggregates of primary carbon spheres. During ageing in the atmosphere, soot aggregates often collapse into compact globules, with restructuring driven by a condensate of atmospheric vapours on the aggregate surface. Analysis of the recent laboratory experiments of lightly coated aggregates suggested that the spatial distribution of condensate on the soot agglomerates may determine its fate with respect to restructuring. When a vapour condenses in the junction between the spheres, the capillary and disjoining forces are likely to generate mechanical stresses sufficient for plastic deformation of an agglomerate. Therefore, the agglomerate restructuring is directly related to the domination of one of the two scenarios of vapour condensation: if uniform condensation on the surface of primary carbon spheres dominates, the aggregate backbone will remain fractal; if condensation in the junctions between the primary spheres ("capillary condensation") dominates the aggregate will likely collapse. Here we propose a model describing the vapour condensation on a soot aggregate, consisting of two spherical carbon particles, to elucidate the conditions at which one of the two condensation scenarios is realized. We wrote the closed-form solutions for the amount of vapour condensed as a function of time in both scenarios, and compared the results for different values of the physico-chemical parameters.

1 Introduction

Soot is a major environmental pollutant which deteriorates air quality and affects human health. Moreover, soot nanoparticles serve as condensation nuclei for atmospheric aerosols, light absorbers and scatterers, impacting the climate (Bond et al.,2013;Shiraiwa,Selzle & Pöschl,2012). Soot nanoparticles are fractal agglomerates of graphitic spherical monomers mixed with organic or inorganic products of combustion. The optical properties of soot and transport properties of soot in human respiratory tract strongly depend on the morphology of soot agglomerates (Broday & Rosenzweig, 2011; Xue et al.,2009). Therefore, in order to assess the negative impacts of soot on both climate and human health one has to know the microstructure of soot nanoparticles.

When soot nanoparticles are exposed to other organic and inorganic products of the combustion process, or to water vapour, they often restructure, evolving from the branched fractal structures

to globules (Mikhailov, Vlasenko, Kiselev & Ryshkevich, 1998; Weingartner, Baltensperger & Burtscher, 1995). However, restructuring is not a universal feature, and the same soot may restructure in one vapour, but not in another (Chen et al., 2016; Schnitzler, Gac & Jäger, 2017; Skillas, Künzel, Burtscher, Baltensperger & Siegmann,1998)). It was also shown that the restructuring depends on the amount of condensed vapour (Bambha, Dansson, Schrader & Michelsen, 2013; Ghazi & Olfert,2013; Pagels, Khalizov ,McMurry &Zhang,2009). Chen et al.(2016) exposed soot to vapours of various polycyclic aromatic hydrocarbons (PAHs), which have similar chemical structure and properties, and comparable amounts of PAHs were condensed on soot particles. However, they found that while some PAHs (e.g. phenanthrene) induced restructuring, other (e.g. anthracene) did not. We observed similar difference in soot restructuring after exposing it to various organic vapours (Chen et al.,2018). Here we present a model based on the kinetics of vapour condensation on soot aggregate surface, which explains the difference in soot restructuring behavior.

2 Theory

Condensation of vapours on a soot aggregate can take place both on the convex surface of the spherical monomers and in the (concave) gaps between them. Most likely condensate is present as both a thin liquid film on the surface, and as a capillary condensate in the gaps. However, for simplicity we consider here only two limiting cases: when all the condensate coats the spherical monomers as a uniform film, or when all the condensate is located in the gaps. To even further simplify the problem, we consider condensation in one gap in a dimer, and condensation on the surface of a single monomer (Figure 1). We hypothesize that when the capillary condensation dominates, the solvation forces in the gap induce the soot aggregate restructuring (Chen et al.,2018).

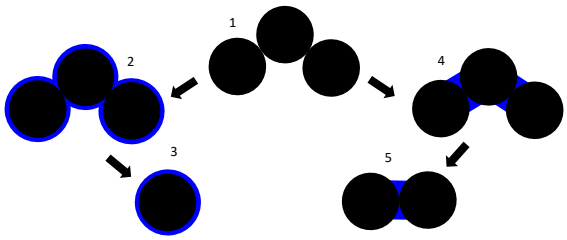

Figure 1: Schematic of a soot aggregate (1) and different scenarios of condensation on its surface. One limiting case is the formation of a uniform film on the surface of the spheres (2), which can be modeled as condensation on a single sphere (3). Another limiting case is a “capillary condensation” (4) – filling the gap between the spheres with no condensation on the surface. It can be modeled for a dimer (5).

2.1 Material Balance

The monomer diameter in most of the atmospheric soot is in the $10 - 50$ nm range range(Olfert & Rogak, 2019), which is small enough to assume the free-molecular (kinetic) regime of condensation. Then the rate of growth of a liquid shell or meniscus (droplet) by vapour condensation will be determined by the following material balance equation for the number of condensate molecules N:

$$\frac{\mathrm{d}N}{\mathrm{d}t} = J\,, \tag{1}$$

where

$$N = n_{\mathrm{l}} V\,, \tag{2}$$

$$J = A\frac{1}{4}\alpha v_{\mathrm{T}}\left\{n_0 - n_{\mathrm{sat}}\right\}\,. \tag{3}$$

In Eq. 2 n_{l} is the number density of the liquid phase, and V is the volume of the droplet. Eq. 3 describes the free–molecular flux to the surface of the growing droplet, where α is the molecular accommodation coefficient, v_{T} is the mean thermal velocity of the molecules, n_0 is the unperturbed vapour number density far from the droplet, n_{sat} is the number density of saturated vapour near the droplet surface, and A is the area of the droplet. It should be noted that A and V are different for the two cases of condensation considered here. Eq. 3 suggests that the scenario of condensation is defined by interplay between surface area A and concentration difference $(n_0 - n_{\mathrm{sat}})$. Obviously $A_{\mathrm{sph}} > A_{\mathrm{gap}}$, but as shown below, $(n_0 - n_{\mathrm{sat}})_{\mathrm{sph}} < (n_0 - n_{\mathrm{sat}})_{\mathrm{gap}}$. Thus the main question is in how the product of the two factors compares for the case of the sphere and the gap.

The pressure of saturated vapour near the droplet surface p_{sat} depends on its curvature κ according to the Kelvin equation,

$$p_{\mathrm{sat}} = p_\infty \exp\left[\frac{\gamma}{n_{\mathrm{l}} k_{\mathrm{B}} T}\kappa\right]\,. \tag{4}$$

In the above equation, p_∞ is pressure of the saturated vapour at the flat surface ($R \to \infty$), γ is the vapour-liquid surface tension, k_{B} is the Boltzmann constant, T is the absolute temperature. Assuming the vapour is an ideal gas, we can rewrite Eq. 4 as

$$n_{\mathrm{sat}} = n_\infty \exp\left[\frac{1}{2}\ell_{\mathrm{K}}\kappa\right]\,, \tag{5}$$

where n_∞ is the number density of the saturated vapour at the flat surface and ℓ_{K} the characteristic Kelvin length defined as

$$\ell_{\mathrm{K}} \equiv \frac{2\gamma}{n_l k_{\mathrm{B}} T}\,. \tag{6}$$

Using Kelvin equation (Eq. 5), Eq. 6, and Eqs. 2–3, we can rewrite the material balance Eq. 1 in the form:

$$\frac{\mathrm{d}V}{\mathrm{d}t} = A\frac{1}{4}\alpha v_{\mathrm{T}}\frac{1}{n_{\mathrm{l}}}\left\{n_0 - n_\infty \exp\left[\frac{1}{2}\ell_{\mathrm{K}}\kappa\right]\right\}\,. \tag{7}$$

2.2 Dimensionalization

First, we introduce the dimensionless parameter, which describes the deviation on the vapour from the chemical equilibrium with the condensate, the supersaturation ζ is defined as

$$\zeta \equiv \frac{n_0 - n_\infty}{n_\infty}\,. \tag{8}$$

Using Eq. 8, we rewrite Eq. 7 as

$$\frac{\mathrm{d}V}{\mathrm{d}t} = A\frac{1}{4}\alpha v_\mathrm{T}\frac{n_0}{n_\mathrm{l}}\left\{1 - \frac{1}{\zeta+1}\exp\left[\frac{1}{2}\ell_\mathrm{K}\kappa\right]\right\}\,. \tag{9}$$

The main characteristic length scale in the problem is the radius of the monomer, R_s. The characteristic time scale in the kinetic regime is determined by thermal velocity v_T, and the length scale R_s. For convenience, we will include other parameters from Eq. 9 when introducing the characteristic time scale τ, namely:

$$\tau \equiv \frac{4n_\mathrm{l}R_\mathrm{s}}{\alpha v_\mathrm{T} n_0}. \tag{10}$$

Then Eq. 9 reads

$$\frac{\mathrm{d}V}{\mathrm{d}t} = A\frac{R_\mathrm{s}}{\tau}\left\{1 - \frac{1}{\zeta+1}\exp\left[\frac{1}{2}\ell_\mathrm{K}\kappa\right]\right\}\,. \tag{11}$$

We introduce dimensionless variables denoting them with a tilde:

$$\tilde{R} = R/R_\mathrm{s}, \qquad \tilde{t} = t/\tau. \tag{12}$$

The parameters n_0, n_l, α, v_T became incorporated in $\tilde{t}$. Since R_s is the only linear parameter of the droplet (be it on a surface or in the gap), for area, volume, curvature, and Kelvin length we can introduce the following dimensionless variables:

$$\tilde{A} = R_\mathrm{s}^{-2}A\,, \qquad \tilde{V} = R_\mathrm{s}^{-3}V\,, \qquad \tilde{\kappa} = \kappa R_\mathrm{s}\,, \qquad \tilde{\ell}_\mathrm{K} = \ell_\mathrm{K}/R_\mathrm{s}\,. \tag{13}$$

Eqs. 12 and13 allow us rewrite Eq. 11 in dimensionless form:

$$\frac{\mathrm{d}\tilde{V}}{\mathrm{d}\tilde{t}} = \tilde{A}\left\{1 - \frac{1}{\zeta+1}\exp\left[\frac{1}{2}\tilde{\ell}_\mathrm{K}\tilde{\kappa}\right]\right\}\,. \tag{14}$$

2.3 Linearization

If $\ell_\mathrm{K}\kappa \ll 1$, which is typically fulfilled for the condensation on soot (Chen et al.,2018), the Kelvin equation can be linearized:

$$n_\mathrm{sat} \simeq n_\infty\left[1 + \frac{1}{2}\ell_\mathrm{K}\kappa\right] = n_\infty\left[1 + \frac{1}{2}\tilde{\ell}_\mathrm{K}\tilde{\kappa}\right]\,. \tag{15}$$

The curvature $\tilde{\kappa}$, as well as the area $\tilde{A}$ and the volume $\tilde{V}$ are the geometric characteristics of the droplet and calculated differently for a sphere and for a gap. For example, if we consider condensation on a droplet that has the shape of a sphere, then its curvature will be equal to $2\tilde{R}^{-1}$, where $\tilde{R} = R/R_{\rm s}$ is a dimensional radius of the sphere. Using linearized Kelvin equation Eq. 15, we can rewrite the material balance Eq. 14 in the form:

$$\frac{\mathrm{d}\tilde{V}}{\mathrm{d}\tilde{t}} = \tilde{A}\left\{1 - \frac{1+\frac{1}{2}\tilde{\ell}_{\rm K}\tilde{\kappa}}{\zeta+1}\right\} = \tilde{A}\frac{1}{\zeta+1}\left\{\zeta - \frac{\tilde{\ell}_{\rm K}\tilde{\kappa}}{2}\right\}. \tag{16}$$

In the following, we consider separately the solution of Eq. 1 for condensation on the sphere and condensation in the gap between two spheres. The interplay between the three terms $(\tilde{A},\, \tilde{\kappa},\, \mathrm{d}\tilde{V}/\mathrm{d}\tilde{t})$ in Eq. 16 will determine the dominant regime of condensation, leading to two different outcomes, as depicted in Figure 1.

2.4 Model for Vapour Condensation on a Sphere

Consider vapour condensation on a sphere (Seinfeld &Pandis, 2006), where parameters $\tilde{A}$ and $\mathrm{d}\tilde{V}/\mathrm{d}\tilde{t}$ in Eqs. 2–3 and $\tilde{\kappa}$ in Eq. 5 are given by the area, volume, and curvature of a spherical shell, respectively:

$$\tilde{A} = R_{\rm s}^{-2}A_{\rm sph} = 4\pi\tilde{R}^2\,, \tag{17}$$

$$\tilde{V} = R_{\rm s}^{-3}V_{\rm sph} = \frac{4}{3}\pi(\tilde{R}^3 - 1)\,, \tag{18}$$

$$\tilde{\kappa} = 2\tilde{R}^{-1}\,. \tag{19}$$

Then, Eq. 16 can be rewritten bearing in mind Eqs. 17–19 as

$$\frac{\mathrm{d}\tilde{R}}{\mathrm{d}\tilde{t}} = \frac{1}{\zeta+1}\left\{\zeta - \frac{\tilde{\ell}_{\rm K}}{\tilde{R}}\right\}. \tag{20}$$

If $\zeta \neq 0$, the solution of Eq. 20 with the natural initial condition $\tilde{R}\,|_{\tilde{t}=0} = 1$ is

$$\tilde{t} = \frac{\zeta+1}{\zeta}\left\{\tilde{R} - 1 + \frac{\tilde{\ell}_{\rm K}}{\zeta}\ln\left[\frac{\zeta\tilde{R} - \tilde{\ell}_{\rm K}}{\zeta - \tilde{\ell}_{\rm K}}\right]\right\}. \tag{21}$$

Eq. 21 relates time to radius in an explicit form, $\tilde{t}(\tilde{R})$. Inverting this dependence to $\tilde{R}(\tilde{t})$ would describe the evolution of the radius of the droplet growing on a surface of the sphere as a result of condensation.

2.5 Model for Vapour Condensation in the Gap between the Spheres

Eq. 16 obtained above determines the rate of droplet growth irrespective of the droplet geometry, here we apply it to condensation in the gap between two spheres. Unlike the straightforward expression for volume, area, and curvature for a spherical droplet, this case is more complex.

The simplest geometry to represent the condensate in the gap would be a cylinder (Figure 2, so the droplet's volume $V_{\rm gap}$ is defined by the difference between the volume of the cylinder and volumes of two spherical caps (Ivanova,Khalizov & Gor, 2020). Then, the parameters $\tilde{A}_{\rm gap}$ and $\tilde{V}_{\rm gap}$ can be readily defined,

$$\tilde{A}_{\rm gap} = 4\pi \sin\theta(1-\cos\theta)\,, \tag{22}$$

$$\tilde{V}_{\rm gap} = \frac{2}{3}\pi(\cos\theta-1)^2(2\cos\theta+1)\,, \tag{23}$$

where the angle θ is defined between the centres of the two spheres and the three phase contact point. Unlike in the case of condensate on a sphere, the surface of the meniscus formed between two spheres must have negative curvature, but a cylindrical meniscus will not support capillary condensation because its surface curvature is positive. Hence, following our previous work (Chen et al.,2018), we used the circular approximation (Butt & Kappl,2009) by taking curvature as $\tilde{\kappa} = -\tilde{R}_{\rm out}^{-1}$ to account for the Kelvin effect, while using cylindrical shape for $\tilde{A}_{\rm gap}$ and $\tilde{V}_{\rm gap}$. Furthermore, following Rose(1958), the curvature can be expressed as a function of the filling angle θ:

$$\tilde{\kappa} = -\left(\frac{1}{\cos\theta}-1\right)^{-1}. \tag{24}$$

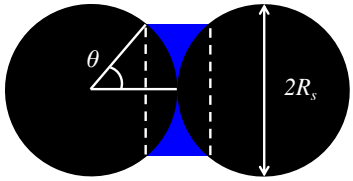

Figure 2: Two-dimensional projection of the model droplet geometry for condensation in the gap.

Using Eq. 24 in the linearized Kelvin equation (Eq. 15) we get the number density of saturated vapour near the meniscus in the gap

$$n_{\rm sat} \simeq n_\infty \left[1 - \frac{\tilde{\ell}_{\rm K}}{2}\frac{\cos\theta}{1-\cos\theta}\right]. \tag{25}$$

Using Eqs. 22, 23 and 25 in Eq. 16, we get

$$\frac{(\zeta+1)\cos\theta \mathrm{d}\theta}{\zeta + \frac{\tilde{\ell}_{\rm K}}{2}\frac{\cos\theta}{1-\cos\theta}} = \mathrm{d}\tilde{t}. \tag{26}$$

Integrating Eq. 26 with the initial condition $\theta\,|_{\tilde{t}=0} = 0$ gives

$$\tilde{t} = \frac{2\,(\zeta+1)}{2\zeta-\tilde{\ell}_{\rm K}}\left\{\sin\theta + \frac{2\tilde{\ell}_{\rm K}}{2\zeta-\tilde{\ell}_{\rm K}}\left[\theta - I\right]\right\}, \tag{27}$$

where we introduced I as

$$I \equiv \int \frac{\mathrm{d}\theta}{1+(\frac{\tilde{\ell}_{\rm K}}{2\zeta}-1)\cos\theta}. \tag{28}$$

The in integral in Eq. 28 can be readily taken analytically giving

$$I = \frac{\zeta}{\sqrt{(4\zeta - \tilde{\ell}_{\mathrm{K}})\tilde{\ell}_{\mathrm{K}}}} \arctan\left(\sqrt{\frac{4\zeta - \tilde{\ell}_{\mathrm{K}}}{\tilde{\ell}_{\mathrm{K}}}} \tan\frac{\theta}{2}\right). \tag{29}$$

As we showed (Ivanova et al.,2020), the closed form solution of the approximate geometry, is a good approximation for a more rigorous model, where the meniscus of the condensate in the gap is a catenoid, and the problem could be solved only numerically.

3 Results: Competition Between Condensation in Different Regions

The solutions for $\tilde{R}(\tilde{t})$ and $\theta(\tilde{t})$ derived above allow to analyse the competition between the two processes: condensation on the surface of a soot particle and condensation in the gap between the two soot particles. In line with the reduced length and time it is convenient to measure the amount condensed in "reduced units", so that it varies from 0 to 1. Characteristic number of molecules ν could be determined as a number of liquid molecules which is necessary to completely fill the gap between the two spheres:

$$\nu \equiv \frac{2}{3}\pi n_{\mathrm{l}} R_{\mathrm{s}}^3, \tag{30}$$

which equals to $\frac{1}{2}$ of the number of liquid molecules in a spherical droplet of the size of a carbon sphere (radius R_{s}). Therefore, the reduced number of molecules will be

$$\tilde{N}_{\mathrm{sph}} \equiv N_{\mathrm{sph}}/\nu. \tag{31}$$

For the condensation on a sphere, using Eqs. 30 and 31, Eq. 18 gives

$$\tilde{R} = \left(\tilde{N}_{\mathrm{sph}}/2 + 1\right)^{1/3}. \tag{32}$$

Eqs. 23 and 30 give the relation between the reduced number of molecules in the gap $\tilde{N}_{\mathrm{gap}}$ and the angle θ

$$\tilde{N}_{\mathrm{gap}} = (\cos\theta - 1)^2 (2\cos\theta + 1) \tag{33}$$

The maximum amount of liquid that can condense in the gap, which corresponds to the totally filled gap, is given by Eq. 33 at $\theta = \pi/2$:

$$\tilde{N}_{\mathrm{max}} = 1. \tag{34}$$

The equations for reduced properties allow to compare the characteristic times of the two processes at different values of the parameters $\tilde{\ell}_{\mathrm{K}}$ and ζ. Since both dependencies are in the form $\tilde{t} = \tilde{t}(\tilde{N})$, the following algorithm to represent the data is convenient:

- Choose the $\tilde{\ell}_{\mathrm{K}}$ and ζ of interest.
- Set the range of θ value between 0 and $\pi/2$.
- Calculate the corresponding time $\tilde{t}_{\mathrm{gap}}$ (Eq. 27).
- Calculate corresponding $\tilde{N}_{\mathrm{gap}}$ (Eq. 33).
- From $\tilde{N}_{\mathrm{sph}} = \tilde{N}_{\mathrm{gap}}$ calculate the radius of the liquid film on the soot surface $\tilde{R}$ using Eq. 32.
- For each value of $\tilde{R}$, calculate the corresponding time using Eq. 21.

Figure 3 shows the results of calculations of the amount of fluid condensed in the gap and on the surface of a single sphere.

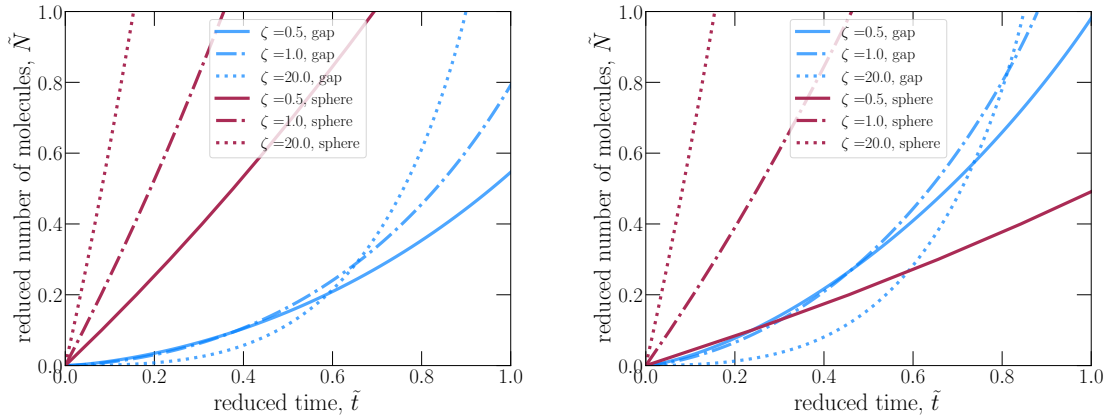

Figure 3: Model predictions for competitive condensation at two different characteristic $\tilde{\ell}_{\mathrm{K}}$, left panel shows calculations for $\tilde{\ell}_{\mathrm{K}} = 0.2$, and right panel for $\tilde{\ell}_{\mathrm{K}} = 0.4$. For both values of $\tilde{\ell}_{\mathrm{K}}$, the calculations are performed for $\zeta = 0.5$, 1.0, and 20.0.

4 Discussion

In our previous work (Chen et al.,2018; Ivanova et al.,2020), we introduced the dimensionless parameter

$$\chi \equiv \frac{\ell_{\mathrm{K}}}{R_{\mathrm{s}}}\frac{1}{\zeta} = \frac{\tilde{\ell}_{\mathrm{K}}}{\zeta}\,. \tag{35}$$

This parameter combines the Kelvin effect and supersaturation, and, as we demonstrated, it is a single parameter which determines the preferential region for condensation. When $\chi \gg 1$ condensation in the gap dominates, when $\chi \lesssim 1$ the condensation on the sphere dominates. This

parameter is an excellent measure for quick qualitative predictions, however one cannot control this parameter directly, as it depends on both $\tilde{\ell}_{\mathrm{K}}$ (property of the condensate and monomer) and ζ (experimental conditions). Therefore, here we wrote the expressions in terms of the two variables. Another modification made here is in the dimensionless time $\tilde{t}$. In our previous work we introduced dimensionless time proportional to $(n_0 - n_\infty)$, which did not properly reflect the acceleration of the condensation process with the increase of n_0. Here, we introduced $\tilde{t} \propto n_0$ instead.

One special case is worth discussing here separately. Equations for condensate on a sphere (Eq. 21) and in the gap (Eq. 27 are valid for both $\zeta > 0$ (supersaturated vapour) and $\zeta < 0$ (undersaturated vapour), but give discontinuity for $\zeta = 0$. When $\zeta = 0$ Eq. 20 for the sphere gives

$$\frac{\mathrm{d}\tilde{R}}{\mathrm{d}\tilde{t}} = -\frac{\tilde{\ell}_{\mathrm{K}}}{\tilde{R}}\,, \tag{36}$$

which gives (with $\tilde{R}\mid_{\tilde{t}=0} = 1$)

$$\tilde{t} = -\frac{1}{\tilde{\ell}_{\mathrm{K}}} \ln\left(\tilde{R} - 1\right). \tag{37}$$

Eq. 26 for the gap gives

$$\frac{2}{\tilde{\ell}_{\mathrm{K}}} \left(1 - \cos\theta\right) \mathrm{d}\theta = \mathrm{d}\tilde{t} \tag{38}$$

integrating in with $\theta\mid_{\tilde{t}=0} = 0$ we get

$$\tilde{t} = \frac{2}{\tilde{\ell}_{\mathrm{K}}} \left(\theta - \sin\theta\right). \tag{39}$$

5 Conclusion

The presented model suggests that the tendency of a soot agglomerate to restructure as a result of vapour condensation is determined by the value of two dimensionless parameters: supersaturation of the condensing vapour ζ, and $\tilde{\ell}_{\mathrm{K}}$, the ratio of the Kelvin length to the radius of a soot monomer. While the parameter $\tilde{\ell}_{\mathrm{K}}$ includes the condensate properties, such as surface tension and molar volume, it does not vary much for different condensates. The supersaturations ζ, on the contrary, can change in a wide range, and therefore it is the main factor controlling the soot restructuring. Due to its simple analytical form, our model can be incorporated into atmospheric models to improve simulations of the soot aerosol ageing and its impact on direct radiative forcing.

References

[1] Bambha R.P., Dansso M. A., Scharader P.E. & Michelsen H.A. (2011). Effects of volatile coatings and coating removal mechanisms on the morphology of graphitic soot. Carbon, 61, 80-96

[2] Bond T. C., Doherty S. J., Fahey D., Forster P., Berntsen T., DeAngelo, B. J., . . . others (2013). Bounding the role of black carbon in the climate system: A scientific assessment. J. Geophys. Res. Atmos. 118 (11), 5380?5552.

[3] Broday D. M. & Rosenzweig R. (2011). Deposition of fractal-like soot aggregates in the human respiratory tract. J. Aerosol Sci., 42 (6), 372?386.

[4] Butt H.-J. & Kappl M. (2009). Normal capillary forces. Adv. in Colloid Interface Sci., 146 (1-2), 48?60.

[5] Chen C., Enekwizu O. Y., Fan X., Dobrzanski C. D., Ivanova E. V., Ma Y., . . . Khalizov A. F. (2018). Single parameter for predicting the morphology of atmospheric black carbon. Environ. Sci. Technol., 52 (24), 14169?14179.

[6] Chen C., Fan X., Shaltout T., Qiu C., Ma Y., Goldman A. & Khalizov A. F. (2016). An unexpected restructuring of combustion soot aggregates by subnanometer coatings of polycyclic aromatic hydrocarbons. Geophys. Res. Lett., 43 (20), 1?9.

[7] Ghazi R. & Olfert J. (2013). Coating mass dependence of soot aggregate restructuring due coatings of oleic acid and dioctyl sebacate. Aerosol Sci. Technol., 47 (2), 192?200.

[8] Ivanova E. V., Khalizov A. F. & Gor G. Y. (2020). Kinetic model for competitive condensation of vapor between concave and convex surfaces in a soot aggregate. Aerosol Sci. Technol. 55(3), 302-315.

[9] Mikhailov E. F., Vlasenko S. S., Kiselev A. A. & Ryshkevich T. I. (1998). Restructuring factors of soot particles. Ivz. Atmos. Ocean. Phys., 34, 307-317.

[10] Olfert J. & Rogak S. (2019). Universal relations between soot effective density and primary particle size for common combustion sources. Aerosol Sci. Technol., 53 (5), 485?492.

[11] Pagels J., Khalizov A. F., McMurry P. H. & Zhang R. Y. (2009). Processing of soot by controlled sulphuric acid and water condensation ? Mass and mobility relationship. Aerosol Sci. Technol., 43 (7), 629?640.

[12] Rose W. (1958). Volumes and surface areas of pendular rings. J. Appl. Phys., 29 (4), 687?691.

[13] Seinfeld J. H. & Pandis S. N. (2006). Atmospheric chemistry and physics: From air pollution to climate change (2nd Aufl.). John Wiley & Sons.

[14] Shiraiwa M., Selzle K. & Pöschl U. (2012). Hazardous components and health effects of atmospheric aerosol particles: reactive oxygen species, soot, polycyclic aromatic compounds and allergenic proteins. Free Radical Res., 46 (8), 927?939.

[15] Skillas G., Künzel S., Burtscher H., Baltensperger U. & Siegmann K. (1998). High fractal-like dimension of diesel soot agglomerates. J. Aerosol Sci., 29 (4), 411?419.

[16] Weingartner E., Baltensperger U. & Burtscher H. (1995). Growth and structural change of combustion aerosols at high relative humidity. Environ. Sci. Technol., 29 (12), 2982?2986.

[17] Xue H., Khalizov A. F.,Wang L., Zheng J., Zhang R. et al. (2009). Effects of dicarboxylic acid coating

Authors

Prof. Dr. Gennady Y. Gor
New Jersey Institute of Technology
Department of Chemical and Materials Engineering
323 Dr Martin Luther King Jr Blvd
07102 Newark, NJ, USA
Tel.: +1 (973) 596-2944
e-mail: gor@njit.edu
Web: http://porousmaterials.net/

Ella V. Ivanova
New Jersey Institute of Technology
Department of Chemical and Materials Engineering
323 Dr Martin Luther King Jr Blvd
07102 Newark, NJ, USA
Tel.: +1 (973) 596-3568
e-mail: ei26@njit.edu
Web: http://porousmaterials.net/

Prof. Dr. Alexei F. Khalizov
New Jersey Institute of Technology
Department of Chemistry and Environmental Science
Department of Chemical and Materials Engineering
323 Dr Martin Luther King Jr Blvd
07102 Newark, NJ, USA
Tel.: +1 (973) 596-3583
e-mail: khalizov@njit.edu
Web: https://centers.njit.edu/krg/

Influence of coating solution concentration on particle surface structure during fluidized bed spray granulation

Maike Orth, Delaram Alibabaei, Swantje Pietsch-Braune, Stefan Heinrich

Abstract: In fluidized bed spray granulation, the resulting product properties are strongly dependent on the process conditions, including process parameters, material characteristics, and apparatus specifications. One parameter that influences the surface structure of the granules is the solids concentration of the injected solution which affects the liquid properties as well as the interaction at the solid-liquid interface. To investigate this effect, spray coating experiments were performed in a lab-scale fluidized bed with glass particles and sodium benzoate solutions of varied concentrations. To characterize the surface structure of coated particles, the surface roughness was determined using confocal laser-scanning microscopy. In general, particles with a smooth surface were produced at high solution concentrations, whereas a low solids content lead to the formation of a rough coating layer.

1 Introduction

1.1 Motivation

In contrast to natural particle fluid systems like soils, functionalized particles are produced or designed in technical processes in such a way that they fulfil a certain function. For a lot of these applications, further research is required in order to understand, optimize and model the process as small deviations result in unwanted particle structures and properties. One process that can be used to produce functionalized particles is fluidized bed spray granulation or coating. Fluidized bed particle formulation processes are applied in various industries, like the pharmaceutical, chemical, and food industry, to produce a broad variety of particulate products. Examples include instant food powders, catalysts, detergents, and fertilizers among many more granular products that are an important part in industrial processes as well as everyday life (Boerefijn and Hounslow 2005; Reynolds et al. 2005).

Fluidized beds have been applied at industrial scale since 1922 and have been used for the structurization of particles by granulation for several decades (Winkler 1926). The principle of a fluidized bed is based on overcoming the gravitational and interparticle forces by a gas stream that passes through a particle bed, so the particles can move freely within the bed. Objects of greater specific gravity sink, whereas objects of lower specific gravity float (Kunii and

Levenspiel 1991). In order to induce particle formulation and structurization, a solid-containing liquid is sprayed onto the particles, while they are fluidized by gas. In case of granulation or coating, the liquid spreads on the particle surface and evaporates due to the heated fluidization gas, forming a solid shell around the core (Uhlemann and Mörl 2000). Alternatively, a molten liquid can be injected in a fluidized bed. The shell formation then happens due to the cooling and solidification of melt droplets on the particle surface (Jannin and Cuppok 2013). Another possible particle formulation process is agglomeration, during which "blackberry-like" structures made of multiple connected primary particles are formed. This process is induced if the viscous and capillary forces are stronger than the kinetic force of two colliding wet particles causing the formation of a liquid bridge and later solidification into a solid bridge (Iveson et al. 2001).
Since the layer formation in fluidized bed spray granulation strongly depends on the process conditions, the process can be designed in such a way that particles with the desired properties are produced. The particle growth is influenced by several micro-processes like the deposition and spreading of droplets and the evaporation of the liquid. The knowledge of the effect of different process and material parameters on those processes and the resulting granules is invaluable to produce tailor-made particles for specific applications.

1.2 Previous works

The granulation in a fluidized bed and the factors influencing the surface morphology of the resulting granules have been investigated in several previous works. Many of these studies are focused on the dependence of the coating layer structure on the process parameters, see e.g. Orth et al. (2022), Rieck et al. (2015), Hampel (2015), Diez et al. (2018), Dewettinck and Huyghebaert (1998) for solution coating or Schmidt et al. (2017) for suspension coating.

In most of the studies investigating spray solution properties, agglomeration processes were conducted rather than coating, see Hemati et al. (2003), Pont et al. (2001) and Rajniak et al. (2007). Generally, an increased solids concentration in the binder and thus higher binder viscosity was found to favor agglomeration over layer growth. Saleh et al. (1999) studied the influence of process and solution parameters on particle growth by both, coating and agglomeration, using sand as primary particles and an aqueous sodium chloride solution as coating liquid. With increasing binder concentration, the growth rate, coating efficiency and percentage of formed agglomerates were also increased due to the higher viscous forces.

In contrast to the agglomeration process, in granulation and coating the correlation between the spray solution concentration and the particle structure is yet to be investigated. Therefore, this work is focused on the coating process and the influence of coating solution concentration on the interactions at the solid-liquid interface and the surface morphology of the produced granules.

2 Materials and methods

2.1 Materials

Megalux glass beads (Swarco, Germany) with a mean diameter of 1280 µm were used as primary particles in all experiments. Due to the non-porous and smooth surface, no droplet imbibition occurs during spraying of the liquid, making the glass particles suitable as a model substance to investigate the formation of the coating layer on the particle surface. Additionally, the glass beads provide a high sphericity and are insoluble in water, so an aqueous solution can be sprayed onto the particles. The main material properties of the Megalux beads, as measured in this work, are shown in Table 1.

Table 1: Properties of Megalux glass beads.

Mean diameter	1280	µm
Sphericity	0.94	–
Particle density	2511	kg/m³
Surface roughness	0.1	µm

As coating material, sodium benzoate, also known as E211, was used which is a white, crystalline powder that is used as a preservative in food industry. Additionally, it has a good solubility in water. The sodium benzoate was injected into the fluidized bed in form of an aqueous solution with a varied solids concentration up to 32 wt%.

2.2 Coating experiments

The coating experiments were carried out in the laboratory-scale fluidized bed system ProCell®5 with the GF3 process chamber with a diameter of 180 mm at the air inlet (Glatt, Germany). A scheme of the plant is shown in Figure 1. For the injection of the coating solution, a two-fluid nozzle (type 970-S4, Schlick, Germany) with an orifice size of 1.2 mm was installed in the middle of the sieve plate distributor in bottom-spray configuration. Compressed air was used for the atomization of the liquid which was conveyed to the nozzle by a peristaltic pump (Medorex TB, Germany).

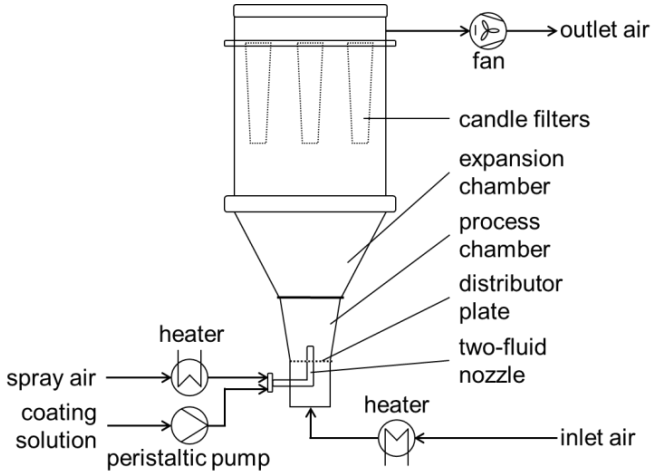

Figure 1: Scheme of the fluidized bed set-up for coating experiments.

All experiments were performed batch-wise with an initial bed mass of 3 kg of glass beads. The amount of injected solution was adapted in such a way that 600 g of solids were sprayed onto the particles per experiment. The fluidization air flow was set to 200 m³/h which enabled a stable fluidization of the glass particles throughout the whole experiment. The inlet air temperature of the fluidization air was kept constant at 70 °C and the spray air pressure to atomize the injected liquid was 1 bar. The sodium concentration of the coating solution was varied between 15 and 32 wt%, with the lower limit being defined by the duration of the experiment and the upper limit being constrained by the saturation of the solution which was determined beforehand. To maintain the same drying conditions for all experiments, the spray rate was chosen in such a way that the water mass flow injected into the process chamber was identical. An overview of the spray rates and sodium benzoate concentrations is given in Table 2.

Table 2: Spray parameters for coating experiments.

Liquid spray rate [g/min]	Sodium benzoate concentration [wt%]
20.6	15
21.9	20
23.3	25
25.0	30
25.7	32

2.3 Analysis of coating solution and product particles

In order to find connections between the coating solution properties and the resulting granule characteristics, the different solutions as well as the solid-liquid interactions and the particle surface structure were analyzed. Therefore, the liquid viscosity, the contact angle and the surface roughness were measured.

2.3.1 Characterization of rheological behavior via viscosity measurement

The rheological behavior of a liquid determines the liquid's flow properties. To quantify this behavior, the dynamic viscosity which indicates a material's resistance to deformation at given conditions can be measured. The measurement procedure was carried out in a rotary rheometer (RHEOTEST® RN 4.1, Rheotest, Germany) with a coaxial cylinder set-up at 20 °C. All coating solutions at different solids concentrations have been analyzed at shear rates up to 2000 1/s.

2.3.2 Characterization of solid-liquid phase interaction via contact angle measurement

The sessile drop method according to DIN EN ISO 19403-2 (Deutsches Institut für Normung e.V. 2020) was conducted to determine the contact angle of sodium benzoate solutions on a glass and a sodium benzoate surface. The contact angle is based on the force balance of the interfacial energies at the gas-liquid, gas-solid, and solid-liquid interfaces and characterizes the wetting behavior of a liquid on a solid surface. At a contact angle of 0 °, the surface is completely wetted by the liquid, for angles below 90 ° partial wetting takes place, an angle above 90 ° indicates negligible wetting, and at 180 ° the material is non-wetting (Adam et al. 2009; Dallmann 2011).

To mimic the surfaces that the liquid droplets interact with during the coating process – glass particles and already coated particles – glass slides and glass slides coated with a sodium benzoate film have been used. For each coating solution, three droplets with a volume of 3 µl have been placed on both investigated surfaces. The spreading of each droplet was recorded with a frequency of 100 Hz over a duration of five seconds using a highspeed camera (NX-S2, Imaging Solutions GmbH, Germany). For the determination of the contact angle, the obtained images were evaluated using the open-source software ImageJ (University of Wisconsin, USA).

2.3.3 Characterization of surface structure via confocal laser-scanning microscopy

In contrast to a conventional light microscope, where the entire sample is illuminated by a light source causing the detection of unfocused planes, only a small part of the sample is illuminated at each time in a confocal laser-scanning microscope. During scanning the position of the focal point on the sample changes. At different positions along the vertical axis the area within the field of view is scanned. From a set of those two-dimensional images the three-dimensional surface structure of the sample is reconstructed. Therefore, the confocal laser technology allows for the acquisition of height information as well as images with a large depth of field (Keyence 2015).

To measure the surface roughness of the particles, the 3D Laser Scanning Confocal Microscope VK160K (Keyence, Japan) was used. The microscope works according to the previously explained principle. Surface data acquisition can be performed at a magnification of the factors 10, 20, 50, and 100. To validate the surface structure, three particles per sample have been evaluated at two different areas on the surface respectively at a magnification of 50.

As a quantifier for the surface morphology, the surface roughness was determined. Roughness consists of a sequence of peaks and valleys forming a complex shape due to their difference in height, depth, and intervals (Keyence 2015). In DIN EN ISO 4287:2010-07 (Deutsches Institut für Normung e.V. 2010) and DIN EN ISO 25178-2:2012 (Deutsches Institut für Normung e.V. 2012) several parameters that are based on either areas or lines on the surface are defined. In this work, one of the most commonly used roughness quantifiers, the arithmetical mean height

S_a was used for the characterization of the roughness. The surface-based arithmetical mean height is defined as the average height difference of each point on the surface from the mean height of the particle surface within a measurement area A:

$$S_a = \frac{1}{A} \iint_A \left| h(x,y) - \bar{h} \right| \mathrm{d}x \, \mathrm{d}y. \quad (1)$$

Image processing was performed on the measured surface profile using a Gauss filter to smooth the profile and a surface shape correction filter to avoid an influence of the particle shape on the roughness quantification.

3 Results and discussion

3.1 Viscosity of coating solutions at different solids concentrations

Firstly, the shear stress and shear rate data that were obtained during the viscosity measurements were evaluated in order to determine the rheological behavior of the sodium benzoate solutions. For all curves a nearly linear behavior was observed indicating a Newtonian flow behavior with a constant dynamic viscosity over the investigated shear rate range. Consequently, the viscosity of each coating solution can be simply described by one mean value. Those viscosities are depicted in Figure 2 in dependence on the sodium benzoate concentration of the solution.

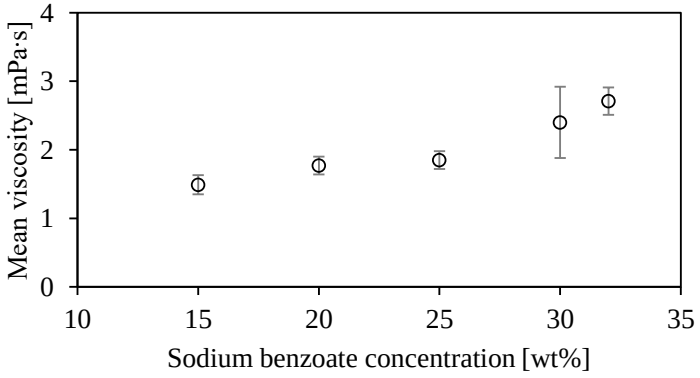

Figure 2: Mean viscosity of the sodium benzoate solutions at different concentrations.

The measured viscosities are in agreement with the rule proposed by Kern (Kern 1983) that suggests that for an aqueous salt solution with a concentration below 30 %, as used for most of the solutions in this work, the viscosity should be less than twice the viscosity of water. This is the case for the solutions with a sodium benzoate concentration below 30 wt%. Figure 2 shows an increasing viscosity with increasing solids concentration. As expected, the additional sodium benzoate in the higher concentrated solutions increase the internal friction of the liquid and thus the internal resistance to flow causing the observed increase in viscosity (Viswanath et al. 2007). Due to this increased resistance to deformation, more deviations occurred at higher viscosities. The different viscosities of the spray solutions are expected to influence the atomization of the liquid and therefore the droplet characteristics such as droplet size which in turn affects the surface structure of the granules (Hede et al. 2008; Orth et al. 2022).

3.2 Contact angle between coating solutions and different surfaces

In Figure 3, the contact angles of coating solution droplets on a glass surface are shown over the time span of five seconds after the initial contact between liquid and solid. The curves are similar for all solutions, starting at the highest contact angle that then quickly decreases over time as the droplet spreads on the surface. The highest initial contact angle was reached for the concentration of 32 wt% at 69.1 ± 1.2 °, while the lowest initial contact angle of 47.0 ± 0.9 ° was recorded for the lowest concentration of 15 wt%. After five seconds a contact angle between 19 ° and 23 ° was reached for all solutions indicating that partial wetting occurs which enables a good spreading of the solutions on the glass surface. Based on the measured contact angles over time, the fastest spreading is expected for droplets of the 15 wt% solution on the glass surface of the primary particles. At higher concentrations, the increased viscosity of the solution causes a higher flow resistance of the liquid and thus hinders the spreading of the droplet.

It has to be noted though that the measurement on the even glass slide does not consider the influence of the curved surface of the glass particles on droplet spreading and can therefore only be used to estimate the wetting behavior. Moreover, in the contact angle measurement, the droplet is slowly placed on the sample surface, whereas in the fluidized bed process, the droplets are accelerated by the spray air and the fluidization air before colliding with the also moving particles.

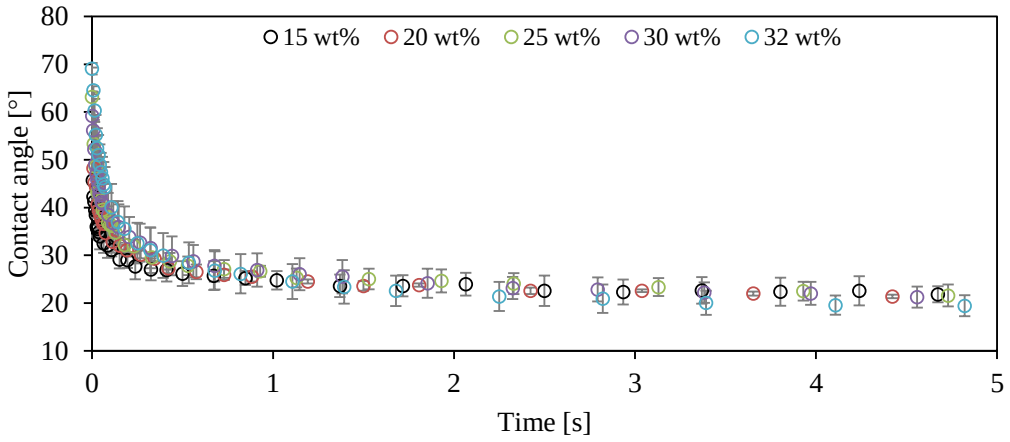

Figure 3: Contact angle of coating solutions with different concentrations on glass surface.

Once the particles are partially or completely covered with sodium benzoate, droplets come in contact with either pure glass, both, glass and sodium benzoate, or pure sodium benzoate upon droplet-particle collisions. As depicted in Figure 4, the contact angle curve over time on a sodium benzoate film generally shows the same trend as the measurements on glass for all solutions except for the concentration of 20 wt%. Since sodium benzoate is well soluble in water, not only spreading of the droplets is occurring but also dissolution of the sodium benzoate film. Hence, the recorded data represents the combined effect of both of these phenomena. In addition, the higher roughness of the sodium benzoate film compared to the smooth surface of the glass slide also influences the contact angle. Since all measured angles are below 90 °, the contact angle decreases with increasing roughness meaning that slightly higher contact angles than the measured ones are expected on a sodium benzoate surface (Busscher et al. 1984; Wenzel 1936). Nevertheless, Figure 4 shows a generally slower droplet spreading on the

sodium benzoate layer compared to the glass slides indicating that once a first sodium benzoate layer is formed on the particles during the coating, the wetting behavior of the droplets on the particle surface is changed.

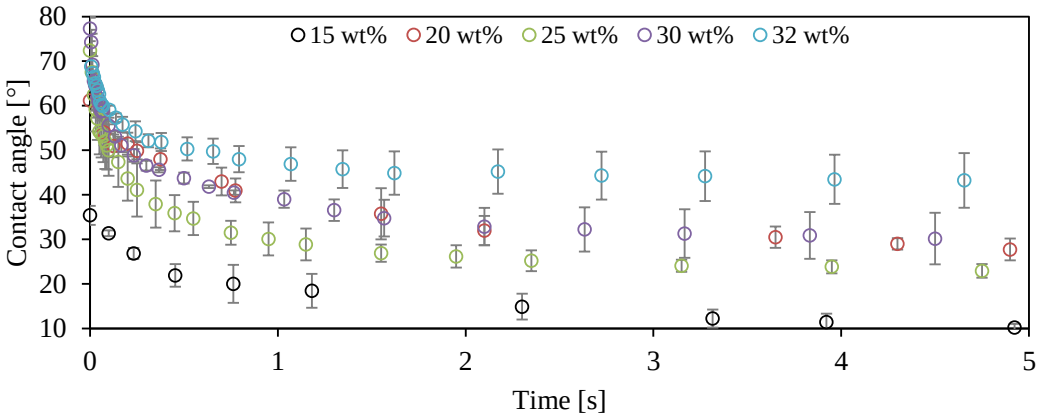

Figure 4: Contact angle of coating solutions with different concentrations on sodium benzoate surface.

3.3 Influence of solids concentration on surface roughness

During the fluidized bed spray granulation or coating, the formation of the coating layer and the resulting surface structure are dependent on several micro-processes occurring within the droplets and at the solid-liquid interface. The surface roughness for the particles coated with solutions with different sodium benzoate concentrations is depicted in Figure 5. Based on the results of the viscosity and contact angle analysis, a higher surface roughness could be expected at higher solids concentrations due to the slower spreading of droplets on the particle surface. However, in the concentration range from 20 wt% to 32 wt% the exact opposite trend was observed. Only for a concentration of 15 wt%, a lower surface roughness of 6.35 ± 2.02 µm was measured.

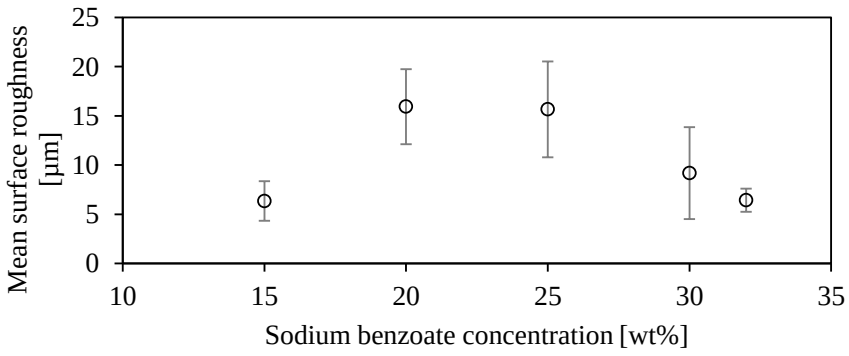

Figure 5: Surface roughness of particles coated with differently concentrated solutions.

To explain the trend for the surface roughness, the crystallization of sodium benzoate has to be considered. Once injected into the process chamber, the water in the droplets begins to evaporate, eventually causing an over-saturation of sodium benzoate in the shrinking droplet. In the

over-saturated droplet, nuclei are formed which then grow into larger crystals. The crystal growth depends on the solids concentration in the droplet in such a way that a high concentration and therefore high over-saturation upon evaporation of the water lead to the precipitation of numerous small nuclei in a short drying time. Those small crystals then form a dense coating with a smooth surface. In contrast, at a low sodium benzoate concentration in the injected droplets and hence a lower over-saturation within the droplet upon evaporation, larger crystals grow on the particle surface resulting in a higher surface roughness. Those needle shaped crystals can be seen in the microscope image recorded for the coating with a 20 wt% solution in Figure 6. Since the same water mass flow and the same air temperature were set for all experiments, equal drying conditions are assumed, so the saturation of the droplets is only influenced by the concentration of the solution.

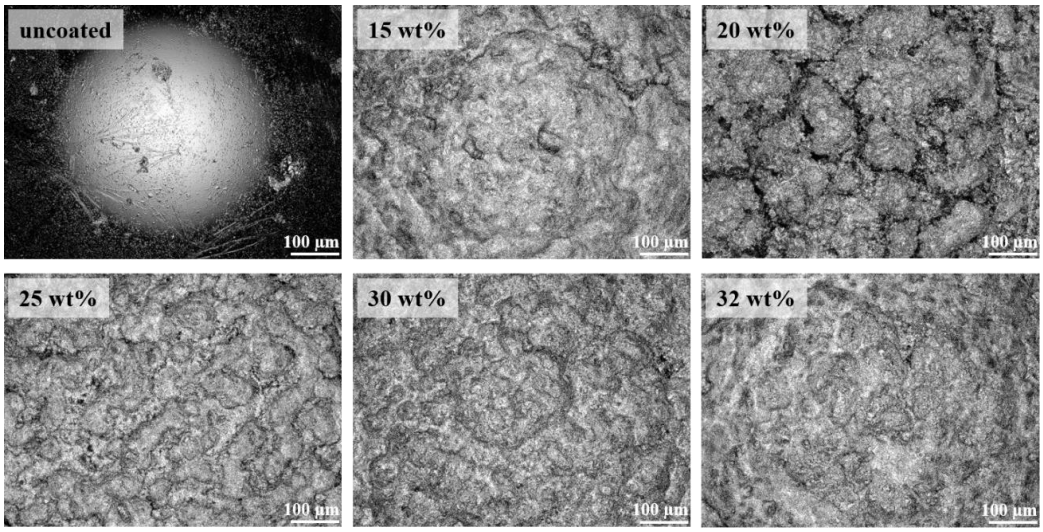

Figure 6: Laser-scanning microscope images of uncoated and coated particles.

While the crystallization of sodium benzoate explains the decreasing surface roughness with increasing solids concentration, it does not give a reason for the lower roughness measured for the particles coated with the 15 wt% solution. One explanation might be the small amount of sodium benzoate that is injected into the process chamber per time step. After the formation of nuclei, crystal growth occurs by attachment of molecules or atoms from the solution to the nuclei. Because of the strong dilution of the solids in the solution, this attachment might be hindered by the unavailability of further sodium benzoate molecules near an already formed nucleus. With this reduced crystallization, the improved wetting behavior of the 15 wt% solution, especially on a sodium benzoate surface (see Figure 4), leads to the formation of a smoother particle surface. Additionally, the already deposited salt might be partially dissolved again upon contact with another droplet spreading the solid even further on the surface. This phenomenon is most likely to occur for the lowest concentration at which the solution is the least saturated. As the experiment with the 15 wt% solution was the longest due to the lowest spray rate, effects like over-spray and abrasion that can cause mass loss and influence the surface structure are assumed to be more pronounced compared to the other runs.

4 Conclusion

To investigate the influence of the coating solution concentration on the surface structure, fluidized bed spray granulation experiments were performed with coating solutions of different concentrations. The focus of this work was the particle growth by layering rather than agglomeration which has already been researched in previous studies. The surface morphology of the product particles was analyzed by means of confocal laser-scanning microscopy to determine the surface roughness. Furthermore, the liquid viscosity and contact angle were measured in order to obtain a deeper understanding about the interactions at the solid-liquid interface.

In conclusion, the coating solution concentration has a significant impact on the layer formation in fluidized bed spray granulation. In the experiments conducted in this work, the roughness seems to be mainly determined by the sodium benzoate crystals on the particle surface rather than droplet spreading speed. Thus, the surface roughness decreases with increasing solids concentration between 20 wt% and 32 wt% despite the diminished wettability and flowability. Only at very low concentrations, this trend is reversed resulting in a smoother surface for the particles coated with the 15 wt% solution.

To improve the investigation of the connection between liquid properties, the phenomena occurring at the solid-liquid interface, and the granule surface morphology, the droplet characteristics should be further analyzed. Moreover, the contact angle measurement directly on the particle surface instead of a simplified even surface and the droplet spreading behavior in case of accelerated droplets and particles would be of interest. In addition, the process can be simulated using the coupling of computational fluid dynamics (CFD) and the discrete element method (DEM) in order to improve the general understanding of the fluidized bed process and the micro-processes happening within the particle bed.

References

[1] Adam, G.; Läuger, P.; Stark (2009): Physikalische Chemie und Biophysik. Fünfte, überarbeitete Auflage. Dordrecht, Heidelberg, London, New York: Springer (Springer-Lehrbuch).

[2] Boerefijn, R.; Hounslow, M. J. (2005): Studies of fluid bed granulation in an industrial R&D context. *Chemical Engineering Science* 60 (14): 3879–3890.

[3] Busscher, H. J.; van Pelt, A.W.J.; Boer, P. de; Jong, H. P. de; Arends, J. (1984): The effect of surface roughening of polymers on measured contact angles of liquids. *Colloids and Surfaces* 9 (4): 319–331.

[4] Dallmann, S. (2011): Reinigung superhydrophober Oberflächen. Dissertation. Technische Universität Dortmund, Dortmund.

[5] Dewettinck, K.; Huyghebaert, A. (1998): Top-Spray Fluidized Bed Coating: Effect of Process Variables on Coating Efficiency. *LWT - Food Science and Technology* 31 (6): 568–575.

[6] Diez, E.; Meyer, K.; Bück, A.; Tsotsas, E.; Heinrich, S. (2018): Influence of process conditions on the product properties in a continuous fluidized bed spray granulation process. *Chemical Engineering Research and Design* 139: 104–115.

[7] Deutsches Institut für Normung e.V. (2020): DIN EN ISO 19403-2 Paints and varnishes - Wettability - Part 2: Determination of the surface free energy of solid surfaces by measuring the contact angle.

[8] Deutsches Institut für Normung e.V. (2012): DIN EN ISO 25178-2:2012 Geometrical product specifications (GPS) - Surface texture: Areal - Part 2: Terms, definitions and surface texture parameters.

[9] Deutsches Institut für Normung e.V. (2010): DIN EN ISO 4287:2010-07 Geometrical product specifications (GPS) - Surface texture: Profile method - Terms, definitions and surface texture parameters.

[10] Hampel, N. (2015): Diskontinuierliches und kontinuierliches Pelletcoating im Wurster-Wirbelschichtprozess. Dissertation. Otto-von-Guericke-Universität Magdeburg, Magdeburg.

[11] Hede, P. D.; Bach, P.; Jensen, A. D. (2008): Two-fluid spray atomisation and pneumatic nozzles for fluid bed coating/agglomeration purposes: A review. *Chemical Engineering Science* 63 (14): 3821–3842.

[12] Hemati, M.; Cherif, R.; Saleh, K.; Pont, V. (2003): Fluidized bed coating and granulation: influence of process-related variables and physicochemical properties on the growth kinetics. *Powder Technology* 130 (1-3): 18–34.

[13] Iveson, S. M.; Litster, J. D.; Hapgood, K.; Ennis, B. J. (2001): Nucleation, growth and breakage phenomena in agitated wet granulation processes: a review. *Powder Technology* 117 (1-2): 3–39.

[14] Jannin, V.; Cuppok, Y. (2013): Hot-melt coating with lipid excipients. *International journal of pharmaceutics* 457 (2): 480–487.

[15] Kern, D. Q. (1983): Process heat transfer. Tokyo: McGraw-Hill International.

[16] Keyence (2015): 3D Laser Scanning Confocal Microscope VK-X250K/X260K, VK-X150K/X160K, VK-X120K/X130K: User's Manual.

[17] Kunii, D.; Levenspiel, O. (1991): Fluidization engineering. Second edition. Stoneham, Massachusetts: Butterworth-Heinemann (Butterworth-Heinemann Series in Chemical Engineering).

[18] Orth, M.; Kieckhefen, P.; Pietsch, S.; Heinrich, S. (2022): Correlating Granule Surface Structure Morphology and Process Conditions in Fluidized Bed Layering Spray Granulation. *KONA Powder and Particle Journal* 39: 230–239.

[19] Pont, V.; Saleh, K.; Steinmetz, D.; Hémati, M. (2001): Influence of the physicochemical properties on the growth of solid particles by granulation in fluidized bed. *Powder Technology* 120 (1-2): 97–104.

[20] Rajniak, P.; Mancinelli, C.; Chern, R. T.; Stepanek, F.; Farber, L.; Hill, B. T. (2007): Experimental study of wet granulation in fluidized bed: impact of the binder properties on the granule morphology. *International journal of pharmaceutics* 334 (1-2): 92–102.

[21] Reynolds, G. K.; Fu, J. S.; Cheong, Y. S.; Hounslow, M. J.; Salman, A. D. (2005): Breakage in granulation: A review. *Chemical Engineering Science* 60 (14): 3969–3992.

[22] Rieck, C.; Hoffmann, T.; Bück, A.; Peglow, M.; Tsotsas, E. (2015): Influence of drying conditions on layer porosity in fluidized bed spray granulation. *Powder Technology* 272: 120–131.

[23] Saleh, K.; Cherif, R.; Hemati, M. (1999): An experimental study of fluidized-bed coating: influence of operating conditions on growth rate and mechanism. *Advanced Powder Technology* 10 (3): 255–277.

[24] Schmidt, M.; Bück, A.; Tsotsas, E. (2017): Shell porosity in spray fluidized bed coating with suspensions. *Advanced Powder Technology* 28 (11): 2921–2928.

[25] Uhlemann, Hans; Mörl, Lothar (2000): Wirbelschicht-Sprühgranulation. Berlin, Heidelberg: Springer (VDI-Buch).

[26] Viswanath, D. S.; Tushar, K. G.; Prasad, D.H.L.; Dutt, N.V.K.; Rani, K. Y. (2007): Viscosity of Liquids. Theory, Estimation, Experiment, and Data. Dordrecht: Springer Netherlands.

[27] Wenzel, R. N. (1936): Resistance of solid surfaces to wetting by water. *Industrial & Engineering Chemistry* 28 (8): 988–994.

[28] Winkler, F. (1926): Verfahren zum Herstellen von Wassergas. Applied for by IG Farbenindustrie AG. Patent no. DE437970C.

Acknowledgements

Maike Orth acknowledges funding from the German Research Foundation within the DFG Graduate School GRK 2462 “Processes in natural and technical Particle-Fluid-Systems (PintPFS)” (Project No. 390794421).

Authors

Maike Orth, M.Sc.
Hamburg University of Technology
Institute of Solids Process Engineering and Particle Technology
Denickestraße 15
21073 Hamburg
Tel.: +49 (0) 40 - 42878 / 4279
e-mail: maike.orth@tuhh.de
Web: www.tuhh.de/spe

Delaram Alibabaei, B.Sc.
Hamburg University of Technology
Institute of Solids Process Engineering and Particle Technology
Denickestraße 15
21073 Hamburg

Dr.-Ing. Swantje Pietsch-Braune
Hamburg University of Technology
Institute of Solids Process Engineering and Particle Technology
Denickestraße 15
21073 Hamburg
Tel.: +49 (0) 40 - 42878 / 3139
e-mail: swantje.pietsch@tuhh.de
Web: www.tuhh.de/spe

Prof. Dr.-Ing. habil. Dr. h.c. Stefan Heinrich
Hamburg University of Technology
Institute of Solids Process Engineering and Particle Technology
Denickestraße 15
21073 Hamburg
Tel.: +49 (0) 40 - 42878 / 3750
Fax: +49 (0) 40 - 42878 / 2678
e-mail: stefan.heinrich@tuhh.de
Web: www.tuhh.de/spe

About modeling rheology and agglomeration of wet particle systems

Stefan Luding

Abstract: This brief article is a review of our recent results on the flow-behavior and rheology of dry and wet cohesive particles. For weak and moderate strength of attractive forces, a new set of rheological laws was derived from particle simulations. This local granular rheology is based on the □(*I*) and □(*I*) rheology, generalized by multiplicative correction terms that depend on the inertial number *I* and on other dimensionless variables (like confining stress *P**, or the cohesive strength, as quantified by the local Bond number Bo) that characterize the local situation, the state the particles are in. Each correction relates to one (or more) mechanisms that are active in the powder – and the correction terms fall back to unity, i.e., become inactive, when a mechanism is not important, not relevant. Only if attractive forces are strong enough, when the local Bond number Bo>1, agglomeration kicks in and the rheology that is based on homogeneous flow situations becomes questionable.

1 Introduction

The behavior of particulate systems or granular matter – for example sand, powders, suspended particles as colloids or macro-molecules – is of interest for a wide range of industries and research disciplines. These materials are intrinsically disordered, come with a wide distribution of particle sizes and materials/mixtures and can behave both solid- or fluid-like, dependent on the balance between energy input (external parameters: agitation, driving) and energy dissipation (e.g., due to material properties: contact deformation, friction, viscosity). The micro-mechanical processes in particle systems are active at multiple scales (from nanometers to meters) and understanding them better is an essential challenge for both science and application, i.e., finding the reasons for natural/industrial disasters like avalanches or silo-collapse.

To understand the fundamental micro-mechanics one can use particle simulation methods. However, large-scale applications (due to their enormous particle numbers) must be addressed by upscaled coarse grains or by continuum theory. To bridge the gap between the discrete and continuum scales, so-called micro-macro transition methods translate particle positions, velocities, and forces into density-, stress-, and strain-fields. These macroscopic quantities must be compatible with the conservation equations for mass, momentum, and energy of continuum

theory. Possibly, non-classical fields are needed to describe the micro-structure or the statistical fluctuations, e.g. the kinetic stress, before one can solve real application problems.

2 Granular state space

The particles are in different states: in different applications, in different systems, they are locally experiencing different situations. State variables are the shear or deformation rate, as quantified by the inertial number I (as relating the pressure- to the rate-time-scale) or the confining stress, as quantified by the dimensionless pressure P^* (as relating the contact-stiffness- to the pressure-time-scale, both squared). State variables can be interdependent, e.g., the inertial number depends inversely on the square-root of pressure.

On the other hand, the cohesive strength, strictly speaking, is a material parameter, as quantified by the gravity Bond number Bo_g that relates the cohesive forces to the gravity force on a single particle. However, the more relevant comparison is between the cohesive force and the local confining forces $f \propto Pd^2$, as quantified by the local Bond number Bo, which also renders it a state variable. See publications by Shi et al. (2020) and Roy et al. (2017) for the detailed definitions and rheology results from simulations, and Fig.1 for the state space spanned by I and P^*.

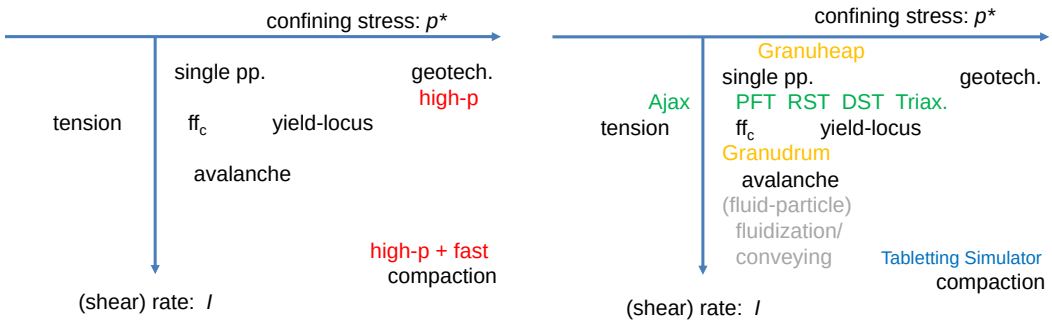

Figure 1: Schematic diagram of granular states in the plane of confining stress (to the right), tension (to the left) and dimensionless shear or deformation rate (vertical down); the left panel shows the state variables at their respective relevant location in state-space, while the right panel also indicates a selection of experiments that can be used at that states. [The experimental abbreviations are: Ajax Tensile Tester, PFT=particle flow tester, RST=ring shear tester, DST=direct shear tester, Triax=triaxial geotechnical tester, and the Granu* abbreviates GRANUTOOLS devices like heap-test or rotating drum.]

Evidently, most experiments can operate only in a limited domain in parameter space. Therefore, the tensile regime was combined with results from the RST device by Garcia-Trinanes et al. (2019) and the drum was connected to heap and RST situations by Shi et al. (2020b). The role of cohesion at various states/situations was studied by Roy et al. (2017); Shi et al. (2020) numerically, and by Jarray et al. (2019) experimentally – see also references therein.

2.1 Bridging between compression and tension

Powders with cohesive forces allow to range from compressive shear to tensile testing (Garcia-Trinanes et al. 2019). Measurement and prediction of cohesive powder behaviour related to aspects/phenomena such as flowability, flooding or arching in silos is challenging. Previous attempts in comparing different testers did not yield reliable data (showing considerable scatter and uncertainty in key quantities). Studies to build a reliable experimental database using reference materials are needed to evaluate the repeatability and effectiveness of shear testers and the adopted procedures.

Shi et al. (2018) studied the effect of particle size on the yield locus for different grades of limestone (calcium carbonate). We use the non-linear Warren Spring relation for shear stress: $\tau(\sigma)/C=(\sigma/T+1)^{1/n}$, with confining stress σ, to obtain the values of cohesion C, tensile strength T, and the shear index n. We recover linear ($n = 1$) yield loci for large, free flowing particles, with respectively small C and T, with consistent, finite macroscopic friction $C/T = 0.7$. For particle size decreasing below 70 μm the response becomes more and more cohesive (larger C and T) and non-linear ($1<n<2$) – see Garcia-Trinanes et al. 2019; the latter $n>1$ implies that a linear fit ($n=1$) to the yield locus of a cohesive powder is not making much sense.

Then Garcia-Trinanes et al. (2019) compare the values of the parameters C, T and n obtained from two different shear testers (Schulze and Brookfield PFT). Both testers run at positive confining stresses (slightly different ranges and principles) and give identical results for large fractions (weakly cohesive). For strongly cohesive samples, the PFT results are very similar to the ring shear tester, with slightly smaller values for C, T, and n.

Finally, the (non-linearly extrapolated) values of T were compared with a direct, transverse measurement running at negative stresses, using the Ajax tensile tester, and very good agreement was found – validating the Warren Spring equation for negative stresses (Garcia-Trinanes et al. 2019). Further experiments with a variety of cohesive powders are needed to confirm the connection between moderate compression and tension, and also to confirm (or rebut) this systematic, consistent differences between shear testers for, so far, only one cohesive powder.

2.2 Bridging between low and high stress, slow and fast deformations

Because the flow behavior of powders depends on both their flow/deformation rate and confining stresses, as well as on their cohesive strength, it is difficult to measure/quantify powders with only one experiment. Commonly used characterization tests, which cover a wide range of states, were compared by Lumay et al. (2019): including (static, free surface) angle of repose, (quasi-static, confined) ring shear steady state angle of internal friction, and (dynamic, free surface) rotating drum flow angle/slope, using free flowing, moderately and strongly cohesive limestone powders.

Free flowing powder gives good agreement of the measured angles (slopes or shear resistance) among all different situations (devices), while the cohesive powders are more interesting. Starting from the flow angle in a rotating drum and going slower, one can extrapolate to the limit of zero rotation rate. However, the angle of repose measured from the static heap is considerably larger, possibly due to its special history. When the ring shear tester explores its lowest

confining stress limit, the steady state angle of internal friction of the cohesive powder becomes comparable with the flow angle (at the free surface) in the zero-rotation rate limit of the rotating drum test, but only when defining an appropriate effective stress for the flow zone. Finally, when stretching the confining stress to extremely large values (GPa) by using a tableting tester, the qualitative behavior (increase of shear resistance, macroscopic friction with decrease in particle size) is confirmed, but the almost linear behavior in the low stress range (kPa to MPa) turns to an increasingly non-linear growth – details see Lumay et al. (2019) and Shi et al. (2018).

Also here, further experiments with a variety of cohesive powders are needed to confirm the connection between moderate to large compression/confining stress, and tension, and also to confirm the systematic, consistent qualitative trends, so far reported for one cohesive powder.

3 Granular rheology

Here, a short summary of recent results on formulating a general local granular rheology is presented, based on an earlier review by Luding et al. (2016). When formulating a granular rheology, the starting point is the successful, simple, and elegant so-called $\mu(I)$-rheology (Shi et al. 2020), which relates the so-called macroscopic (bulk) friction, i.e., the shear-stress to pressure ratio $\mu = \tau / p$ (in a sheared particulate system in steady state) to the inertial number, i.e., the dimensionless strain-rate:

$$I = \dot{g} d_0 \Big/ \sqrt{p' / r}$$

with (for example) local shear rate $\dot{g}$, diameter d_0 = 0.0022 m, mass-density ρ= 2000 kg/m^3, and pressure p'. The relation that describes well a wide variety of flows of hard, cohesionless particles, at various strain rates is:

$$\mu(I) = \mu_0 + (\mu_\infty - \mu_0)\,\frac{1}{1 + I_0/I} \tag{1}$$

with $\mu_0 = 0.15$, $\mu_\infty = 0.42$, and $I_0 = 0.06$, matching our simulation data (Roy et al. 2017), where μ_0 and μ_∞ represent the zero and infinite strain rate limits, respectively, and the characteristic dimensionless strain-rate is I_0, above which inertia effects considerably kick in. Since our older simulations (Roy et al. 2017) concern particle simulations with a very small coefficient of particle contact friction, μ_p = 0.01, the dependence of the coefficients in Eq. (1) on friction is not considered, however, Shi et al. (2020) extended and generalized the rheology for a wide range of coefficients of friction.

The first correction to the $\mu(I)$-rheology is relevant for soft particles, as based on early results; it was originally given as linear additive term to the above rheology for small strain-rates, however, it can nicely be re-phrased as multiplicative correction factor:

$$\mu(I, p) = \mu(I)\left(1 - \left(\frac{p}{p_0}\right)^{1/2}\right) f_\mu(\mathrm{Bo}) \tag{2}$$

with the dimensionless pressure $p = p' \, d_0 / k$, the characteristic pressure at which this correction becomes considerable, $p_0 = 0.9$, and the stiffness $k = 100$ N/m. This correction accounts for a range of particle stiffness (or softness), but also for different magnitudes of gravity, as one would find in a centrifuge or on the moon. Describing granular flows using such a local approach, in opposition to non-local models, saves the beautiful simplicity of locality and nevertheless extends the basic model by including neglected features. Additional corrections f_μ(Bo) for cohesive particles involve non-linear functions of the Bond-number (see Roy et al. 2017; Shi et al. 2020; and references therein), but are omitted in the following.

Both dimensionless state variables can be expressed as a ratios of time-scales, namely $I = t_g / t_p$ and $p = \left(t_p / t_c \right)^2$, where the subscripts denote strain-rate-, pressure- and contact-stiffness-time-scales, respectively. To complete the rheology for soft, compressible particles, a relation for the density as function of pressure and shear rate is missing:

$$\phi(I,p) = \phi_c \left(1 + \frac{p}{p_\phi^c} \right) \left(1 - \frac{I}{I_\phi^c} \right) g_\phi(\mathrm{Bo}) \tag{3}$$

with the critical or steady state density under shear, in the limit of vanishing pressure and inertial number $\phi_c = 0.648$, the strain rate for which dilation would turn to fluidization $I^c{}_\phi = 0.85$, and the typical pressure level for which softness leads to huge densities $p^c{}_\phi = 0.33$ (Luding et al. 2016). Both correction terms could be more complex functions, but are presented in their first order linear term only, valid only for sufficiently small arguments: Too large inertial numbers would fully fluidize the system so that the rheology should be that of a granular fluid, for which kinetic theory applies, while too large pressure would lead to enormous overlaps, for which the contact model and the particle simulation become questionable. The considered inertial numbers are $I < 0.1$, while the pressures are $p < 0.01$. Additional corrections g_μ(Bo) for cohesive particles (Shi et al. 2020) are omitted in the following.

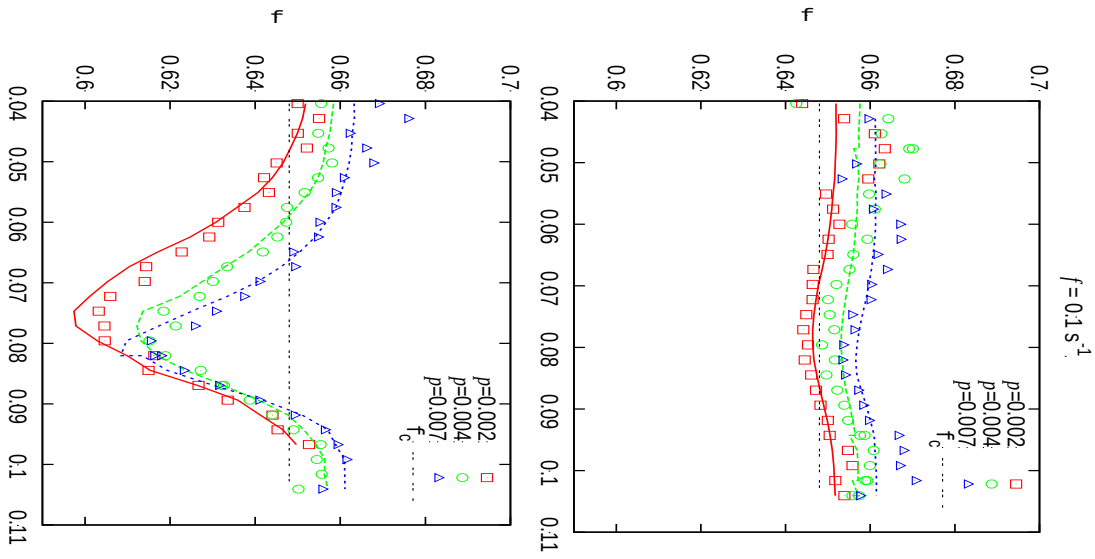

Figure 2: Density for rapid (left) and moderate (right) rotation frequency, plotted against the radial distance r, with data from particle simulations (from Luding et al. 2016), using the external rotation frequency f, given above the panels, filtered at three different (approx.) pressure levels, p, as given in the inset (i.e. red, green and blue correspond to: close to the surface, in the middle, and closer to the bottom). The lines correspond to Eq. (3), with all parameter values given in the main text; the horizontal lines give the low stress and strain-rate limit ϕ_c that, notably, is not the asymptotic limit.

From a rapid and moderate external rotation frequency, f, of the split-bottom ring shear cell, with split at R_s = 0.085 m, representative data from Roy et al. (2017), are plotted in Fig. 2 against the radial position. Higher confining stress corresponds to a higher density, deeper below the free surface, while the density is reduced in the shear band, proportional to the local shear-rate, due to dilatancy. Overall, the simulation data agree very well with the corrected density prediction from the analytical Eq. (3), where only local information enters, besides some scatter and more systematic deviations in the tails of the shear band, away from the split, with very small local strain rates (the statistics is poor, and the system is not yet in steady state).

The macroscopic friction, i.e., the shear stress ratio μ, is plotted in Fig. 3, against the radial position for the same data-sets, in comparison with the classical rheology of Eq. (1) and the pressure-dependent rheology, Eq. (2). The pressure dependence is improved when using the latter, especially in the tails, for the slower rotation rate, where the classical rheology has no pressure dependence. Nevertheless, in the tails the stress ratio does not agree well with theory, indicating missing additional correction terms that account for a combination of very low strain-rate and finite granular temperature effects, playing a role in those regimes.

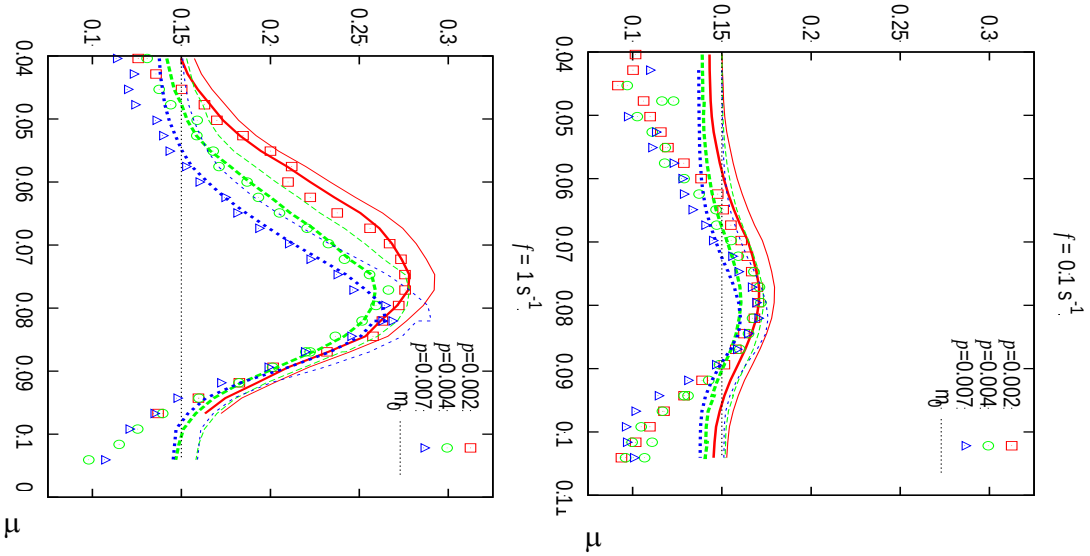

Figure 3: Shear stress ratio μ, for the same simulations as in Fig. 2 (from Luding et al. 2016). Lines correspond to Eq. (1), classical rheology (thin lines), or Eq. (2), corrected soft rheology (thick lines); parameters are given in main text. The horizontal dotted lines give the constant low strain-rate limit, μ_0.

4 Conclusion and Outlook

In conclusion, particle simulations can complement experiments, and the micro-macro transition can guide the development of new rheological particle-flow or continuum scale rheology models for density and shear stress ratio. The presented rheology includes and combines various mechanisms, as quantified by characteristic dimensionless numbers – for various different material properties including contact friction and attractive forces (Shi et al. 2020). The original, simple, scalar $\mu(I)$ and $\phi(I)$ rheology for flowing rigid, cohesionless particles was generalized to take into account the effects of large confining stress and/or softness (compressibility) of the particles, as well as attractive contact forces (Roy et al. 2017; Shi et al. 2020). Both the local density and shear stress to pressure ratio are well predicted by an improved, pressure dependent local rheology model, especially in the centre of the shear band – not so much in the tails, where the mechanism of creep becomes relevant for the shear resistance and needs to be included, as proposed by Roy et al. (2017). The deviations that still occur in the tails can be due to several reasons: (i) the statistics is much worse in areas where the strain rate is small, (ii) the system has not yet reached the true steady state – as reported previously (see Roy et al. 2017 and references therein), (iii) there can be non-local effects as encompassed, e.g., by a "fluidity" or granular temperature variable, (iv) there can be a missing parameter that encompasses the micro-structure, or further additional local corrections are needed, not considered so far. Ongoing research is aiming at finding such further corrections for very small strain rates, but also for cohesive particles. As next step the implementation of novel multi-purpose, generalized flow/rheology models into continuum solvers is needed. A further goal is the development of fully tensorial flow models, to account for all the non-Newtonian aspects of particulate and granular matter, for both static and dynamic situations and transients as well.

References

[1] Shi, H., Roy, S., Weinhart, T., Magnanimo, V. Luding, S. (2020): Steady state rheology of homogeneous & inhomogeneous cohesive granular materials, *Granular Matter* 22, 14

[2] Roy, S., Luding, S., Weinhart, T. (2017): A general(ized) local rheology for wet granular materials, *New J. Phys.* 19, 043014

[3] Shi, H., Lumay, G., Luding, S. (2020b): Stretching the limits of dynamic and quasi-static flow testing on cohesive limestone powders, *Powder Technology* 367, 183-191

[4] Garcia-Trinanes, P., Luding, S., Shi, H. (2019): Tensile strength of cohesive powders, *Advanced Powder Technology* 30(12), 2868-2880

[5] Jarray, A., Shi, H., Scheper, B. J., Habibi, M., Luding S. (2019): Cohesion-driven mixing and segregation of dry granular media, *Scientific Reports* 9(12), 13480

[6] Shi, H., Mohanty, R., Chakravarty, S., Cabiscol, R., Morgeneyer, M., Zetzener, H., Ooi, J. Y., Kwade, A., Luding, S., Magnanimo, V. (2018): Effect of Particle Size and Cohesion on Powder Yielding and Flow, *KONA* 2018014, 226-250

[7] Luding, S., Singh, A. Roy, S. Vescovi, D., Weinhart, T., Magnanimo, V. (2016): From particles in steady state shear bands via micro-macro to macroscopic rheology laws, in: *Proceedings of the 7th International Conference on the Discrete Element Method*, Xikui Li, Yuntian Feng, Graham Mustoe (Eds.), ISBN: 978-981-10-1925-8 (Print) 978-981-10-1926-5 (Online)

Author

Stefan Luding, Prof. Dr. rer.-nat. Multi Scale Mechanics
Department Thermal and Fluids Engineering, Faculty of Engineering Technology
Universiteit Twente (UT), P.O. Box 217, 7500 AE Enschede, NL
Phone: +31-(0)53 489-4212, Secr.: -3371
e-mail: s.luding@utwente.nl,
web-site: https://www2.msm.ctw.utwente.nl/sluding/

Retention Characteristics of Biopolymer Materials Studied by Inverse Supercritical Fluid Chromatography

Isabella Jung, Pavel Gurikov, Irina Smirnova

Abstract: The research project presented (funded by German Research Foundation program "Processes in Natural and Technical Particle Fluid Systems") focuses on physicochemical interactions between coated and uncoated biopolymer aerogels and different fluids in Supercritical Fluid Chromatography (SFC) for the characterization of highly porous and ultralight biopolymer aerogel surfaces as potential carrier matrices for life science applications. An important key parameter of the solute retention in terms of thermodynamic evaluation represents the retention factor k. Therefore, k of different organic solutes with different polarity on several highly porous polysaccharide and protein aerogel matrices are measured. The interactions between solutes and biopolymer aerogels were determined with the quantitative linear solvation energy relationship model (LSER). A modified van't-Hoff equation was constructed to determine the transfer enthalpy of the solute from the fluid phase to the biopolymer surface. Furthermore, a cellular automaton model is formulated to describe diffusion dynamics and adsorption of solutes in supercritical liquid phases.

1 Supercritical Fluid Chromatography

SFC is an established separation technique in analytical chemistry. Complex mixtures can be investigated with regard to their composition. In SFC, a supercritical fluid above its critical pressure (often carbon dioxide, CO_2) is used as mobile phase. By injecting a mixture of substances into the flow of the mobile high-pressure phase, the sample is flushed into a column filled with fine particles, the so-called, stationary phase. The separation of the sample mixture takes place on the surface of the stationary phase due to adsorptive interactions of the particle types and depends on the migration velocity of the contained components in the mobile phase along the separation path.[1] This retention difference is quantified as the retention time. Retention time and shape of the peak signal of molecules in the sample are used to explain physicochemical interactions between stationary phase and sample to determine thermodynamic quantities such as the enthalpy of the adsorption surface energy as well as

surface heterogeneity. From the change of the retention factor at different temperatures and constant pressure, the change of the partial molar enthalpy at infinite dilution in the mobile and stationary phase can be determined (Fig. 1).[2]

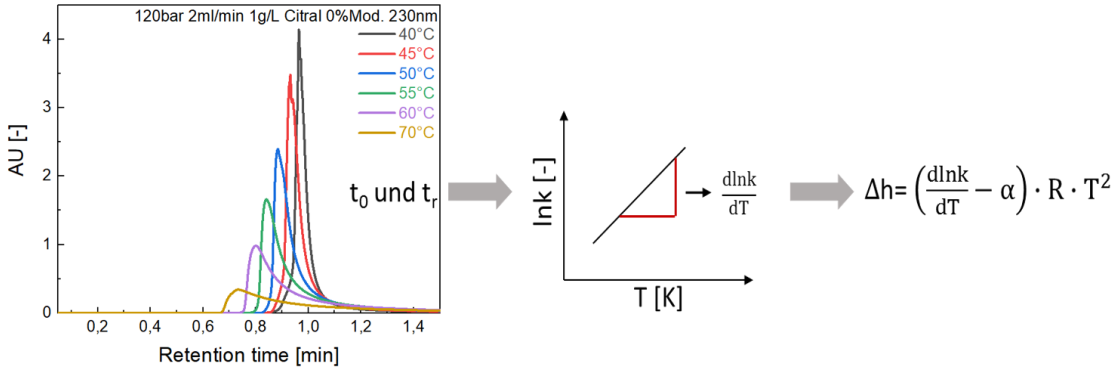

Figure 1: Calculation scheme of the adsorption enthalpy.

2 Aerogels – Ultralight Carrier Matrices

Aerogels are characterized by low density (0.004 to 0.5 g/cm^3), high specific surface area (100 to 1600 m^2/g), extremely high porosity (95 to 99.8%) and low thermal conductivity (< 0.02 W/mK).[3] The porous materials are produced by a sol-gel process, which involves specific synthesis procedures such as mixing of gel and colloidal solution (sol). The gel produced serves as a wide-meshed, three-dimensional network which interstices (pores) contain either a liquid (lyogel) or gaseous (aerogel/xerogel) phase. Depending on what has led to the crosslinking of the gel, i.e., depending on the pore filling, hydrogels (aqueous solutions) or alcohol gels (alcohol-filled interstices) are formed. In most cases, the filling of the gel pores with gaseous components is directly related to a drying process.[4] The sol-gel process is particularly suitable for inorganic (silica aerogels) and organic aerogels (resorcinol-formaldehyde aerogels).[5] Organic aerogels made from natural substances represent another group that does not undergo the classic sol-gel process. Biopolymers such as cellulose, chitin, alginate, pectin and starch serve as well-known representatives of this aerogel group. In this work, the production of biopolymer aerogels is presented (Fig 2).

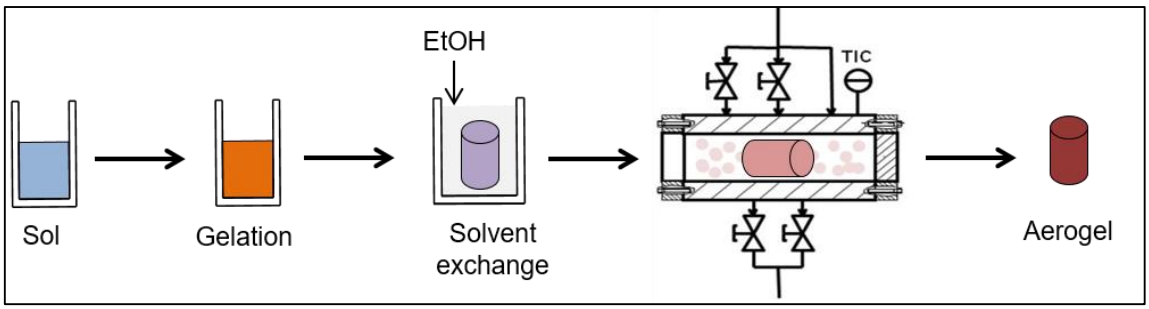

Figure 2: Schematic illustration of the aerogel production process.

The initial state of gel formation is the extracted biopolymers, which are usually in dried and powdered form. Gel formation of biopolymers occurs through the directional formation of networks or gels by the inclusion of water molecules, for example, in the complex structure of biopolymers (primary, secondary, tertiary structure). Trigger factors for this gel network formation include the induction of temperature (proteins), the change in pH (chitosan, cellulose), and the presence of (metal) ions (alginate, pectin). When these biopolymer powders get in contact with water, intra- and intermolecular interactions are formed and, in the case of alginate, ionic cross-links are formed due to the presence of metal ions. To obtain a solid gel network, fluid removal is required. This step is performed by drying the gels and is one of the most difficult steps in aerogel synthesis. The liquid in the gel network is replaced by an air or gas phase without causing excessive damage due to pore collapse. Optimal drying can achieve high porosities through small pores in the dried biopolymer network, especially in the case of biopolymers. The gels used in this work were dried using supercritical drying with CO_2 (sc-CO_2).[6] The basic principle of this process is to exchange the aqueous component in the gel network with solvent (usually ethanol) and taking it into supercritical state. The liquid component is brought to supercritical conditions (120 bar, 60°C) by increasing the temperature and pressure and is successively discharged from the gel, resulting in a dry and highly porous aerogel matrix structure. Shaping of aerogels was followed by supercritical drying. Particles in the micrometer range are required to produce the column material for use in supercritical fluid chromatography. A colloid mill was used to produce very small microparticles of the polysaccharides and both types of proteins. In this work, the gelation of the protein aerogels was thermally induced, whereas the polysaccharide gels were produced by chemical crosslinking. A colloid mill was used to produce the microparticles, with the solid particles suspended in liquid undergoing size reduction. The grinding system uses a tapered rotor, which moves around the stator at a set rotor speed (3000-26000 rpm). After complete solvent exchange, the alcogel particles of all prepared biopolymers were processed in the mill. Screening of the grinding settings was carried out using the protein gels as an example; the optimum settings were transferred to the polysaccharide gels. The agglomerates of the protein alcogels, after processing the protein-rapeseed oil emulsion, were again passed through the colloid mill breaking large particles into fine fractions. Size reduction was performed for larger alcogel particles at a rotor speed of 22,000 rpm and a gap width of 900 µm. Subsequently, the produced aerogel microparticles were subjected to solvent exchange and supercritical dried using CO_2. The prepared aerogel particles were evaluated in detail regarding their morphological and structural properties (e.g., specific surface area, pore volumes, skeletal and bulk density, particle size distribution and scanning electron microscopy). For chromatographic analysis and characterization of the prepared biopolymer aerogels, the particles were packed into commercial HPLC columns with a length of 100 mm x 4.6 mm for polysaccharide aerogels and 5 mm x 4.6 mm for protein aerogels. The particles were packed into the column using a dry vibration method and introduced into the supercritical fluid chromatography (Fig. 3).

Evaluation of retention time (residence time of solute on stationary phase) was performed using a python script specifically introduced for the application of aerogels as stationary phase. Highest Peak Method (HPM) was developed for the analysis of retention times. The determination of the dead times for the prepared aerogel columns was performed by detecting the negative peaks formed in the chromatographic spectrum. Perturbations were evaluated for all produced aerogel columns. The dead times were determined at the same wavelength as the

retention times of the respective test substances. Twenty-five organic substances were tested in this study.

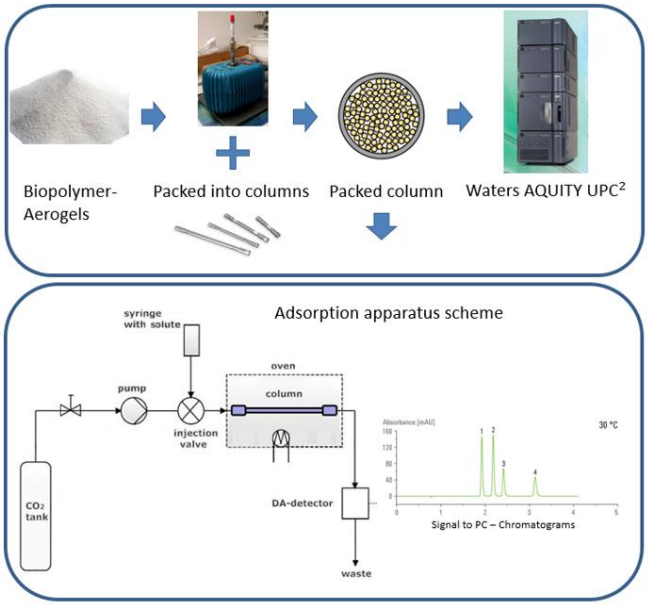

Figure 3: Schematic description of column filling via dry vibration process and SFC operation principle.

3 Linear Solvation Energy Relationship (LSER)

The LSER model is a method for characterization of stationary phases in SFC. The model describes properties of the analytes by inducing descriptors representing physiochemical properties. The model is used to predict the retention behavior of an analyte on a stationary phase or to capture the nature of the interactions in SFC and describe their relevance with respect to the solute's retention. Furthermore, the model describes the physiochemical properties of the stationary phase.[7] This includes the properties of functional groups of the stationary phase e.g., interactions with π-electrons, different hydrogen bindings, dipole-dipole interactions among others. Besides the theoretical description of aerogels, the information obtained can be used for practical purposes such as the supercritical impregnation of aerogels with organic compounds for the medical and food industry.

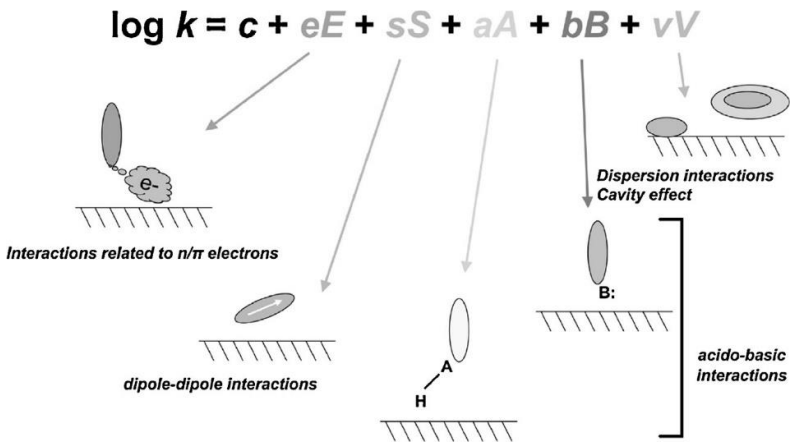

Figure 4: Interactions characterized by descriptors of the LSER model.[8]

Abraham's model is the most commonly used representation of the LSER model and is shown in Equation (1).

$$SP = c + eE + sS + aA + bB + vV \quad (1)$$

SP often corresponds to log k. The different terms (eE, sS, aA, bB, vV) represent the interaction between the solute and the mobile or stationary phase. The c constant includes the phase ratio in the chromatography column used, $\frac{V_s}{V_m}$, where V_s is the volume of the stationary phase and V_m is that of the mobile phase. [9] The c constant includes the volume of the mobile phase to the equation. The capital factors of the individual terms (E, S, A, B, V) are the descriptors of the analytes. Lower-case system constants result from a multilinear regression of the descriptors of the used analytes and their retention factors: positive values represent a stronger interaction with the stationary phase, whereas negative values imply stronger interaction with the mobile phase.[10]

4 Results

4.1 Supercritical Drying of Aerogels and Characterization

The main achievements and insights of this work are: 1) micro-aerogel particles were produced for the first time, 2) HPLC columns were successfully loaded with aerogel particles and 3) structural differences between biopolymer aerogels were found.

In order to characterize the prepared biopolymer aerogels as well as to evaluate the adsorption behavior on different organic aerogels, the structural properties were measured. Specific internal surface area, shrinkage of the gels during processing, bulk and skeletal density, porosity, particle size distribution and breaking strength were determined. For the protein aerogel production, pH was the main influencing variable. The polysaccharide aerogels (Fig.5)

produced had an internal surface area of 260-450 m^2/g, with alginate achieving the highest values in terms of specific surface area, pore volume and radius. Biopolymer powders (no aerogel) were used as reference. Potato protein isolate (PPI) at pH3 and whey protein isolate (WPI) at pH3 showed the largest specific surface area among all aerogels investigated. For WPI, the specific surface area decreased with increasing pH. In case of PPI, PPI pH7 was found to be the aerogel with the smallest specific surface area. At pH 7, PPI and WPI had the largest pore radius. Pore radius did not correlate with pore volumes. Skeletal density ranged from 1.25 g/cm^3 to 1.65 g/cm^3 and were only slightly larger than those of corresponding powders. Compared to the cellulose and chitosan aerogel particles, the alginate aerogel particles are more spherical and show smooth surface. Under high magnification, highly porous but dense structures were identified. Both, cellulose and chitosan aerogels showed coarse-pored and less dense macroscopic structures. Particles of chitosan and cellulose aerogels are less uniform and tend to agglomerate. Powder particles are generally more inhomogeneous than the aerogel particles and do not reveal any porous structures. However, only fracture sites lead to permeable fragments.

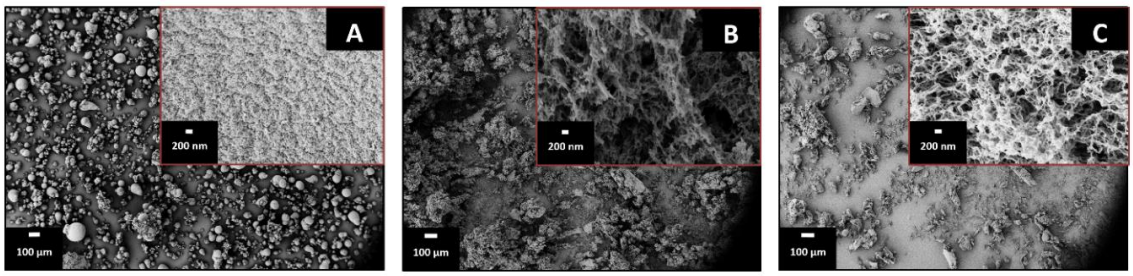

Figure 5: SEM images of polysaccharide aerogel particles at different magnifications. A: alginate aerogel, B: cellulose aerogel, C: chitosan aerogel.

4.2 SFC: Retention Time on Different Biopolymer Aerogels/Powders

The main findings of this work with regard to the retention parameters obtained are: 1) with increasing process temperature retention times of all solutes decreased, indicating an adsorption process; 2) significant differences in the adsorption behavior of aerogels and powders were found; 3) polar solutes showed higher retention times than non-polar substances, independent of the stationary phase; 4) influence of steric hindrance showed an impact on the retention behavior and allowed a first classification of the functional groups involved in the adsorption process.

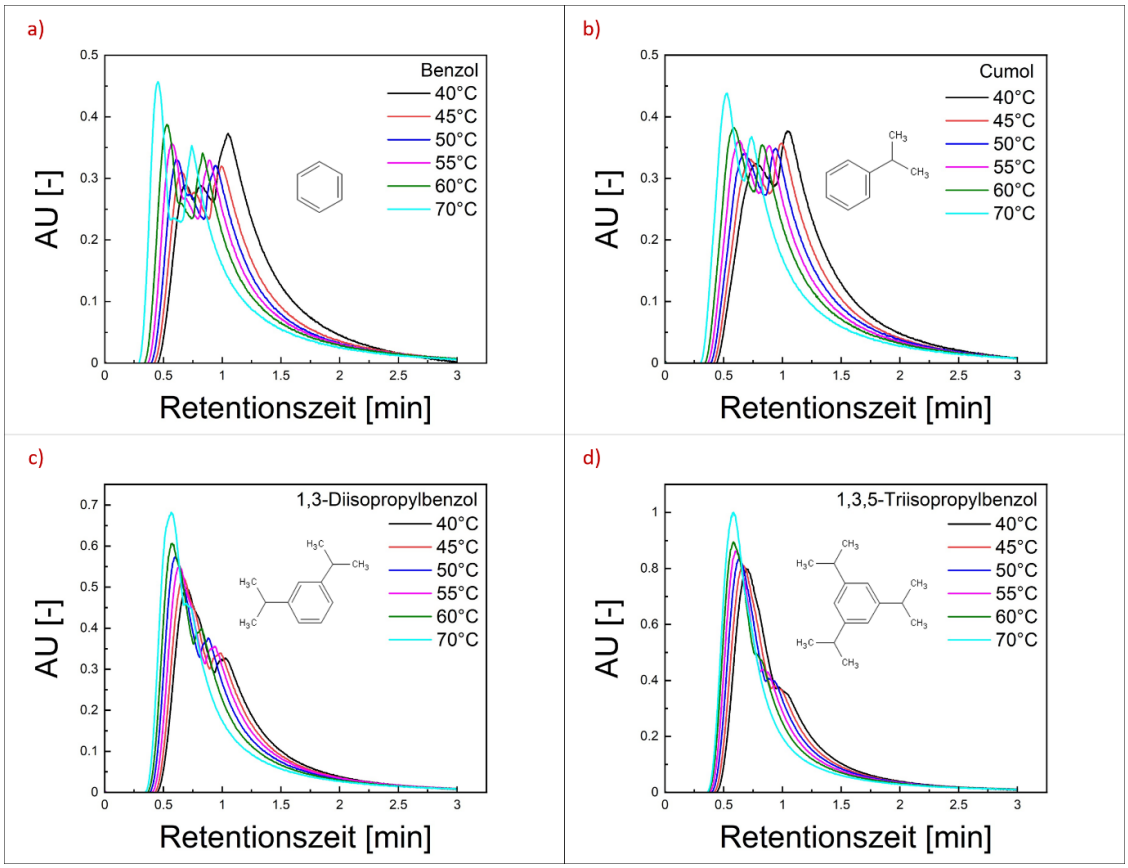

Figure 6: Chromatograms of benzole, cumol, 1,3-diisopropylbenzene and 1,3,5-triisopropylbenzene on alginate aerogel.

In the following, the results of three selected solutes are presented, which were used to describe the influence of steric hindrance in the adsorption process on alginate aerogels. Figure 6 plots the spectra of the solutes used to study steric hindrance for alginate powder and alginate aerogel at 40°C. The adsorption spectra obtained differ strongly in terms of peak shape due to tailing and fronting effects of the chromatogram, which were achieved by macro-porous properties. In contrast, aerogel powder showed significantly lower retention times with a single peak in the spectrum. When comparing polar and non-polar solutes on the aerogel column, it is remarkable, that polar solutes generally have a longer retention time. Linear relationship was found, whereby sterically hindered solutes achieved lower retention factors than smaller, unhindered molecules (e.g., cumol). Furthermore, the increased retention times for sterically unhindered molecules showed a dependency of the retention behavior on the π-electron system. Reduction of adsorption was achieved by increasing the degree of substitution as well as the resulting inhibition of the π-electron system of the substance.

Table 1: Descriptors of sterically hindered solutes with regard to electrostatic interactions.

Solute	Benzene	Cumol	1,3-Diiso-propyl-benzene	1,3,5-Tri-isopropyl-benzene
E (electrostatic interactions)		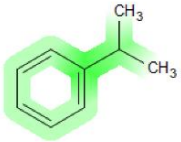	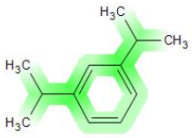	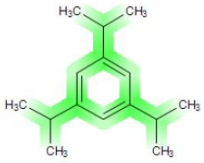

Determination of the logarithmic retention factor (lnk) allowed direct comparison of all columns in terms of adsorption behavior. For this purpose, lnk was plotted against temperature. The result was a linear correlation of all retention factors of the analytes used. The analytes listed as examples (Table 1) benzene cumene, 1,3-diisopropylbenzene and 1,3,5-triisopropylbenzene showed the adsorption trend depending on their molecular size and the interacting functional groups (Fig.7).

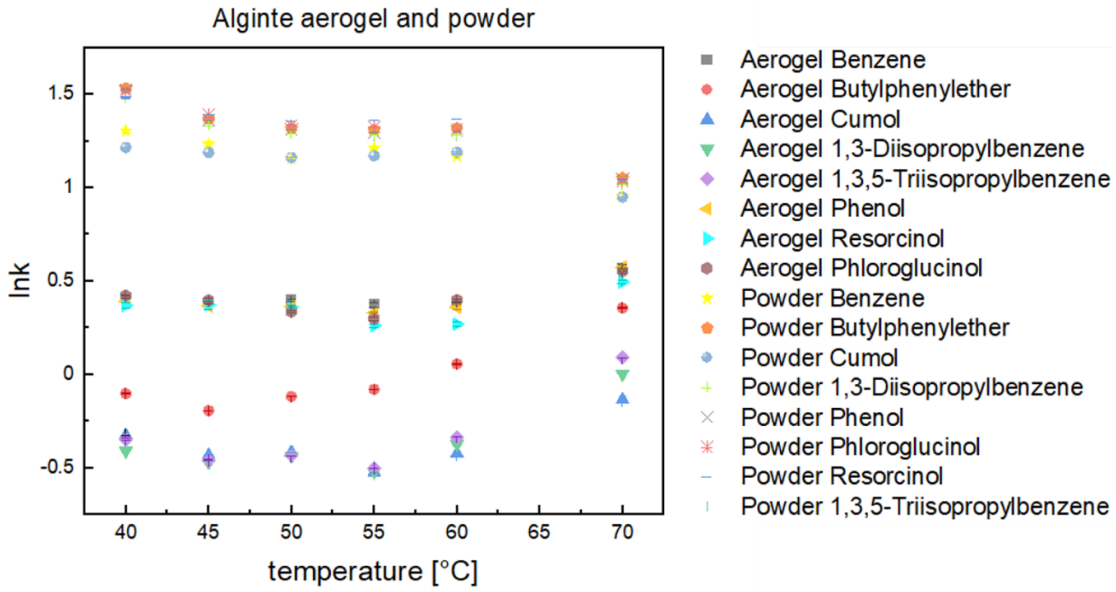

Figure 7: Dependency of retention factor (plotted as natural logarithm of k) on process temperature.

For further analysis of the adsorption behavior on an alginate column, the adsorption enthalpies were determined. Figure 8 shows courses of different sized molecules using alginate aerogel as an example stationary phase.

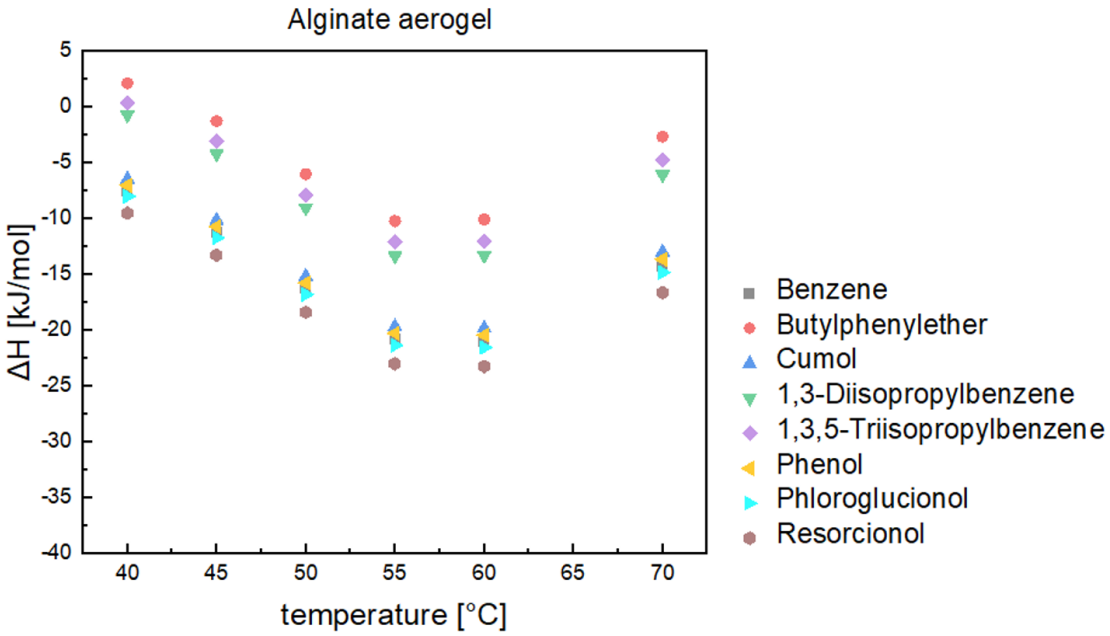

Figure 8: Adsorption enthalpies of sterically hindered solutes at 120 bar, 2ml/min, 40°C-70°C.

The adsorption enthalpy curves for the shown solutes present the highest amount of energy is released at 60°C. The adsorption increases continuously from 40°C to 60°C and decreases from 60°C to 70°C. The enthalpy of adsorption describes the enthalpy change during the transition of the analyte from the mobile to the stationary phase. In the case of alginate, most of the values are negative i.e., energy is released during adsorption (exothermic process). The adsorption of resorcinol, phloroglucinol, phenol, benzene and cumol released the highest amount of energy. This increase in adsorption energy can be explained by the relatively low degree of substitution and the unhindered access to the pi electronic system of the molecules. The adsorption of these analytes with the OH- groups of alginate seems to be particularly energetic. A direct correlation between the length of retention time and the amount of enthalpy of adsorption could not be shown. Furthermore, the retention times decreased despite increasing adsorption enthalpies in the range 40°C to 60°C. A possible explanation may be the increasing elution strength of CO_2 at higher temperatures. Therefore, the elution force of the mobile phase (CO_2) is higher than the enthalpy of the adsorption.

4.3 Modelling based on Linear Solvation Energy Relationship

In this section, the system constants determined by the multilinear regression are presented. Furthermore, aerogel-interactions are visualized in a spider diagram according to their system constants.

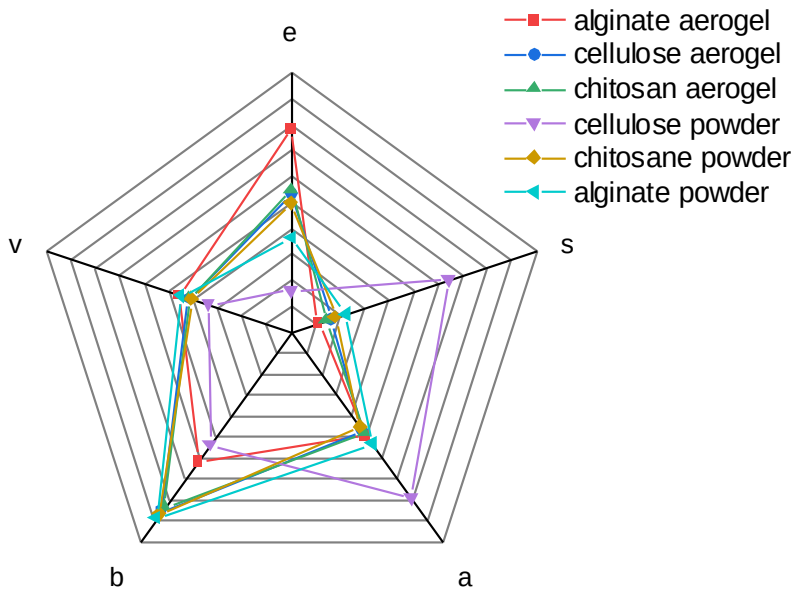

Figure 9: Visualization using a spider diagram with powder and aerogel columns made of alginate, cellulose and chitosan.

In Figure 9, the interactions of solutes (steric hindrance) with different stationary aerogel and powder phases are shown. This visualization allows a direct comparison of the system constants for the biopolymer aerogels and powders. The system constants a and b showed for nearly all stationary phases (except cellulose powder) dominant interactions. Overall, the hydrogen bonding basicity and acidity are the most important aspects for the adsorption on the biopolymer aerogel columns. Effects such as dipole-dipole interactions (s), the Mc-Gowan volume of the analyte (v) and the electrons in π- and n-orbitals (e) play a subordinate role in the interaction with the stationary phases. Powdered alginate showed similar values like the biopolymer aerogels. However, the interaction with π-electrons decreased.

5 Summary and Outlook

In this study, aerogel micro-particles were successfully produced and characterized for the first time. Method development for the identification of interactions between porous particles and solutes was performed by supercritical fluid chromatography; a LSER model was used for quantification and prediction of interactions. Cold plasma coating might serve as a functionalization tool for hydrophobization of aerogel surfaces. For complex protein aerogel structures, solid state NMR measurements are planned to be used to identify functional surface groups. Modelling of adsorption processes could predict the adsorption behavior of solutes not yet tested. MD-Simulation and Cellular automata should therefore be considered.

References

[1] Saito, M. History of supercritical fluid chromatography: Instrumental development. *Journal of Bioscience and Bioengineering* 115, 590–599 (2013).

[2] Roth, M. Determination of thermodynamic properties by supercritical fluid chromatography. *Journal of Chromatography A* 1037, 369–391 (2004).

[3] *Aerogels handbook*. (Springer, 2011).

[4] Zhao, S., Malfait, W. J., Guerrero-Alburquerque, N., Koebel, M. M. & Nyström, G. Biopolymer Aerogels and Foams: Chemistry, Properties, and Applications. Angew. Chem. Int. Ed. 57, 7580–7608 (2018).

[5] Schmidt, H. K. Das Sol-Gel-Verfahren: Anorganische Synthesemethoden. Chemie in unserer Zeit 35, 176–184 (2001).

[6] Subrahmanyam, R., Gurikov, P., Dieringer, P., Sun, M. & Smirnova, I. On the Road to Biopolymer Aerogels—Dealing with the Solvent. *Gels* 1, 291–313 (2015).

[7] West, C. Current trends in supercritical fluid chromatography. *Anal Bioanal Chem* 410, 6441–6457 (2018).

[8] Galea, C., Mangelings, D. & Vander Heyden, Y. Characterization and classification of stationary phases in HPLC and SFC – a review. *Analytica Chimica Acta* 886, 1–15 (2015).

[9] Abraham, M. H. & McGowan, J. C. The use of characteristic volumes to measure cavity terms in reversed phase liquid chromatography. *Chromatographia* 23, 243–246 (1987).

[10] West, C. & Lemasson, E. Unravelling the effects of mobile phase additives in supercritical fluid chromatography—Part II: Adsorption on the stationary phase. *Journal of Chromatography A* 1593, 135–146 (2019).

Author

Isabella Jung, M.Sc.
Technische Universität Hamburg-Harburg
Institut für Thermische Verfahrenstechnik
Eißendorfer Straße 38
21073 Hamburg
Tel.: +49 (0) 40 - 42878 / 2688
Fax: +49 (0) 40 - 42878 / 4606
e-mail: isabella.jung@tuhh.de
Web: www.tuhh.de/v8

Jun.-Prof. Dr. Ing. Pavel Gurikov
Technische Universität Hamburg-Harburg
Institut für Thermische Verfahrenstechnik
Eißendorfer Straße 38
21073 Hamburg
Tel.: +49 (0) 40 - 42878 / 4275
Fax: +49 (0) 40 - 42878 / 4606
e-mail: pavel.gurikov@tuhh.de
Web: www.tuhh.de/v8

Univ.-prof. Dr. Ing. Irina Smirnova
Technische Universität Hamburg-Harburg
Institut für Thermische Verfahrenstechnik
Eißendorfer Straße 38
21073 Hamburg
Tel.: +49 (0) 40 - 42878 / 3040
Fax: +49 (0) 40 - 42878 / 4606
e-mail: irina.smirnova@tuhh.de
Web: www.tuhh.de/v8

Recent Advances and Uses of Aerogels for Biomedical Applications

Carlos A García-González

Abstract: Aerogels are nanostructured materials with attractive and unique physicochemical properties: high and open porosity, high specific surface area, lightweight. Namely, aerogels can be exploited for biomedical applications (Figure 1), including drug delivery, wound treatments and regenerative medicine (García-González et al., 2019). The use of aerogels as carriers of bioactive compounds may result in an increase in the solubility and the modified release of certain drugs. Moreover, aerogels are particularly favorable for oral and mucosal administration routes (García-González et al., 2021). In terms of production, the aerogels can be easily scaled-up using supercritical CO_2 and the manufacturing of aerogel-based drug products under good manufacturing practices (GMP) is possible. For wound treatments, aerogels have outstanding capacity to absorb wound fluid thus contributing to haemostasis, healing and regeneration of the skin. The local release of bioactive compounds from aerogels at the wound site can be specifically used for the treatment of wounds under different healing phases (Bernardes et al, 2021). Finally, for regenerative medicine, aerogels mimic the extracellular matrix and the correct choice of the source (e.g., polysaccharide and proteins) can have relevant biological implications to promote tissue regeneration, such as the promotion of the attachment and growth of cells or the promotion of cell differentiation towards certain lineages. The technological combination of aerogel processing with 3D-printing technology has been recently implemented to provide enhanced performances to aerogels for regenerative medicine purposes (Iglesias-Mejuto et al., 2021). In this work, the most recent advances and uses of aerogels for biomedical applications (Figure 2) are herein outlined.

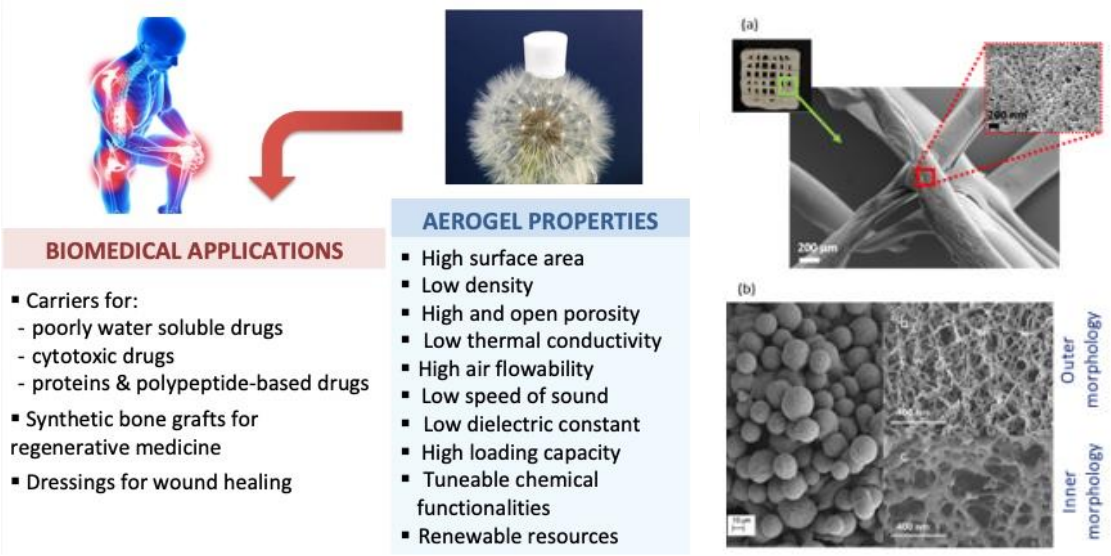

Figure 1: Potential biomedical applications of aerogels based on their properties (left), and examples of aerogels obtained in combination with 3D-printing technology.

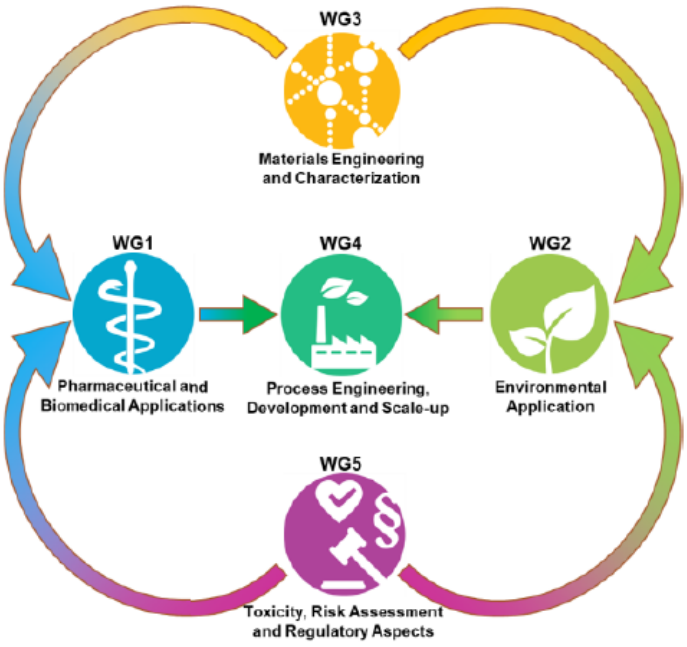

Figure 2: Organization chart of AERoGELS COST Action to bring together the knowledge on research and technology of aerogels at the European level from academia, industry and regulatory experts. For AERoGELS Action further information and updates, please visit the website https://cost-aerogels.eu.

Acknowledgments

Work carried out in the framework of the COST Action CA18125 “Advanced Engineering and Research of aeroGels for Environment and Life Sciences” (AERoGELS) and funded by the European Commission. This research was funded by Xunta de Galicia [ED431C 2020/17], MCINN [PID2020-120010RB-I00], Agencia Estatal de Investigación [AEI] and FEDER funds. Work also supported by Ignicia Programme from Axencia Galega de Innovación (Xunta de Galicia, IN855A 2021/13).

References

[1] García-González C.A., Budtova T., Durães L., Erkey C., Del Gaudio P., Gurikov P. et al. (2019): An Opinion Paper on Aerogels for Biomedical and Environmental Applications. *Molecules*, 10(9):1815

[2] García-González C.A., Sosnik A., Kalmár J, De Marco I., Erkey C., Concheiro A. et al. (2021): Aerogels in drug delivery: From design to application. *Journal of Controlled Release*, 332:40-63

[3] Bernardes B.G., Del Gaudio P., Alves P., Costa R., García-González C.A., Oliveira A.L. (2021): Bioaerogels: Promising nanostructured materials in fluid management, healing and regeneration of wounds. *Molecules*, 26:3834

[4] Iglesias-Mejuto A., García-González C.A. (2021): 3D-printed alginate-hydroxyapatite aerogel scaffolds for bone tissue engineering. *Materials Science & Engineering C*, 131:112525

Author

Carlos A García-González, PhD Eng
Universidade de Santiago de Compostela
iMATUS
Department of Pharmacology, Pharmacy and Pharmaceutical Technology
I+D Farma group (GI-1645)
Health Research Institute of Santiago de Compostela (IDIS)
Faculty of Pharmacy
Campus Vida s/n
15782 Santiago de Compostela (Spain)
Tel.: +34 881814882
e-mail: carlos.garcia@usc.es
Web: https://aerogelslab.egd.gal/